Experimental Generation and Manipulation of Quantum Squeezed Vacuum via Polarization Self-Rotation in Rb Vapor

Travis Scott Horrom

Scaggsville, MD

Master of Science, College of William and Mary, 2010
Bachelor of Arts, St. Mary's College of Maryland, 2008

A Dissertation presented to the Graduate Faculty
of the College of William and Mary in Candidacy for the Degree of
Doctor of Philosophy

Department of Physics

The College of William and Mary
May 2013

©2013
Travis Scott Horrom
All rights reserved.

APPROVAL PAGE

This Dissertation is submitted in partial fulfillment of
the requirements for the degree of

Doctor of Philosophy

Travis Scott Horrom

Approved by the Committee, March, 2013

Committee Chair
Research Assistant Professor Eugeniy E. Mikhailov, Physics
The College of William and Mary

Associate Professor Irina Novikova, Physics
The College of William and Mary

Assistant Professor Seth Aubin, Physics
The College of William and Mary

Professor John B. Delos, Physics
The College of William and Mary

Professor and Eminent Scholar Mark D. Havey, Physics
Old Dominion University

ABSTRACT

Nonclassical states of light are of increasing interest due to their applications in the emerging field of quantum information processing and communication. Squeezed light is such a state of the electromagnetic field in which the quantum noise properties are altered compared with those of coherent light. Squeezed light and squeezed vacuum states are potentially useful for quantum information protocols as well as optical measurements, where sensitivities can be limited by quantum noise. We experimentally study a source of squeezed vacuum resulting from the interaction of near-resonant light with both cold and hot Rb atoms via the nonlinear polarization self-rotation effect (PSR). We investigate the optimal conditions for noise reduction in the resulting squeezed states, reaching quadrature squeezing levels of up to 2.6 dB below shot noise, as well as observing noise reduction for a broad range of detection frequencies, from tens of kHz to several MHz. We use this source of squeezed vacuum at 795 nm to further study the noise properties of these states and how they are affected by resonant atomic interactions. This includes the use of a squeezed light probe to give a quantum enhancement to an optical magnetometer, as well as studying the propagation of squeezed vacuum in an atomic medium under conditions of electromagnetically induced transparency (EIT). We also investigate the propagation of pulses of quantum squeezed light through a dispersive atomic medium, where we examine the possibilities for quantum noise signals traveling at subluminal and superluminal velocities. The interaction of squeezed light with resonant atomic vapors finds various potential applications in both quantum measurements and continuous variable quantum memories.

TABLE OF CONTENTS

Page

Acknowledgments v

Dedication vi

List of Tables vii

List of Figures viii

CHAPTER

1 Introduction 2

- 1.1 Quantum noise and squeezed light 2
- 1.2 Development of squeezing research 5
- 1.3 Applications of squeezed light 7
  - 1.3.1 Optical measurements 7
  - 1.3.2 Optical communications and quantum information 8
  - 1.3.3 Quantum memory 10
  - 1.3.4 Quantum sensing and imaging 11
- 1.4 Squeezing with resonant atoms 12
- 1.5 Dissertation outline 15

2 Squeezed light states 17

- 2.1 The Wave equation 17
- 2.2 Electromagnetic waves in free space 18
- 2.3 Field quantization 19
  - 2.3.1 Creation and annihilation operators 20
  - 2.3.2 Quadrature operators 21
  - 2.3.3 Electric field operator 22

2.4 Coherent states 23

2.5 Squeezed coherent states 26

2.6 Nonlinear processes in atoms 30

2.7 Sideband model of squeezing and two-photon formalism 31

3 Nonlinear polarization self-rotation effect 34

3.1 Polarization self-rotation 34

3.1.1 PSR effect in atomic vapor 34

3.1.2 PSR squeezing 35

3.1.3 Polarization squeezing 39

3.2 Theoretical squeezing levels 41

3.3 Limitations for squeezing generation 42

4 Resonant light-atom interactions 45

4.1 Alkali atoms and ^{87}Rb 45

4.2 Density matrix and slowly varying envelope approximation 47

4.3 Three-level atom Λ system 49

4.4 Nonlinear magneto-optical rotation 54

4.5 Polarization self-rotation g parameter 58

4.6 Dark states and electromagnetically-induced transparency 60

4.7 Quantum noise operators 64

5 Quadrature noise detection 67

5.1 Homodyne detection 67

5.2 Spectrum analysis 70

5.3 Experimental detection schemes 71

5.3.1 Detection scheme #1: Interferometric 72

5.3.2 Detection scheme #2: Copropagating 74

6 Squeezed vacuum generation and optimization in hot atomic vapor 78

6.1 Squeezing generation experimental setup 79

6.2 Pump laser focusing 80

6.3 Vapor cell selection 81

6.4 Detector alignment 82

6.5 Limitations due to classical laser noise 83

6.6 Detuning dependence 85

6.7 Temperature dependence 87

6.8 Power dependence 90

6.9 Best squeezing results 92

6.10 Effect of magnetic field on squeezing 93

6.11 Squeezing generation summary 98

7 Pulsed squeezing generation 99

7.1 Quantum information application for pulsed squeezed light 100

7.2 Quadrature noise pulse shaping 102

8 Quantum enhanced magnetometer 106

8.1 Magnetometer setup 107

8.2 Experimental observations 109

8.3 Magnetometer summary 115

9 Slow and fast squeezed light studies 117

9.1 Introduction 117

9.2 Dispersion 117

9.3 Experimental setup 118

9.4 Pulse delay/advancement measurements 124

9.5 Chapter summary 127

10 EIT noise filtering experiments 129

10.1 Introduction 129

10.2 Theory 131

10.3 Zeeman EIT 133

10.3.1 Zeeman experimental setup 134

10.3.2 Filtering observations 137

10.4 Hyperfine EIT 142

10.4.1 Hyperfine experimental setup 143

10.4.2 Undesirable excess phase-dependent noise 144

10.4.3 Hyperfine filtering observations 147

10.4.4 Noninvasive EIT probe 149

10.5 EIT noise filtering summary 151

11 PSR and quadrature noise studies in cold atomic vapor 154

11.1 Polarization rotation in cold ^{87}Rb atoms 154

11.1.1 Experimental setup 155

11.1.2 Experimental results 157

11.1.3 Self-rotation and Faraday rotation 160

11.2 Quadrature noise of light interacting with a cold atomic gas 170

11.2.1 Experimental setup 171

11.2.2 Experimental results 172

11.3 Summary and future improvements 174

12 Conclusions and outlook 178

APPENDIX A
Cavity vs free-space modes 181

APPENDIX B
Description of numerical simulations 183

APPENDIX C
List of electronics used 185

APPENDIX D
Permissions 187

Bibliography 189

Vita 206

ACKNOWLEDGMENTS

There are many people I wish to thank for their involvement in the completion of this dissertation work, as well as for their guidance and support throughout my academic career.

First, thank you to my adviser Dr. Eugeniy E. Mikhailov, for patiently guiding me through this work and for continually expanding my knowledge and motivating me to become a better scientist. Also, a very special thanks to Dr. Irina Novikova, for always being available to explain a concept, and always knowing the next step to take in an experiment.

I would like to thank the other members of our lab group at William & Mary. It has been a pleasure working alongside Nate Phillips, Matt Simons, Gleb Romanov, Ellie Radue, and Mi Zhang. Thanks especially to Gleb, who carried out much of this research with me, and Nate who assisted with the preparation of this manuscript. I am very grateful to our collaborators Robinjeet Singh, Salim Balik, Mark D. Havey, Arturo Lezama, and John P. Dowling.

I would also like to thank my entering graduate class, for accompanying me on this journey known as grad school, and for helping to make my time here enjoyable and fulfilling. I appreciate the welcoming and knowledgeable community that encompasses the physics department here at William & Mary. Thanks to those who played volleyball, football, or put it all on the line and helped to win those t-shirts in floor hockey. I would also like thank my respectable office mates, Josh and Alena Devan.

I acknowledge those who got me started down this path, and would like to thank Prof. Charles Adler whose enthusiasm for physics and teaching helped spark my interest in the field, Prof. Josh Grossman for helpful advice and guidance, and Dr. Frank Narducci who has always been generous with his time and support. I also thank my college roommate Grady, for tossing around a football with me while working on quantum mechanics homework.

Lastly, I wish to express my great appreciation to my family for their constant support and love. Thank you Doug, Diane, Alex, Tristan, Susannah, and especially Mom and Dad for always being there and and giving me every opportunity in life. Above all, I thank my beloved wife Victoria Marshall, to whom I dedicate this dissertation. This work would not have been possible without your never-ending belief in me and support.

Dedicated to my wonderful wife Tori.

LIST OF TABLES

Table Page

6.1 Maximum squeezing levels (dB) observed for several focusing lenses. f is the focal length in mm, and the third column shows the range of pump powers where the squeezing was present. Pump laser tuned near $F_g = 1 \rightarrow F_e = 1$. Cell temperature is 71° C. 81

6.2 Range of temperatures and calculated atomic densities for isotopically pure ^{87}Rb 87

LIST OF FIGURES

Figure Page

1.1 Quantum uncertainty for the projection of the X1 quadrature vs phase χ. (a) Coherent state. (b) Phase squeezed state. (c) Amplitude squeezed state. 4

2.1 Quantum uncertainty of a coherent state shown in a phasor diagram. . . . 25

2.2 Quantum uncertainty shown in phasor diagrams and the projection of the X1 quadrature vs phase χ. (a) Coherent state. (b) Phase squeezed state. (c) Amplitude squeezed state. (d) Squeezed coherent vacuum. 29

3.1 Variance of the electric field after undergoing rotation vs local oscillator phase χ. This is compared to the shot noise (SNL), which is the variance of an unsqueezed vacuum ($E_0^2/4$). gL is set to 2. 39

4.1 D_1 line energy spacing of ^{87}Rb 46

4.2 D_1 line absorption resonances of ^{85}Rb and ^{87}Rb shown with saturation spectroscopy. The transitions are labeled $F_g \rightarrow F_e$. 46

4.3 Three-level lambda-scheme. 49

4.4 Transmission and dispersion of a medium undergoing EIT. (Blue) -Im(χ). (Red) Re(χ). χ is the electric susceptibility. 63

5.1 Detection scheme #1: LO-local oscillator, Sq.Vac.-squeezed vacuum, PBS-polarizing beamsplitter, PZT-piezo-electric transducer, $\lambda/2$-half-wave plate, NPBS- nonpolarizing 50/50 beamsplitter, BPD-balanced photodetector. . . 72

5.2 Detection scheme #2: Co-propagating LO. $\lambda/4$-quarter-wave plate. 74

5.3 Shot noise power vs frequency for several total LO powers. The dark noise is the result of blocking all light. Spectrum analyzer settings: RBW=10 kHz, VBW=30 Hz. 77

6.1 Experimental setup for hot atomic squeezer: ECDL-Extended cavity diode laser, $\lambda/2$-half waveplate, GP-Glan polarizer, L-lens, Sq.Vac-Squeezed vacuum. 79

6.2 Noise power vs interferometer visibility $\mathcal{V}$. The shot noise level is 0 dB. Visibility was decreased by intentional misalignment of a steering mirror into the NPBS. Pump laser is tuned to $F_g = 2 \rightarrow F_e = 1$ 83

6.3 Comparison of the noise power spectral density of the laser residual intensity noise detected by a single photodiode (a) and balanced PD (b) for different laser intensities. Intensity of the laser doubles between subsequent traces (i), (ii), (iii). The bottom trace (iv) corresponds to the dark noise of the detector. 84

6.4 Noise power vs laser detuning for several phase angles. Shot noise level is 0 dB. Each trace shows a different arbitrary constant phase-angle χ. Pump laser power is 10 mW. Cell temperature is 65.5° C. The upper plot shows the saturated absorption spectrum of the D_1 ^{87}Rb line, with the dotted lines indicating the transition frequencies. Isotopically pure ^{87}Rb vapor cell with no buffer gas present. 85

6.5 Noise power vs Rb cell temperature. Shot noise level is 0 dB. Pump laser locked to $F_g = 1 \rightarrow F_e = 1$ transition, pump power 15 mW. 1.4 MHz detection frequency. The data is fit to a polynomial function (solid line) to guide the eye only. 88

6.6 Noise power vs Rb cell temperature. Shot noise level is 0 dB. Pump laser locked to $F_g = 2 \rightarrow F_e = 2$ transition, power at 21 mW. 1.4 MHz detection frequency. Left: Minimum and maximum noise levels shown. Right: Zoomed view of minimum noise. Polynomial fits are to guide the eye. . . . 89

6.7 Minimum noise vs squeezer input pump power for three ^{87}Rb transitions. Shot noise level is 0 dB. Cell temperatures are 73, 73, 57 °C respectively and laser frequency is tuned directly to each resonance. Detection frequency is set to 1.4 MHz. Fit lines are to guide the eye. 91

6.8 Minimum noise vs power and noise frequency for $F_g = 2 \rightarrow F_e = 2$ transition. Shot noise level is 0 dB. Cell temperatures is 57 °C. RBW=10 kHz, VBW=30 Hz. 92

6.9 Minimum noise vs noise frequency for several laser powers tuned to the $F_g = 2 \rightarrow F_e = 2$ transition. Shot noise level is 0 dB. Cell temperatures is 57 °C. RBW=10 kHz, VBW=30 Hz. 93

6.10 Noise spectrum of squeezed and anti-squeezed quadratures vs detection frequency. $F_g = 2 \rightarrow F_e = 2$ transition. Laser pump power = 7.0 mW. RBW=10 kHz, VBW=30 Hz. $T_{sq} = 66°$C. Detection #2. 94

6.11 Minimum noise vs noise frequency for $F_g = 2 \rightarrow F_e = 2$ transition. Laser pump power = 7.0 mW. RBW=0.9 Hz. $T_{sq} = 66°$C. Detection #2. SQL indicates the approximate standard quantum limit (shot noise level), which should be constant over all frequencies. 94

6.12 Experimental setup. The description of components is provided in the text. 96

6.13 Noise power (dB) of (a) anti-squeezed and (b) squeezed quadratures vs applied longitudinal magnetic field. Inset zooms in on small fields used for this experiment. The spectrum analyzer is set to 1 MHz central frequency with the RBW=100 kHz. 97

7.1 Modulation of the quantum noise with different pulse shapes. Top plots: magnetic field pulses applied to the atoms. Bottom plots: resultant squeezed noise pulses compared with the shot noise limit (SNL). Desired noise pulse shapes were: Gaussian (a, b, and e), triangular (c and f), and square (d). The dashed lines indicate the desired pulse shapes. 104

7.2 A 100 μs triangular pulse of squeezed noise. Limits of the current supply bandwidth cause visible oscillations in the magnetic field, which show up in the squeezed spectrum. 105

8.1 Experimental setup. The squeezer prepares an optical field with reduced noise properties, which is used as a probe for the magnetometer. SMPM fiber: single-mode polarization-maintaining fiber, $\lambda/2$: half-wave plate, PhR: phase-retarding wave plate, PBS: polarizing beam splitter, GP: Glan polarizer, BPD: balanced photodetector. Axes x and y coincide with horizontal and vertical polarization axes of all PBSs in our setup, axis z is along beam propagation direction. Inserts show the polarization of squeezed vacuum (Sq.Vac) field and laser field before the magnetometer cell (a) and right before the last PBS (b). 108

8.2 Sample of the magnetometer response to the longitudinal magnetic field. The narrow feature at zero field is due to repeated coherent interactions of atoms with the light field. Cell temperature is 40° C, density is 6×10^{10} atoms/cm^3, and probe power is 6 mW. 110

8.3 Magnetometer response (solid) and probe transmission (dashed) vs atomic density. Density uncertainties due to temperature fluctuations correspond to the size of the markers. Laser power is 6 mW. Cell temperatures range from 25-70° C in 5 degree increments. 111

8.4 Magnetometer quantum noise spectrum with (a) shot-noise-limited and (b) polarization-squeezed probe fields. Laser probe power is 6 mW. Left: magnetometer cell temperature of 43°C with a magnetic field modulation at 30 kHz. RBW=28.6 Hz. Right: magnetometer cell temperature of 35°C with modulation at 220 Hz. The insert shows the low frequency part of the noise spectrum (0 to 1 kHz) RBW=0.9 Hz. 112

8.5 Magnetometer quantum-noise-floor spectra with polarization-squeezed (light trace) and coherent probe (dark trace) fields taken at different temperatures/atomic densities of the magnetometer. (a) 25°C, (b) 35°C, (c) 50°C, (d) 55°C, (e) 60°C, (f) 70°C. Laser probe power is 6 mW. Spectrum analyzer resolution bandwidth is 28.6 Hz. 113

8.6 Noise suppression level vs atomic density normalized to shot noise level for several noise frequencies. Positive values indicate noise suppression, negatives indicate noise amplification. This level is found by averaging the coherent probe noise level subtracted from the squeezed probe noise level over 100 points (2 kHz) centered around the chosen noise frequency. The average uncertainty of ±0.35 dB is not included in the plot for clarity. Laser probe power is 6 mW. 115

8.7 NMOR magnetometer sensitivity as a function of the atomic density with polarization-squeezed (a) and coherent (b) (shot-noise-limited) optical probes. Errorbars are smaller than the size of the markers. Laser probe power is 6 mW. Detection frequency is 500 kHz. 116

9.1 Experimental setup for group velocity studies. B_z indicates the direction of applied magnetic field. $\lambda/2$ and $\lambda/4$ are half and quarter wave plates. . . . 119

9.2 Energy level diagram showing multiple lambda-schemes between the strong (solid) and weak (dashed) polarizations. 119

9.3 Rotation response of the medium vs magnetic field for several laser powers. This response indicating polarization rotation is shown in arbitrary units of the voltage measured from the balanced photodiode. Overall offsets on the y-axis are meaningless. T_I=50° C. 121

9.4 Slope of the rotation response (in Volts per Gauss) around zero magnetic field vs the input laser power. T_I=50° C. 122

9.5 Noise power vs time for the bypass optical path and interaction path where light passes through the second vapor cell. The noise traces can be fit to sine waves to compare the phases and determine a difference in group velocity. Differences in noise power level is attributed to absorption and atomic noise from the interaction cell. T_{Sq}=66° C, T_I=50° C. 122

9.6 Minimum noise level vs laser power for both the input and output signals from the interaction vapor cell. The input noise power is measured along the bypass path. The light is squeezed for noise levels under 0 dB. T_{Sq}=66° C, T_I=50° C. 123

9.7 Pulse delay versus laser power for signals traveling through the interaction vapor cell compared to those from the bypass path. Negative values indicate delays (slow light) while positive values indicate advancement (fast light). Results for the strong coherent probe (solid blue) as well as two trials for the pulses (red and pink points) are shown. 125

10.1 Illustration of a Lorentzian transmission profile. ω_0 is the carrier frequency. $T_\pm$ are the transmissions at the sideband frequencies $\Omega_\pm$. 132

10.2 Experimental setup: $\lambda/2$- half-wave plate, $\lambda/4$- quarter-wave plate, Sq-Squeezed vacuum, LO- Local oscillator, AOM- Acousto-optical modulator, BPD- Balanced photodetector. The insert shows relevant ^{87}Rb sublevels and optical fields. The weak probe field is depicted with dashed lines, the control with solid. δ is the two-photon detuning. 134

10.3 (a) EIT lineshape: Solid line shows fit. Peak transmission= 52%, FWHM= 4 MHz, control power= 4.2 mW, EIT cell temperature T_{EIT}= 46° C. (b) Quadratures noise power spectra. (i) input max. noise, (ii) input min. noise, (iii) expected max. noise, (iv) expected min. noise, (v) measured max. noise, (vi) measured min. noise. Squeezer pump power= 21.6 mW, squeezing cell temperature T_{sq}= 59° C. We removed data points in the output noise between 0.8 and 1.1 MHz due to a large spike caused by the beatnote between the local oscillator and the control field which was detuned by 900 kHz and leaked into the detection. 137

10.4 (a) EIT lineshape: Solid line shows fit. Peak transmission= 50%, FWHM= 2 MHz, control power= 3.8 mW, EIT cell temperature T_{EIT}= 50° C. (b) Quadratures noise power spectra. (i) input max. noise, (ii) input min. noise, (iii) expected max. noise, (iv) expected min. noise, (v) measured max. noise, (vi) measured min. noise. Squeezer pump power=13 mW, squeezing cell temperature T_{sq}= 57° C. 138

10.5 (a) EIT lineshape: Solid line shows fit. Peak transmission= 25%, FWHM= 1.4 MHz, control power= 2.3 mW, EIT cell temperature T_{EIT}= 50° C. (b) Quadratures noise power spectra: with noise power minimization at 300 kHz (solid-blue line) and at 1.2 MHz (dashed-green line). Squeezer pump power=15 mW, squeezing cell temperature T_{sq}= 57° C. 140

10.6 Noise power spectrum with control field set to 6.9 mW (a) and blocked (b). LO phase angle is continuously scanned. 141

10.7 Energy level diagrams for hyperfine EIT. (a) Probe laser on $F_g = 1 \rightarrow F_e = 1$. (b) Probe laser on $F_g = 2 \rightarrow F_e = 2$ 142

10.8 Noise power vs detection frequency after interaction with the EIT vapor cell. (a) Coherent probe at 25°. (b) Coherent probe at 65°. (c) Squeezed probe at 25°. (d) Squeezed probe at 65°. Input minimum and maximum noise levels shown in black (c, d). The coherent probe uses a PBS to block the squeezed vacuum polarization. RBW=10 kHz, VBW=30 Hz. Local oscillator phase is scanning. Probe on $F_g = 1 \rightarrow F_e = 1$ 145

10.9 Average excess noise contrast (max - min) vs atomic density. $F_g = 1 \rightarrow F_e = 1$ transition. The exponential fit is to guide the eye. 146

10.10 Noise power vs detection frequency at several probe leakage powers. Leakage probe power is approximately (a) 4.3 μW, (b) 1.6 μW, (c) 0.6 μW,(d) 0.2 μW. $F_g = 1 \rightarrow F_e = 1$. T_{EIT}=55° C. 147

10.11 Modified EIT filtering experimental setup. 148

10.12 (a) EIT transmission: Peak=34%, FWHM=155 kHz. (b) Noise power vs detection frequency after EIT interaction. Shot noise is 0 dB. Shown are the input min. and max. noise (black dotted), the output min. and max. noise (solid blue), and the output max. noise when about 2 μW of the wrong polarization is added to the probe beam (dotted pink). $F_g = 2 \rightarrow F_e = 2$ transition. 149

10.13 (a) EIT transparency window. Lineshape recorded using 10 μW coherent probe and measuring light intensity. (b, c) Noise spectrum from squeezed vacuum probe, EIT detuned (b) +1.3 MHz and (c) -1.3 MHz. Squeezed vacuum is produced at ω_0 which is in resonance with the $F_g = 1 \rightarrow F_e = 1$ transition. 151

10.14 Noise spectrum for detuned EIT with three control powers: 3, 2, and 1 mW. EIT widths (FWHM) are 240, 150, and 90 kHz respectively. 152

11.1 Schematic diagram of the experimental arrangement. 156

11.2 Partial diagram of the ^{87}Rb levels scheme indicating the trapping and probe transitions. 157

11.3 (Left) The probe field self-rotation angle as a function of time, with t = 0 referring to the MOT laser switch off time. We compare the case of the repumper laser on (a) and off (b). Probe laser power = 600 μW, detuning = -1 GHz . (Right) Rotation angle vs. detuning with repumper laser on (a) and off (b). (c) is the result in (b) but 20 times magnified. Measurement taken at 3 ms. Vertical dash-dot lines mark locations of the $F_g = 2 \rightarrow F_e = 1$ and $F_g = 2 \rightarrow F_e = 2$ D$_1$ line transitions corresponding to 0 GHz and 0.82 GHz detunings. 159

11.4 Calculated polarization rotation around the $F_g = 2 \rightarrow F_e = 1$ (corresponds to zero detuning) and $F_g = 2 \rightarrow F_e = 2$ hyperfine transitions as a function of detuning. (a) Pure Faraday rotation ($B = 0.01\Gamma, \epsilon = 0$). (b) Pure PSR rotation ($B = 0, \epsilon = \pm 25°$), black solid (red dashed) lines correspond to positive (negative) ellipticity. (c) Combined Faraday and PSR effects ($B = 0.01\Gamma, \epsilon = \pm 25°$). Parameters: $C = 3$, $I = 2$ mW/cm^2, $\gamma = 0.001\Gamma$. . 162

11.5 Probe rotation angle vs. initial ellipticity at 3 ms measured at 80 MHz (a) and at -80 MHz (b) detunings relative to the $F_g = 2 \rightarrow F_e = 1$ transition. Probe laser power = 1.8 μW. 163

11.6 Probe laser rotation angle vs. initial ellipticity and time measured at two detunings. Probe laser power = 11.4 μW, detunings are +80 MHz (a) and -80 MHz (b). 164

11.7 Rotation angle vs probe laser power and time at opposite initial ellipticities. Probe laser detuning is -80 MHz, probe ellipticities are +30° (a) and $-30°$ (b). 165

11.8 (Left) Rotation angle vs probe laser power for different probe ellipticities. Probe detuning is -80 MHz, ellipticity $+30°$ (a) and $-30°$ (b). (Right) Simulated rotation angle vs. probe laser power for different ellipticities and magnetic fields. Probe laser detuning is -80 MHz, ellipticities are $+30°$ (a,c), $-30°$ (b,d), and $0°$ (e). Magnetic fields are B= 0.01Γ (a,b,e) and B= 0Γ (c,d). 165

11.9 Comparison of the experimental data (top 4 plots) and calculated (bottom 4 plots) rotation angle dependence on probe laser detuning at opposite initial ellipticities $+25°$ (solid lines) and $-25°$ (dashed lines) for different probe laser powers: 2 μW (a and a'), 10 μW (b and b'), 100 μW (c and c'), and 2000 μW (d and d'). Experimental data is taken at 3 ms. Results of calculations are for beam cross-section = 10^{-3} cm^2, B= 0.01Γ, $\gamma = 0.001\Gamma$, and C= 3. Vertical dash-dot lines mark locations of the $F_g = 2 \rightarrow F_e = 1$ and $F_g = 2 \rightarrow F_e = 2$ D$_1$ line transitions corresponding to 0 GHz and 0.82 GHz detunings. 168

11.10 Dependence of rotation angle on probe laser detuning and measurement time for different probe laser powers and ellipticities: power 10 μW, $\epsilon = +25°$ (a); power 10 μW, $\epsilon = -25°$ (b); power 600 μW, $\epsilon = +25°$ (c); power 600 μW, $\epsilon = -25°$ (d). 169

11.11 Phase-dependent noise vs detuning for different cooperativity parameters and decay rates. Parameters are $\gamma = 10^{-1}\Gamma$ (a), $\gamma = 10^{-2}\Gamma$ (b), $\gamma = 10^{-3}\Gamma$ (c), and $\gamma = 10^{-4}\Gamma$ (d); (i) C=100, (ii) C= 900, (iii) C= 1700; $\Omega = 30\Gamma$, $B = 0$ in all cases. 170

11.12 Schematic diagram of the experimental setup used for noise measurements. 171

11.13 Noise power in the squeezed channel vs the quadrature angle. Phase-dependent excess noise: Laser power = 1.3 mW, Detuning = -200 MHz (a) modified quantum noise in the vacuum channel, (b) shot-noise level. The noise trace is measured at 1.4 MHz central frequency of the SA, RBW= 100 kHz, and is averaged over 512 traces. 173

11.14 Results of the experiment (a, b, and c) and numerical simulations (d) for minimum (solid line) and maximum (dashed line) noise levels dependence on the PSR driving laser detuning for different PSR driving laser powers. (a) laser power 0.47 mW, (b) 1.3 mW, (c) 7.5 mW. Parameters for numerical simulation (d) power = 10 mW, beam cross- 10^{-3} cm^2, $\gamma = 0.1\Gamma$, C= 10, $B = 0$. 175

EXPERIMENTAL GENERATION AND MANIPULATION OF QUANTUM SQUEEZED VACUUM VIA POLARIZATION SELF-ROTATION IN RB VAPOR

CHAPTER 1

Introduction

Squeezed light is a nonclassical state of the electromagnetic field with altered photon statistics compared to “normal” coherent laser light. Creating these states has become an area of major focus in quantum optics in the last few decades because squeezed light can be used to reduce the uncertainty in many optical precision measurements. Squeezed states are also interesting for studies in quantum information science, because of their nonclassical nature. Manipulating the quantum noise in squeezed states adds another interesting dimension to the study of electromagnetic radiation, and provides a new tool for investigating the quantum-mechanical nature of the world.

1.1 Quantum noise and squeezed light

Everything in nature is subject to the laws of quantum mechanics, including light. The concept of photons, particle-like bundles of energy with $E = h\nu$, implies quantization. Wave-particle duality, for light as well as matter, has been a fundamental principle of quantum mechanics since its invention, illuminating observations such as black-body radiation and the photoelectric effect [1]. So the nature of light is inherently quantum-mechanical.

One of the foundations of quantum mechanics is the Heisenberg Uncertainty Principle, which states that certain pairs of observables in a system cannot be known simultaneously to better than a certain precision. For a particle, it states that the product of uncertainties in its position (Δx) and momentum (Δp) are limited by the inequality $\Delta x \Delta p \geq \hbar/2$. A similar uncertainty relation in optics can be expressed in terms of the amplitude and phase quadratures of light: $\Delta \mathrm{X1}\, \Delta \mathrm{X2} \geq 1/4$. This implies that one cannot know the exact amplitude and phase of a light signal simultaneously. Therefore, there is a fundamental limit on any measurement involving light.

In any real experiment, there are some extra uncertainties on measurements of the properties of a system. These uncertainties may come from many different sources, and they combine to form noise on top of the signal being measured. In optical measurements, noise sources could arise from thermal fluctuations, mechanical instabilities, frequency drifts, vibrations, etc, that change in time. Measurements are also subject to electronic noise, coming from any fluctuations present in the detectors or other electronics used in the signal processing. These effects will add noise to the amplitude and phase of the detected light signal, however, there are many techniques and detection schemes to suppress these noise sources.

Quantum noise, however, comes directly from the quantum-mechanical nature of light due to the limit imposed by the Heisenberg Uncertainty Principle, and cannot be suppressed by any classical means. This is a consequence of the ever-present quantum fluctuations of the electromagnetic (EM) field, resulting in nonzero variances of the amplitude and phase quadrature operators in a coherent state of light. For coherent states of light, the quantum uncertainties are equal in the amplitude and phase quadratures, and the quantum noise has no phase dependence. This quantum noise is known as the *shot noise*, and can be thought of as arising from the discrete nature of photons. It is important to note that these fluctuations exist even for the vacuum state with an average of zero photons. Vacuum fluctuations often enter into a measurement and add noise, for example, through the empty port of a beamsplitter. If the classical and electronic noise can be sufficiently suppressed, a measurement is then limited only by quantum uncertainty. *Therefore, the minimum possible noise of an optical measurement will be due to random quantum fluc-*

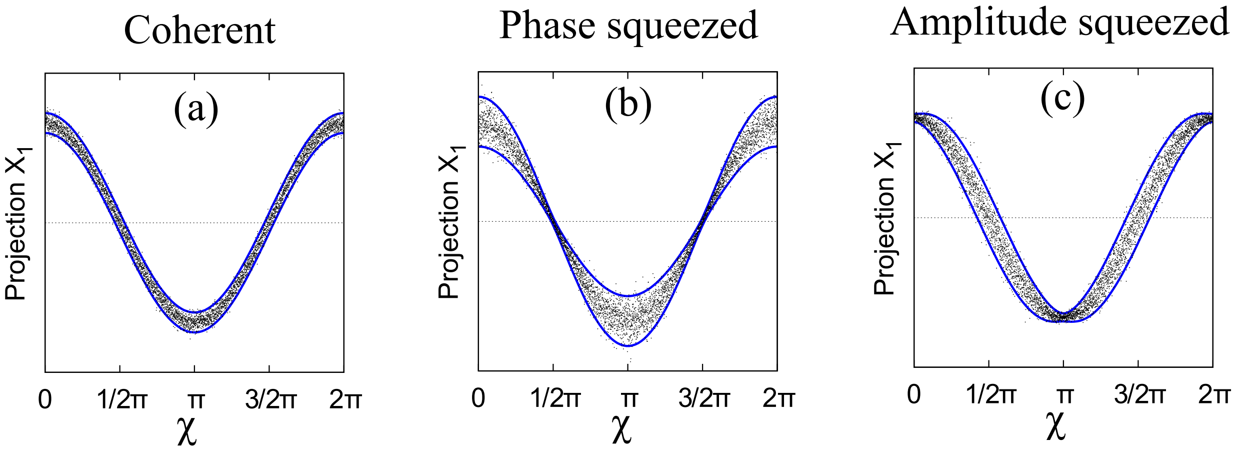

FIG. 1.1: Quantum uncertainty for the projection of the X1 quadrature vs phase χ. (a) Coherent state. (b) Phase squeezed state. (c) Amplitude squeezed state.

tuations of the electromagnetic field, which cannot be subtracted out of the measurement. This minimum noise level is referred to as the *standard quantum limit* (SQL) or *shot noise limit* (SNL).

To provide a further enhancement to measurements, we look to quantum-mechanical states of light called *squeezed states*, where we can manipulate the quantum noise. While the Heisenberg Uncertainty Principle puts a limit on the combination of uncertainties of the amplitude and phase of light, it does not limit these properties individually. Therefore, if the quantum uncertainty in the amplitude for example is reduced, the phase uncertainty would need to increase to satisfy Heisenberg's principle. This is accomplished by quantum squeezed states. While normal coherent states have equal quantum fluctuations in the amplitude and phase quadratures, squeezed states have unequal fluctuations, where one quadrature uncertainty is reduced, or "squeezed", and the other is increased or "stretched" in compensation. This is illustrated in Fig. 1.1. The angle χ is the phase of light with respect to a reference phase. While coherent light has equal uncertainty in its amplitude and phase, the squeezed states show variable uncertainty that is stretched or squeezed for different aspects of the light signal.

Squeezed light is created by building correlations between the amplitude and phase of the light using higher order nonlinear interactions with atoms. This can cause the light to experience amplification and reduction of its quadratures without adding extra noise to the system. The manipulation of quantum noise and altered photon statistics makes squeezed light an interesting topic of study, and a useful tool in quantum optics.

1.2 Development of squeezing research

The field of quantum optics took off in the 1960s after the invention of the laser. Researchers applying quantum mechanics to light soon began searching for purely quantum effects such as single photons and antibunching [2]. Proposals for the creation of two-photon coherent states, later known as squeezed states, immediately followed [3]. The development of the theory as well as possible means of generating and detecting squeezed light progressed in the late 70s and early 80s. Yuen *et al.* proposed that squeezed light could be used to reduce the noise in optical communications, and outlined a means of producing it that relied on four-wave mixing (4WM)[4, 5]. In 1981 Caves suggested using squeezed vacuum to improve the sensitivity of an interferometer [6], and four years later with Schumaker, came out with a two-photon formalism convenient for describing squeezed light and the processes that generate it [7, 8]. Due to the two-photon nature of squeezed light, there are several candidates for nonlinear interactions that can lead to squeezing. Walls, in 1983, published a comprehensive summary of the theory of squeezed light as well as the several possible methods in which it could be created and detected, though it had not yet been seen experimentally [3].

Experimental verification did not take long to follow. The first experiment to create a quantum squeezed state was performed by the group of Slusher *et al.* in 1985, who used a 4WM process in an atomic beam of sodium (Na) [9]. This was quickly followed by other successful detections. Shelby *et al.* observed suppression of quantum noise in 1986, again using a 4WM process, but now in a nonlinear optical fiber ring [10]. Some of the best early squeezing results were reported by Kimble *et al.* , who used a crystal to form an optical parametric oscillator (OPO) to generate squeezed light and were able to show the interferometric improvement proposed by Caves [11, 12]. Investigations were made using both continuous-wave and pulsed light, with advancements being made in the latter by Slusher *et al.* in 1987 using parametric down conversion in a nonlinear crystal [13, 14]. In just two years after the first detection of squeezed light, several groups were making advances in its theory and detection using multiple generation processes [15]. Next came the detection of bright squeezed states by yet another nonlinear process, second harmonic generation (SHG), in the late 80s and early 90s [16, 17, 18, 19]. There were also experiments investigating semiconductor lasers that could produce squeezed light directly, which met with some success [20, 21]. A description of each experimental method used to generate squeezed light and the early developments can be found in Ref. [2].

Each method had its own advantages and its own experimental difficulties. The noise suppressions achieved started at modest levels in very sensitive experiments, but the squeezing levels and stability have improved steadily with optimization of the experimental methods and materials. Noise suppression levels that started at fractions of a dB have now exceeded -10 dB in some applications, meaning more than a factor of 10 less noise than is seen in a coherent state. The best squeezing from second harmonic generation reached levels of -3 dB in a doubly resonant system used by Kurz *et al.* [18]. Four-wave mixing in atomic vapors has given squeezing levels of up to -3.5 dB in rubidium (Rb) vapor [22]. The atomic Kerr effect in cold Rb atoms has also shown up to -3.5 dB noise reduction [23]. Experiments in pulsed fiber squeezing using the Kerr effect are described in Ref. [24], and more recent advances have brought these noise reduction levels to around -7 dB [25]. Methods using twin beams have also been successful in showing high levels of correlation, where two nonclassical beams are produced, and squeezing is observed when the beams are measured together [26, 27, 28]. Parametric processes in nonlinear crystals have been the most successful in terms of maximum squeezing levels. The group of Schnabel *et al.* has observed -12.3 dB noise suppression at a wavelength of 1550 nm and -12.7 dB at 1064 nm, using optical parametric processes in crystals for the application of squeezing to gravitational wave detection [29, 30].

It is clear that different methods used for generating squeezed light will produce states with different physical properties, and thus will be more useful for certain applications than others. For example, the gravitational detector LIGO uses laser light at 1064 nm, and so any squeezer used for this application needs to produce squeezed vacuum at this wavelength. However, it may be desirable to have squeezed light produced at 1550 nm for optical communications, or at 795 nm to match an atomic absorption line. Aside from the wavelength of light, there are several other factors such as detection bandwidth and light power for which different applications will have specific requirements, and so it is important to match the squeezing method with the desired application.

1.3 Applications of squeezed light

1.3.1 Optical measurements

Squeezed light only became an important area of study when real world applications for it were proposed. Because manipulation of the noise quadratures in squeezed light is possible, one natural application for squeezing is in precision optical measurements. Any shot-noise-limited optical measurement can potentially be improved by the reduced uncertainty levels of a squeezed state. It is true that when one property of a light state is reduced, the orthogonal quadrature must necessarily increase in compensation, but for many measurements, we are only interested in measuring one property of the light at a time, for example we measure only the amplitude and not the phase.

One of the first and still one of the most important uses for squeezed light is to improve the sensitivity of an interferometer as Caves proposed in Ref. [6]. More specifically, squeezing can be used to improve the most sensitive interferometer in the world in the LIGO experiment for detection of gravitational waves. When classical and electronic noise can be sufficiently suppressed, measurements become limited by quantum noise. In the case of a sensitive interferometer like in LIGO, the dominant source of noise is caused by the vacuum fluctuations that enter into the empty port of a beamsplitter. This vacuum noise is not correlated with anything in the measurement and becomes the limiting source of noise. If this vacuum state however, is replaced by a squeezed state, the fluctuations of the measured quadrature can be reduced, resulting in an overall more precise measurement. In fact, much of the development of squeezed light and squeezed vacuum has been for this purpose, and one of the main improvements for advanced LIGO, the next generation detector, comes from using squeezed vacuum [31].

Gravitational wave detection is not the only place squeezed states find application. Any shot-noise-limited optical measurement can be a candidate for improvement. Alternate interferometric measurements, such as those used for measuring polarization, can show improvements in sensitivity [32]. Other examples include applications which depend on amplitude modulation such as absorption measurements, where the signal-to-noise ratio is boosted by decreasing the amplitude noise [33, 34]. Polzik *et al.* showed that squeezed light could be used to improve a wide range of atomic spectroscopy measurements and worked towards providing a squeezing source for these purposes [35]. It has also been shown that squeezed light with reduced uncertainty in the quadrature being detected can be used to improve the sensitivity of optical magnetometers [36, 37]. Other examples could include improvements in frequency standards, timekeeping, and quantum positioning [38], as well as reduced noise in biological measurements [39]. These applications and many more can take advantage of the manipulation of signal noise using squeezed states of light.

1.3.2 Optical communications and quantum information

Another application coming from a reduction in the detected noise quadrature in squeezed light, is in optical communications as proposed in Ref. [4], where noise limitations have approached the quantum level. Squeezed light can improve communications by reducing the noise levels of light used, and thus boosting the SNR. Noise can also be reduced by using phase-sensitive amplification, and by injecting squeezed vacuum into empty beamsplitter ports whenever possible. This reduction in noise can increase the number of distinguishable states of light leading to an overall increase in the amount of information that can be encoded [2]. In practice, using squeezed light in communications can be a great challenge due to the fragility of quantum states and the losses associated with optical communications [40]. However, squeezed states may still find their place in communications by making use of their nonclassical properties.

Optical communications in recent years have gone well beyond the classical world. It has been shown that certain tasks can be performed more efficiently using qubits and quantum states rather than only classical information. This boost comes from the fact that quantum states can exhibit entanglement, nonlocal correlations existing between two objects or states. Once entanglement can be achieved in communication channels, this opens the door for secure communications by quantum cryptography, as well as quantum teleportation, and quantum entanglement swapping [41]. These sorts of processes have become major topics of study in recent years both theoretically and experimentally, growing the fields of quantum communications and quantum information science [42].

In the early 90s, Ou *et al.* demonstrated that nondegenerate parametric amplification in a nonlinear crystal could be used to create an Einstein-Podolski-Rosen (EPR) entangled state, and that the resulting superposition of output beams was a squeezed state [43]. It was later shown that other various schemes can be used to create entangled states using squeezed light by mixing two squeezed states together, and quantum teleportation using squeezed light was observed [44, 45]. In quantum teleportation, entanglement allows a quantum state to be transfered from one location to another instantaneously. Schemes have also been proposed and implemented that use squeeze-state entanglement for quantum cryptography [46, 47]. The nature of the quantum states involved in these communication methods makes eavesdropping on the information sent nearly impossible. There is also the capability of coupling squeezed light to atoms, thus transferring the entanglement in the light onto distant groups of atoms [48]. This is important for the goal of creating quantum networks and quantum computers. Many other quantum information applications using the nonclassical properties of squeezed states exist, including quantum error correction, entanglement purification, and creating even more exotic quantum states [47, 49, 50]. Using squeezed light as a reliable source of entanglement makes it very useful for quantum communication as well as potential applications in quantum computing and fundamental studies of quantum mechanics.

1.3.3 Quantum memory

Squeezed light is a quantum state with no classical analogue. Further utility of squeezed states of light comes in the form of squeezing as a quantum probe. Squeezing provides a convenient measure of a light field's nonclassical nature, namely the reduction and amplification of its noise quadratures. Therefore, we can use squeezed light as a probe to test different quantum mechanical processes. As an example, Furusawa *et al.* were able to observe quantum teleportation of a squeezed state, confirming that the quantum state and noise reduction were preserved after teleportation [51]. Any such process with the goal of preserving a quantum state could possibly be tested with squeezed states, which are very sensitive to losses and interactions with the environment.

Another important process for quantum computing and communication is that of quantum storage and memory. Quantum memory is a necessity for storing information in quantum computers, and in quantum repeaters needed for communication [52, 53]. Many protocols have been proposed and implemented using light as the information carrier which can be strongly coupled to some atomic memory device. Squeezed states of light can be an invaluable tool for probing these memories. As in other quantum processes, the quantum mechanical state of information must be preserved in a memory. The general technique used for a quantum memory is as follows. Information is encoded into a state of light, which then interacts with the atomic memory to transfer the information onto the state of the atoms, and hold it for some period of time. The information is then transferred back to a state of light, and the retrieved state should resemble the original quantum state [52].

To fully test whether the quantum features of the state are preserved in the memory, a nonclassical state such as a squeezed state can be used. If we store a quantum squeezed state of light, the retrieved state should also be squeezed and display the same nonclassical properties. Only by using a quantum probe can you fully test the fidelity of the memory in storing your quantum state. Several groups to date have successfully demonstrated atomic memory for pulses of squeezed light in hot and cold Rb vapor [54, 55, 56, 57].

1.3.4 Quantum sensing and imaging

Finally, we look at some specialized applications where the quantum noise properties of squeezed light and squeezed vacuum can be advantageously used for sensing and imaging techniques.

The phase-dependent quadrature noise associated with squeezed states gives an extra degree of freedom to use in measurements. Squeezed vacuum can be used as a noninvasive probe because it contains very few photons, but changes in the quantum noise properties caused by the object being probed or imaged can be measured. In this way, Mikhailov *et al.* were able to accurately measure the optical parameters of a cavity by probing with squeezed vacuum [58]. The same type of measurement can be performed to weakly probe the absorptive properties of an atomic medium. Another important tool in quantum sensing that can use squeezed states is that of nondemolition measurement [23]. In this technique, a quantum measurement can be made while avoiding the added "back-action" noise of the measurement, by ensuring this noise is hidden in a quadrature not being detected. This can be achieved by coupling laser beams in a nonlinear medium.

There are also applications for squeezing in the new subfield of "quantum imaging" where spatial rather than temporal correlations of squeezed probes can be used. First, as expected, if bright squeezed light can be employed in imaging with noise fluctuations below shot noise levels, we can get improvements in image resolution. Improvements have also been predicted in areas like quantum pointing of beams, quantum lithography and microscopy, and noiseless images [38]. There have been advances in using twin squeezed beams with spatial correlations existing between them for imaging purposes [28, 59]. For example, spatial information about an object can be gained from measuring only the quantum noise levels of squeezed beams incident upon the object, and the resolution is improved compared to the classical approach [60].

We have seen a number of applications for quantum squeezed states of light, and there are a great many more not mentioned or still being developed [2]. This active area of research will no doubt continue to produce new technologies and new studies making use of the noise properties and quantum characteristics of squeezed light. It is important to again note that each different application of squeezing will have different requirements as to the properties of the squeezed light used. For this reason, several different methods for producing squeezed states are still being used and explored experimentally.

1.4 Squeezing with resonant atoms

For this dissertation, we will focus on squeezed vacuum produced in atomic vapors, specifically through a nonlinear light-atom interaction known as polarization self-rotation (PSR). Atomic samples are interesting for squeezed light generation due to the strong nonlinearities which can appear when light is tuned near atomic resonances. Atoms provide a broad range of possibilities due to our ability to manipulate and tune interactions with atomic vapors. Resonant interactions with atoms have been known to generate squeezed light since the early studies of squeezing. The first experimental demonstration of squeezing and other early experiments made use of 4WM in atomic Na [9, 61]. Four-wave mixing remains a reliable source of squeezing today, with more recent experiments using Rb rather than Na [22]. Another effect shown to produce squeezing in atoms uses the nonlinear Kerr effect, which can cause a change in the index of refraction of the atomic medium due to simple two-level absorptive interactions. Experiments using cold cesium atoms [62] and cold rubidium atoms [23] were performed in cavities, producing noise suppressions of -1.8

and -3.5 dB respectively.

An alternate, and very simple atomic interaction that can lead to squeezing is the polarization self-rotation effect. In this $\chi^{(3)}$ nonlinear effect, the polarization of a near-resonant beam of light rotates as it travels through a material that is circularly birefringent. It was first proposed in Ref. [63] that this type of nonlinearity could lead to quadrature squeezing in semiconductors and waveguides due to a process known as cross-phase modulation (XPM). Given a strong pump beam that is linearly polarized, small rotations in this beam can project changes onto the vacuum state in the orthogonal polarization, which are correlated in such a way as to produce squeezed vacuum. This effect was used to successfully generate squeezed vacuum from a semiconducting crystal [64], and then using nonlinear optical fibers [65, 66].

Polarization self-rotation squeezing was extended to atomic vapors in the theoretical work by Matsko *et al.* in 2002 [67]. They predicted that squeezing levels as high as -8 dB could be possible using this method in warm Rb atoms. Detailed studies into PSR in both ^{87}Rb and ^{85}Rb further indicated that vacuum squeezing should be possible in ^{87}Rb [68]. This was first demonstrated the following year by Ries *et al.* on the ^{87}Rb D_2 line, but initial squeezing levels were small (-0.85 dB) [69]. Atomic PSR squeezing was placed somewhat in doubt when Hsu *et al.* failed to see squeezing using this method due to the overwhelming effect of atomic noise, and published the null result consistent with their theory [70]. Further demonstrations however, proved the validity of the PSR squeezing method, at least on the D_1 line of ^{87}Rb [71, 72, 73, 74]. The best atomic PSR squeezing reported has been a noise suppression of -3 dB, falling below theoretical predictions due to limitations imposed by atomic noise [74].

These results for atomic PSR squeezing come from rather recent experiments, so there is still room for improvement in this method. There are also proposals for using cold rather than hot atoms to generate higher levels of squeezing [70]. However, even with modest noise suppression levels, PSR offers several advantages over other squeezing generation schemes. The first is in its simplicity. Squeezed vacuum can be generated via PSR using only a diode laser and an atomic vapor cell in a single-pass configuration. The power requirements are low, on the order of milliwatts, and the setup could be easily miniaturized. The squeezing is produced without placing the atoms in a cavity and the vacuum can be separated from the pump using polarizers or beamsplitters, rather than, for example, a Sagnac interferometer. Within the range where squeezed vacuum is produced, the strength of the interaction can be tuned to fit the experiment by changing light intensity and atomic density, and the temperature ranges necessary are easily achieved without the need of cryogenics. Overall, PSR squeezing offers a source of squeezed vacuum with is much less expensive, less complicated, and potentially more stable than most other squeezing methods.

Generating squeezed light via PSR in atomic Rb relies on near-resonant interactions of light with the atomic energy levels of the atoms. As a result, the squeezed vacuum is created at these atomic frequencies automatically (795 nm for the ^{87}Rb D_1 line). This is especially appealing for applications using squeezed states at these frequencies. This could include spectroscopy measurements, atomic frequency standards, optical magnetometers, and other experiments exploring resonant interactions.

Another main application for this type of squeezed light generation is in continuous variable (CV) quantum memories and information [75]. Using continuous rather than discrete variables for quantum information has attracted much attention because it avoids the need for single photon production and detection. One of the most promising protocols for CV quantum memory uses atomic vapors under conditions of electromagnetically-induced transparency (EIT) to slow and store pulses of light [76, 77]. This has been well established in cold and hot atomic vapors and has been demonstrated using rubidium atoms [78, 79]. Squeezed vacuum generated at atomic Rb wavelengths can serve as a very useful quantum probe for these types of memories.

The other important characteristic of squeezed light is the bandwidth of noise that can be suppressed. While there have been examples of squeezed light generated by parametric down conversion near 800 nm [80], the output of such nonlinear crystals is generally quite broad, and may not be as useful for probing spectral features such as EIT which are much narrower [81]. PSR squeezing however, has been shown to provide noise suppression at the lowest noise frequencies, down to around 20 kHz, and maybe even as low as 100 Hz [37, 71]. To produce low-frequency squeezed light in nonlinear crystals, researchers can make use of narrowband lasers, high-quality cavities, and feedback electronics, but this again greatly adds to the cost and complexity of the experiment. Atomic memories also require a pulsed source of squeezed light which can be difficult to achieve in crystal squeezers, but may be accomplished more easily using atomic squeezing [81]. Despite these difficulties, squeezed light generated in nonlinear crystals has been used in atomic quantum memory experiments successfully [54, 55, 56, 57]. But, atomic PSR squeezing may provide a simpler, more compact, more flexible, and less expensive source of squeezed vacuum for such experiments.

1.5 Dissertation outline

In this dissertation, we present the results of experimental studies into the generation of quantum squeezed vacuum using the nonlinear polarization self-rotation effect in hot and cold ^{87}Rb atomic vapor. We have attempted to maximize the noise reduction at low noise frequencies by determining the optimal experimental parameters including pump light intensity, magnetic field, atomic density, and one-photon detuning for several atomic transitions of ^{87}Rb where squeezing is observed. We investigate the interaction of squeezed vacuum with coherent atomic media and effects such as EIT, slow light, and polarization rotations. We also study the changes to the quantum noise as a result of these effects, and other noise sources such as those resulting from the interaction of light with atoms; these additional noise sources can obscure squeezed light experiments. We present these experimental findings in the context of applying them to enhanced precision measurements as well as continuous variable quantum information protocols, most specifically to atomic quantum memories.

Chapter 1 has focused on the development of different methods of squeezed state production and on the applications of squeezed light. Chapter 2 provides some of the theoretical background and foundations relevant to the study of quantum noise and squeezed light. Chapter 3 is dedicated to the details behind squeezing production via the polarization self-rotation effect. In Chapter 4, we consider the effect of light interacting with resonant atoms, and derive some of the properties of interactions important to our experiments by considering a three-level atom Λ system. Chapter 5 considers the detection of quantum noise in a light signal, and details two different noise detection schemes used in the experiments. The remaining chapters are dedicated to the experimental results of our squeezed vacuum experiments. We first present the progress in optimizing the squeezed vacuum production in warm ^{87}Rb vapor cells in Chapter 6. Our method of pulsed squeezing production is central to Chapter 7. We then summarize the results of three experiments in which we send squeezed vacuum into a second atomic vapor cell to study the interactions of coherent atomic processes and quantum squeezed states. These include the quantum enhancement of an optical magnetometer in Chapter 8, the study of changes to the group velocity of squeezed vacuum in Chapter 9, and a demonstration of EIT frequency filtering of squeezed vacuum in Chapter 10. In Chapter 11, we present a study of PSR for light propagating through a cloud of cold ^{87}Rb atoms held in a magneto-optical trap (MOT), and discuss the prospects for PSR squeezing in cold atoms. We conclude in Chapter 12 with a summary and a discussion of the prospects for PSR as a useful source of squeezed light in the future.

CHAPTER 2

Squeezed light states

In this chapter, starting with Maxwell's equations, we build the framework for light quantization and squeezed states. We discuss quantum uncertainty, and motivate how certain nonlinear processes can lead to noise quadrature alteration in light states.

2.1 The Wave equation

The propagation of light in a medium is described by Maxwell's equations:

$$\nabla \cdot \mathbf{E} = \rho/\epsilon_0 \tag{2.1}$$

$$\nabla \cdot \mathbf{B} = 0 \tag{2.2}$$

$$\nabla \times \mathbf{E} = -\frac{\partial \mathbf{B}}{\partial t} \tag{2.3}$$

$$\nabla \times \mathbf{B} = \mu_0 \epsilon_0 \frac{\partial \mathbf{E}}{\partial t} + \mu_0 \mathbf{J} \tag{2.4}$$

Here, **E** is the electric field and **B** is the magnetic induction. ρ and **J** are the charge and current densities of electrons, and assuming the absence of free charge in a dielectric, these are equal to the bound charge and current densities in the medium. ϵ_0 and μ_0 are the permittivity and permeability of free space.

By taking the curl of equation 2.3 and using the identity $\nabla \times (\nabla \times \mathbf{V}) = \nabla(\nabla \cdot \mathbf{V}) - \nabla \cdot (\nabla \mathbf{V})$ along with equation 2.4, we find

$$\nabla^2 \mathbf{E} = \frac{\partial}{\partial t}\left(\mu_0 \epsilon_0 \frac{\partial \mathbf{E}}{\partial t} + \mu_0 \frac{\partial \mathbf{J}}{\partial t}\right). \tag{2.5}$$

In a dielectric material, the bound current is $\mathbf{J} = \partial \mathbf{P}/\partial t$ where $\mathbf{P}$ is the macroscopic polarization of the material. Thus we arrive at the electromagnetic wave equation for light in an atomic sample.

$$\nabla^2 \mathbf{E} - \mu_0 \epsilon_0 \frac{\partial^2 \mathbf{E}}{\partial t^2} = \mu_0 \frac{\partial^2 \mathbf{P}}{\partial t^2} \tag{2.6}$$

The polarization is defined in terms of the average dipole moment of the atoms,

$$\mathbf{P} = \frac{N}{V}\langle \mathbf{d} \rangle, \tag{2.7}$$

with N being the number of atoms contained in the volume V. The dipole moment is defined as $\langle \mathbf{d} \rangle = e\langle \mathbf{r} \rangle$ where e is the electric charge. It will play the central role in describing the atomic response to a light field.

2.2 Electromagnetic waves in free space

In the case of the electromagnetic field propagating in the absence of an atomic medium, $\mathbf{P} = 0$ and the right-hand side of the wave equation 2.6 vanishes leaving the homogeneous wave equation.

$$\nabla^2 \mathbf{E} - \frac{1}{c^2}\frac{\partial^2 \mathbf{E}}{\partial t^2} = 0, \tag{2.8}$$

where $c = 1/\sqrt{\mu_0 \epsilon_0}$ is the speed of light in a vacuum.

The solution to equation 2.8 takes the form

$$\mathbf{E}(z,t) = \frac{E_0}{2}\left[\mathcal{E}(z,t)e^{-i\omega t} + \mathcal{E}^*(z,t)e^{i\omega t}\right]\mathbf{p}(z,t), \tag{2.9}$$

written as the sum of the positive and negative frequency components (ω) for a monochromatic light wave traveling in the z direction. E_0 is a real positive amplitude. $\mathcal{E}(z,t) = \mathcal{E}_0(t)e^{-ikz}$ is the complex amplitude of the wave with the wave vector $k = \omega/c$. $\mathbf{p}(z,t)$ is the direction in which the electric field oscillates, the polarization of light, and so for example if the light stays linearly polarized in the x direction, $\mathbf{p}(z,t) = \hat{\mathbf{x}}$.

Alternatively, equation 2.9 can be written in terms of the quadrature amplitudes X1 and X2.

$$\mathbf{E}(z,t) = E_0\left[\mathrm{X1}(z,t)\cos\omega t + \mathrm{X2}(z,t)\sin\omega t\right]\mathbf{p}(z,t) \tag{2.10}$$

We call X1 and X2 the *amplitude* and *phase* quadratures respectively, and can express their relation to the complex amplitude of the electric field as follows:

$$\mathrm{X1}(z,t) = \frac{\mathcal{E}(z,t) + \mathcal{E}^*(z,t)}{2} \tag{2.11}$$

$$\mathrm{X2}(z,t) = \frac{-i[\mathcal{E}(z,t) - \mathcal{E}^*(z,t)]}{2}. \tag{2.12}$$

These quadratures can be directly observed in experiment. We will often be interested in the fluctuations of amplitude and phase with time, $\delta\,\mathrm{X1}(t)$ and $\delta\,\mathrm{X2}(t)$, which can be present as noise in the light signal.

2.3 Field quantization

For a quantum-mechanical treatment of the electromagnetic (EM) field, we exploit the connection between EM fields in a cavity and a simple harmonic oscillator, and quantize the light field. First, consider an EM field polarized in the x direction in a one-dimensional perfect cavity. The running-mode electric field will have the form [82]

$$\mathbf{E}(z,t) = \sum_j A_j q_j(t) e^{ik_j z}\hat{\mathbf{x}}. \tag{2.13}$$

Here $k_j = \omega_j/c$ is the wave vector with ω_j being the frequency of oscillation and q_j is a time-dependent amplitude. A_j is a normalization factor. In this case, the cavity will only support modes with $k_j = j\pi/L$ for integer values j to satisfy the boundary conditions. From Maxwell's equations, we find the magnetic field to be

$$\mathbf{B}(z,t) = \frac{1}{c^2}\sum_j A_j \frac{\dot{q}_j(t)}{k_j} e^{ik_jz}\hat{\mathbf{y}}. \tag{2.14}$$

Now we write down the classical Hamiltonian.

$$\mathcal{H} = \frac{1}{2}\int(\epsilon_0 E^2 + B^2/\mu_0)dV \tag{2.15}$$

We find that by choosing $A_j = \sqrt{\frac{\omega_j^2}{\epsilon_0 V}}$, we can identify $q_j(t)$ with the position coordinate of the harmonic oscillator, and recognize $\dot{q} = p$ as the momentum coordinate. Now plugging in equations 2.13 and 2.14 for the cavity leads to

$$\mathcal{H} = \frac{1}{2}\sum_j(\omega_j^2 q_j^2 + p_j^2), \tag{2.16}$$

which is the exact Hamiltonian for a simple harmonic oscillator.

We can now carry out canonical quantization and replace the variables q and p by the Hermitian operators $\hat{\mathbf{q}}$ and $\hat{\mathbf{p}}$ with the commutation relation $[\hat{\mathbf{q}}_i, \hat{\mathbf{p}}_j] = i\hbar\delta_{ij}$.

2.3.1 Creation and annihilation operators

It is useful to introduce the nonhermitian creation and annihilation operators for photons $\hat{\mathbf{a}}$ and $\hat{\mathbf{a}}^\dagger$.

$$\hat{\mathbf{a}} = \sqrt{\frac{1}{2\hbar\omega}}(\omega\,\hat{\mathbf{q}} + i\,\hat{\mathbf{p}}) \tag{2.17}$$

$$\hat{\mathbf{a}}^\dagger = \sqrt{\frac{1}{2\hbar\omega}}(\omega\,\hat{\mathbf{q}} - i\,\hat{\mathbf{p}}) \tag{2.18}$$

We find that these operators obey the commutation $[\hat{\mathbf{a}}_i, \hat{\mathbf{a}}_j^\dagger] = \delta_{ij}$ and that we can rewrite the Hamiltonian in terms of them.

$$\hat{\mathbf{H}} = \sum_j \hbar\omega_j \left(\hat{\mathbf{a}}_j^\dagger \hat{\mathbf{a}}_j + \frac{1}{2} \right) \tag{2.19}$$

The eigenstates of this Hamiltonian are the number states or Fock states $|n\rangle$, where n corresponds to the number of photons in the state. The creation and annihilation operators act to add or subtract photons as follows.

$$\hat{\mathbf{a}}^\dagger |n\rangle = \sqrt{n+1}\,|n+1\rangle \tag{2.20}$$

$$\hat{\mathbf{a}}\,|n\rangle = \sqrt{n}\,|n-1\rangle \tag{2.21}$$

The zero photon state is known as the *vacuum state* $|0\rangle$. By repeatedly applying the creation operator, we can build any number state from the vacuum.

$$|n\rangle = \frac{(\hat{\mathbf{a}}^\dagger)^n}{\sqrt{n!}}\,|0\rangle \tag{2.22}$$

It is important to note that when applying the Hamiltonian (eq. 2.19) to the vacuum state, $\hat{\mathbf{H}}\,|0\rangle$, we find a nonzero energy of $\hbar\omega/2$, which is the zero point energy arising from vacuum fluctuations.

2.3.2 Quadrature operators

The electric field and Hamiltonian can also be written in terms of the quadrature amplitudes introduced in the previous section. By integrating the square of equation 2.10 over a small volume element, we come to the classical Hamiltonian in terms of X1 and X2.

$$\mathcal{H} = \sum_j \hbar\omega_j (\mathrm{X1}_j^2 + \mathrm{X2}_j^2) \tag{2.23}$$

We again can perform a canonical quantization by making the identifications

$$q = \sqrt{\frac{2\hbar}{\omega}}\,\mathrm{X1}, \quad p = \sqrt{2\hbar\omega}\,\mathrm{X2}\,. \tag{2.24}$$

This gives us the quantum operators $\hat{\mathbf{X1}}$ and $\hat{\mathbf{X2}}$ with commutation relationship $[\hat{\mathbf{X1}}_i, \hat{\mathbf{X2}}_j] = \frac{i}{2}\delta_{ij}$. It follows that X1 and X2 must follow the Heisenberg uncertainty relation,

$$\Delta\,\mathrm{X1}\,\Delta\,\mathrm{X2} \geq \left|\frac{1}{2i}\langle[\hat{\mathbf{X1}}, \hat{\mathbf{X2}}]\rangle\right| = \frac{1}{4}. \tag{2.25}$$

Note that these operators are also Hermitian ($\hat{\mathbf{X}} = \hat{\mathbf{X}}^\dagger$) meaning they each have real eigenvalues corresponding to the value of an observable. We will see that these quadrature uncertainties can be directly detected as the quantum noise in our experiment. We also have the simple relationships between the quadrature amplitude operators, and the creation and annihilation operators.

$$\hat{\mathbf{X1}} = \frac{\hat{\mathbf{a}} + \hat{\mathbf{a}}^\dagger}{2} \tag{2.26}$$

$$\hat{\mathbf{X2}} = \frac{(\hat{\mathbf{a}} - \hat{\mathbf{a}}^\dagger)}{2i} \tag{2.27}$$

2.3.3 Electric field operator

We now have useful forms of the time-dependent electric field operator for a monochromatic light field, written in terms of either $\hat{\mathbf{a}}$ and $\hat{\mathbf{a}}^\dagger$, or $\hat{\mathbf{X1}}$ and $\hat{\mathbf{X2}}$.

$$\hat{\mathbf{E}}(z,t) = \frac{E_0}{2}\left[\hat{\mathbf{a}}\,e^{i(kz-\omega t)} + \hat{\mathbf{a}}^\dagger\,e^{-i(kz-\omega t)}\right] \tag{2.28}$$

$$\hat{\mathbf{E}}(z,t) = E_0\left[\hat{\mathbf{X1}}\cos\left(\omega t - kz\right) + \hat{\mathbf{X2}}\sin\left(\omega t - kz\right)\right] \tag{2.29}$$

Note that we wish to describe light in free space by using the operators $\hat{\mathbf{a}}$ and $\hat{\mathbf{a}}^\dagger$ for the cavity modes. The extension to free space will change the normalization of the electric field operator, however this can be absorbed into the amplitude E_0, and the distinction will not be important (see discussion in Appendix A).

In this dissertation, we will often be interested in the vacuum state $|0\rangle$, so it is instructive to find the expectation value and variance of the electric field operator of the vacuum state. By applying equations 2.20 and 2.21, it is easily seen that the mean electric field is zero, but that the expectation of its square is nonzero, giving rise to nonzero fluctuations in the electric field of the vacuum.

$$\langle 0| \hat{\mathbf{E}}(z,t) |0\rangle = 0 \tag{2.30}$$

$$\langle 0| \hat{\mathbf{E}}(z,t)^2 |0\rangle = \frac{E_0^2}{4} \tag{2.31}$$

2.4 Coherent states

The Fock states $\{|n\rangle\}$ with well-defined numbers of photons are nonclassical states of light. These number states contain no well-defined phase, and do not match the model of an oscillating electric field generally used to describe classical light. The state that best models a classical harmonic oscillator, and thus the light produced by a laser, is the *coherent state*, $|\alpha\rangle$. Coherent states of light have a well defined phase and a Poissonian number distribution; they closely resemble the output states of a coherent laser.

We find that the coherent states are eigenstates of the annihilation operator, such that

$$\hat{\mathbf{a}} |\alpha\rangle = \alpha |\alpha\rangle . \tag{2.32}$$

It is not surprising that the eigenstates of the annihilation operator can model classical light, because as we have seen, the electric field operator is proportional to $\hat{\mathbf{a}}$, and we generally describe classical light according to its electric field. The eigenvalue α is a complex amplitude completely analogous to the classical amplitude $\mathcal{E}$ from equation 2.9, with the normalization condition $\langle\alpha|\,\alpha\rangle = 1$. Coherent states can be created by displacing the vacuum state using the unitary displacement operator [2]

$$|\alpha\rangle = \hat{\mathbf{D}}(\alpha)\,|0\rangle\,, \tag{2.33}$$

with the displacement operator being defined as

$$\hat{\mathbf{D}}(\alpha) = e^{\left(\alpha\,\hat{\mathbf{a}}^{\dagger}\,-\alpha^{*}\,\hat{\mathbf{a}}\right)}. \tag{2.34}$$

In the basis of the Fock states, the coherent states can be written as an infinite series [82].

$$|\alpha\rangle = e^{-|\alpha|^2/2}\sum_{n}\frac{\alpha^n}{\sqrt{n!}}\,|n\rangle \tag{2.35}$$

By applying the number operator $\hat{\mathbf{n}} = \hat{\mathbf{a}}^{\dagger}\,\hat{\mathbf{a}}$ to a coherent state, we find the expectation value for the number of photons in the state.

$$\langle\alpha|\,\hat{\mathbf{a}}^{\dagger}\,\hat{\mathbf{a}}\,|\alpha\rangle = \alpha^{*}\alpha = |\alpha|^2. \tag{2.36}$$

We find the same result for the variance of the number of photons

$$(\Delta\,\mathrm{n})^2 = \langle\alpha|\,\hat{\mathbf{n}}^2\,|\alpha\rangle - \langle\alpha|\,\hat{\mathbf{n}}\,|\alpha\rangle^2 = |\alpha|^2, \tag{2.37}$$

which is characteristic of a Poissonian distribution.

We now wish to find the uncertainties of the quadrature operators $\hat{\mathbf{X1}}$ and $\hat{\mathbf{X2}}$ for a coherent state.

$$\Delta\,\mathrm{X1} = \sqrt{\langle\hat{\mathbf{X1}}^2\rangle_\alpha - \langle\hat{\mathbf{X1}}\rangle_\alpha^2} = 1/2 \tag{2.38}$$

$$\Delta\,\mathrm{X2} = \sqrt{\langle\hat{\mathbf{X2}}^2\rangle_\alpha - \langle\hat{\mathbf{X2}}\rangle_\alpha^2} = 1/2 \tag{2.39}$$

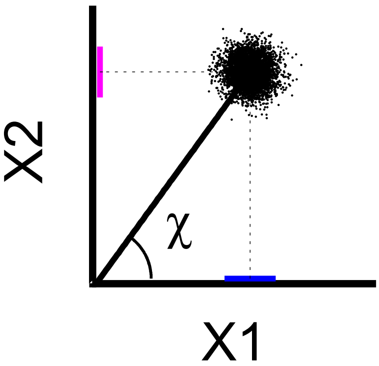

FIG. 2.1: Quantum uncertainty of a coherent state shown in a phasor diagram.

Here we have used the definitions of the quadrature operators (equations 2.26 and 2.27) and the commutator $[\hat{\mathbf{a}}, \hat{\mathbf{a}}^\dagger] = 1$. So for a coherent state, the Heisenberg uncertainty relation of equation 2.25 becomes an equality.

$$\Delta\,\mathrm{X1}_\alpha\,\Delta\,\mathrm{X2}_\alpha = \frac{1}{4} \tag{2.40}$$

This means that the coherent state is a minimum uncertainty state with the uncertainty equally distributed between its quadratures. We can represent light states using phasor diagrams, as shown in Fig. 2.1, where the amplitude is the length of a vector and the light phase is an angle χ with respect to a reference phase. The quantum uncertainty is represented by a ball of noise at the end of the vector. The quadrature uncertainties then will be the projections of this uncertainty onto X1 and X2. The noise power of a quadrature will be determined by the variance of the operator, the square of its uncertainty,

$$V1_\alpha = \Delta\,\mathrm{X1}^2 = 1/4 \tag{2.41}$$

$$V2_\alpha = \Delta\,\mathrm{X2}^2 = 1/4, \tag{2.42}$$

and so there will be an equal amount of quantum noise on the amplitude and phase of a coherent light signal. Another important result is for the vacuum state $|0\rangle$, with an average of zero photons.

$$\Delta\,\mathrm{X1}_0 = \Delta\,\mathrm{X2}_0 = \frac{1}{2} \tag{2.43}$$

So the vacuum state is also a minimum uncertainty state with the same amount of noise (or vacuum fluctuations) distributed over its quadratures ($V1_0 = V2_0 = 1/4$). For this reason, the naturally occurring vacuum state will often be referred to as a *coherent vacuum*. On a phasor diagram, the vacuum state will show a ball of uncertainty centered at the origin, with the average amplitude being 0.

These quantum fluctuations, which are always present in coherent bright states and coherent vacuum, put a limit on the precision of any optical measurement. This level of uncertainty or noise in a measurement, due only to quantum fluctuations, defines the standard quantum limit (SQL), which cannot be surpassed by any classical means.

2.5 Squeezed coherent states

The uncertainty relation of equation 2.25 dictates that the product of uncertainties of the amplitude and phase quadratures of light must be greater than a certain value. However, it is not a general requirement that the uncertainty in each quadrature be equal ($\Delta\,\mathrm{X1} = \Delta\,\mathrm{X2}$) as is the case for coherent states and the vacuum. A squeezed state is a state in which one quadrature uncertainty is reduced to below the value found in a coherent state ($\Delta\,\mathrm{X}_{\mathrm{sq}} < 1/2$). To satisfy the uncertainty principle, the uncertainty of the conjugate variable must be increased in compensation, that is, if the X1 quadrature is squeezed, the X2 quadrature must be stretched, its uncertainty increased. Therefore, when measuring noise, one would observe that the X1 noise level falls below shot noise (squeezed) while the X2 noise level would rise above shot noise (antisqueezed). Individually measuring the noise of light quadratures, and thus the squeezing and antisqueezing levels, can be achieved through homodyne detection, discussed in a later section.

To generate such a squeezed state, labeled $|\xi, \alpha\rangle$, from a coherent state, we apply the squeezing operator $\hat{\mathbf{S}}$.

$$|\xi, \alpha\rangle = \hat{\mathbf{S}}(\xi)\,|\alpha\rangle = \hat{\mathbf{D}}(\alpha)\,\hat{\mathbf{S}}(\xi)\,|0\rangle \tag{2.44}$$

The squeezing operator is defined [2]

$$\hat{\mathbf{S}}(\xi) = \exp\left(\frac{1}{2}\xi^*\,\hat{\mathbf{a}}^2 - \frac{1}{2}\xi\,\hat{\mathbf{a}}^{\dagger 2}\right). \tag{2.45}$$

In this definition, $\hat{\mathbf{a}}$ and $\hat{\mathbf{a}}^\dagger$ are the same creation and annihilation operators for photons. ξ is the squeezing parameter defined as

$$\xi = r_s e^{2i\theta_s}. \tag{2.46}$$

It contains the variable r_s which is the *degree of squeezing* or *squeeze factor* as well as θ_s, the *squeezing angle*. The value of these variables will be determined by the process leading to squeezed light generation.

We can now investigate the properties of a squeezed state. The following relations will be helpful [2].

$$\hat{\mathbf{S}}^\dagger(\xi) = \hat{\mathbf{S}}^{-1}(\xi) \tag{2.47}$$

$$\hat{\mathbf{S}}^\dagger(\xi)\,\hat{\mathbf{a}}\,\hat{\mathbf{S}}(\xi) = \hat{\mathbf{a}}\cosh r_s - \hat{\mathbf{a}}^\dagger\,e^{-2i\theta_s}\sinh r_s \tag{2.48}$$

$$\hat{\mathbf{S}}^\dagger(\xi)\,\hat{\mathbf{a}}^\dagger\,\hat{\mathbf{S}}(\xi) = \hat{\mathbf{a}}^\dagger\cosh r_s - \hat{\mathbf{a}}\,e^{2i\theta_s}\sinh r_s \tag{2.49}$$

Now we find that the expectation value for the number of photons in a squeezed state is

$$\langle\alpha|\,\hat{\mathbf{S}}^\dagger\,\hat{\mathbf{a}}^\dagger\,\hat{\mathbf{a}}\,\hat{\mathbf{S}}\,|\alpha\rangle = |\alpha|^2 + \sinh^2 r_s. \tag{2.50}$$

Recall that a coherent state has an average $|\alpha|^2$ photon number; here we have an addition of the ‘sinh’ term dependent on the squeeze factor r_s. Also, the mean number of photons in a squeezed vacuum will be nonzero, and will depend only on this squeeze factor. Using equations 2.48 and 2.49, we see how two orthogonal quadrature operators are affected for a squeezed state.

$$\hat{\mathbf{S}}^\dagger\, \hat{\mathbf{X1}}\, \hat{\mathbf{S}} = \frac{1}{2}\left[\left(\hat{\mathbf{a}} + \hat{\mathbf{a}}^\dagger\right)\cosh r_s - \left(\hat{\mathbf{a}}\, e^{2i\theta} + \hat{\mathbf{a}}^\dagger\, e^{-2i\theta_s}\right)\sinh r_s\right] \tag{2.51}$$

$$\hat{\mathbf{S}}^\dagger\, \hat{\mathbf{X2}}\, \hat{\mathbf{S}} = \frac{1}{2i}\left[\left(\hat{\mathbf{a}} - \hat{\mathbf{a}}^\dagger\right)\cosh r_s + \left(\hat{\mathbf{a}}\, e^{2i\theta} - \hat{\mathbf{a}}^\dagger\, e^{-2i\theta_s}\right)\sinh r_s\right] \tag{2.52}$$

We can choose to define our quadratures in such a way that we set the squeezing angle to zero, $\theta_s = 0$. In this case, the relationships reduce to

$$\hat{\mathbf{S}}^\dagger\, \hat{\mathbf{X1}}\, \hat{\mathbf{S}} = \hat{\mathbf{X1}}\, e^{-r_s} \tag{2.53}$$

$$\hat{\mathbf{S}}^\dagger\, \hat{\mathbf{X2}}\, \hat{\mathbf{S}} = \hat{\mathbf{X2}}\, e^{r_s}, \tag{2.54}$$

where we have used the fact that $\cosh x + \sinh x = e^x$ and $\cosh x - \sinh x = e^{-x}$. This leads to the minimum and maximum quadrature uncertainties in a squeezed state of light:

$$\Delta\,\mathrm{X1} = \frac{e^{-r_s}}{2}, \qquad \Delta\,\mathrm{X2} = \frac{e^{r_s}}{2}. \tag{2.55}$$

This shows that a squeezed state in this formalism is still a minimum uncertainty state ($\Delta\,\mathrm{X1}\,\Delta\,\mathrm{X2} = 1/4$) but now with unequal quadrature uncertainty levels. Depending on the degree of squeezing r_s, one quadrature is squeezed ($\Delta\,\mathrm{X1} < 1/2$) while the orthogonal quadrature is stretched ($\Delta\,\mathrm{X2} > 1/2$).

In a phasor diagram, this is equivalent to the circle of uncertainty being squeezed into an ellipse. We demonstrate this idea in Fig. 2.2. The top plots depict the uncertainties of the X1 and X2 quadratures one would expect for a coherent state (a) and for squeezed states (b, c) with different squeezing angles and an arbitrary squeezing parameter. Fig. 2.2(d) depicts a squeezed vacuum, where the squeezing ellipse sits at the origin because there is no coherent amplitude. The bottom plots show the projection of the X1

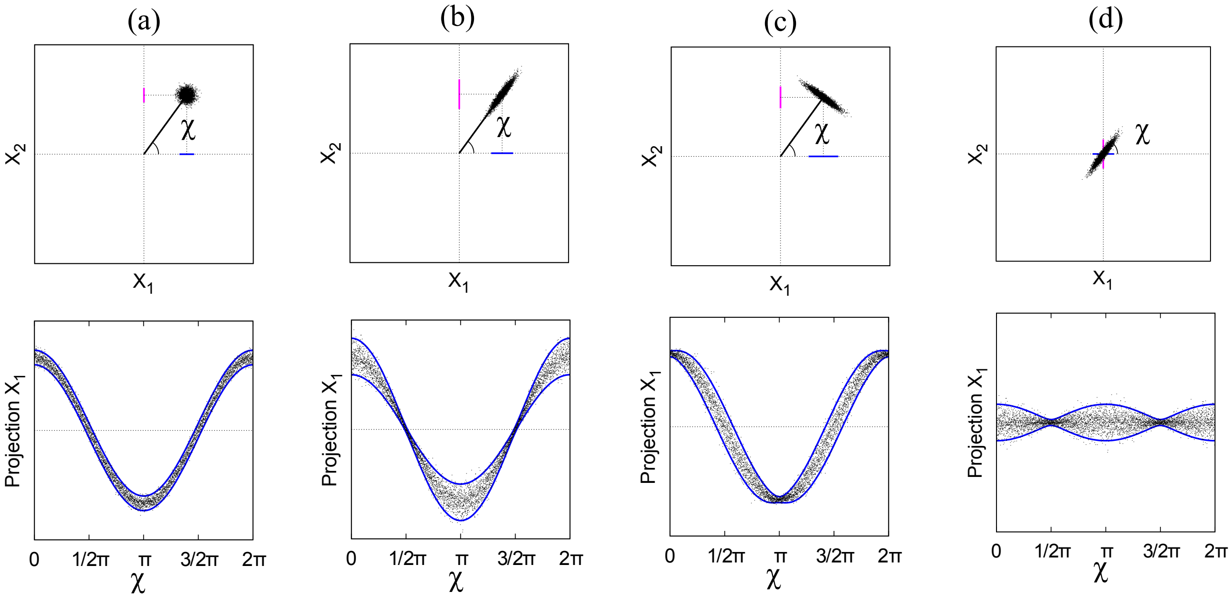

FIG. 2.2: Quantum uncertainty shown in phasor diagrams and the projection of the X1 quadrature vs phase χ. (a) Coherent state. (b) Phase squeezed state. (c) Amplitude squeezed state. (d) Squeezed coherent vacuum.

quadrature as the phase angle χ is changed. This demonstrates how the uncertainty of the squeezed states is phase dependent. It is clear that for (b), the phase uncertainty is reduced, while in (c), the amplitude uncertainty is reduced. A squeezed vacuum state displays phase-dependent noise as the squeezing ellipse is rotated around the origin (in Fig. 2.2(d)).

If $r_s = 0$, there is no squeezing and we see that the quadrature uncertainties return to those seen in a coherent state ($\Delta\,\mathrm{X} = 1/2$). One should note that it is also possible, and more common in experiments, to have a squeezed state that is not a minimum uncertainty state. In this case, while one quadrature noise reaches levels below shot noise, the orthogonal quadrature may have excess noise far above the shot noise level. It is also important to note that the squeezing operator $\hat{\mathbf{S}}$ involves two-photon processes, being made up of the terms $\hat{\mathbf{a}}^2$ and $\hat{\mathbf{a}}^{\dagger 2}$. This explains how squeezed light may be generated by making use of certain two-photon interactions.

2.6 Nonlinear processes in atoms

Squeezed states of light can be generated as the result of reducing the noise in one quadrature while amplifying the noise in the orthogonal quadrature in compensation. This type of process, creating correlations between the two quadratures, can be achieved through several multi-photon nonlinear processes.

To study such processes, we must include the interaction of light with matter in the electromagnetic wave equation (equation 2.6). The presence of the electric field induces a dipole polarization inside the atomic medium. A simple form of the polarization is

$$\mathbf{P} = \epsilon_0 \left(\chi \mathbf{E} + \chi^{(2)} \mathbf{E}^2 + \chi^{(3)} \mathbf{E}^3 + ... \right). \tag{2.56}$$

Here, $\chi^{(n)}$ is the dimensionless, n^{th} order electric susceptibility, which depends on the structure of the atomic material. For weak fields and low atomic densities, most materials respond linearly with electric field, and the polarization only includes the first term of the above equation. However, at greater light intensities, the higher order terms $\chi^{(2)}$ and $\chi^{(3)}$ begin to contribute, giving rise to many important nonlinear processes. This is the basis for the field of nonlinear optics, where the light field itself can affect the optical properties of the atomic material.

Here are a couple simplified forms of the two-photon Hamiltonians describing nonlinear processes [2, 3].

$$\hat{\mathbf{H}} = i\hbar \left[\alpha \chi^{(2)} \, \hat{\mathbf{a}}^2 - \alpha \chi^{(2)} \, \hat{\mathbf{a}}^{\dagger 2} \right] \tag{2.57}$$

$$\hat{\mathbf{H}} = i\hbar \left[\alpha^2 \chi^{(3)} \, \hat{\mathbf{a}}^2 - \alpha^2 \chi^{(3)} \, \hat{\mathbf{a}}^{\dagger 2} \right] \tag{2.58}$$

$\hat{\mathbf{a}}^\dagger$ and $\hat{\mathbf{a}}$ are again the photon creation and annihilation operators, and α is the amplitude of a classical pump field. Equation 2.57 describes a simple parametric amplifier. Equation 2.58 describes a four-wave mixing (FWM) process or a nonlinear Kerr process. Other processes such as parametric down conversion and second harmonic generation will have similar Hamiltonians. These processes display the nonlinearities which can, under the right circumstances, build up correlations between light quadratures and lead to squeezing. To see this more explicitly, consider the time-evolution operators resulting from these Hamiltonians.

$$|\psi(t)\rangle = \hat{\mathbf{U}}(t)\,|\psi(0)\rangle = e^{-i\hat{\mathbf{H}}\,t/\hbar}\,|\psi(0)\rangle \tag{2.59}$$

By inserting the above Hamiltonians into this equation, it is clear that these operators will closely resemble the squeezing operator from equation 2.45, with the strength of the n^{th} order susceptibilities determining the amount of squeezing or antisqueezing produced.

As an example of how a nonlinear process can lead to squeezed light phenomenologically, consider the nonlinear optical Kerr effect. In any atomic medium where this effect is present, the refractive index of the material will change based on the intensity of a strong laser passing through it. The index of refraction, in turn, will change the phase of the light passing through the material. Therefore, amplitude fluctuations in the light will modulate the refractive index, which will modulate the phase, and so the amplitude and phase quadrature fluctuations become correlated [2].

2.7 Sideband model of squeezing and two-photon formalism

We will find that squeezing production relies on multiple photon nonlinear effects, and correlations building between these photons. This leads us to the correlated sideband picture of squeezed light.

Thus far, we have treated only monochromatic light—a clear oversimplification. More rigorously, we should consider a light field at the carrier frequency ω_0, and any noise or modulation at sideband frequencies $\pm\Omega$, resulting from beatnotes of the carrier with nearby frequencies. In the case of quantum noise, vacuum photons exist at all frequencies. The modulation to the carrier light field at each frequency Ω is the result of contributions from the sideband photons at $\omega_0 + \Omega$ and $\omega_0 - \Omega$. The sideband photons from the vacuum have no regular phase relationship between them, and so are uncorrelated. This results in random modulation of both the amplitude and phase of the carrier light at all frequencies, and is the source of the shot noise or quantum noise.

Squeezing of the light field can be achieved by reducing this quantum noise on one quadrature while increasing it on the orthogonal quadrature. This is accomplished by creating pairs of correlated sideband photons, that is, photons at the frequencies $\omega_0 \pm \Omega$ that have a well-defined phase between them. Depending on this phase relationship, the carrier signal is modulated such that its amplitude and phase quadratures change. This is basically the quantum analogue of classical amplitude or phase modulation (AM, PM). By replacing uncorrelated vacuum photons with pairs of strongly correlated sideband photons, the quantum noise on a light signal is dramatically altered, leading to squeezed and antisqueezed noise levels. The strength of the correlations between photons, as well as the decoherence of this correlation, determines the level of squeezing attainable.

Because squeezed light is a two-photon process, it is convenient to describe it using the two-photon formalism developed by Caves and Shumaker [7]. To describe the photons at sideband frequencies $\pm\Omega$, we can use the creation and annihilation operators in Fourier space,

$$\hat{\mathbf{a}}_+ = \hat{\mathbf{a}}(\omega_0 + \Omega) \tag{2.60}$$

$$\hat{\mathbf{a}}_- = \hat{\mathbf{a}}(\omega_0 - \Omega), \tag{2.61}$$

and it is easy to see that $\hat{\mathbf{a}}^\dagger(\omega_0 + \Omega) = \hat{\mathbf{a}}(\omega_0 - \Omega)^\dagger$. We define the quadrature operators [7],

$$\hat{\mathbf{X1}}(\Omega) = \frac{\sqrt{\frac{\omega_0+\Omega}{\omega_0}}\,\hat{\mathbf{a}}_+ + \sqrt{\frac{\omega_0-\Omega}{\omega_0}}\,\hat{\mathbf{a}}_-^\dagger}{2} \tag{2.62}$$

$$\hat{\mathbf{X2}}(\Omega) = \frac{\sqrt{\frac{\omega_0+\Omega}{\omega_0}}\,\hat{\mathbf{a}}_+ - \sqrt{\frac{\omega_0-\Omega}{\omega_0}}\,\hat{\mathbf{a}}_-^\dagger}{2i}. \tag{2.63}$$

Notice that the normalization factors go to 1 for small Ω. We can also write the two-photon squeezing operator, now including photons from both sidebands ($\pm\Omega$),

$$\hat{\mathbf{S}}(\xi,\Omega) = \exp\left(\frac{1}{2}\xi^{*}\,\hat{\mathbf{a}}_{+}\,\hat{\mathbf{a}}_{-} - \frac{1}{2}\xi\,\hat{\mathbf{a}}_{+}^{\dagger}\,\hat{\mathbf{a}}_{-}^{\dagger}\right), \tag{2.64}$$

where $\xi = r_s e^{2i\theta_s}$ remains unchanged from equation 2.46. The two-photon squeezing operator gives insight into the types of interactions which can lead to the generation of squeezed light. Several nonlinear interactions of light with matter can produce photon pairs with the necessary correlations to produce squeezed states.

When recording the quantum noise, the carrier frequency ω_0 is selected by the local oscillator in the homodyne detection scheme, and the noise power at a certain frequency Ω is the result of the combined effect of both sidebands. The phase-dependent noise observed in squeezed states is due to interference between the upper and lower sideband, made possible by the coherent phase between them.

CHAPTER 3

Nonlinear polarization self-rotation effect

3.1 Polarization self-rotation

The nonlinear process known to produce quadrature squeezed vacuum which is examined in this dissertation is the polarization self-rotation (PSR) effect. PSR is a rotation of the axis of polarization of near-resonant light as it travels through a nonlinear atomic sample. Here we see how this effect can lead to squeezed vacuum states, and discuss theoretical predictions as well as limitations for this method.

3.1.1 PSR effect in atomic vapor

Any polarization of light can be decomposed into its left- and right-handed circularly-polarized components σ^- and σ^+. For linearly polarized light, these components are equal. For initially elliptically polarized light, σ^- and σ^+ have unequal strengths, that cause unequal couplings to the different Zeeman substates of an atomic system. This leads to an imbalance in ground state populations due to optical pumping and differing ac Stark shifts [83]. These in turn, cause the index of refraction experienced by the two polarizations to differ, inducing circular birefringence and linear dichroism in the medium. As a result, the σ^- and σ^+ components of a light signal travel at different phase velocities and acquire a phase shift with respect to one another. It is easy to see that this phase shift will cause the axis of ellipticity for the light to rotate as it propagates through the atomic medium. If $\sigma^\pm = (E_x \pm iE_y)/2$ in terms of the x and y polarization components of the electric field, and the circular polarization components acquire a phase shift, $\sigma^+ = \sigma_0^+ e^{-i\phi}, \quad \sigma^- = \sigma_0^- e^{i\phi}$, then the polarization components will undergo a rotation as follows.

$$\begin{pmatrix} E_x \\ E_y \end{pmatrix} = \begin{pmatrix} \cos\phi & \sin\phi \\ -\sin\phi & \cos\phi \end{pmatrix} \begin{pmatrix} E_{x0} \\ E_{y0} \end{pmatrix} \tag{3.1}$$

If we assume a small initial ellipticity $\epsilon(0) \ll 1$, the polarization rotation angle arising from the phase shift($\varphi = \phi$) is [67]

$$\varphi = g\epsilon(0)L, \tag{3.2}$$

where L is the length of the medium, and g is the *self-rotation parameter* which is dependent on the light intensity and the properties of the atomic system. The distinctive feature of PSR is that the strength and direction of rotation depends on the initial light ellipticity, and it does not require the presence of an external magnetic field.

3.1.2 PSR squeezing

Self-rotation can lead to squeezed light by correlating fluctuations in the amplitude and phase quadratures similar to the case of a simple Kerr medium. Imagine a strong field polarized along the y direction co-propagating with a weak field polarized along the x direction. These fields on their own are each linear, but they combine to form a slightly elliptically polarized beam which will rotate under PSR according to equation 3.2. Due to this rotation, the strong field projects a portion of itself onto the weaker orthogonal field.

Now if we assume a relative phase between the x and y polarizations, the weak field can experience phase-sensitive amplification or reduction due to the projection of the strong field, depending on the phase between x and y [67]. This analysis holds true even if we assume the weak x-polarized field arises solely due to vacuum fluctuations. Therefore, due to PSR, the x-polarized vacuum fluctuations can interact with a strong linearly y-polarized beam in an atomic medium, leading to a phase-sensitive amplification of these fluctuations: i.e. resulting in a squeezed vacuum field on the x polarization.

To better understand the squeezing mechanism, we consider the idea of cross-phase modulation (XPM). A strong y-polarized field is decomposed into its right (σ^+) and left (σ^-) handed circular components. When two photons are simultaneously absorbed from these fields, it is possible to have the simultaneous emission of two photons into the vacuum x polarization due to stimulated emission. Due to the ground state coherence of the system, the phases of the scattered photons become correlated. These correlated photons lead to a modification of the quadrature noise levels of the x polarization as described in section 2.7. Note that this is closely related to a four-wave mixing process, which also has been shown to generate squeezed light states [22].

To predict the amount of squeezing quantitatively, we start with a classical electric field traveling in the z direction with both x and y polarized components.

$$\mathbf{E}(z,t) = E_x(z)e^{i[kz-\omega t+\phi(z)]}\hat{\mathbf{x}} + E_y(z)e^{i[kz-\omega t]}\hat{\mathbf{y}} + \mathbf{c.c.} \tag{3.3}$$

E_x and E_y are real amplitudes, ϕ is the relative phase between the polarization components, and **c.c.** denotes the complex conjugate, being the negative frequency components in this case. The ellipticity of light is given by [67]

$$\epsilon = \frac{1}{2}\arcsin\frac{i\left(E_x^- E_y^+ - E_y^- E_x^+\right)}{|E_x|^2 + |E_y|^2}, \tag{3.4}$$

where $E^{\pm}$ are the positive and negative frequency components of the field. Assuming that

$E_y \gg E_x$,

$$\epsilon(z) \approx \frac{E_x(z)}{E_y(z)} \sin\phi(z). \tag{3.5}$$

We see how the electric field changes due to a rotation by the small angle φ by applying the rotation matrix

$$\begin{bmatrix} \cos\varphi & \sin\varphi \\ -\sin\varphi & \cos\varphi \end{bmatrix} \approx \begin{bmatrix} 1 & \varphi \\ -\varphi & 1 \end{bmatrix}. \tag{3.6}$$

Applying this rotation to the initial field ($z = 0$) and inserting the angle of rotation from equation 3.2, we find that the x component of the field after propagating a distance L through the medium is

$$\mathbf{E_x}(L,t) \approx \left[E_x(0)e^{i\phi} + \varphi E_y(0)\right] e^{i(kL-\omega t)} + \mathbf{c.c}. \tag{3.7}$$

For now, we assume there is no absorption in the medium. Inserting equations 3.2 for the rotation angle, and 3.5 for the ellipticity, we have the rotated field:

$$\mathbf{E_x}(L,t) \approx E_x(0)\left[e^{i\phi(0)} + gL\sin\phi(0)\right] e^{i(kL-\omega t)} + \mathbf{c.c}. \tag{3.8}$$

To describe a nonclassical squeezed vacuum, we must move to a quantum description of the light. The initial x polarization of the light is given according to the electric field operator as shown in equation 2.28,

$$\hat{\mathbf{E}}_x(z,t) = \frac{E_0}{2}\left[\hat{\mathbf{a}}_x\, e^{i(kz-\omega t)} + \hat{\mathbf{a}}_x^\dagger\, e^{-i(kz-\omega t)}\right], \tag{3.9}$$

where we now have the real amplitude E_0 for the quantized vacuum field. We replace the exponential phase in this operator by a simple phase angle χ.

$$\hat{\mathbf{E}}_x(z,t) = \frac{E_0}{2}\left[\hat{\mathbf{a}}_x\, e^{i\chi} + \hat{\mathbf{a}}_x^\dagger\, e^{-i\chi}\right] \tag{3.10}$$

Because changes to the quantum noise seen in squeezed vacuum will be phase-dependent, to measure it, we need to use phase-sensitive homodyne detection as will be described in section 5.1. For this reason, the phase-dependent operator shown above is used, where χ is the relative phase of the field of interest with respect to a local oscillator of the same frequency used in detection.

The ellipticity operator is [67]

$$\hat{\epsilon}(z) = E_0 \frac{\hat{\mathbf{a}}_x(z) - \hat{\mathbf{a}}_x^\dagger(z)}{2iE_y(z)}. \tag{3.11}$$

After rotation, the quantum version of equation 3.8 is as follows,

$$\hat{\mathbf{E}}_x(\chi, L) = \frac{E_0}{2} \left[\hat{\mathbf{a}}_x(0)\left(e^{i\chi} - igL\cos\chi\right) + \hat{\mathbf{a}}_x^\dagger(0)\left(e^{-i\chi} + igL\cos\chi\right)\right], \tag{3.12}$$

written in terms of the creation and annihilation operators of the x-polarized field before rotation ($z = 0$). We can now analyze this operator for the case where this x-polarized beam is the vacuum state. The expectation value $\langle 0| \hat{\mathbf{E}}_x |0\rangle$ is trivially zero. However, the expectation value of the square of the field operator is nonzero. We then find the variance to be

$$\langle \hat{\mathbf{E}}_x(\chi, L)^2 \rangle = \frac{E_0^2}{4}\left(1 - 2gL\sin\chi\cos\chi + g^2L^2\cos^2\chi\right). \tag{3.13}$$

Recall from equation 2.31 that the variance of a coherent vacuum field is $E_0^2/4$. Now after the field is rotated, we see the same variance with the additional terms dependent on g, L, and the phase χ. This translates into phase-dependent noise which can be either larger than or smaller than the noise of the coherent vacuum, i.e. a squeezed vacuum state. The variance from equation 3.13 is plotted in Fig. 3.1 versus the phase χ. The amount of squeezing or antisqueezing achievable is set by the rotation parameters g and L, while the local oscillator phase angle χ sets the quadrature to be detected. As an example, when $\chi = \pi/2 \pm n$, for any whole number n, the noise of the squeezed vacuum will be equal to that of the unsqueezed coherent vacuum ($E_0^2/4$). However, with the correct choice of

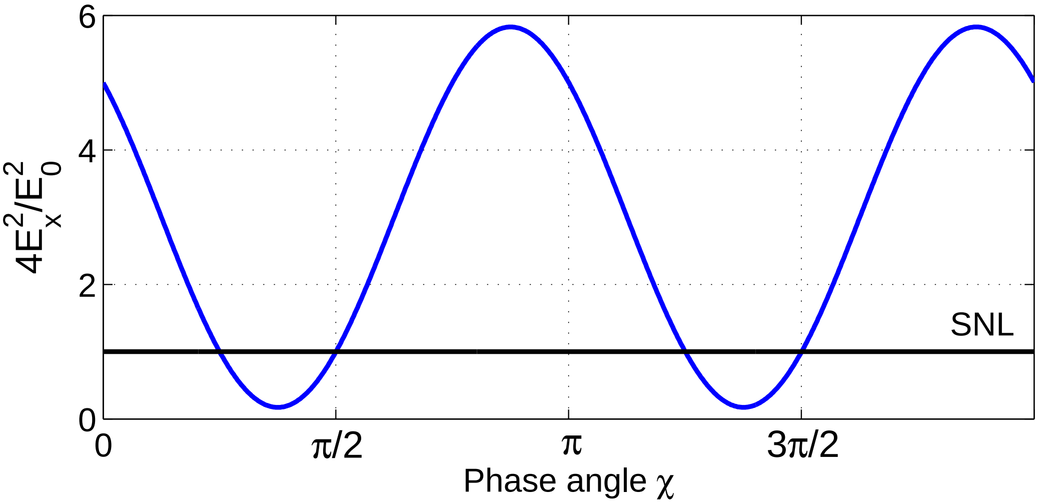

FIG. 3.1: Variance of the electric field after undergoing rotation vs local oscillator phase χ. This is compared to the shot noise (SNL), which is the variance of an unsqueezed vacuum ($E_0^2/4$). gL is set to 2.

phase angle, we can detect the maximal amount of squeezing for a given rotation medium.

3.1.3 Polarization squeezing

The x polarization of the output state of light from such a PSR medium is a quadrature-squeezed vacuum. It is important to note however, that when the strong y polarization is included, this state can be considered to be a polarization-squeezed state (PSS) [74, 84, 85]. In polarization squeezing, one compares the variances of the Stokes parameters of the field as described in Ref. [85].

$$\hat{\mathbf{S}}_0 = \hat{\mathbf{a}}_x^\dagger \hat{\mathbf{a}}_x + \hat{\mathbf{a}}_y^\dagger \hat{\mathbf{a}}_y \tag{3.14}$$

$$\hat{\mathbf{S}}_1 = \hat{\mathbf{a}}_x^\dagger \hat{\mathbf{a}}_x - \hat{\mathbf{a}}_y^\dagger \hat{\mathbf{a}}_y \tag{3.15}$$

$$\hat{\mathbf{S}}_2 = \hat{\mathbf{a}}_x^\dagger \hat{\mathbf{a}}_y + \hat{\mathbf{a}}_y^\dagger \hat{\mathbf{a}}_x \tag{3.16}$$

$$\hat{\mathbf{S}}_3 = i\left(\hat{\mathbf{a}}_y^\dagger \hat{\mathbf{a}}_x - \hat{\mathbf{a}}_x^\dagger \hat{\mathbf{a}}_y\right) \tag{3.17}$$

These operators can be shown to follow the commutation relations

$$[\hat{\mathbf{S}}_0, \hat{\mathbf{S}}_i] = 0 \tag{3.18}$$

$$[\hat{\mathbf{S}}_i, \hat{\mathbf{S}}_j] = \epsilon_{ijk} 2i\, \hat{\mathbf{S}}_k, \tag{3.19}$$

where ϵ_{ijk} is the Levi-Civita symbol for i= 1, 2, 3. Thus, one can form the Heisenberg Uncertainty relations

$$\Delta S_i \Delta S_j \geq \frac{1}{2i} \langle [S_i, S_j] \rangle, \tag{3.20}$$

and compare the uncertainties of polarization-squeezed states to coherent states.

In our case, with a linear y-polarized coherent state $|\alpha_y\rangle$, the only nonzero uncertainty relation is

$$\Delta S_2 \Delta S_3 \geq \langle \hat{\mathbf{S}}_1 \rangle = \alpha_y^2, \tag{3.21}$$

using $\hat{\mathbf{a}}_y \, |\alpha_y\rangle = \alpha_y \, |\alpha_y\rangle$. A state will then be polarization-squeezed if ΔS_2 or ΔS_3 is less than α_y.

However, using these definitions, the fluctuations of these Stokes parameters are related to the fluctuations of the orthogonal x-polarized vacuum field.

$$\delta S_2 = \alpha_y (\delta a_x^\dagger + \delta a_x) \tag{3.22}$$

$$\delta S_3 = -i\alpha_y (\delta a_x^\dagger - \delta a_x). \tag{3.23}$$

Therefore, by considering both polarizations, the quadrature vacuum squeezing is equivalent to creating a polarization-squeezed state. In experiments detailed in Chapters 8 and 9, we use a squeezed vacuum co-propagating with the strong orthogonal polarization to probe an atomic medium, and so these probes can be considered to be polarization squeezed.

3.2 Theoretical squeezing levels

Early predictions showed great promise for PSR in Rb as a source for high levels of vacuum squeezing [67, 86]. To maximize the squeezing levels, one can minimize the quantum fluctuations of the electric field given in Eq. 3.13 to find the optimal phase angle χ_{opt}. Next, the absorption loss in the medium α is approximated using a beamsplitter model, and the achievable squeezing levels are found to be simply [67]

$$S = 3^{1/2} \left(\frac{\alpha}{g} \right)^{1/3}, \tag{3.24}$$

for a self-rotation medium with large rotation and small absorption. S is the ratio of squeezed to unsqueezed vacuum fluctuations. Now the absorption α and self-rotation parameter g must be found for the atomic system of interest to make a quantitative prediction.

In Refs. [67] and [86], this is done by modeling the atomic vapor on a simple few-level system (X-scheme or Λ-scheme), and solving the optical Bloch equations for the density matrix elements, similar to the calculations shown in section 4.5. The absorption and rotation can be found from these elements and then the appropriate parameters can be plugged in for realistic experimental conditions. In this manner, quadrature noise reduction levels of between 6 and 10 dB were predicted for transitions on the D_1 line of ^{87}Rb .

To predict the degree of squeezing more accurately, more recent attempts have been made which include the full hyperfine and Zeeman degeneracy spectrum of the ground and excited state energy levels [87]. This theoretical treatment also made use of the Heisenberg-Langevin equations for atomic operators, taking into account the Langevin forces to include quantum fluctuations of the atomic medium as well as the light. This is more accurate than a beamsplitter model which just assumes some vacuum fluctuations entering due to losses.

Using this method, our collaborator A. Lezama is able to run detailed numerical simulations of the quantum noise under a variety of experimental conditions. These predictions show that the noise reduction is severely limited by excess noise arising from interactions between the light and the atoms, as well as the atomic motion [72]. The predicted squeezing levels for conditions matching a vapor cell experiment were on the order of -1 dB or less, but could be improved by optimizing the simulation parameters.

It is also shown that reducing the Doppler broadening by using cold rather than hot atoms can improve the possible squeezing levels by making use of resonant noise peaks. The result of one simulation carried out by Lezama is shown in Chapter 11 for cold atoms in a Doppler-free regime. High squeezing levels approaching -10 dB are predicted to be seen using cold atoms, depending on the input conditions (see Fig. 11.11). We investigate this possibility experimentally in Chapter 11.

3.3 Limitations for squeezing generation

While polarization self-rotation effects are predicted to produce fairly high squeezing levels in some models, there are several factors that limit the amount of noise reduction that we can generate and detect in practice. Several noise sources, both fundamental and technical can couple into the system and raise the overall noise on the light signal.

We have mentioned that absorption of light in the atomic medium will act as a loss and bring coherent vacuum noise. This can be included in the squeezing predictions, and prompts us to search for these quantum states using materials with strong rotation and low loss. It is also clear that the quantum uncertainty in the states of the atoms used in squeezing generation can contribute to adding excess noise to the system. Additional noise can come from different interactions of the light with the atoms, such as from spontaneous emission or from scattering of photons from the strong polarization into the vacuum polarization of interest [72]. Other effects of the light-atom interaction are possible, such as nonlinear interactions that can transfer noise from the input light onto the atoms. This contribution of “back action” can amplify the uncertainty in a measurement [88].

In theory, these fundamental noise sources can be included in the squeezing predictions, though the simulations become more and more complicated. Many of the effects that resonant interactions can have on quantum noise are not well understood and still under investigation.

Other limitations to squeezing can come about due to atomic interactions at high optical depths. Self-rotation saturates at high atomic densities [68], and so squeezing will not continue to increase after a certain point by increasing the optical depth. Also, at moderately high optical depths and high laser intensities, self-focusing can come into play [89]. Self-focusing is a nonlinear effect in which the changes in light intensity across the Gaussian profile of a laser beam in an atomic medium cause the light to focus or defocus because of changes to the index of refraction of the medium. This is often observed in dense atomic vapors if the light intensity is high enough, and is observed to limit the squeezing generation [90]. Self-focusing may limit the squeezing generation by causing a mode mismatch between the strong and weak polarizations in the atomic vapor, and thus limiting the PSR interaction. Self-focusing can also decrease the detected noise reduction levels by changing the spatial profile of the laser beams used, to a point where they are harder to mode-match and detect. Because it appears at high atomic densities and laser powers, the same conditions where high self-rotation is expected, self-focusing is one of the main limiting factors in PSR squeezing generation.

Finally, there are many ways in which a squeezed vacuum state may degrade before its detection, contributing to the technical noise or loss of detection efficiency. Any optical loss, which the light experiences on mirrors, lenses, detectors, etc, will degrade the quantum squeezed state and add more coherent vacuum noise to the light. The quantum efficiency of the photodiodes used is less than 100%, and so some signal is always lost. Also, if the classical noise in the local oscillator is high enough, or if all pump photons during the squeezing process are not filtered from the vacuum polarization, the balanced detector may not be able to subtract the unwanted noise. In this case, the detection may not be shot-noise-limited, and noise reduction due to squeezing will be more difficult to detect. If a squeezed state is used to further probe another atomic medium, as we study in Chs. 8, 9, and 10, more sources of noise involving interactions with these atoms are possible. This can include some mechanisms already mentioned, such as spontaneous emission from the atoms, or other undesirable processes such as four-wave mixing which can add noise to the system.

In experiment, great care must be taken to avoid these sources of excess noise, which will reduce the noise suppression measured in squeezed states to levels lower than is predicted. Extra sources of noise are often the reason why squeezed light states generated are not true minimum uncertainty states. In practice, to be considered a useful squeezed state, the amount of noise reduction generated in a squeezing process must be high enough so that the minimum quadrature noise is still below the shot noise level once the light reaches detection.

CHAPTER 4

Resonant light-atom interactions

In this chapter, we give details of the atomic species used in the experiments described in this dissertation. We also investigate the interaction of light with atoms in a three level Λ-scheme and derive the effects of some simple atomic processes including nonlinear magneto-optical rotation (NMOR), polarization self-rotation (PSR), and electromagnetically-induced transparency (EIT).

4.1 Alkali atoms and ^{87}Rb

The atom studied in this work is ^{87}Rb . Rubidium, atomic number 37, is an alkali element, meaning it has only one valence electron in its outer shell, making it useful for atomic physics experiments. The ground state of this electron is in the $5^2S_{1/2}$ state, with the first excited states being $5^2P_{1/2}$ and $5^2P_{3/2}$, exciting the electron to the p orbital with total angular momentum, $\mathbf{J} = \mathbf{L} + \mathbf{S}$, equal to 1/2 or 3/2. Here, $\mathbf{L}$ and $\mathbf{S}$ are the orbital angular momentum and spin angular momentum. The transitions from the ground state to these two excited states are known as the D$_1$ line (795 nm) and D$_2$ line (780 nm) of ^{87}Rb respectively.

Our studies focus on the D$_1$ line, which is further split into hyperfine levels due to the interaction of the electron angular momentum and the nuclear spin ($\mathbf{I}$). With $\mathbf{I} = 3/2$ for

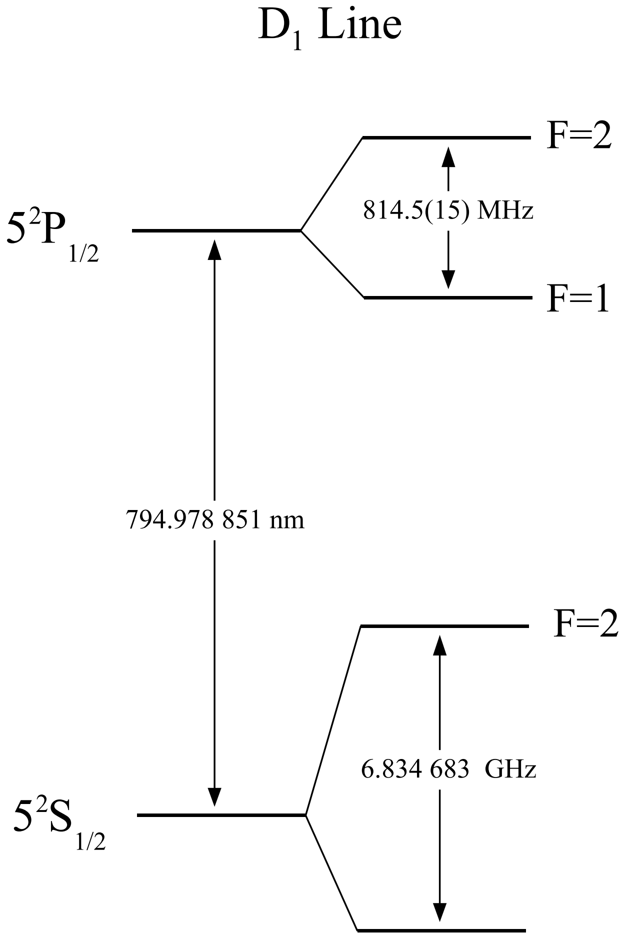
D$_1$ Line
$5^2P_{1/2}$
F=2
814.5(15) MHz
F=1
794.978 851 nm
F=2
6.834 683 GHz
$5^2S_{1/2}$

FIG. 4.1: D$_1$ line energy spacing of ^{87}Rb .

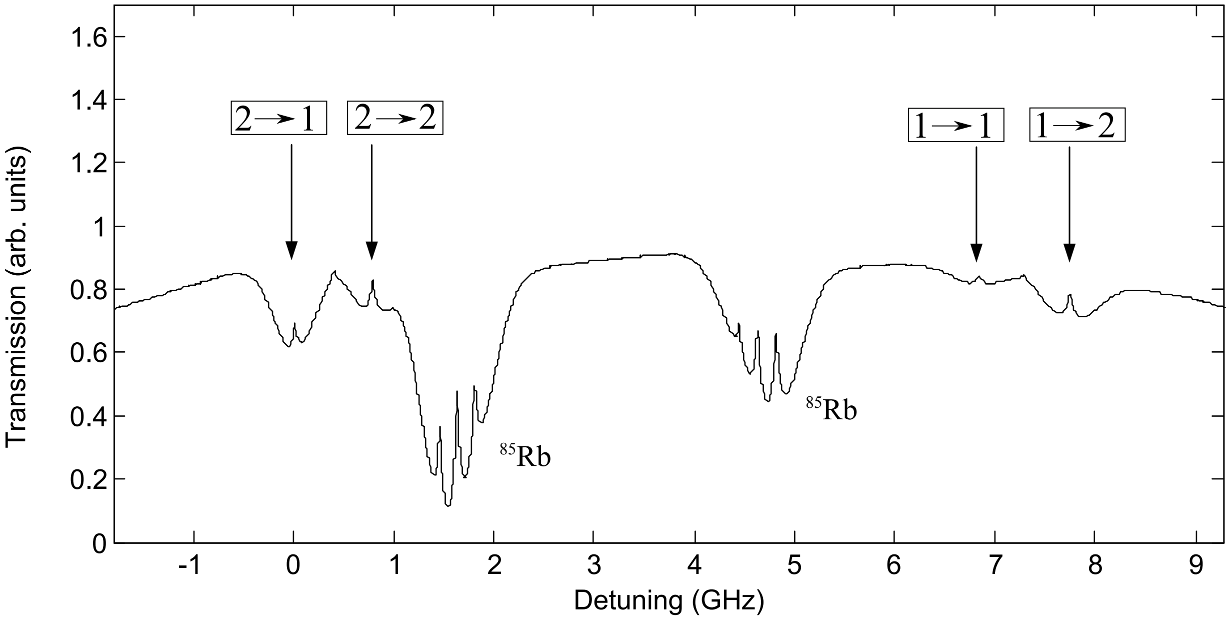

FIG. 4.2: D$_1$ line absorption resonances of ^{85}Rb and ^{87}Rb shown with saturation spectroscopy. The transitions are labeled $F_g \to F_e$.

both the ground state and the D_1 excited state, the hyperfine quantum number, $\mathbf{F} = \mathbf{J} + \mathbf{I}$, can have the values of $\mathbf{F} = 1$ and $\mathbf{F} = 2$. This results in four atomic resonances available in ^{87}Rb for light tuned close to 795 nm: $\mathbf{F}_g = 1, 2 \rightarrow \mathbf{F}_e = 1, 2$. These levels are shown in figures 4.1 and 4.2. We have observed squeezed vacuum generation near three of the four transitions in hot atoms as discussed in chapter 6. The hyperfine energy levels can be further split into Zeeman substates due to the interaction of a magnetic field with the magnetic dipole moments of the electrons. This gives us several m_F states to work with in the ^{87}Rb atoms, three for the $F = 1$ levels ($m_F = -1, 0, 1$) and five for the $F = 2$ levels ($m_F = -2, -1, 0, 1, 2$). This level structure allows for a wide range of possible effects for near-resonant light interacting with the electrons.

4.2 Density matrix and slowly varying envelope approximation

To describe the propagation of light in a medium, we use the density matrix approach. We start with the nonhomogeneous wave from equation 2.6 (note, $\mu_0 \epsilon_0 = 1/c^2$). We treat the atom quantum-mechanically and the light classically.

$$\nabla^2 \mathbf{E} - \frac{1}{c^2} \frac{\partial^2 \mathbf{E}}{\partial t^2} = \frac{1}{\epsilon_0 c^2} \frac{\partial^2 \mathbf{P}}{\partial t^2} \tag{4.1}$$

$\mathbf{P}$ is the polarization induced in the medium, and is described by the average dipole moment of the atoms.

$$\mathbf{P} = \frac{N}{V} \langle \mathbf{d} \rangle, \tag{4.2}$$

with N being the number of atoms contained in the volume V. The dipole moment is $\langle \mathbf{d} \rangle = e \langle \mathbf{r} \rangle$ where e is the electric charge.

We wish to write equation 4.1 in terms of the density matrix of the atomic system.

The density matrix is defined for a pure state $|\psi(t)\rangle$ as

$$\hat{\rho}(t) = |\psi(t)\rangle\langle\psi(t)|. \tag{4.3}$$

The expectation value of an operator $\hat{\mathbf{A}}$ can be calculated from the density operator using the trace,

$$\langle\hat{\mathbf{A}}\rangle = \mathrm{Tr}(\hat{\rho}\,\hat{\mathbf{A}}). \tag{4.4}$$

For a given basis $\{|n\rangle\}$, the density operator is

$$\hat{\rho} = \sum_{m,n} |m\rangle \langle m| \,\hat{\rho}\, |n\rangle \langle n| \tag{4.5}$$

with matrix elements $\rho_{mn} = \langle m| \,\hat{\rho}\, |n\rangle$. The diagonal elements represent the probabilities of being in the states $|m\rangle$, while the off-diagonals are the expectation values of coherence between states $|m\rangle$ and $|n\rangle$.

Using equations 4.4 and 4.5, we can write the expectation value of the dipole operator $\hat{\mathbf{d}}$ in terms of the density matrix as follows,

$$\langle\hat{\mathbf{d}}\rangle = \langle\psi| \,\hat{\mathbf{d}}\, |\psi\rangle = \sum_{m,n} \mu_{mn}\rho_{mn}, \tag{4.6}$$

where we have defined the dipole moment matrix elements $\mu_{mn} \equiv \langle m| \,\hat{\mathbf{d}}\, |n\rangle$. Now we have the wave equation in terms of the density matrix elements.

$$\nabla^2\mathbf{E} - \frac{1}{c^2}\frac{\partial^2\mathbf{E}}{\partial t^2} = \frac{1}{\epsilon_0 c^2}\frac{N}{V}\sum_{m,n}\mu_{mn}\frac{\partial^2\rho_{mn}}{\partial t^2} \tag{4.7}$$

We can reduce this second order equation to first order by using the slowly varying envelope approximation (SVEA) [82]. We rewrite the electric field and density matrix elements (polarization) in terms of their envelope functions $(\mathcal{E}, \tilde{\rho}_{mn})$, which change slowly

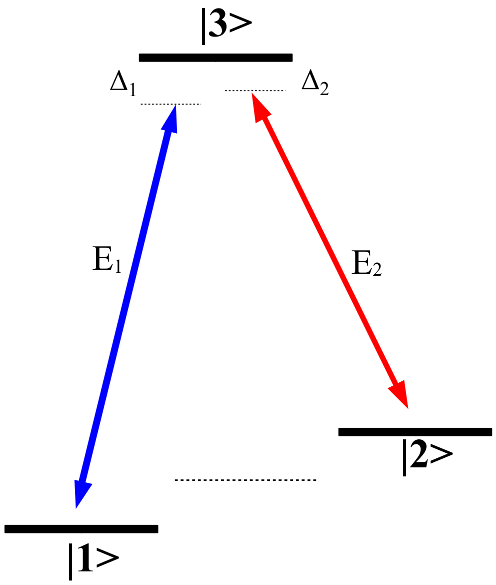

FIG. 4.3: Three-level lambda-scheme.

in time and space compared with the optical frequency ν and wavevector $k = \nu/c$.

$$E_j(z,t) = \mathcal{E}_j(z,t)e^{ik_jz-i\nu_jt} + \mathcal{E}_j^*(z,t)e^{-ik_jz+i\nu_jt} \tag{4.8}$$

$$\rho_{mn} = \tilde{\rho}_{mn}e^{ik_{mn}z-i\nu_{mn}} \tag{4.9}$$

We assume a plane monochromatic wave for the electric field. By substituting the above expressions into equation 4.7, and keeping only the first time and spatial derivatives of the slowly-varying amplitudes, we find a first order wave equation for the envelope functions.

$$\frac{\partial}{\partial z}\mathcal{E} + \frac{1}{c}\frac{\partial}{\partial t}\mathcal{E} = \frac{ik}{2\epsilon_0}\frac{N}{V}\sum_{m,n}\mu_{mn}\tilde{\rho}_{mn} \tag{4.10}$$

This equation can now be solved for a given system to find the time and spatial dependence of the electric field in a medium.

4.3 Three-level atom Λ system

Many important atomic physics interactions can be modeled using a three-level Λ-scheme as shown in Fig. 4.3.

Here, we use ω_i for the atomic frequencies and ν_i for the optical frequencies. We have two optical fields defined in terms of their slowly varying amplitudes,

$$E_1 = \mathcal{E}_1(z,t)e^{ik_1z-i\nu_1t} + c.c. \qquad\qquad E_2 = \mathcal{E}_2(z,t)e^{ik_2z-i\nu_2t} + c.c. \tag{4.11}$$

The separations between the excited and ground states are $\omega_{31} = \omega_3 - \omega_1$ and $\omega_{32} = \omega_3 - \omega_2$. There also may be a splitting between the ground state levels, $\omega_{21} = \omega_2 - \omega_1$. The optical fields may be detuned from the resonances by $\Delta_1 = \nu_1 - \omega_{31}$ and $\Delta_2 = \nu_2 - \omega_{32}$. The one-photon detunings can change due to detuning the laser fields from state $|3\rangle$, or due to shifts to the ground state levels. This leads to the two-photon detuning $2\delta = \Delta_1 - \Delta_2 = \nu_1 - \nu_2 - \omega_{21}$. Note that the two-photon detuning is equal to the ground state splitting if the light fields are in resonance with $|3\rangle$ (for the case of no splitting).

For this system, we have the matrix elements ρ_{mn}, for the density operator as follows.

$$\hat{\rho} = \begin{pmatrix} \rho_{11} & \rho_{12} & \rho_{13} \\ \rho_{21} & \rho_{22} & \rho_{23} \\ \rho_{31} & \rho_{32} & \rho_{33} \end{pmatrix} \tag{4.12}$$

The diagonal elements indicate the population of each level while the off-diagonal elements describe the coherences between energy levels. The dynamics of the system will be determined by the Hamiltonian of the atoms combined with the Hamiltonian of the light-atom interactions.

$$\hat{\mathbf{H}} = \hat{\mathbf{H}}_{atoms} + \hat{\mathbf{H}}_I \tag{4.13}$$

The atomic Hamiltonian describes the energy of each level.

$$\hat{\mathbf{H}}_{atoms} = \hbar\omega_3|3\rangle\langle 3| + \hbar\omega_2|2\rangle\langle 2| + \hbar\omega_1|1\rangle\langle 1| \tag{4.14}$$

In the dipole approximation, the interaction Hamiltonian is $\hat{\mathbf{H}}_I = -\hat{\mathbf{d}} \cdot E$. For this system we find

$$\hat{\mathbf{H}}_I = -\mu_{13}|1\rangle\langle 3|E_1 - \mu_{13}|3\rangle\langle 1|E_1^* - \mu_{23}|2\rangle\langle 3|E_2 - \mu_{23}|3\rangle\langle 2|E_2^*, \tag{4.15}$$

noting that we are considering the case where $\mu_{mn} = \mu_{nm}$.

Now, with the full Hamiltonian, we use the Von Neumann equation to find the equations of motion of the density operator.

$$\frac{d}{dt}\hat{\rho} = \frac{-i}{\hbar}[\hat{\mathbf{H}}, \hat{\rho}] \tag{4.16}$$

This leads us to the density matrix equations of motion.

$$\dot{\rho}_{11} = \frac{-i}{\hbar}\left(\mu_{13}E_1\rho_{13} - \mu_{13}E_1^*\rho_{31}\right) \tag{4.17}$$

$$\dot{\rho}_{22} = \frac{-i}{\hbar}\left(\mu_{23}E_2\rho_{23} - \mu_{23}E_2^*\rho_{32}\right) \tag{4.18}$$

$$\dot{\rho}_{12} = \frac{-i}{\hbar}\left(\hbar\omega_1\rho_{12} - \hbar\omega_2\rho_{12} - \mu_{13}E_1^*\rho_{32} + \mu_{23}E_2\rho_{13}\right) \tag{4.19}$$

$$\dot{\rho}_{13} = \frac{-i}{\hbar}\left(\hbar\omega_1\rho_{13} - \hbar\omega_3\rho_{13} - \mu_{13}E_1^*\rho_{33} + \mu_{13}E_1^*\rho_{11} + \mu_{23}E_2^*\rho_{12}\right) \tag{4.20}$$

$$\dot{\rho}_{23} = \frac{-i}{\hbar}\left(\hbar\omega_2\rho_{23} - \hbar\omega_3\rho_{23} + \mu_{13}E_1^*\rho_{21} - \mu_{23}E_2^*\rho_{33} + \mu_{23}E_2^*\rho_{22}\right) \tag{4.21}$$

The other equations of motion can be found by using the facts that $\rho_{11} + \rho_{22} + \rho_{33} = 1$ and $\rho_{nm} = \rho_{mn}^*$.

We can separate out the fast-oscillating time dependence in these expressions by again making the substitutions from equations 4.8 and 4.9. The interesting density matrix substitutions are as follows.

$$\rho_{12} = \tilde{\rho_{12}}e^{i(\nu_1-\nu_2)t-i(k_1-k_2)z} \tag{4.22}$$

$$\rho_{13} = \tilde{\rho_{13}}e^{i\nu_1 t-ik_1 z} \tag{4.23}$$

$$\rho_{23} = \tilde{\rho_{23}}e^{i\nu_2 t-ik_2 z}, \tag{4.24}$$

where $\tilde{\rho}_{mn}$ are slowly varying in time and space. Now, we apply the rotating-wave approximation (RWA) by neglecting fast oscillating terms such as $e^{\pm i(2\nu_n)}$. These fast oscillations will not have a strong effect on the atomic populations. The equations of motion are rewritten as follows,

$$\dot{\tilde{\rho}}_{11} = i\Omega_1^*\tilde{\rho}_{31} - i\Omega_1\tilde{\rho}_{13} \tag{4.25}$$

$$\dot{\tilde{\rho}}_{22} = i\Omega_2^*\tilde{\rho}_{32} - i\Omega_2\tilde{\rho}_{23} \tag{4.26}$$

$$\dot{\tilde{\rho}}_{12} = -i(2\delta)\tilde{\rho}_{12} + i\Omega_1^*\tilde{\rho}_{32} - i\Omega_2\tilde{\rho}_{13} \tag{4.27}$$

$$\dot{\tilde{\rho}}_{13} = -i\Delta_1\tilde{\rho}_{13} + i\Omega_1^*(\tilde{\rho}_{33} - \tilde{\rho}_{11}) - i\Omega_2^*\tilde{\rho}_{12} \tag{4.28}$$

$$\dot{\tilde{\rho}}_{23} = -i\Delta_2\tilde{\rho}_{23} - i\Omega_1^*\tilde{\rho}_{21} + i\Omega_2^*(\tilde{\rho}_{33} - \tilde{\rho}_{22}), \tag{4.29}$$

We have also introduced the Rabi frequencies, Ω_i.

$$\Omega_i = \frac{\mu_{i3}\mathcal{E}_i}{\hbar} \tag{4.30}$$

These indicate the coupling strengths between the light fields and the transitions. Now, we wish to include various decay and dephasing mechanisms. Due to spontaneous emission, we must add radiative decay terms from the excited state to the two ground states: $\gamma_3 = \Gamma_{3\rightarrow 1} + \Gamma_{3\rightarrow 2}$. We assume there is no radiative decay from the ground states. Also, the nonradiative decoherence of $\tilde{\rho}_{mn}$ is γ_{mn}. We have γ_{31}, γ_{32}, and γ_{21}. In the radiative decay limit, these are 1/2 the rate of radiative decays from each state. In general, these will also include the dephasing rates caused by collisions with the cell wall, buffer gas atoms, etc. We consider a closed system where the population exchange rate between the ground states γ_{12} can encompass various loss and repumping rates. Including these decays, the equations of motion become

$$\dot{\tilde{\rho}}_{11} = i\Omega_1^*\tilde{\rho}_{31} - i\Omega_1\tilde{\rho}_{13} + \Gamma_{3\to1}\tilde{\rho}_{33} \tag{4.31}$$

$$\dot{\tilde{\rho}}_{22} = i\Omega_2^*\tilde{\rho}_{32} - i\Omega_2\tilde{\rho}_{23} + \Gamma_{3\to2}\tilde{\rho}_{33} \tag{4.32}$$

$$\dot{\tilde{\rho}}_{12} = -\left(2i\delta + \gamma_{12}\right)\tilde{\rho}_{12} + i\Omega_1^*\tilde{\rho}_{32} - i\Omega_2\tilde{\rho}_{13} \tag{4.33}$$

$$\dot{\tilde{\rho}}_{13} = -\left(i\Delta_1 + \gamma_{13}\right)\tilde{\rho}_{13} + i\Omega_1^*(\tilde{\rho}_{33} - \tilde{\rho}_{11}) - i\Omega_2^*\tilde{\rho}_{12} \tag{4.34}$$

$$\dot{\tilde{\rho}}_{23} = -\left(i\Delta_2 + \gamma_{23}\right)\tilde{\rho}_{23} - i\Omega_1^*\tilde{\rho}_{21} + i\Omega_2^*(\tilde{\rho}_{33} - \tilde{\rho}_{22}). \tag{4.35}$$

Note that the states $|1\rangle$ and $|2\rangle$ gain population from the spontaneous decay of $|3\rangle$. State $|3\rangle$ will lose an equal amount of population. Also, the coherences depend upon the one and two photon detunings $(\Delta_1, \Delta_2, 2\delta)$. We are now in a position to solve for properties of the system. We write the wave equation for the envelope functions (equation 4.10) in terms of the Rabi frequencies using equation 4.30.

$$\frac{\partial\Omega_i}{\partial z} + \frac{1}{c}\frac{\partial\Omega_i}{\partial t} = \frac{ik}{2\epsilon_0\hbar}\frac{N}{V}\sum_{mn}\mu_{mn}^2\tilde{\rho}_{mn} \tag{4.36}$$

Using the equations of motion, we solve for the steady state density matrix elements $\tilde{\rho}_{mn}$ by setting all time derivatives $\dot{\tilde{\rho}}_{mn}$ to zero. We also define the generalized decay parameters

$$\Gamma_{12} = i2\delta + \gamma_{12} \tag{4.37}$$

$$\Gamma_{13} = i\Delta_1 + \gamma_{13} \tag{4.38}$$

$$\Gamma_{23} = i\Delta_2 + \gamma_{23}. \tag{4.39}$$

We arrive at equations for the ground state coherence,

$$\tilde{\rho}_{12} = \frac{\frac{\Omega_1^*\Omega_2}{\Gamma_{23}^*}(n_{32}) + \frac{\Omega_1^*\Omega_2}{\Gamma_{13}}(n_{31})}{\Gamma_{12} + \frac{|\Omega_1|^2}{\Gamma_{23}^*} + \frac{|\Omega_2|^2}{\Gamma_{13}}}, \tag{4.40}$$

and the polarization elements,

$$\tilde{\rho}_{13} = \frac{i\Omega_1^*}{\Gamma_{13}} \left\{ \frac{\left[\Gamma_{12} + \frac{|\Omega_1|^2}{\Gamma_{23}^*}\right](n_{31}) - \frac{|\Omega_2|^2}{\Gamma_{23}^*}(n_{32})}{\Gamma_{12} + \frac{|\Omega_1|^2}{\Gamma_{23}^*} + \frac{|\Omega_2|^2}{\Gamma_{13}}} \right\} \tag{4.41}$$

$$\tilde{\rho}_{23} = \frac{i\Omega_2^*}{\Gamma_{23}} \left\{ \frac{\left[\Gamma_{12}^* + \frac{|\Omega_2|^2}{\Gamma_{13}^*}\right](n_{32}) - \frac{|\Omega_1|^2}{\Gamma_{13}^*}(n_{31})}{\Gamma_{12}^* + \frac{|\Omega_1|^2}{\Gamma_{23}} + \frac{|\Omega_2|^2}{\Gamma_{13}^*}} \right\} \tag{4.42}$$

in terms of the atomic populations, the Rabi frequencies, and the generalized decay terms. ($n_{mn} = \tilde{\rho}_{mm} - \tilde{\rho}_{nn}$) gives the atomic population difference between the states $|m\rangle$ and $|n\rangle$. Equations 4.41 and 4.42 are fairly general to a three-level system and can be substituted into equation 4.36 to find the effect of the polarization on an input light field (E_1 or E_2). They can also, in principle, be used in equations 4.31 and 4.32 to solve for the steady state populations.

4.4 Nonlinear magneto-optical rotation

We saw that elliptically polarized light can interact with a resonant atomic medium in such a way that the axis of polarization rotates as the light travels through the medium. This is closely related to another well-known effect, nonlinear magneto-optical rotation (NMOR) of the polarization [91, 92, 93, 94]. In particular, we will examine the nonlinear Faraday effect, which comes about from a nonzero magnetic field parallel to the direction of light propagation [95, 96].

In this effect, polarization rotation results not from the ellipticity of light, but is due to shifts of the Zeeman energy levels caused by the presence of the magnetic field. The process is as follows: the atoms are optically pumped by the light causing additional dichroism of the atomic vapor. The atomic alignment then precesses in the nonzero magnetic field and the polarization of light rotates due to the interaction with the atoms [91].

By using the three level model developed in the previous section, we can describe the Faraday rotation for a strong linearly-polarized light field, traveling in the z direction, interacting with an alkali atom in an external magnetic field.

The interaction of an atom with a magnetic field **B** is given by [97]

$$H_B = -\mu_B g_F F_z B_z, \tag{4.43}$$

where $\mu_B = \frac{e\hbar}{2m_e}$ is the Bohr magneton, with e being the electron charge and m_e the electron mass. g_F is the gyromagnetic Landé ratio, F_z is the total angular momentum quantum number, and B_z is the z component of the magnetic field. For weak magnetic fields, the energy levels will split linearly according to

$$\hbar\delta = \mu_B g_F m_F B_z \tag{4.44}$$

Given this energy shift, we find the propagation equations of the light intensity and rotation angle in a three-level model by using equation 4.36. We assume a strong, monochromatic and linearly polarized input light field. In Fig. 4.3, E_1 and E_2 are the right and left-handed circularly-polarized components of the linear field ($E_1 = \sigma_+, E_2 = \sigma_-$). For the degenerate case of no Zeeman splitting, the one-photon detunings of the light fields will be equal, $\Delta_1 = \Delta_2 \equiv \Delta$. We identify the Zeeman shift to a level (equation 4.44) as half the two-photon detuning, δ.

If the states $|1\rangle$ and $|2\rangle$ correspond to the $m_F = -1$ and $m_F = +1$ Zeeman sublevels, it is easy to see that their energies shift in opposite directions in response to magnetic field, and we can redefine the generalized decay parameters from equations 4.38 and 4.39 as

$$\Gamma_{12} = 2i\delta + \gamma_{12} \tag{4.45}$$

$$\Gamma_{13} = i(\Delta + \delta) + \gamma_{13} \tag{4.46}$$

$$\Gamma_{23} = i(\Delta - \delta) + \gamma_{23}. \tag{4.47}$$

We also make the following identifications, and relabel the decoherence rates as

$$\gamma_{13} = \gamma_{31} = \gamma_{23} = \gamma_{32} \equiv \gamma \tag{4.48}$$

$$\gamma_{12} = \gamma_{21} \equiv \gamma_0. \tag{4.49}$$

For now we assume that the one-photon detuning is zero ($\Delta = 0$), so that the laser is exactly on resonance for the case of no magnetic field.

We can further make the following approximations,

$$\gamma_0\gamma \ll |\Omega|^2 \qquad\qquad |\delta|, \gamma_0 \ll \gamma, |\Omega| \tag{4.50}$$

where $|\Omega|^2 \equiv |\Omega_1|^2 + |\Omega_2|^2$. This allows us to simplify the equations for the polarizations (4.41, 4.42) by writing out the generalized decay parameters and keeping only terms linear in δ.

We can also estimate the atomic populations. In the zeroth order,

$$\tilde{\rho}_{11,22} \simeq \frac{|\Omega_{1,2}|^2}{|\Omega|^2} \qquad \tilde{\rho}_{33} \simeq 0. \tag{4.51}$$

To lowest order, the excited state is nearly unpopulated, and if the light polarizations have equal strength ($|\Omega_1|^2 = |\Omega_2|^2$), the ground states will be populated equally ($\tilde{\rho}_{11} \simeq \tilde{\rho}_{22} \simeq 1/2$).

We arrive at a simple form for the polarizations.

$$\tilde{\rho}_{31} \simeq \frac{i\Omega_1}{|\Omega|^4}\left(\frac{\gamma_0}{2}|\Omega|^2 - i\delta|\Omega_2|^2\right) \tag{4.52}$$

$$\tilde{\rho}_{32} \simeq \frac{i\Omega_2}{|\Omega|^4}\left(\frac{\gamma_0}{2}|\Omega|^2 + i\delta|\Omega_1|^2\right) \tag{4.53}$$

We insert these expressions into equation 4.36,

$$\frac{\partial\Omega_i}{\partial z} + \frac{1}{c}\frac{\partial\Omega_i}{\partial t} = i\kappa\tilde{\rho}_{3i}, \tag{4.54}$$

where we have introduced the real coefficient, κ, defined as

$$\kappa = \frac{\nu}{2\epsilon_0 \hbar c}\frac{N}{V}\mu^2 = \frac{3\pi c^2}{2\nu^2}\frac{N}{V}\gamma. \tag{4.55}$$

Again, $\nu = kc$ is the optical frequency, and we are now only concerned with the polarizations $\tilde{\rho}_{31}$ and $\tilde{\rho}_{32}$. Note that κ can also be expressed in terms of $\gamma = \gamma_{3i}$ by using the Weisskopf-Wigner spontaneous emission decay rate [82], for an atom decaying from the excited state $|3\rangle$ to the ground state $|i\rangle$.

$$\gamma = \frac{\nu^3 \mu^2}{3\pi\epsilon_0 \hbar c^3} \tag{4.56}$$

If we assume the input light is continuous and not changing in time, the time derivative in equation 4.54 is ignored and we have the optical Bloch equations for Ω_1 and Ω_2.

$$\frac{\partial \Omega_1}{\partial z} \simeq -\kappa \frac{\Omega_1}{|\Omega|^4}\left(\frac{\gamma_0}{2}|\Omega|^2 - i\delta|\Omega_2|^2\right) \tag{4.57}$$

$$\frac{\partial \Omega_2}{\partial z} \simeq -\kappa \frac{\Omega_2}{|\Omega|^4}\left(\frac{\gamma_0}{2}|\Omega|^2 + i\delta|\Omega_1|^2\right) \tag{4.58}$$

We now make the substitutions $\Omega_1 = |\Omega_1|e^{i\phi_1}$ and $\Omega_2 = |\Omega_2|e^{i\phi_2}$, and separate these equations into their real and imaginary parts. The real part will describe how the light intensity changes with distance in the medium.

$$\frac{\partial |\Omega|^2}{\partial x} = -\kappa\gamma_0. \tag{4.59}$$

The imaginary part will describe the index of refraction of the material and the changes in phase of the light. In this case, because the fields E_1 and E_2 represent the orthogonal circular polarization components of the input light, the phase difference between the fields will correspond to a rotation of the light polarization, $2\varphi = \phi_1 - \phi_2$.

$$\frac{\partial \varphi}{\partial z} = -\frac{\kappa\delta}{2|\Omega|^2} \tag{4.60}$$

Now, performing the simple integration over z, we have the expressions for the light intensity and polarization rotation angle after traveling a distance z through the medium.

$$|\Omega(z)|^2 = |\Omega(0)|^2 - \kappa\gamma_0 z \tag{4.61}$$

$$\varphi = -\frac{\delta}{2\gamma_0}\ln\left(\frac{|\Omega(z)|^2}{|\Omega(0)|^2}\right) \tag{4.62}$$

Note that the rotation angle in this case is proportional to δ, which according to equation 4.44 is proportional to B_z. Thus, for small magnetic fields and linearly polarized light, the result is a polarization rotation angle $\varphi_B \sim B_z$. The nonlinear Faraday rotation is therefore useful for optical magnetometers [37, 98], as we study in Chapter 8.

4.5 Polarization self-rotation g parameter

Using a similar procedure as described above in a Λ-configuration, we can calculate the properties of light interacting with a medium and undergoing polarization self-rotation. Now, the rotation is due to the unequal strengths of the circular components of light rather than a magnetic field. These components can again be pictured as the two optical fields in Fig. 4.3, $(E_1 = \sigma_+, E_2 = \sigma_-)$.

We consider the case where the dominant contribution to the polarization rotation is due to a second excited state $|e\rangle$ (not shown in Fig. 4.3). While the light fields are near-resonant with state $|3\rangle$, they are detuned from $|e\rangle$ by an amount Δ_e. If the ellipticity ϵ is small, and we assume no additional absorption from the off-resonant interaction, the intensity and polarization rotation angle will take the same form as in equations 4.61 and 4.62 for the nonlinear Faraday rotation. We assume zero magnetic field, so there is no Zeeman splitting, but now with unequal strengths of the fields, the ground states can experience different ac Stark shifts due to their different couplings with the excited state

$|e\rangle$ (in particular $\mu_{1e} = -\mu_{2e}$). This will result in the two-photon detuning 2δ, equal to [99]

$$2\delta \sim \frac{|\Omega_1(0)|^2 - |\Omega_2(0)|^2}{\Delta_e}. \tag{4.63}$$

Simplifying equation 4.62, we have

$$\varphi = -\frac{\delta}{2\gamma_0} \ln\left(1 - \frac{\kappa\gamma_0 z}{|\Omega(0)|^2}\right) \simeq \frac{\delta\kappa z}{2|\Omega(0)|^2}. \tag{4.64}$$

By inserting δ, from the Stark shifts we find,

$$\varphi = \frac{|\Omega_1|^2 - |\Omega_2|^2}{|\Omega(0)|^2} \frac{\kappa z}{4\Delta_e}, \tag{4.65}$$

but the first term is just another way to write the ellipticity of light assuming that ϵ is small and does not change substantially in the medium [86].

$$\epsilon = \frac{1}{2} \arcsin \frac{|E_1|^2 - |E_2|^2|}{|E_1|^2 + |E_2|^2} \approx \frac{1}{2} \frac{|\Omega_1|^2 - |\Omega_2|^2}{|\Omega|^2}, \tag{4.66}$$

(Compare with equations 3.4 and 3.5 in section 3.1.3).

Therefore, we find the familiar self-rotation angle from equation 3.2.

$$\varphi_{PSR} = g\epsilon z \tag{4.67}$$

Thus we identify, in this simple three-level model, the self-rotation parameter

$$g = \frac{\kappa}{2\Delta_e} = \frac{3\pi c^2}{4\nu^2} \frac{N}{V} \frac{\gamma}{\Delta_e}. \tag{4.68}$$

In a more complete model, the rotation response will be slightly altered by the more complex Zeeman structure of all atomic levels.

We now see how the interplay of these variables determine the self-rotation in an atomic vapor, and therefore also the possible squeezing levels obtainable in this system.

By substituting the appropriate experimental parameters into equation 4.68 for g, one can use equation 3.13 for the variance of the electric field to predict the possible squeezing levels in a PSR system.

4.6 Dark states and electromagnetically-induced transparency

Consider the interaction Hamiltonian from equation 4.13 for a general three level system.

$$\hat{\mathbf{H}}_I = -\mu_{13}|1\rangle\langle 3|E_1 - \mu_{13}|3\rangle\langle 1|E_1^* - \mu_{23}|2\rangle\langle 3|E_2 - \mu_{23}|3\rangle\langle 2|E_2^* \tag{4.69}$$

One can show that there exists an eigenstate $|D\rangle$ for the interaction Hamiltonian with an eigenvalue of 0, i.e. $\hat{\mathbf{H}}\,|D\rangle = 0$. This condition is satisfied for the state

$$|D\rangle = \frac{\mu_{23}E_2^*\,|1\rangle - \mu_{13}E_1^*\,|2\rangle}{\sqrt{\mu_{13}^2|E_1|^2 + \mu_{23}^2|E_2|^2}}, \tag{4.70}$$

when the difference in laser frequencies is equal to the difference in energy of the ground states ($\nu_1 - \nu_2 = \omega_2 - \omega_1$). An eigenvalue of 0 indicates that atoms in the state $|D\rangle$ do not interact with the light fields, and so $|D\rangle$ is said to be a "dark state". For an ideal dark state, atoms that are pumped into this state will remain there indefinitely because they become noninteracting. This is the most basic form of coherent population trapping (CPT) [100].

The dark state picture is quite useful for understanding some interesting properties of a three-level atomic system. In the previous two examples for NMOR and PSR interactions of a linearly polarized light field, the lowest order solution to the system is the ideal dark state, when $\delta = 0$. When the condition $\nu_1 - \nu_2 = \omega_2 - \omega_1$ is not met, the atoms begin to interact with the light, adding corrections to the dark state solution.

Because atoms in the dark state do not interact with the laser fields, for a narrow range of frequencies (where $\nu_1 - \nu_2 \approx \omega_{21}$), light that would normally be absorbed by the atoms is instead transmitted, and the atomic medium becomes transparent. This is a simple form of electromagnetically-induced transparency (EIT) [101]. Also, the dispersive properties of the medium for a dark state will depend on the ground state coherence, due to the fact that $|D\rangle$ is made up of the ground states $|1\rangle$ and $|2\rangle$.

EIT is an important effect with a multitude of applications in atomic physics [102]. In EIT, one generally uses a strong *control field* (E_c) to dictate the properties of the atomic medium, and a weaker *probe field* (E_p) to gain information about the medium, for example the absorption as a function of the detuning.

We now derive the optical properties of the probe field in an EIT system for a Λ-configuration, such as that shown in Fig. 4.3. Note that 2δ could correspond to, for example, a Zeeman splitting ($\delta <$ MHz) or hyperfine splitting ($\delta \sim$ GHz) of an atomic groundstate (for $\Delta_1 = \Delta_2 = 0$).

We are interested in the electric susceptibility $\chi = \frac{P}{\epsilon_0 E}$, where P is the polarization and E is the electric field. By solving the density matrix equations (4.31 to 4.35) in steady state, we can substitute the relevant matrix element into

$$\chi = \frac{N}{\epsilon_0 V E} \sum_{mn} \mu_{mn} \rho_{mn} \approx \frac{\tau \tilde{\rho}_{mn}}{\Omega_i}, \tag{4.71}$$

where $\tau = \frac{\nu \mu^2}{2\epsilon_0^2 \hbar^2 c}$ is a constant.

We designate $E_1 = E_p$ as the weak probe field, and $E_2 = E_c$ as the strong control field. Therefore, we wish to find the susceptibility experienced by the probe field.

$$\chi = \frac{\tau \tilde{\rho}_{13}}{\Omega_1} \tag{4.72}$$

We start with the expression for $\tilde{\rho}_{13}$ in equation 4.41. Given the large difference in light intensity between the two fields, we can make the following assumptions, where all atomic population is pumped into the ground state $|1\rangle$.

$$|\Omega_1|^2 \ll |\Omega_2|^2, \tag{4.73}$$

$$\tilde{\rho}_{33} = \tilde{\rho}_{22} \approx 0, \tag{4.74}$$

$$\tilde{\rho}_{11} \approx 1. \tag{4.75}$$

By inserting the populations and ignoring the $|\Omega_1|^2$ terms, $\tilde{\rho}_{13}$ simplifies to

$$\tilde{\rho}_{13} = -i\Omega_1^* \frac{\Gamma_{12}}{\Gamma_{21}\Gamma_{13} + |\Omega_1^*|^2}. \tag{4.76}$$

Again, $\Gamma_{12} = 2i\delta + \gamma_0$ and $\Gamma_{13} = i(\Delta_1 + \delta) + \gamma$.

We can further assume that $\Delta, \delta, \gamma_0 \ll \gamma, \Omega_2$ for small detunings. In this case, we ignore the smallest terms and find

$$\tilde{\rho}_{13} = -i\frac{\Omega_1^*}{\gamma} \left\{ \frac{i\delta + \frac{\gamma_0}{2}}{i\delta + \left(\frac{\gamma\gamma_0 + |\Omega_2|^2}{2\gamma}\right)^2} \right\}. \tag{4.77}$$

Thus we obtain the final expression for the susceptibility

$$\chi = \tau \frac{\Gamma}{2\gamma} \left\{ \frac{\delta - i\frac{\gamma_0}{2}}{\delta^2 + \left(\frac{\Gamma}{2}\right)^2} \right\}, \tag{4.78}$$

where we have defined the constant $\Gamma \equiv \left(\frac{\gamma\gamma_0 + |\Omega_2|^2}{\gamma}\right)$.

From equation 4.78, we have found the absorption α and the index of refraction n of the material, proportional to the imaginary and real parts of the susceptibility [82].

$$\alpha \sim \mathrm{Im}[\chi(\nu)] \tag{4.79}$$

$$n \sim 1 + \frac{\mathrm{Re}[\chi(\nu)]}{2} \tag{4.80}$$

We see that the imaginary and real parts of the susceptibility for a weak probe propagating

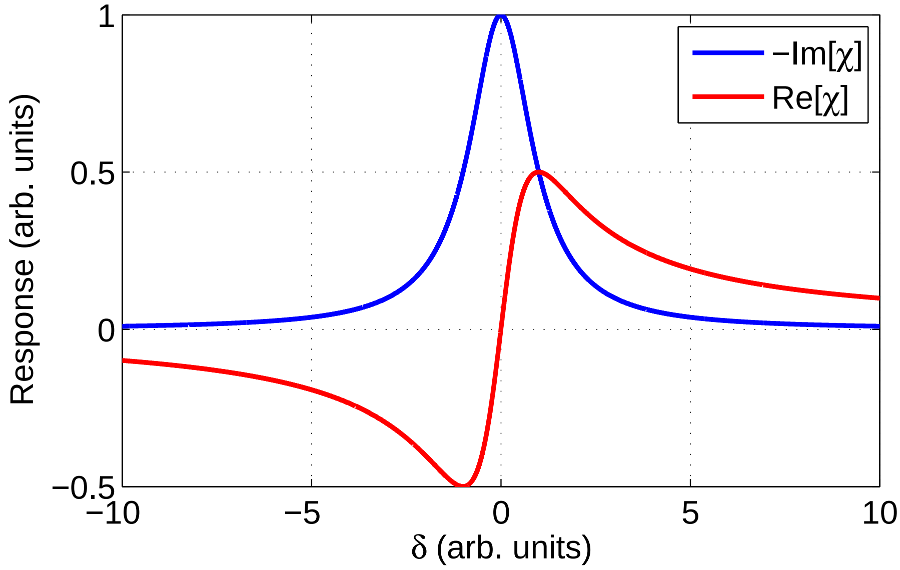

FIG. 4.4: Transmission and dispersion of a medium undergoing EIT. (Blue) -Im(χ). (Red) Re(χ). χ is the electric susceptibility.

in an EIT medium are

$$\mathrm{Im}[\chi] = -\tau \frac{\Gamma}{2\gamma} \left\{ \frac{\frac{\gamma_0}{2}}{\delta^2 + \left(\frac{\Gamma}{2}\right)^2} \right\} \tag{4.81}$$

$$\mathrm{Re}[\chi] = \tau \frac{\Gamma}{2\gamma} \left\{ \frac{\delta}{\delta^2 + \left(\frac{\Gamma}{2}\right)^2} \right\} \tag{4.82}$$

We plot the basic shape of these functions versus the detuning δ in Fig.4.4. The imaginary term shows a Lorentzian transmission lineshape (bracketed term) as expected [101] with respect to δ. The transmission peak is symmetric around $\delta = 0$, where the EIT condition ($\nu_1 - \nu_2 = \omega_2 - \omega_1$) is exactly met (see Fig. 4.4, blue trace). Note that in equation 4.81, the characteristic EIT width (FWHM) is given by Γ. This term depends on the intensity of the control beam $|\Omega_2|^2$, as well as the decay rates γ, γ_0.

The real part of the susceptibility is proportional to the index of refraction n seen by the light, and thus indicates the dispersion of the medium ($\frac{\partial n}{\partial \nu}$). For simple EIT, the dispersion has an antisymmetric shape centered around $\delta = 0$ (see Fig. 4.4, red trace). One should note that the dispersion of the medium is closely related to the polarization rotations resulting from PSR and the nonlinear Faraday effect.

We use the unique properties of an EIT medium for the experiments described in this dissertation. In Chapter 9, we describe how steep dispersion in an atomic vapor can lead to changes in the group velocity of light propagating through it, and investigate this effect while using pulses of squeezed light. Then in Chapter 10, we describe our experiments studying the interaction of quantum light states with resonant atoms, and use the frequency-dependent absorption in an EIT medium to manipulate squeezed vacuum states.

It should be stressed that a three-level model is only an approximation of the behavior in an atomic system. To accurately predict the complete behavior of a light-atom interaction, the full level-scheme as well as all decoherence mechanisms must be included. Also, more complicated models are necessary for reliable predictions of the quantum noise properties of a system.

4.7 Quantum noise operators

To fully describe a system, one must consider both the light and the atoms quantum-mechanically, including the noise of the system. This can be accomplished by recasting the wave equation, from equation 4.10, with quantum operators,

$$\frac{\partial}{\partial z}\,\hat{\mathbf{a}}(z,t)+\frac{1}{c}\frac{\partial}{\partial t}\,\hat{\mathbf{a}}(z,t)=igN\,\hat{\sigma}_{mn}(z,t), \tag{4.83}$$

where g is a constant proportionality factor. Note that we now use the annihilation operator to describe the optical fields ($\mathcal{E}\rightarrow\hat{\mathbf{a}}$), and the atomic operators to describe the atoms in place of the density matrix elements ($\rho_{mn}\rightarrow\hat{\sigma}_{mn}$). Now, the atomic evolution can be described by using the set of Heisenberg-Langevin equations [103].

$$\frac{\partial}{\partial t}\,\hat{\sigma}_{mn}=\frac{i}{\hbar}\left[\hat{\mathbf{V}},\hat{\sigma}_{mn}\right]-\Gamma_{mn}\,\hat{\sigma}_{mn}+\hat{\mathbf{F}}_{mn} \tag{4.84}$$

The first two terms are familiar, being analogous to equation 4.16 with the interaction Hamiltonian $\hat{\mathbf{V}}$, and including the decay terms explicitly. In the last term, $\hat{\mathbf{F}}_{mn}$ are the Langevin force operators, and are necessary for the quantum description of the system. These operators will compensate for the energy seemingly lost from the system due to the decays, but which can actually contribute as back action noise from the atoms to the light fields. For example, spontaneous emission will cause the population to decay from state $|3\rangle$, but the emitted light can also add noise to the light field.

This prompts us to rewrite equations 4.31 through 4.35. In terms of these operators, they will take the form

$$\dot{\hat{\sigma}}_{11} = i\,\hat{\mathbf{a}}_1^\dagger\,\hat{\sigma}_{31} - i\,\hat{\mathbf{a}}_1\,\hat{\sigma}_{13} + \Gamma_{31}\,\hat{\sigma}_{33} + \hat{\mathbf{F}}_{11} \tag{4.85}$$

$$\dot{\hat{\sigma}}_{22} = i\,\hat{\mathbf{a}}_2^\dagger\,\hat{\sigma}_{32} - i\,\hat{\mathbf{a}}_2\,\hat{\sigma}_{23} + \Gamma_{32}\,\hat{\sigma}_{33} + \hat{\mathbf{F}}_{22} \tag{4.86}$$

$$\dot{\hat{\sigma}}_{12} = +i\,\hat{\mathbf{a}}_1^\dagger\,\hat{\sigma}_{32} - i\,\hat{\mathbf{a}}_2\,\hat{\sigma}_{13} - \Gamma_{12}\,\hat{\sigma}_{12} + \hat{\mathbf{F}}_{12} \tag{4.87}$$

$$\dot{\hat{\sigma}}_{13} = +i\,\hat{\mathbf{a}}_1^\dagger(\hat{\sigma}_{33} - \hat{\sigma}_{11}) - i\,\hat{\mathbf{a}}_2^\dagger\,\hat{\sigma}_{12} - \Gamma_{13}\,\hat{\sigma}_{13} + \hat{\mathbf{F}}_{13} \tag{4.88}$$

$$\dot{\hat{\sigma}}_{23} = -i\,\hat{\mathbf{a}}_1^\dagger\,\hat{\sigma}_{21} + i\,\hat{\mathbf{a}}_2^\dagger(\hat{\sigma}_{33} - \hat{\sigma}_{22}) - \Gamma_{23}\,\hat{\sigma}_{23} + \hat{\mathbf{F}}_{23}\,. \tag{4.89}$$

These equations must be solved to find the evolution of the creation and annihilation operators. For this three-level system, the relevant propagation equations are

$$\frac{\partial}{\partial z}\,\hat{\mathbf{a}}_1(z,t) + \frac{1}{c}\frac{\partial}{\partial t}\,\hat{\mathbf{a}}_1(z,t) = ig_1N\,\hat{\sigma}_{13}(z,t) \tag{4.90}$$

$$\frac{\partial}{\partial z}\,\hat{\mathbf{a}}_2^\dagger(z,t) + \frac{1}{c}\frac{\partial}{\partial t}\,\hat{\mathbf{a}}_2^\dagger(z,t) = ig_2N\,\hat{\sigma}_{32}(z,t). \tag{4.91}$$

In the case of self-rotation, with a strong linearly-polarized input field, the two fields described by $\hat{\mathbf{a}}_1$ and $\hat{\mathbf{a}}_2^\dagger$ are the right and left-handed circular polarization components, and the noise on the vacuum polarization can be found using the relationships,

$$E_x = E^+ + E^- \tag{4.92}$$

$$E_y = -i(E^+ - E^-), \tag{4.93}$$

if $E^\pm$ are the circular light components (E_1 and E_2 in this case).

It is possible to obtain the Langevin noise operators from the fluctuation-dissipation theorem [104]. Due to their complexity however, we cannot find an analytic solution to the Heisenberg-Langevin and propagation equations. It was also found that the full hyperfine and Zeeman degeneracy spectrum must be taken into account to accurately predict the quantum noise [72]. Therefore, for theoretical noise predictions, we rely on numerical simulations such as those carried out by A. Lezama, and in this dissertation, we mostly concentrate on experimental observations of the quantum noise.

CHAPTER 5

Quadrature noise detection

5.1 Homodyne detection

In section 2.5, we calculated the variance of the quadrature operators $\hat{X1}$ and $\hat{X2}$. These operators correspond to direct observables, and so the noise power of the amplitude and phase quadratures can be measured. An intensity measurement of the light, however, only gives information about the amplitude. If a light state is amplitude squeezed, the noise reduction will be visible in the light intensity, but for phase-squeezed states, a phase-dependent measurement is required. Also, to measure squeezed vacuum states, or squeezed states with very few photons, we need a way to amplify the quantum noise signal to levels above electronic noise, and do so without adding more noise to the system.

To achieve this, we make use of *homodyne detection*. In this detection scheme, the weak signal we wish to measure is mixed with a strong local oscillator (LO) beam on a 50/50 beamsplitter. The two outputs of the beamsplitter are then sent to a balanced photodetector (BPD), two identical photodiodes whose signals are subtracted.

We start off classically with our two fields, the weak input field with amplitude $\mathcal{E}_{in}(t)$, and the stronger local oscillator with amplitude $\mathcal{E}_{lo}(t)$, and an arbitrary phase $e^{i\chi}$ compared to the input field. These amplitudes are described by their mean values with time-varying quadrature fluctuations.

$$\mathcal{E}_{in}(t) = \mathcal{E}_{in} + \delta\,\mathrm{X1}_{in}(t) + \delta\,\mathrm{X2}_{in}(t) \tag{5.1}$$

$$\mathcal{E}_{lo}(t) = \left[\mathcal{E}_{lo} + \delta\,\mathrm{X1}_{lo}(t) + \delta\,\mathrm{X2}_{lo}(t)\right] e^{i\chi} \tag{5.2}$$

The mean-valued amplitudes ($\mathcal{E}_{in}, \mathcal{E}_{lo}$) are static in time, so the noise of the signal will come only from the quadrature fluctuations. The two beams combine on a 50/50 beamsplitter whose outputs are sent to two identical photodiodes $D1$ and $D2$. The outputs are the same except for the phase shift introduced by the beamsplitter.

$$\mathcal{E}_{D1} = \sqrt{1/2}\mathcal{E}_{lo}(t) + \sqrt{1/2}\mathcal{E}_{in}(t) \tag{5.3}$$

$$\mathcal{E}_{D2} = \sqrt{1/2}\mathcal{E}_{lo}(t) - \sqrt{1/2}\mathcal{E}_{in}(t) \tag{5.4}$$

The intensities of these beams, which will be converted to the photocurrents i_{D1} and i_{D2}, are proportional to the squares of the amplitudes, $|\mathcal{E}_{D1}|^2$ and $|\mathcal{E}_{D2}|^2$. We keep only terms multiplied by $\mathcal{E}_{lo}$, which is large compared to $\mathcal{E}_{in}$, and when the photocurrents are subtracted, we end up with [2]

$$i_{-}(t) \sim |\mathcal{E}_{D1}|^2 - |\mathcal{E}_{D2}|^2 \approx 2\mathcal{E}_{lo}\left[\delta\,\mathrm{X1}_{in}\cos\chi + \delta\,\mathrm{X2}_{in}\sin\chi\right]. \tag{5.5}$$

This equation for the detected signal holds as long as the input beam is weak compared with the local oscillator ($\mathcal{E}_{in} \ll \mathcal{E}_{lo}$). Upon taking the variance of this signal to analyze the noise, we have

$$\Delta i_{-}^2 \sim 4\mathcal{E}_{lo}^2\left[\delta\,\mathrm{X1}_{in}^2\cos^2\chi + \delta\,\mathrm{X2}_{in}^2\sin^2\chi\right]. \tag{5.6}$$

We see that with homodyne detection, the quadrature fluctuations of the input are amplified by the amplitude of the local oscillator $\mathcal{E}_{lo}$, which allows us to raise the noise level above the electronic noise. However, this signal does not depend on the noise of the local oscillator ($\delta\,\mathrm{X}_{lo}$), or on the strength of the input amplitude ($\mathcal{E}_{in}$). By controlling the phase

χ of the local oscillator compared to the input, we can select the noise quadrature that we measure; for $\chi = 0$, we measure only X1, and for $\chi = \pi/2$, only X2.

We find that the same derivation holds true for the quantum case where the output state of the beamsplitter is

$$\left|\sqrt{1/2}\alpha_{lo} + \sqrt{1/2}\alpha_{in}\right\rangle_r \left|\sqrt{1/2}\alpha_{lo} - \sqrt{1/2}\alpha_{in}\right\rangle_t . \tag{5.7}$$

The subscripts r and t denote the reflected and transmitted states described by the operators

$$\hat{\mathbf{A}}_r = \hat{\mathbf{A}}_{D1} = \sqrt{1/2}\left(\hat{\mathbf{A}}_{in} + \delta\,\hat{\mathbf{X1}}_{in} + \delta\,\hat{\mathbf{X2}}_{in}\right) + \sqrt{1/2}\left(\hat{\mathbf{A}}_{lo} + \delta\,\hat{\mathbf{X1}}_{lo} + \delta\,\hat{\mathbf{X2}}_{lo}\right) e^{i\chi} \tag{5.8}$$

$$\hat{\mathbf{A}}_t = \hat{\mathbf{A}}_{D2} = \sqrt{1/2}\left(\hat{\mathbf{A}}_{in} + \delta\,\hat{\mathbf{X1}}_{in} + \delta\,\hat{\mathbf{X2}}_{in}\right) - \sqrt{1/2}\left(\hat{\mathbf{A}}_{lo} + \delta\,\hat{\mathbf{X1}}_{lo} + \delta\,\hat{\mathbf{X2}}_{lo}\right) e^{i\chi}. \tag{5.9}$$

And so we get the same basic expression for the variance of the subtracted current as in equation 5.6,

$$\Delta i_-^2 \sim 4\alpha_{lo}^2 \left(\Delta\,\hat{\mathbf{X1}}^2 \cos^2\chi + \Delta\,\hat{\mathbf{X2}}^2 \sin^2\chi\right), \tag{5.10}$$

where α_{lo} is the mean value of the amplitude of the local oscillator field described by $\hat{\mathbf{A}}_{lo}$. Just as when treated classically, the noise quadratures of the input are amplified by the local oscillator amplitude and the detection is phase dependent. Note that the input state could be a weak probe, or even the vacuum state known to have nonzero quadrature fluctuations.

It is clear from equation 5.10 that if the input is a coherent state or a coherent vacuum, the detected noise will depend only on the LO strength α_{lo}, and will carry no phase dependence due to equations 2.38, 2.39 and 2.43. However, if the input state is an ideal squeezed state or squeezed vacuum, the homodyne detection setup will measure

$$\Delta i_-^2 \sim \alpha_{lo}^2 \left(e^{-2r_s}\cos^2\chi + e^{2r_s}\sin^2\chi\right), \tag{5.11}$$

with noise that depends on the phase χ and the amount of squeezing given by r_s (see equation 2.55).

In experiment, to actually measure the variance of the subtracted photodiode current and extract these quadrature fluctuations, we can perform a Fourier transform on the signal or use a spectrum analyzer (SA). Thus, we are able to directly measure the quantum noise floor (shot noise), as well as the squeezing and antisqueezing levels of the light.

5.2 Spectrum analysis

To measure these noise levels, we analyze the signal from the homodyne detection to look at its noise spectrum. As we saw in the previous section, the difference current will depend only on the LO amplitude and the fluctuations of the input state, which in our case is a vacuum or squeezed vacuum state (equation 5.5). Any dc component of the input subtracts out and the noise of the LO is suppressed. To measure the noise power at different detection frequencies, the spectral variance of this current is taken using a spectrum analyzer or Fourier analyzer.

While an oscilloscope measures a signal in the time domain, a spectrum analyzer measures in the frequency domain. Fourier theory states that any time domain signal can be decomposed into several sine waves with different frequencies. Any modulation or noise on top of an optical signal frequency, or carrier, can be thought of as a sideband, a spectral component at a different frequency. When no modulation is added to the signal, the sidebands are only present due to the noise, whether it be classical or quantum. To find the noise power at each frequency, a Fourier transform is performed on the time-varying function.

$$f(\Omega) = \int_{\infty}^{\infty} f(t) e^{-i2\pi\Omega t} dt \tag{5.12}$$

Though the transform contains an integral over infinite time, it can still be performed using a finite time scale and over a certain bandwidth of detection frequencies. Therefore, the noise spectrum of the homodyne signal can be found by taking the Fourier transform on a time-dependent signal directly, with some type of Fourier analyzer. Alternately, a spectrum analyzer can be used, which measures the current power spectrum as a physical value.

A spectrum analyzer, which is often faster than taking the full Fourier transform, combines the input current with an internally generated oscillating signal to measure the beat frequency power. This essentially will pick out the amplitudes of any sinusoidal modulations at certain frequencies. The reference signal's frequency can be swept through a range of detection frequencies. The mixed signal passes through a narrowband filter which defines the resolution bandwidth (RBW), the smallest spectral component spacing which can be resolved. The final output is also averaged for a certain time, the inverse of which is the video bandwidth (VBW), before being displayed. The noise power spectrum is most often displayed as a power ratio on a logarithmic scale in decibels, $\text{dB} = 10\log_{10}(P/P_{ref})$. When referenced to 1 mW, we find the absolute power ratio, such that $0\ \text{dBm} = 10\log_{10}(1\ \text{mW})$. In this way, the noise power in a signal can be displayed as a function of frequency, and the squeezed or antisqueezed noise will become apparent by comparing the relative noise powers of a signal to the shot noise level. A squeezing level of -10 dB means the noise is reduced by a factor of 10; Squeezing of -20 dB gives a factor of 100 less noise, and so on. There is no fundamental limit to the amount one can squeeze a state theoretically, but the actual squeezing level will generally depend on the strength of the nonlinear interaction used, and the optical losses or other experimental challenges.

5.3 Experimental detection schemes

To measure the quantum noise of squeezed vacuum states, we make use of balanced homodyne detection as described in section 5.1. This can be achieved by using two different detection schemes, one in which the vacuum field and local oscillator start off as separate beams, and a second simplified scheme where the two beams are co-propagating.

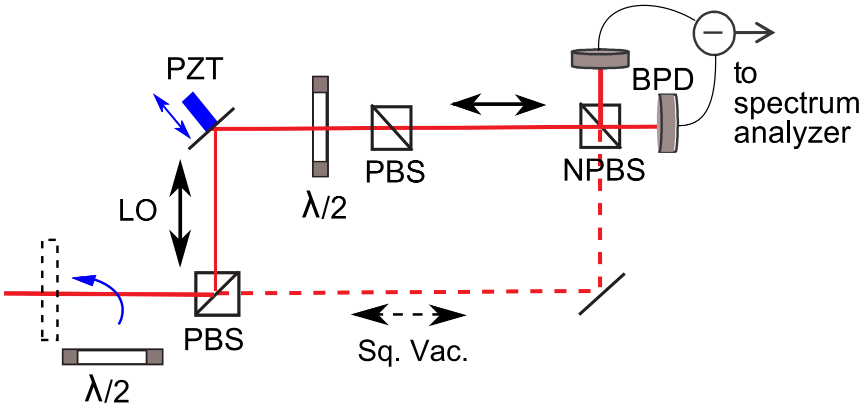

FIG. 5.1: Detection scheme #1: LO-local oscillator, Sq.Vac.-squeezed vacuum, PBS-polarizing beamsplitter, PZT-piezo-electric transducer, $\lambda/2$-half-wave plate, NPBS- nonpolarizing 50/50 beamsplitter, BPD-balanced photodetector.

5.3.1 Detection scheme #1: Interferometric

The first method (#1) is the more common for detecting squeezed vacuum, and must be used when the vacuum field is separate from the strong local oscillator (LO) field. In this method, shown schematically in Fig. 5.1, the squeezed vacuum field is combined with the LO in a Mach-Zender interferometer. The LO need not originate from the same beam as the squeezed vacuum as shown in this setup, but it does need to have a spatial profile matching the vacuum field and a well-defined phase with respect to this field, and so generally, the beams should originate from the same laser. The two beams should also travel similar path lengths and encounter similar optics so that the spatial overlap is very good upon combination.

The LO is directed to a mirror attached to a piezo-electric transducer (PZT), which changes size when a voltage is applied, and therefore changes the distance traveled by the LO beam. This allows the phase χ between the LO and the probe beam (Sq. Vac.) to be swept. Recall that the phase determines the noise quadrature being detected (X1, X2) according to Eq. 5.10. The probe beam and LO are then combined on a 50/50 non-polarizing beamsplitter (NPBS). The NPBS outputs two beams, each containing half the strength of the local oscillator and half the strength of the squeezed vacuum (see equation 5.7). These outputs are then directed to the balanced photodetector (BPD), where the signals are electronically subtracted. The resulting signal is amplified by the LO intensity but only sensitive to fluctuations of the squeezed probe as previously described. The BPD is made from two matched photodiodes (Hamamatsu S5106) with 95% quantum efficiency and a low-noise high-bandwidth TI OPA37U operational amplifier. This gives a relatively flat noise spectrum in a bandwidth from tens of Hertz up to over 2 MHz. The variance of the resulting signal is taken to obtain the noise power spectrum, using either a spectrum analyzer or a Fourier analyzer.

For this detection scheme to function properly, the probe beam and LO must be aligned with near-perfect spatial overlap. This can be checked with the interference visibility,

$$\mathcal{V} = \frac{I_{max} - I_{min}}{I_{max} + I_{min}}, \tag{5.13}$$

where I is the measured intensity. To see this interference, the vacuum field can be replaced by a stronger coherent field by inserting a half-wave plate ($\lambda/2$) at the start of the detection, allowing some transmitted photons into this port. The polarizations of the probe and LO fields also must be the same, and so the second $\lambda/2$ rotates the LO field polarization so that it matches the probe. A PBS or polarizer inserted after the wave plate cleans this polarization and allows for control over the intensity of the LO field. With the proper alignment and beam profiles, when the LO and probe intensities are matched, a perfect visibility ($\mathcal{V} = 1$) should be measured. In reality, we can achieve visibilities up to 98%. Once the interferometer is optimized, the first $\lambda/2$ is removed and the LO is set to a constant power, satisfying the condition $\mathcal{E}_{in} \ll \mathcal{E}_{lo}$. To calibrate the detection to shot noise, the squeezed vacuum is simply blocked, which replaces it with natural coherent vacuum. It is important to note that the local oscillator power (proportional to $\mathcal{E}_{lo}$ or α_{lo}) determines the ultimate shot noise level according to equations 5.6 and 5.10. This level is then used as a reference for all other noise measurements (see Fig. 5.3).

This detection scheme has been successfully employed in many different experiments to measure the noise of squeezed vacuum and squeezed light. By sweeping the PZT voltage,

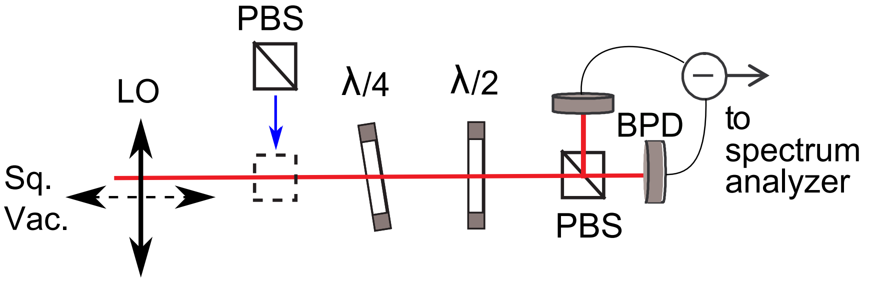

FIG. 5.2: Detection scheme #2: Co-propagating LO. $\lambda/4$-quarter-wave plate.

the phase χ is swept to transition from measuring the minimum (squeezed) and maximum (antisqueezed) quadratures. The main limitations of this method come from the beam overlap and the interferometer stability. If the probe and LO beams travel a long distance separately, or encounter different optics which change the spatial profiles, the resulting imperfect overlap will lead to a degradation in visibility and detected noise suppression upon recombination. Another issue comes with the interferometer phase stability. We have found that providing a constant voltage to the PZT in the LO path does not result in a constant phase angle χ stable enough to detect a particular noise quadrature for extended periods of time. Therefore, to hold the noise at a minimum or maximum, active noise locking is required [105].

The noise locking is achieved with a home-made PI feedback controller. Locking to the noise signal itself proved unstable, and so we instead locked to the photodiode signal, which was modulated due to interference between the LO and a small number of photons which leaked into the vacuum channel of the device. This allowed us to stabilize χ and reliably hold the noise at the minimum or maximum.

5.3.2 Detection scheme #2: Copropagating

The second detection method used in these studies solved some of the problems with the interference method, but is only an option for some of the experiments carried out. Detection scheme #2 is depicted in Fig. 5.2 and was first used to detect squeezed vacuum in Ref. [74].

In this detection method, the LO and probe beams are never separated, allowing for perfect overlap of their spatial profiles. The two beams initially have orthogonal linear polarizations. Then, the beam polarizations are rotated by 45° with respect to the axis of a PBS using a half-wave plate. Thus, the PBS splits the beams with an equal 50/50 ratio, and each beam consists of the same amount of LO and probe intensities. This outputs the same states as the NPBS in the first detection method (equation 5.7), and the homodyne detection works in the same manner. After the PBS, the two split laser beams are directed to the balanced photodiode and the noise can be analyzed. The balanced detector is identical to that used in the first method described above.

In this case, we need a different way to change the phase χ of the LO with respect to the vacuum probe. This is accomplished with a phase-retarder that shifts the phase of one polarization without affecting the perpendicularly-polarized light. We use a quarter-wave plate ($\lambda/4$), which is placed before the $\lambda/2$ and set in such a way that the ordinary and extraordinary axes coincide with the laser beam polarizations. In this arrangement, a small tilt of the quarter-wave plate introduces a controllable phase shift between the squeezed vacuum and LO beam. The phase shift is the result of the beams propagating through a different distance of the birefringent material as the wave plate is tilted. This phase shift could also be accomplished using a Pockels cell, for example, as long as the shift was stable and the losses remained low. Because the two beams are not separated, the phase between them is stable and active locking of χ is not necessary. Instead, to change the phase, and thus the detected quadrature, the $\lambda/4$ is simply rotated to achieve the desired phase and then held at a constant angle with respect to the direction of light propagation.

To calibrate to shot noise, a PBS is inserted into the beam path before the $\lambda/4$ and set in such a way as to block all photons in the vacuum polarization, thereby replacing the squeezed vacuum with coherent vacuum. There is a small loss associated with this due to weak absorption in the polarizer, which decreases the shot noise level by about 0.2 dB. This will decrease the amount of squeezing observed by this amount, but this correction can be taken into account, and this method is much faster and easier than removing the influence of the atoms by cooling or removing the squeezing cell.

Due to the increased detection efficiency coming from the perfect beam overlap and better phase stability, this method has allowed for noise suppression levels of up to 3 dB in similar PSR squeezing setups [74]. However, in some experiments and other methods for generating squeezing, the vacuum field must be separated from the pump field, and so this detection method cannot always be used (see e.g. Chapter 10). Also, there is no way to separately control the power of the pump beam acting as the local oscillator. The photodiodes then see much higher intensities which can lead to saturation or an increase of classical laser noise which is not fully subtracted by the balanced detector.

As noted, the ultimate noise power for the shot noise will depend on the LO intensity. This intensity, which is amplifying the quantum noise, must be strong enough so that the noise level is above the electronic noise, also called "dark" noise. In Fig. 5.3, we show the shot-noise-level noise power compared to the dark noise for different local oscillator powers (in mW). With these photodiodes, we see flat noise spectra over the detection range of 0-2 MHz, which are far above dark noise. Only moderate LO powers are needed to amplify the noise above dark noise. The photodiodes are also able to handle relatively high light intensities when the signals are subtracted, as seen in the figure. Saturation effects can start to be seen at near 2 MHz detection frequencies for the highest power (16 mW). Note that with every doubling of the LO power, the noise power increases by about 3 dB. This is the expected behavior for the quantum noise (Doubling the LO intensity doubles α_{lo}^2 in Eq. 5.10, which doubles the detected noise power: $10\log_{10}(2) = 3.0103$ dB). If there is any classical noise from the local oscillator which is not subtracted in the balanced detection, there will be extra terms in Eq. 5.6 proportional to $\delta\,\mathrm{X}_{lo}$ and the LO intensity, and the noise power will increase by more than 3 dB. This gives us confidence that the laser light we use is shot-noise-limited in most cases, and that the BPD can accurately measure the quantum noise.

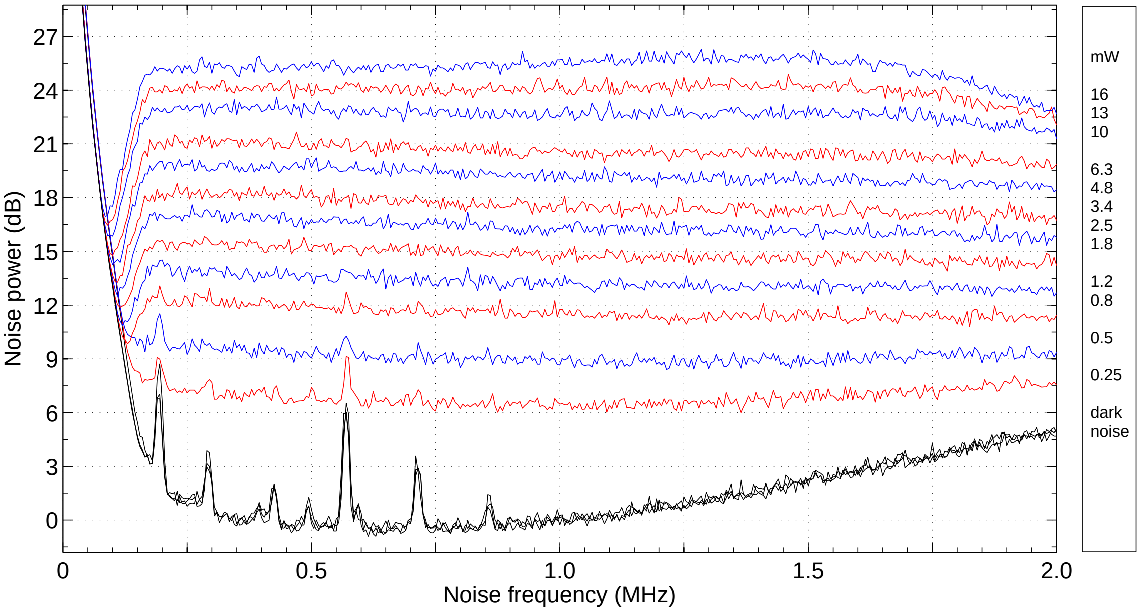

FIG. 5.3: Shot noise power vs frequency for several total LO powers. The dark noise is the result of blocking all light. Spectrum analyzer settings: RBW=10 kHz, VBW=30 Hz.

CHAPTER 6

Squeezed vacuum generation and optimization in hot atomic vapor

Most of the work of this dissertation was carried out with squeezed vacuum generated in hot atomic ^{87}Rb vapor cells. In this chapter, we describe the experimental setup of our hot atomic squeezer and detail our steps towards the optimization of squeezing on the D_1 transition. This includes searching for squeezing on all of the four resonances, $F_g = 1, 2 \rightarrow F_e = 1, 2$, and looking for the proper pump laser power, laser detuning, and atomic density, as well as various other experimental conditions to generate the maximum noise suppression levels. The level of obtainable squeezing is shown to depend on a combination of these related parameters. Moderately high squeezing levels were found near three of the four resonances, $F_g = 1 \rightarrow F_e = 1$, $F_g = 2 \rightarrow F_e = 1$, and $F_g = 2 \rightarrow F_e = 2$, with the highest observed squeezing found very close to the $F_g = 2 \rightarrow F_e = 2$ transition. Efforts to discover squeezed light generated near the $F_g = 1 \rightarrow F_e = 2$ transition as well as brief attempts made looking near the ^{87}Rb D_2 line proved unsuccessful. We also investigate the effect of magnetic fields on the squeezing levels and use this interaction to create a pulsed source of squeezed vacuum.

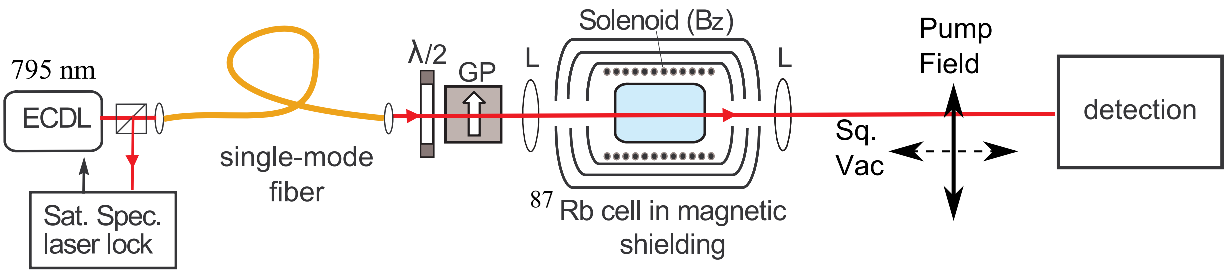

FIG. 6.1: Experimental setup for hot atomic squeezer: ECDL-Extended cavity diode laser, $\lambda/2$-half waveplate, GP-Glan polarizer, L-lens, Sq.Vac-Squeezed vacuum.

6.1 Squeezing generation experimental setup

For studies of squeezed vacuum generated in hot vapor cells, the same basic setup was used for several different experiments. This simple experimental setup is depicted in Fig. 6.1. The output of a DL100 Toptica extended cavity diode laser (ECDL) is tuned to the ^{87}Rb D_1 line (795 nm) and can be tuned to any of the four atomic resonances, then actively locked using a saturated spectroscopy dither lock [106]. The laser output is sent through a polarization-maintaining single-mode fiber to clean its spatial mode, achieving an axially symmetric Gaussian intensity distribution. The maximum achievable power after the fiber is 20 mW. The light then passes through a half-wave plate and Glan polarizer (GP) combination, which serves as a power attenuator and, most importantly, produces a high quality linearly-polarized laser beam. This beam will drive the squeezing process; the orthogonal polarization is initially a natural vacuum field.

The laser beam is focused with a lens ($f = 400$ mm) to achieve a 100 μm beam waste approximately in the center of the 75 mm-long Pyrex cell with isotopically pure ^{87}Rb. The atomic density is controlled with an active heater that holds the cell temperature constant, anywhere between 25 and 85 degrees Celsius ($\pm 1^\circ$) for these experiments. This corresponds to a ^{87}Rb saturated vapor density range between 1.3×10^{10} and 2.2×10^{12} cm^{-3}. The vapor cell is surrounded by a three-layer μ-metal magnetic shield, to minimize the effect from any external fields, and placed inside a solenoid, which gives us precise control over the internal longitudinal magnetic field.

After the cell, we collimate the laser beam with a second lens ($f = 300$ mm) to a beam diameter of about 500 μm. At this output, we have a beam which is made up of the remaining strong linear polarization of the pump, and the vacuum field in the orthogonal polarization. Under the proper conditions, this vacuum field is quadrature squeezed. The fields are then directed through further experiments or detection schemes. The noise properties of the vacuum field can be detected by one of the two methods described in Chapter 5. The pump field and vacuum polarizations are orthogonal, so they can be separated with a polarizing beamsplitter (PBS) if necessary, or the pump can be filtered out with a high quality polarizer. Extreme care is needed to minimize losses to the squeezed vacuum field once it is generated to preserve noise suppression. There is an unavoidable 3% loss from the output window of the glass vapor cell, and further losses are incurred on steering mirrors, lenses, and beamsplitters, giving a total loss of between 5 and 20% depending on the experimental setup.

6.2 Pump laser focusing

The pump laser intensity is an important parameter for determining if PSR squeezing is generated and the significance of the noise reduction. Aside from the input power, this is determined by the beam size and level of focusing of the light within the vapor cell. A smaller beam size means a higher intensity incident on the atoms, but while the beam is focusing or diverging, there also could be an intensity gradient throughout the length of the cell. To experimentally find the best arrangement for our experiments, we tested different beam sizes and degrees of focusing with lenses of different focal lengths. We found that while squeezed vacuum is still generated from an unfocused pump beam, the noise suppression was less, and the pump power could not be increased enough to compensate in our experiment. This led us to using a focused beam. Table 6.1 shows results for maximum squeezing levels observed for different focusing lens strengths. A short focal length implies a smaller minimum spot size with higher intensity, but also a smaller depth of focus, and so with a long cell, there could be a large intensity gradient throughout the atoms, with those near the center of the focus experiencing more light intensity than those farther out. We found that the squeezing levels improved for longer focal lengths, likely due to the fact that the intensity was more uniform over the entire sample region. For very long focal lengths, it is possible that more pump power was required, and more space is needed for beam paths. All further squeezing optimization and experiments are carried out with either the 400 mm or 500 mm focusing lenses. We also found that the focal point of the pump light should be close to the center of the vapor cell for best results.

f(mm)	dB	mW
200	-0.4	3-6
300	-0.9	6-9
400	-1.3	9-15
500	-1.4	9-15
750	-1.0	11-15

TABLE 6.1: Maximum squeezing levels (dB) observed for several focusing lenses. f is the focal length in mm, and the third column shows the range of pump powers where the squeezing was present. Pump laser tuned near $F_g = 1 \rightarrow F_e = 1$. Cell temperature is 71° C.

6.3 Vapor cell selection

The Rb vapor cell found to yield the best PSR squeezing results was a 75 mm long Pyrex cell containing only pure ^{87}Rb . PSR squeezing has also been reported using cells containing some amount of buffer gas, such as neon, which extends the spin coherence time for the atoms interacting with the light [71, 94]. In Ref. [71] for example, -0.9 dB of squeezing was measured in a 75 mm cell with 2.5 Torr neon buffer gas pressure. We also checked a shorter cell (10 mm), in hopes of a more uniform light intensity over the entire interaction length, but the available cell also contained 5 Torr of neon gas. The length of the cell will factor into the obtainable squeezing because a longer cell means a longer interaction length (L in equation 3.2). However, a shorter cell may produce similar results as a longer one if kept at a higher temperature to achieve the same atomic density. We observed a maximum of about -0.6 dB noise reduction using the shorter buffered cell on the $F_g = 2 \rightarrow F_e = 1$ transition at low laser power (∼2 mW).

However, upon full optimization, we observed squeezing closer to -2 dB near the $F_g = 1 \rightarrow F_e = 1$, $F_g = 2 \rightarrow F_e = 1$, and $F_g = 2 \rightarrow F_e = 2$ transitions in the 75 mm cell without buffer gas. It is not immediately clear if the difference comes from the length of the cell, or the presence of buffer gas. While it appears that squeezing can be generated at lower pump laser powers in cells with buffer gas, the highest levels of squeezing are seen in the pure ^{87}Rb cell with higher powers (ranging from 5-20 mW). The 75 mm Rb vapor cell containing no buffer gas is used for squeezing production in all other hot vapor experiments described in this dissertation.

6.4 Detector alignment

Most of the squeezing optimization with hot atoms was carried out using detection scheme #1, where the squeezed vacuum is combined with the LO in a Mach-Zender interferometer. The exact arrangement and path lengths varied depending on the particular study, and so the figure of merit for assuring good alignment and beam overlap was the interference visibility. Maximizing the visibility assures the highest possible efficiency for detection of the squeezing produced, and allows for the results of slightly different setups to be compared accurately. The visibility for these experiments was always kept above 95% to ensure good beam overlap and detection efficiency. Fig. 6.2 shows the effect on noise suppression that imperfect alignment or overlap can have. Starting with a noise suppression level near 2 dB with the best visibility (97%), we see the detected suppression drops quickly with a decrease in visibility (caused by intentional misalignment), dissappearing completely once $\mathcal{V} = 90\%$. Interestingly enough, at very low visibilities, the noise power does not settle to shot noise level, but to some value above, meaning that there is excess noise as compared to a coherent beam. This could be due to different spatial regions of the vacuum and LO beams beams interacting. It is possible that the central, more intense

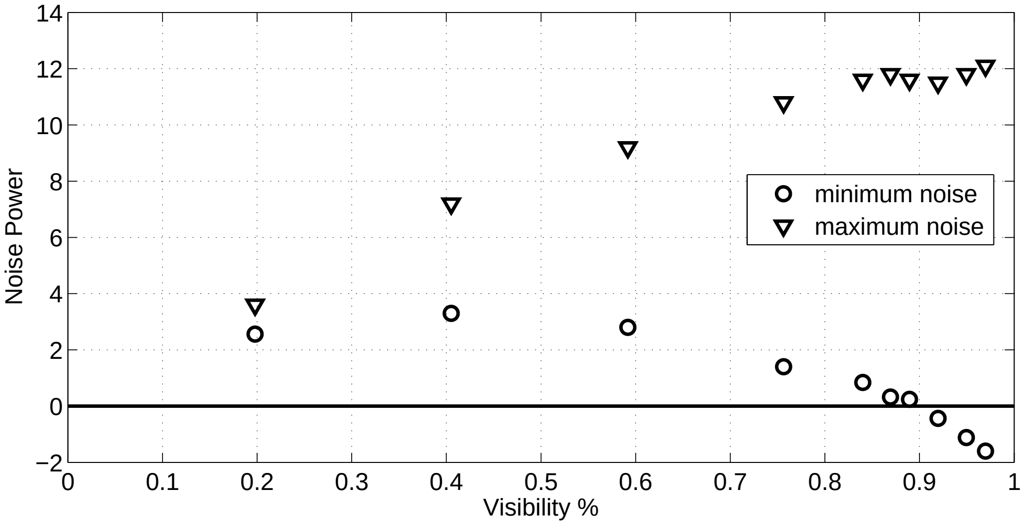

FIG. 6.2: Noise power vs interferometer visibility $\mathcal{V}$. The shot noise level is 0 dB. Visibility was decreased by intentional misalignment of a steering mirror into the NPBS. Pump laser is tuned to $F_g = 2 \rightarrow F_e = 1$.

region of the vacuum beam contains the noise suppression while the outer regions have mostly excess noise, which is then the part being amplified by the LO when alignment is imperfect. These results show how important it is to have very good beam overlap when detecting squeezed light.

6.5 Limitations due to classical laser noise

Unfortunately, our laser had rather large intensity noise at low frequencies, and thus the noise detection was not always shot-noise-limited. We demonstrate this by shining the laser light onto only one photo-diode of the balanced setup. In this configuration, the detector is sensitive to the amplitude noise quadrature of the laser field. As can be seen in Fig. 6.3(a), the noise spectrum is not flat and increases by 6 dBm/$\sqrt{\mathrm{Hz}}$ at every subsequent doubling of the laser power: traces (i), (ii), and (iii). In other words, the noise spectral density scales as the square of the laser power, which is a signature of residual intensity noise (RIN). We found this to be due to phase-to-amplitude noise conversion within the laser. However, our BPD detection is shot-noise-limited at most detection

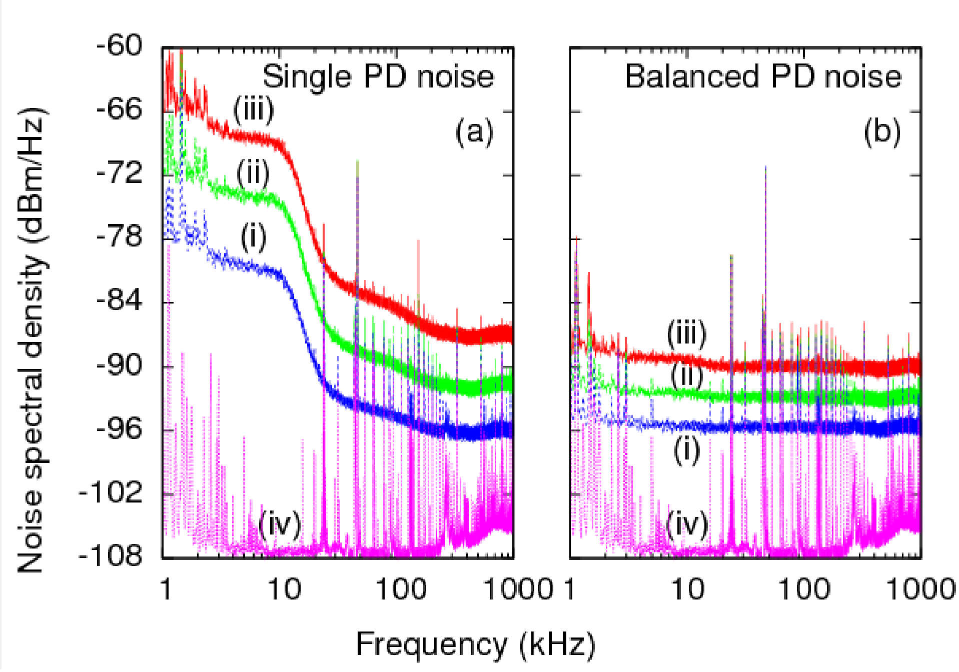

FIG. 6.3: Comparison of the noise power spectral density of the laser residual intensity noise detected by a single photodiode (a) and balanced PD (b) for different laser intensities. Intensity of the laser doubles between subsequent traces (i), (ii), (iii). The bottom trace (iv) corresponds to the dark noise of the detector.

frequencies, and we detect noise at the level of the standard quantum limit (SQL). To prove this, we open both PD of the BPD and carefully match beam intensities arriving to each. As can be seen in Fig. 6.3(b), the spectral density now scales linearly with the laser beam power, i.e. it increases by 3 dBm/$\sqrt{\text{Hz}}$ at each doubling of the laser beam power (see traces (i), (ii), and (iii)). The noise spectrum is generally flat with exceptions of the resonant noise peaks from the electronics (compare to trace (iv) depicting the detector dark noise). Comparing traces in Fig. 6.3(a), where one PD is blocked, and Fig. 6.3(b), where both PD are open, we see that we can easily achieve about 25 dB residual intensity noise suppression. Unfortunately, this is insufficient for truly shot-noise-limited detection at frequencies lower than 200 kHz, indicated by the small rise above the SQL level of the noise spectral density at such frequencies (see also Fig. 6.11). Therefore, while our squeezer offers noise suppression at detection frequencies as low as 100 Hz (Fig. 6.11), we are only shot-noise-limited to start with in this case at frequencies above 200 kHz due to

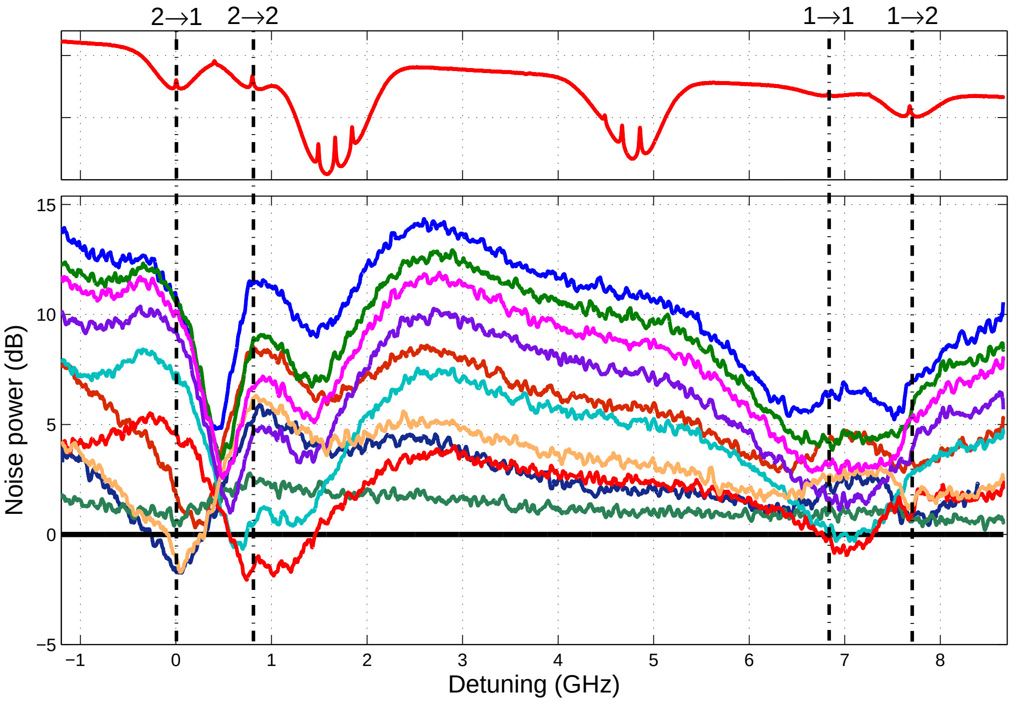

FIG. 6.4: Noise power vs laser detuning for several phase angles. Shot noise level is 0 dB. Each trace shows a different arbitrary constant phase-angle χ. Pump laser power is 10 mW. Cell temperature is 65.5° C. The upper plot shows the saturated absorption spectrum of the D_1 ^{87}Rb line, with the dotted lines indicating the transition frequencies. Isotopically pure ^{87}Rb vapor cell with no buffer gas present.

laser noise. This extra noise can be taken into account in experiments, as it should be present in the coherent and squeezed probes alike. To eliminate it, a high quality laser with exceptional phase and intensity stability could be used.

6.6 Detuning dependence

One of the main factors determining the amount of squeezing, or squeeze factor (equation 2.46), resulting from polarization self-rotation is the light detuning. PSR is a frequency dependent effect, with antisymmetric dispersion-like lineshapes (see Fig. 11.4(b)). The highest squeezing and antisqueezing levels then should occur where PSR is greatest, but this can be complicated by the Doppler widths, power broadening, overlapping transitions, and saturation effects in hot atomic vapors.

By sweeping the detuning of the pump laser slowly across the ^{87}Rb D_1 line transitions, we can monitor the quantum noise level versus the laser detuning. The results for such a measurement are given in Fig. 6.4. In this measurement, the noise power of the squeezer output was measured, using detection scheme #2 with fixed phase angles (χ). Each trace in the figure corresponds to a different phase angle. Squeezing is clearly present at detunings near the $F_g = 2 \rightarrow F_e = 1$, $F_g = 2 \rightarrow F_e = 2$, and $F_g = 1 \rightarrow F_e = 1$ transitions of the ^{87}Rb D_1 line, with nothing below shot noise detected near the $F_g = 1 \rightarrow F_e = 2$ resonance. This is in agreement with previous observations of PSR squeezed vacuum generation [71, 72, 73, 74]. Some differences in the squeezed and antisqueezed noise levels and their response to detuning are likely due to differences in buffer gas, laser power, and cell temperature, though the basic shapes of the noise traces close to the atomic transitions are similar to what is reported in Refs. [73] and [74].

It is important to note that a fixed angle χ does not guarantee the noise to be either minimized or maximized at all laser detunings. The PSR squeezing process outputs vacuum which is squeezed at some squeezing angle, θ_s. This angle will itself depend on the strength of the rotation effect and the laser detuning, and so the phase angle needed to bring the noise to a minimum or maximum will likely change with laser detuning. This is evidenced by looking at the $F_g = 2 \rightarrow F_e = 1$ and $F_g = 2 \rightarrow F_e = 2$ transitions in Fig. 6.4. We see that squeezing is obtained near both transition frequencies, but at the phase-angle where the $F_g = 2 \rightarrow F_e = 1$ transition shows squeezing, the $F_g = 2 \rightarrow F_e = 2$ transition does not, and vice versa. It may not be surprising that near these two transitions, the squeezed vacuum produced has different squeezing angles θ_s, because the self-rotation occurs in opposite directions near one transition versus the other (see Fig. 11.4(b)).

It is also evident that the optimal squeezing conditions will not depend on only one parameter such as detuning, but on the combination of detuning, laser power, atomic density, etc. For example, we have seen evidence in support of Agha *et al.* [73], who observed that in a similar system, the optimal detuning from the $F_g = 2$ transitions increases with increasing laser power. In our experiments with lower laser powers, the squeezing is mostly seen to occur at or near zero detuning from the three transitions mentioned (0 GHz, .815 GHz, and 6.83 GHz in Fig. 6.4), and so we normally lock the pump laser to these frequencies.

6.7 Temperature dependence

We now search for the conditions to optimize squeezing near each of the three transitions where it has been observed. We start by varying the temperature of the Rb cell, while keeping the laser detuning and power fixed, to find the optimal atomic density for PSR and noise reduction. By using equation 1 from Ref. [97], and the ideal gas law, we can easily relate the Rb cell temperature to the atomic density. For convenience, Table 6.2 shows the range of temperatures and densities used in our various experiments.

T(°C)	density ($\frac{atoms}{cm^3}$)
25	1.29×10^{10}
30	2.17×10^{10}
35	3.59×10^{10}
40	6.04×10^{10}
45	9.48×10^{10}
50	1.47×10^{11}
55	2.24×10^{11}
60	3.38×10^{11}
65	5.03×10^{11}
70	7.40×10^{11}
75	1.08×10^{12}
80	1.55×10^{12}
85	2.21×10^{12}

TABLE 6.2: Range of temperatures and calculated atomic densities for isotopically pure ^{87}Rb .

We expect that the squeezing level will improve as the atomic density is increased because the light interacts with more atoms leading to a stronger rotation (see equation 4.68, proportional to n). However, obtainable squeezing levels depend on the combined effect of multiple parameters (detuning, density, laser power), and the optimal atomic density will change for different sets of conditions. The situation is further complicated by factors

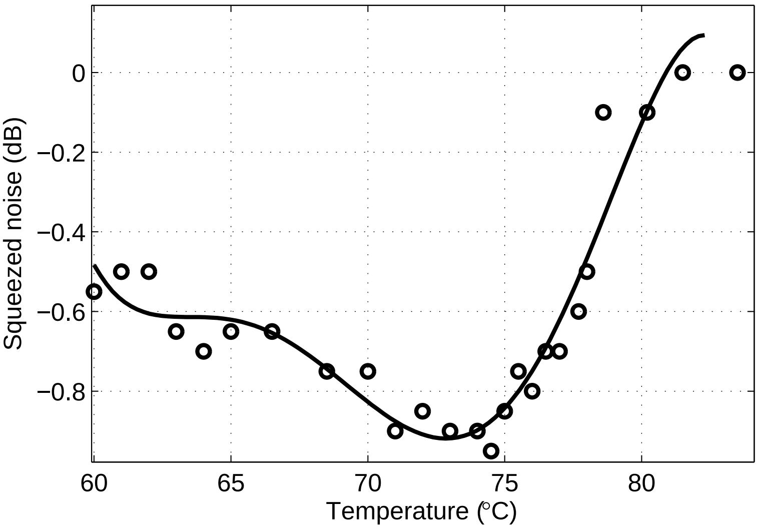

FIG. 6.5: Noise power vs Rb cell temperature. Shot noise level is 0 dB. Pump laser locked to $F_g = 1 \rightarrow F_e = 1$ transition, pump power 15 mW. 1.4 MHz detection frequency. The data is fit to a polynomial function (solid line) to guide the eye only.

such as atomic noise and self-focusing, known to occur at high atomic densities. Therefore, we attempt to locate the optimal squeezing cell temperature experimentally for specific conditions of our experiments.

Figure 6.5 shows the dependence of squeezed noise levels on the cell temperature for the $F_g = 1 \rightarrow F_e = 1$ transition. We see that noise suppression levels improve with increasing temperature, but upon reaching a certain density, the suppression stops improving and the squeezing sharply degrades. The origin of such degradation is not completely understood. One potential explanation is the self-focusing of the light fields as discussed in section 3.3. At these high atomic densities where squeezing is degraded, the squeezer output beam can be seen to change size and shape as the laser is scanned through resonance. The squeezing pump polarization may focus or defocus by a different amount than the weak vacuum polarization, leading to a mismatch of the spatial modes of the probe beam and the LO.

Figure 6.6 shows a comparable set of data for when the laser is locked to the $F_g = 2 \rightarrow F_e = 2$ transition, our transition of choice for most experiments. Here we show the effect on both the squeezing and antisqueezing. The temperature dependence for this

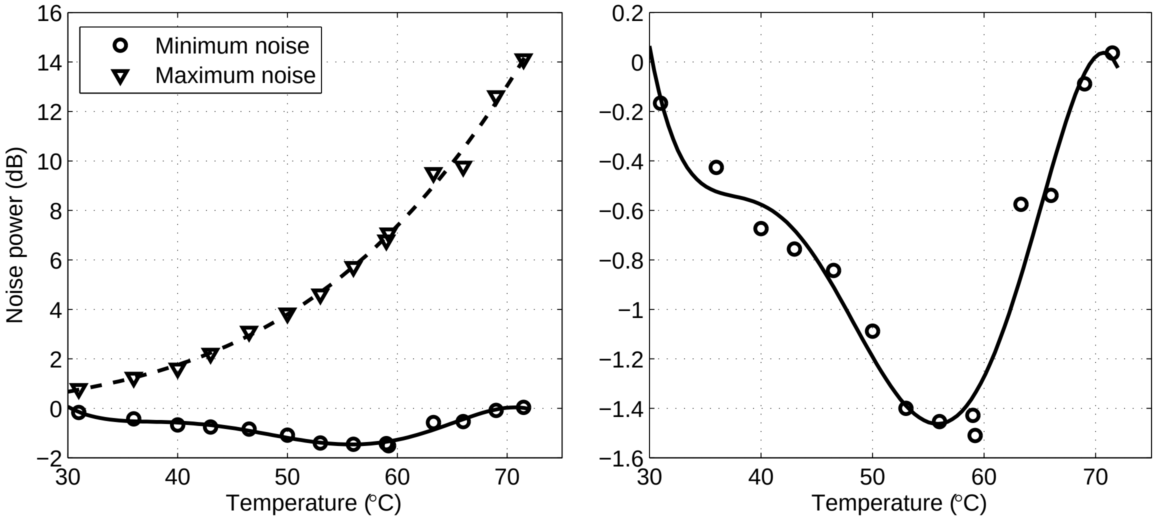

FIG. 6.6: Noise power vs Rb cell temperature. Shot noise level is 0 dB. Pump laser locked to $F_g = 2 \rightarrow F_e = 2$ transition, power at 21 mW. 1.4 MHz detection frequency. Left: Minimum and maximum noise levels shown. Right: Zoomed view of minimum noise. Polynomial fits are to guide the eye.

transition shows similar behavior to Fig. 6.5, but with a lower optimum temperature (for squeezing). The squeezing levels with detunings near the $F_g = 2 \rightarrow F_e = 1$ transition (not shown) displayed nearly the same response to temperature and a similar optimum density as for $F_g = 2 \rightarrow F_e = 2$. Producing noise suppression on these two transitions tended to require lower atomic densities than for the $F_g = 1 \rightarrow F_e = 1$ transition. This could possibly be due to differences in response to the light among the different transitions. We also see in Fig. 6.6 (left) how the maximum noise levels (antisqueezing) are affected. The maximum noise continues to increase with temperature, and so the optimal conditions for noise suppression do not correspond to where one observes the highest contrast of phase-dependent noise. This seems to indicate that at high atomic densities, self-rotation still occurs but there is additional excess noise coming from the atoms which degrades squeezing while also increasing antisqueezing.

One should note that Figs. 6.5 and 6.6 show only noise levels measured at 1.4 MHz detection frequency. While we expect a flat, broadband noise power spectrum, this is not always the case, and the atomic density can play a role in the shape of the noise power spectrum. While not well understood, this may be the case because of atomic effects which add noise at particular detection frequencies. We also suspect that the atomic medium at high densities can amplify the classical laser noise of the pump polarization, which can then couple into the probe polarization.

It is also worth noting that the optimum temperatures for squeezing can change depending on laser power, as well as unwanted atomic interactions, such as self-focusing, which depend on the laser power. In the case of self-focusing, the distance traveled by the output squeezed beam can also be important to optimization of the noise reduction. The above data was collected by recording the minimum and maximum noise levels observed by using detection scheme #1, employing longer path lengths. However, detection scheme #2 guarantees shorter path lengths, and thus may be less sensitive to squeezing detection degradation caused by self-focusing, which can affect the beam focusing at high atomic densities. If the probe and LO polarizations are focusing by different amounts after the squeezer, the spatial mismatch of the beams will get worse with longer propagation distances, and so our first detection method may be more sensitive to this effect. This temperature dependence was also taken with relatively strong laser pump powers (15-21 mW). We found that for the $F_g = 2 \rightarrow F_e = 1$ and $F_g = 2 \rightarrow F_e = 2$ transitions, by using lower pump powers ($\approx$ 7 mW), and with detection scheme #2, the problem of self-focusing was somewhat alleviated, and we measured noise suppressions of over -2 dB for higher cell temperatures (T$\approx$ 66°C).

6.8 Power dependence

The other main parameter influencing the generation of quantum squeezed vacuum via the PSR effect is the laser pump power. We see from Eq. 4.63 that the ac Stark shift, and thus the rotation will depend on the input light intensities. Also, at high powers, self-focusing and saturation effects can contribute, and so the optimum noise reduction should come with the proper balance of pump power and detuning.

In the range of pump powers tested, we found the squeezing levels followed a trend with

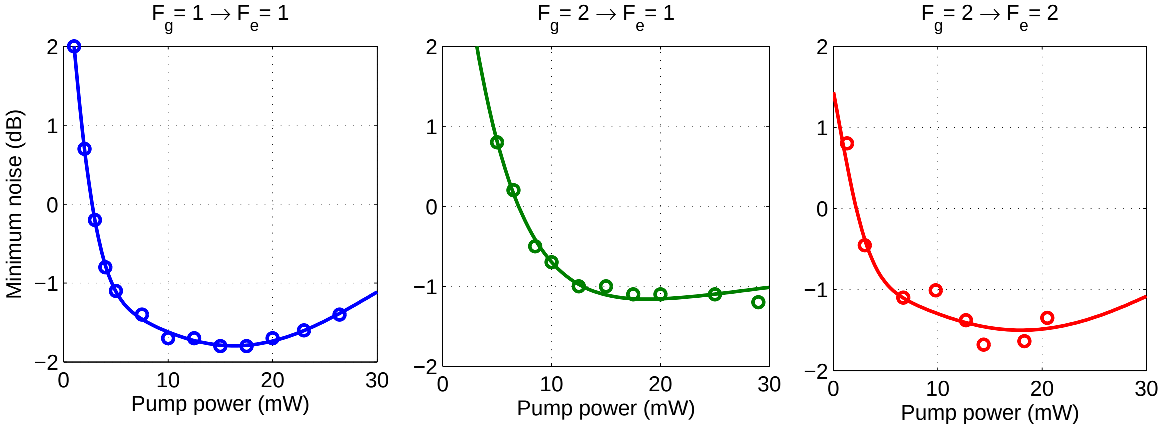

FIG. 6.7: Minimum noise vs squeezer input pump power for three ^{87}Rb transitions. Shot noise level is 0 dB. Cell temperatures are 73, 73, 57 °C respectively and laser frequency is tuned directly to each resonance. Detection frequency is set to 1.4 MHz. Fit lines are to guide the eye.

increasing power as shown in Fig. 6.7. Here we show the power dependence of the minimum noise for the $F_g = 1 \rightarrow F_e = 1$, $F_g = 2 \rightarrow F_e = 1$, and $F_g = 2 \rightarrow F_e = 2$ transitions (left to right), while the cell temperature and beam focus are held constant. The noise reduction appears to follow similar behavior in each case, improving with power until it levels off or starts to worsen. We can see that this allows us to use relatively low laser powers for our squeezer and still obtain good levels of noise reduction, one of the major advantages of this squeezing method. At the same time, the antisqueezed noise levels are largely unaffected by the pump power. We also show the full frequency-dependent behavior with a color plot for the $F_g = 2 \rightarrow F_e = 2$ transition in Fig. 6.8. It is evident that the power dependence is not uniform over every detection frequency. At low pump powers, the noise appears to raise at higher detection frequencies, while at high light powers, noise is added at low frequencies. This may be partially explained by the classical noise of the laser leaking into the detection at low frequencies and high powers. However, we also suspect that there is an extra atomic effect that rotates the squeezing angle, and therefore the noise levels are different for different detection frequencies. This is again illustrated in Fig. 6.9, plotting individual power slices from Fig. 6.8, where it is clear that the noise frequency dependence changes for different laser powers. Keeping this in mind, we keep the pump power at a

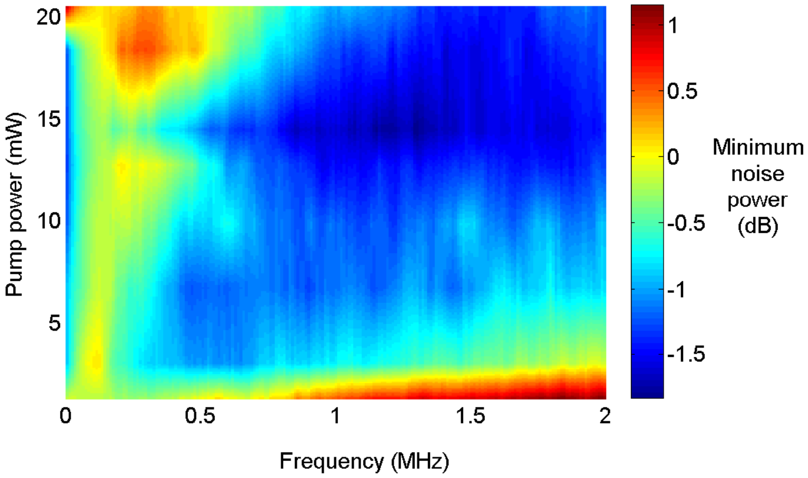

FIG. 6.8: Minimum noise vs power and noise frequency for $F_g = 2 \rightarrow F_e = 2$ transition. Shot noise level is 0 dB. Cell temperatures is 57 °C. RBW=10 kHz, VBW=30 Hz.

moderate level to maintain a flat noise power spectrum with broadband squeezing.

We note that we also observed a frequency dependence of the noise power while measuring the temperature dependence.

6.9 Best squeezing results

By optimizing all of these parameters simultaneously, we have observed the best squeezing results to date for this lab. Our goal was both to achieve the highest possible noise reduction, but also to see this reduction at the lowest possible noise frequency, since for most applications of squeezed vacuum, the detection frequency is important.

Some of our best squeezing results are shown in Figures 6.10 and 6.11. Figure 6.10 shows our maximum noise reduction of -2.60 dB (±0.3). We see that the power spectrum is fairly flat and squeezing is broadband, though the best noise suppression is seen around 0.8 MHz noise frequency. This result was obtained with the pump laser tuned on top of the $F_g = 2 \rightarrow F_e = 2$ transition of the ^{87}Rb D$_1$ line, with a laser input power of 7 mW and cell temperature of 66 °C. The detection range of the spectrum analyzer limits this measurement to detection frequencies above 100-200 kHz.

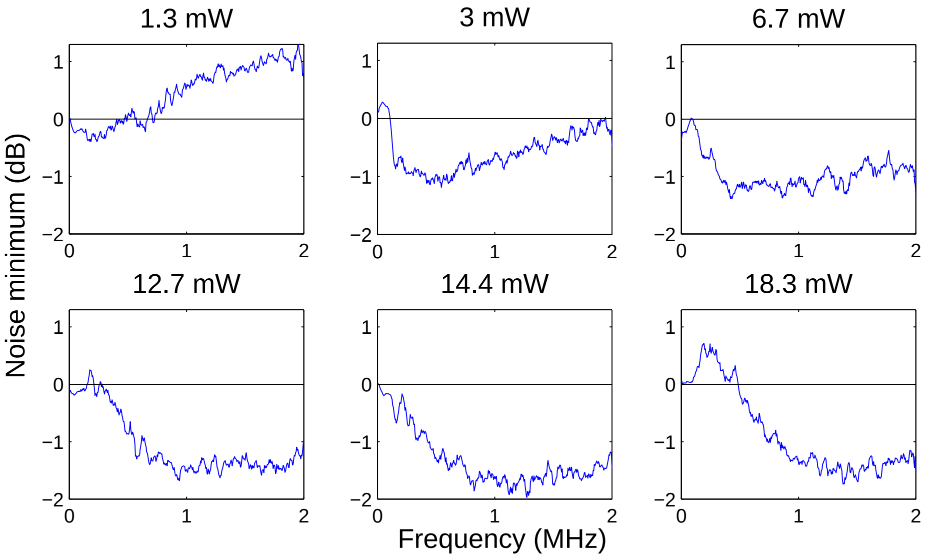

FIG. 6.9: Minimum noise vs noise frequency for several laser powers tuned to the $F_g = 2 \rightarrow F_e = 2$ transition. Shot noise level is 0 dB. Cell temperatures is 57 °C. RBW=10 kHz, VBW=30 Hz.

To probe these lower detection frequencies, we can use a Fourier transform on the time-dependent photodiode signal as described in section 5.2. We measure these low-frequency components with a Lecroy waverunner oscilloscope in its Spectrum Analyzer mode (see App. C). Figure 6.11 shows a squeezing measurement using this method. The noise power is given in dBm/Hz to account for the different resolution bandwidths used for different frequency ranges. We see broadband noise reduction of about -2 dB, with some suppression extending to noise frequencies as low as 100 Hz. This is the lowest detected frequency shown to display noise reduction to date for PSR squeezing and for wavelengths near 795 nm. Note the red line which indicates the true level of the standard quantum limit. At low frequencies, classical laser noise overcomes the shot noise, as discussed in section 6.5, but a reduction of noise is still visible using the squeezed as opposed to coherent vacuum.

6.10 Effect of magnetic field on squeezing

Most calculations of quadrature squeezing via the polarization self-rotation effect are carried out assuming there is no external magnetic field influencing the atoms. For squeez-

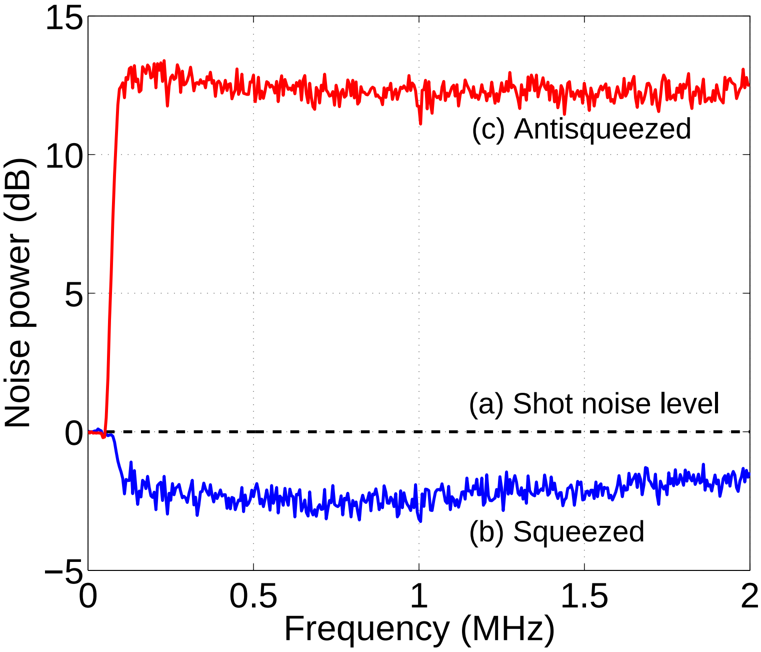

FIG. 6.10: Noise spectrum of squeezed and anti-squeezed quadratures vs detection frequency. $F_g = 2 \rightarrow F_e = 2$ transition. Laser pump power = 7.0 mW. RBW=10 kHz, VBW=30 Hz. $T_{sq} = 66°\text{C}$. Detection #2.

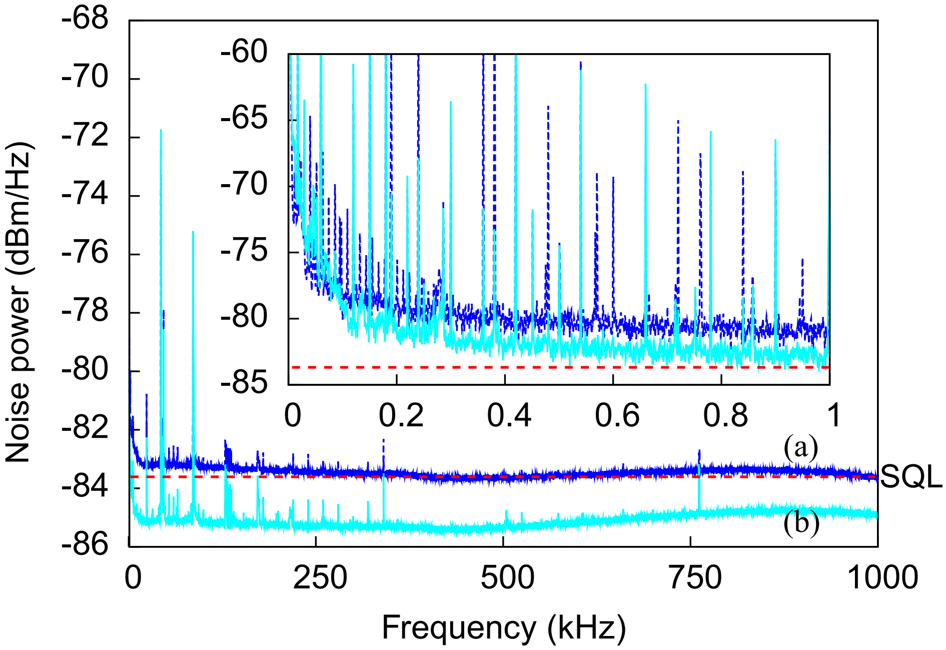

FIG. 6.11: Minimum noise vs noise frequency for $F_g = 2 \rightarrow F_e = 2$ transition. Laser pump power = 7.0 mW. RBW=0.9 Hz. $T_{sq} = 66°\text{C}$. Detection #2. SQL indicates the approximate standard quantum limit (shot noise level), which should be constant over all frequencies.

ing generation, the vapor cell is enclosed in μ-metal shielding to avoid any effects caused by magnetic field. We occasionally can run a high current through these shields for de-Gaussing, to eliminate any field which may have built up near the atoms. However, if there is still some small magnetic field present, this nonzero field will change the polarization rotation experienced by the light due to Zeeman shifts resulting in Faraday rotation. In this section, we investigate the modification of quantum fluctuations of a vacuum optical field after propagating through a Rb vapor under PSR conditions in the presence of a magnetic field. We find that an external magnetic field will always lead to excess noise, and so will generally be detrimental to squeezing, but that this influence can be used in the creation of a form of pulsed squeezed light.

To gain some intuitive understanding of the magnetic field effect on the quadrature noise, one has to consider the effects of Zeeman shifts of the relevant magnetic sublevels. As described in section 4.4, a longitudinal magnetic field results in phase shift between the circular polarization components of the input light, and thus polarization rotation proportional to the field. This extra rotation and change of the detunings disturbs the PSR squeezing process. Experimentally, an external magnetic field is observed to add excess noise to the output light.

To measure the influence of the magnetic field on the quantum noise, we use an identical setup to that described in section 6.5, with detection scheme # 2 as shown in Fig. 6.12. This type of detection allows us to hold the phase angle χ constant while maintaining good beam overlap. We focus on the $F_g = 2 \rightarrow F_e = 2$ transition for the best squeezing levels. Similar results were observed for the other squeezing transitions.

In the absence of magnetic field, we observe a suppression of the quantum noise in the vacuum field below the standard quantum limit (shot noise). This suppression exceeds 2 dB, and spans from around 100 kHz to several MHz (see Fig. 6.10). To add a longitudinal magnetic field to the atoms, we apply a current to the solenoid surrounding the vapor cell. This allows us to create a uniform field of up to several Gauss aligned in either direction parallel to the beam propagation.

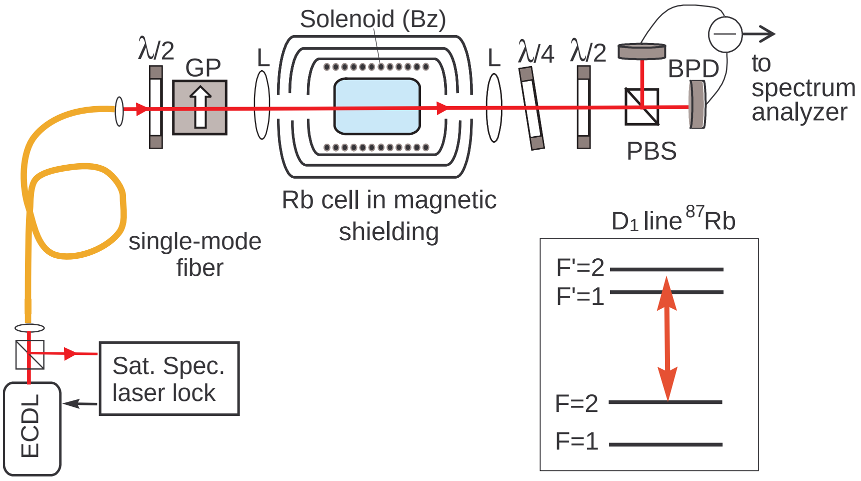

FIG. 6.12: Experimental setup. The description of components is provided in the text.

Fig. 6.13 shows measurements of the minimum (squeezed) and maximum (antisqueezed) noise quadratures as functions of the applied longitudinal magnetic field. It is clear that the squeezed quadrature has a strong dependence on the magnetic field while the anti-squeezed quadrature noise level has a much weaker response. We observed the response to be fairly symmetric around 0 field, meaning that a magnetic field in one longitudinal direction has the same effect on the noise as the field applied in the opposite direction. The noise level, both for the squeezed and antisqueezed quadratures, is observed to increase with the addition of magnetic field, never improving the noise reduction for the squeezed vacuum.

There are several other remarkable features of the observed magnetic field dependence. First, we verified that the change in minimum noise quadrature caused by the applied magnetic field is not accompanied by any changes in its phase with respect to the local oscillator. This means that in Fig. 6.13, the lower trace represents the lowest achievable noise for each magnetic field, and cannot be lowered by adjusting the phase-angle. Therefore, for the best noise suppression, magnetic field should be kept at a minimum.

We also had the ability to apply a transverse magnetic field by using a different orientation of solenoid coils. We observed that the transverse magnetic field has a much

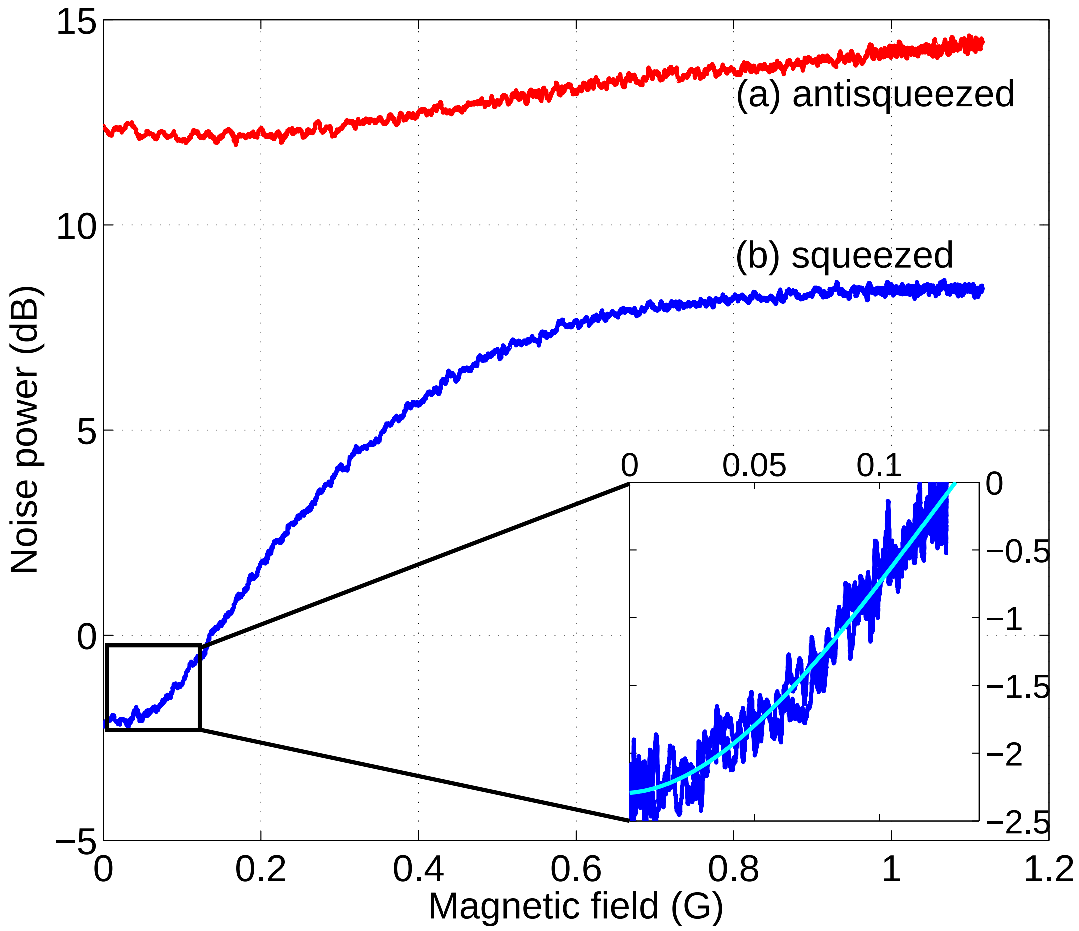

FIG. 6.13: Noise power (dB) of (a) anti-squeezed and (b) squeezed quadratures vs applied longitudinal magnetic field. Inset zooms in on small fields used for this experiment. The spectrum analyzer is set to 1 MHz central frequency with the RBW=100 kHz.

weaker effect on the squeezed quantum noise. In particular, we observed no measurable change or deterioration of quantum noise suppression resulting from transverse magnetic fields up to several Gauss, even though this is a much stronger field than we apply in the longitudinal direction. This difference is likely due to the fact that in the Faraday configuration ($\mathbf{B} \parallel \mathbf{k}$), rotation is linear in the applied field, but in the Voigt configuration ($\mathbf{B} \perp \mathbf{k}$), the effect is quadratic, and therefore much weaker in this case [92].

It is important to note that the overall rotation of the linear pump polarization due to the nonlinear Faraday effect is rather small, and does not modify the shot noise level for small ($B < 0.2$ G) magnetic fields. We also verified that this rotation cannot explain the deterioration of squeezing since it cannot be compensated for by optimizing the angles of the half and quarter waveplates at the detection stage.

Given this dependence of the quadrature noise level on magnetic field, by modifying B_z, we can change the generated noise level from a maximally squeezed, to shot noise and beyond. This provides us with another handle for altering the quantum noise of a light state.

6.11 Squeezing generation summary

In this chapter, we have outlined the experimental details for generation and optimization of squeezed vacuum via PSR in hot ^{87}Rb vapor cells. By studying the influence of such parameters as pump laser detuning, light intensity, and atomic density on the noise suppression levels, we have found a range of conditions where light with quadrature noise levels falling below the standard quantum limit is generated. We have built a squeezer which outputs a robust -2 dB of broadband noise reduction at a 795 nm light wavelength. With careful optimization of the squeezer and detection, we have observed squeezing levels up to -2.6 dB (±0.3) below shot noise, and noise reduction at noise frequencies down to 20 kHz, and possibly as low as 100 Hz. The main limiting factor is classical laser noise which often couples into the noise spectrum below 200 kHz and especially below 20 kHz, raising the overall noise level above the SQL. Once optimized, the squeezed vacuum generated can be used as a reliable quantum probe in further studies. We have also studied the effect of an external magnetic field on the PSR vacuum squeezing generated in hot ^{87}Rb vapor, and find magnetic fields to always add noise to the squeezed quadrature.

We find this method of squeezed vacuum generation simple and reliable for the production of light with about -2 dB noise suppression of it's noise quadratures. Therefore, single-pass PSR squeezing in hot atomic vapors is applicable to many optical measurements and in experiments requiring a quantum probe.

CHAPTER 7

Pulsed squeezing generation

One important application for squeezed light comes from continuous variable quantum information and quantum memory protocols. Due to the steep dispersion possible in atomic vapors under conditions of electromagnetically-induced transparency (EIT), the group velocity of light propagating through such a medium can be drastically reduced [107, 108], which can be used for quantum memory protocols [101]. Studies of quantum memory realizations based on the EIT effect have led to several experiments exploring the propagation and storage of a squeezed state with EIT [55, 56, 57, 109, 110, 111, 112] in connection to quantum memory applications.

We have developed a novel technique which uses the influence of longitudinal magnetic fields on the noise levels in squeezed vacuum generation to create temporal pulses of squeezed vacuum. This may be crucial to the development of a source of pulsed squeezed vacuum used in continuous variable (CV) quantum information protocols. In this chapter, we give a brief background of pulsed squeezed light production for memory applications, and then outline our method of pulse shaping for PSR squeezed light.

7.1 Quantum information application for pulsed squeezed light

As previously stated, much of the interest in squeezed light states comes from its application to CV quantum information protocols. Squeezed light can act as an information carrier which can be coupled to resonant matter systems, such as atoms (warm or cold) [53, 113], "atom-like" defects in solid-state systems (such as nitrogen vacancy centers in diamond) [114], and nanostructures (such as quantum dots) [115]. Due to its quantum nature, squeezed light is a good candidate for testing the fidelity of quantum memories.

Any experimental implementation of continuous variable measurements or operations requires precise knowledge, or better yet, active control over the spatial and temporal profile of the involved optical fields. It becomes important, for example, for reliably reconstructing the quantum states [116], and for matching the bandwidth of an optical signal with the linewidth of a resonant light-atom interaction to achieve optimal coupling [113]. Good examples of the latter use of temporal pulse shaping can be found in realizations of maximally efficient quantum memory in atomic ensembles [117, 118]. Recent comprehensive theoretical studies by Gorshkov *et al.* considered a wide range of potential quantum memory protocols [119, 120, 121, 122, 123], such as: electromagnetically induced transparency (EIT) in a cavity and in free space, far-off-resonant Raman, and a variety of spin echo methods including ensembles enclosed in a cavity, inhomogeneous broadening, and high-bandwidth non-adiabatic storage. Theoretically, high optical depth is necessary to achieve a storage efficiency close to 100 % for most of these memories [119]. In practice however, residual absorption and competing nonlinear processes make atomic ensembles with moderate optical depths most practical. In these situations, shaping of quantum optical signals into predetermined temporal envelopes may be required to achieve optimal efficiency. For example, for EIT-based quantum memories, the efficiency of quantum storage for a given optical depth is fundamentally limited by the balance between the compression of an optical pulse inside the limited length of an atomic ensemble, and the width of the transparency spectral window. Thus, the temporal profile of signal and/or control optical fields must be tailored to minimize losses and store the signal with optimal efficiency [124, 125, 126].

Generating pulses of squeezed light and squeezed vacuum however, can be non-trivial. Many cavity-based crystal squeezers and atomic PSR squeezers operate in the CW regime and generate a continuous squeezed vacuum field. The formation of the pulses has been done externally, using either mechanical choppers or acousto-optical modulators (AOM). Either of these approaches has serious drawbacks: an additional optical element such as an AOM introduces additional losses, and may distort the spatial mode of the generated field due to thermal nonhomogeneities in its nonlinear crystal. Mechanical choppers, such as rotating slits, do not add any losses, but produce only temporal envelopes of fixed shape and duration, which are not ideal for many experiments.

One possible way to modulate the noise level of the PSR squeezing is by controlling the input pump power. In particular, lowering the pump power degrades and eventually kills the squeezing process, and thus makes it possible to shape the noise pulses [73]. However, this variation of the pump laser intensity makes it difficult to reuse the same beam as a LO and accurately measure the quantum noise levels. This problem can be alleviated by using an independent LO field, but at the price of the increased complexity of the experiment, a lower quantum detection efficiency due to the imperfect overlap of the LO and squeezing beams, and a reduced homodyne phase stability. In addition, we note that one cannot modulate the light signal after it is already squeezed due to the resulting degradation of the noise suppression.

However, pulsed squeezed vacuum states can be created, avoiding many of the above problems, by taking advantage of the effect on the squeezing process of an external magnetic field as detailed in the previous section. This method offers an important step toward using PSR squeezed vacuum in CV quantum information protocols.

7.2 Quadrature noise pulse shaping

We see in Fig. 6.13 that adding a longitudinal magnetic field has a dramatic effect on the noise levels of the PSR-generated squeezed vacuum. Therefore, changing the magnetic field B_z with time, translates into changing the squeezed noise time-dependence. By creating arbitrary temporal pulses of the magnetic field, we can generate arbitrary pulse shapes in the squeezed vacuum quadrature noise. This method offers important advantages since it does not change the angle of the squeezing quadrature with respect to the local oscillator, and thus allows convenient pulse shape formation without the need to adjust this angle as well. Also, a modest magnetic field strength does not affect the strong pump field. Thus, this field can be used afterwards as a local oscillator that intrinsically has the same spatial profile as the squeezing beam.

Both the squeezing and anti-squeezing noise levels have a nonlinear response to the longitudinal magnetic field (see Fig. 6.13) which must be taken into account for the generation of arbitrary pulse shapes. To produce the necessary magnetic field pulse shapes, we use a voltage controlled current source, driven by a programmable SRS DS345 function/arbitrary waveform generator.

To demonstrate the capabilities of our method, we chose several different temporal profiles with different parameters for the output squeezed vacuum field. Fig. 7.1 shows a few example pulse shapes: (a) a positive Gaussian pulse of approximately 30 μs duration, (b) a 60 μs negative Gaussian pulse, (c) a negative 200 μs triangular pulse, (d) a positive 1 ms square pulse, (e) a negative 1 ms Gaussian pulse, (f) a positive 1 ms triangular pulse. Here, pulses deemed "positive" start at a maximally squeezed level and show an increase in noise up to shot noise, while for the "negative" pulses, the measured noise starts at the shot noise and then drops to the maximum squeezing level. The desired profile can be reliably reproduced in the measured spectral noise power by calibrating the effect of the magnetic field on the squeezed noise levels (Fig. 6.13). We can use this to determine the transfer function and thus calculate the magnetic field pulses required to produce the desired noise pulse shapes.

We see an excellent mapping from the desired to observed pulse shapes, importantly with no degradation of the maximally squeezed noise quadratures, with the lowest noise levels recorded (maximum squeezing) always occurring at zero magnetic field. The applied magnetic field is chosen so that the quadrature noise moves between the maximally squeezed level (≈ -2.1 dB) and the shot noise level, following the pulse shape we desire. The pulses are smooth and continuous and we have easy control over their duration and repetition rate. This method can be expanded to any other arbitrary pulse shapes (within the detection VBW and RBW) by using the known relationship between squeezing and magnetic field.

The shortest generated and detected pulses are on the order of 30 μs. During the measurements of the squeezing pulses above, we set the spectrum analyzer central frequency to 1 MHz, the resolution bandwidth (RBW) to 100 kHz, and video bandwidth (VBW) to 3 MHz while we monitored the time-dependent noise level with an oscilloscope. The SA bandwidth setting naturally limits the maximum bandwidth of the pulses or shortest possible detected pulse. However, the main limitation on pulse duration was set by the homemade controllable current source which was used to control the solenoid current. The bandwidth of this current source was limited to about 10 kHz and for shorter pulses, it distorted the programmed pulse shapes by adding unwanted transient effects. We can see the ripples of the set current in Fig. 7.2 when the signal bandwidth exceeds the instrumental one. Note however that the detected squeezing accurately follows the distorted magnetic pulse shape, illustrating that it can potentially be modulated much faster. To avoid ring-down oscillations, we smooth the sharp fronts of the input rectangular pulse (see Fig. 7.1(d)).

This pulsing method adds to the utility of PSR squeezing without many of the drawbacks of other methods, and can potentially be used in CV quantum information protocols. The advantages of this squeezing generation method is its simplicity and robustness, good matching of the squeezing parameters to narrow coherent atomic resonances (like EIT

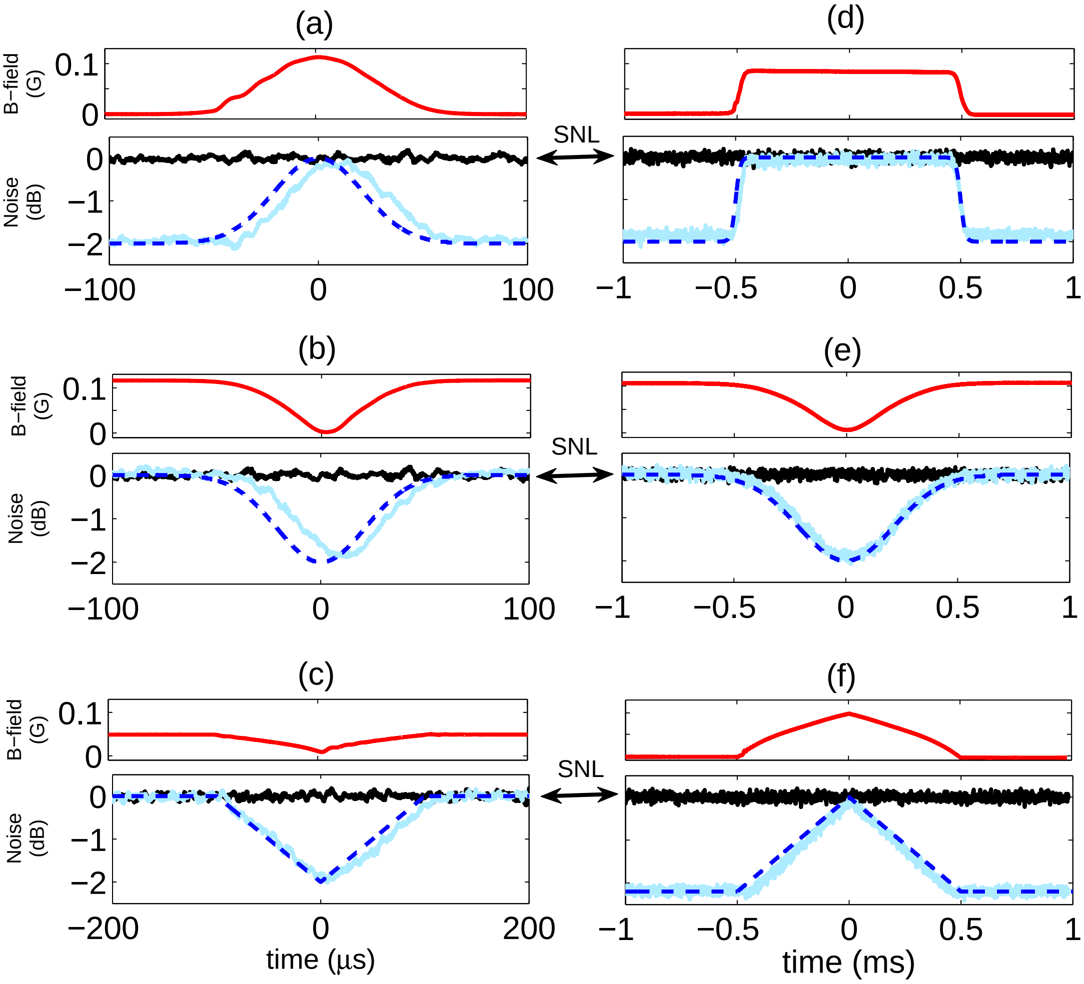

FIG. 7.1: Modulation of the quantum noise with different pulse shapes. Top plots: magnetic field pulses applied to the atoms. Bottom plots: resultant squeezed noise pulses compared with the shot noise limit (SNL). Desired noise pulse shapes were: Gaussian (a, b, and e), triangular (c and f), and square (d). The dashed lines indicate the desired pulse shapes.

or Raman transitions), and the possibility to use the pump field as a local oscillator for perfect spatial mode matching. This technique is thus suitable for time encoding of the quantum states for quantum communication and memory applications.

We employ this pulse shaping method in Chapter 9 for our studies of slow and fast squeezed light.

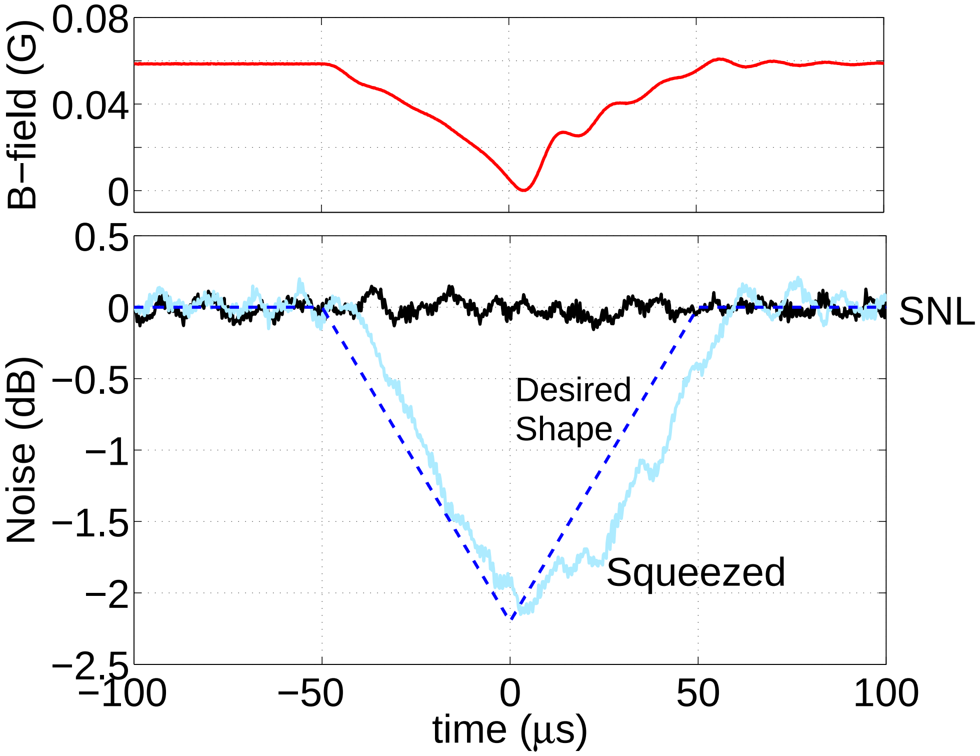

FIG. 7.2: A 100 μs triangular pulse of squeezed noise. Limits of the current supply bandwidth cause visible oscillations in the magnetic field, which show up in the squeezed spectrum.

CHAPTER 8

Quantum enhanced magnetometer

In this chapter, we demonstrate an optical measurement application for the source of squeezed vacuum detailed in the previous chapters. We present our experimental results from studying an optical magnetometer, based on nonlinear magneto-optic (Faraday) rotation (NMOR) [127, 128] in ^{87}Rb . We observe a quantum enhancement to the sensitivity of this device by injecting a polarization-squeezed state of light. We study the performance of such a magnetometer and the measured noise power spectra for several atomic densities to determine the conditions most favorable for high precision and sensitivity. Our prototype device reaches sensitivities of $\sim$1 pT/$\sqrt{Hz}$, and is enhanced, due to the squeezed light probe, for a large range of atomic densities and detection frequencies. We observe that the magnetometer transitions from a shot-noise-limited device at lower atomic densities, to a region where excess noise is observed resulting from interactions of the light with atoms at higher densities.

Optical magnetometers now reach the sub-femtotesla/$\sqrt{\text{Hz}}$ level of sensitivity [88, 98], surpassing superconducting quantum interference device (SQUID) magnetometers [129]. Ultimately, such optical magnetometers are limited by quantum-mechanical noise sources, in particular by the photon shot noise at detection, spin projection atomic noise, and the back action of light noise onto atoms [88, 98, 130]. The former noise source can be addressed with injection of polarization-squeezed light states [36]. Our squeezer offers great advantages for magnetometry measurements in its simplicity and low power requirements, which would allow it to be easily miniaturized. It offers about -2 dB of broadband noise suppression under most experimental conditions, and could be applied to the most sensitive, state-of-the-art optical magnetometers.

8.1 Magnetometer setup

The setup of this experiment is depicted in Fig. 8.1. It contains two important components: the squeezer, which prepares the polarization-squeezed probe beam, and the magnetometer, which can be probed with either the squeezed or shot-noise-limited (unsqueezed) beam.

The operation of the squeezer is discussed in section. 6.1. We lock the squeezing pump laser to the D_1 line $F_g = 2 \rightarrow F_e = 2$ transition of ^{87}Rb with zero detuning and maintain a power of 7 mW. The squeezing cell temperature is held at 66° Celsius, corresponding to an atomic number density of 5.4×10^{11} atoms/cm^3. We find these parameters experimentally to be optimal for noise suppression (squeezing) of 2.0±0.35 dB with respect to the shot noise level at frequencies in the range of several kHz to 1 MHz. Once we account for detection noise, we see noise suppression at frequencies as low as 100 Hz (see Fig. 8.4). The squeezed vacuum state in this case is linearly polarized in the y direction (orthogonal to the x-polarized pump laser field) as shown in Fig. 8.1(a). After the squeezer, we make a collimated magnetometer probe beam from the squeezer output with a waist size of 900 μm. We must treat this probe quantum-mechanically and thus describe quantum fluctuations in both x and y polarizations. The mixing of the squeezed-vacuum field in the y-polarization, with the strong pump field in the orthogonal polarization, creates a polarization-squeezed state [84, 85]. When we set a polarizing beam splitter (PBS) at 45° with respect to the polarization of the squeezed vacuum (see Fig. 8.1(b)), and thus split the laser power 50/50 for the balanced photodetector (BPD), we make the detector

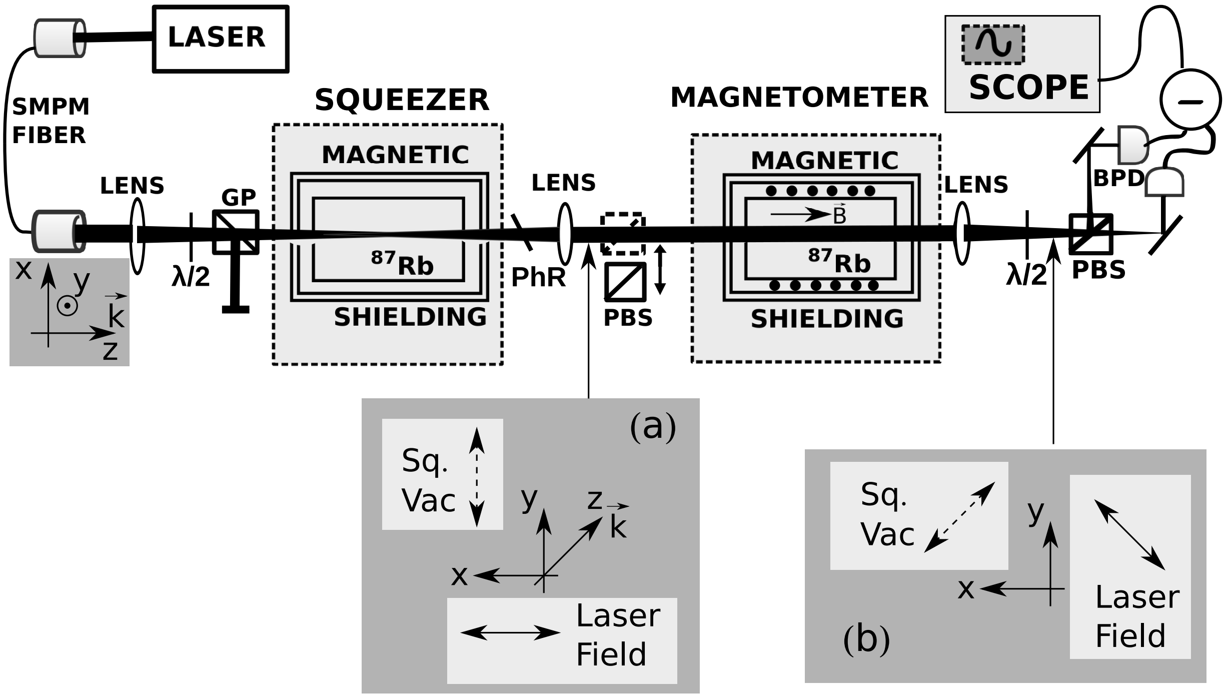
LASER
SMPM FIBER
LENS
GP
λ/2
SQUEEZER
MAGNETIC
^{87}Rb
SHIELDING
LENS
PhR
PBS
MAGNETOMETER
MAGNETIC
B
^{87}Rb
SHIELDING
LENS
λ/2
PBS
BPD
SCOPE
x
y
k
z
(a)
Sq. Vac
y
z
k
x
Laser Field
Sq. Vac
y
x
Laser Field
(b)

FIG. 8.1: Experimental setup. The squeezer prepares an optical field with reduced noise properties, which is used as a probe for the magnetometer. SMPM fiber: single-mode polarization-maintaining fiber, $\lambda/2$: half-wave plate, PhR: phase-retarding wave plate, PBS: polarizing beam splitter, GP: Glan polarizer, BPD: balanced photodetector. Axes x and y coincide with horizontal and vertical polarization axes of all PBSs in our setup, axis z is along beam propagation direction. Inserts show the polarization of squeezed vacuum (Sq.Vac) field and laser field before the magnetometer cell (a) and right before the last PBS (b).

sensitive to the quantum fluctuations in the squeezed vacuum field [36, 74, 131]. We use this polarization-squeezed beam as the probe field for our magnetometer and refer to it as the *squeezed probe*. The laser power of this squeezed probe is 6 mW after absorption loss in the squeezing cell.

The magnetometer itself consists of a similar cell of isotopically enriched ^{87}Rb with the addition of 2.5 Torr Ne buffer gas. The presence of buffer gas in the magnetometer cell extends the coherence times for atoms interacting with the probe beam leading to a sharper NMOR response and a more sensitive device [94]. Without the buffer gas, the NMOR curve is too broad to be useful for magnetometry. The magnetometer cell is also enclosed in magnetic shielding, but an internal solenoid controls the magnetic field ($\mathbf{B}$) which is parallel to the direction of probe beam propagation ($\hat{z}$). We also vary the magnetometer cell temperature to determine the optimal atomic density for the magnetometer response.

After the magnetometer cell, we use a detection scheme to measure the polarization rotation angle of the probe through the atoms. The scheme consists of a PBS set to 45° with respect to the probe light polarization, which splits the probe field at a 50/50 ratio and directs it to the balanced photodetector. The signal from the BPD is sent to an SRS SR560 voltage preamplifier and then to a Lecroy 640Zi oscilloscope to analyze the response of the system to the magnetic field and also measure the quantum noise spectrum (with the spectrum analyzer feature enabled by the scope). We tilt the phase-retarding plate after the squeezer to control the phase shift between orthogonal polarizations and adjust the squeezing angle of the vacuum field relative to the strong field. In this way, we can choose the phase angle to achieve the maximum quantum noise suppression in the squeezed vacuum light. This is equivalent to using detection scheme #2 to measure the noise, but with the magnetometer cell in the middle of the detection.

We can remove the squeezed vacuum field from the squeezed probe beam by inserting a PBS before the magnetometer, which rejects squeezed vacuum in the y polarization and thus creates a shot-noise-limited, unsqueezed, coherent vacuum quantum state in this polarization, orthogonal to the x-polarized pump laser. Meanwhile, it leaves the intensity and the quantum state along the x polarization of the probe virtually unaffected (we disregard small optical losses inside the PBS). We use this normal unsqueezed beam to calibrate the response of our magnetometer, and we call it the *coherent probe*. Such a probe allows us to see the shot noise limit (SQL) of the magnetometer.

8.2 Experimental observations

When we apply a longitudinal magnetic field to the magnetometer cell, the polarization of the probe field rotates due to the NMOR effect, and the photodiodes detect a signal proportional to the angle of rotation (for small angles) and the incident intensity of the light. We fix the intensity of light; thus the BPD signal is proportional only to the

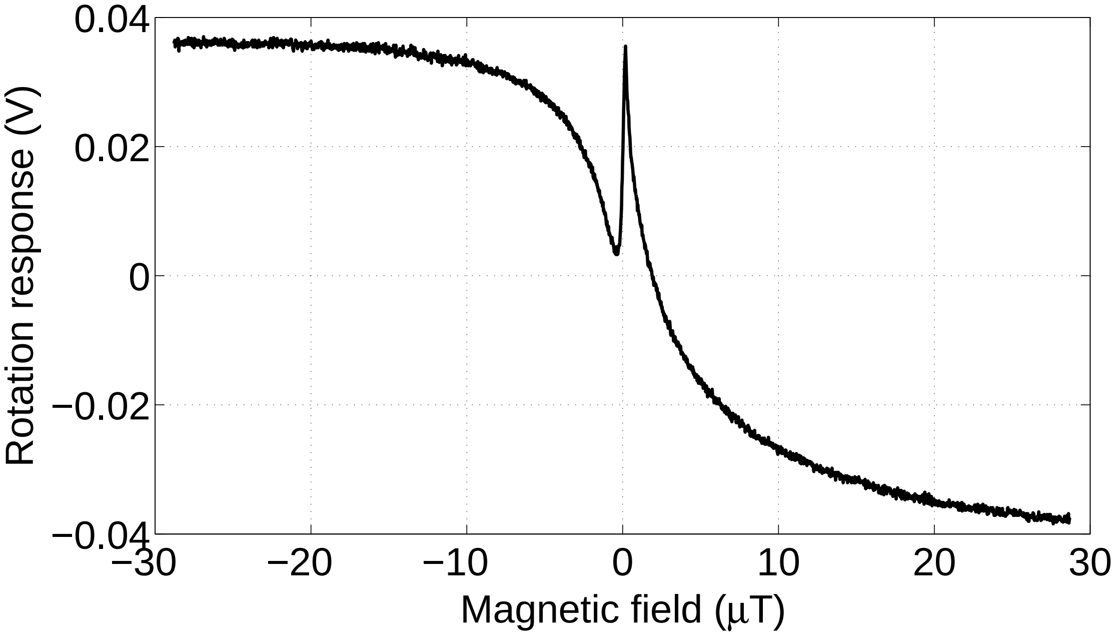

FIG. 8.2: Sample of the magnetometer response to the longitudinal magnetic field. The narrow feature at zero field is due to repeated coherent interactions of atoms with the light field. Cell temperature is 40° C, density is 6×10^{10} atoms/cm^3, and probe power is 6 mW.

angle of rotation. A characteristic response curve is depicted in Fig. 8.2. The broad S-like response is governed by the Zeeman splitting of the ground-state magnetic sublevels and their decoherence time subject to power broadening. The time of flight of the atom in the probe beam is estimated to be around 3.3 μs, which corresponds to a resonance width of 300 kHz, which in turn governs the relevant Zeeman splitting to be about 50 μT for our S-like resonance. The narrow resonance at zero magnetic field is due to velocity changing collisions and repeated interaction of the atoms that diffuse away from the laser beam and then return back to the beam [94, 132]. For such atoms, the effective lifetime in the beam is significantly longer, resulting in a narrower spectral feature. We attribute the asymmetric shape to the presence of other hyperfine levels nearby that break symmetry. We note that if we reduce the power of the probe beam to below 1−2 mW, the narrow resonance disappears, since the probe beam intensity drops below that required to saturate the narrow resonance. The smallest detectable magnetic field (i.e. sensitivity) of the magnetometer is inversely proportional to the slope of this curve; the slope is measured on the steepest part of the response curve on the left side of the narrow peak. This narrow resonance thus increases the response of the magnetometer to very small magnetic fields, and so we maintain the intensity of the probe light at the level of several milliwatts. An easy way to boost the response of the magnetometer is to increase the number of interacting atoms in the magnetometer cell (i.e. increase the cell temperature). The rotation signal slope (and thus the magnetometer response) grows with increasing density for small atomic densities (see Fig. 8.3) but then tends to saturate since with increased atomic density, the probe beam is attenuated which leads to a weaker signal at the BPD [86]. If the density is increased even further, the probe light will eventually be totally absorbed and no response will be detected.

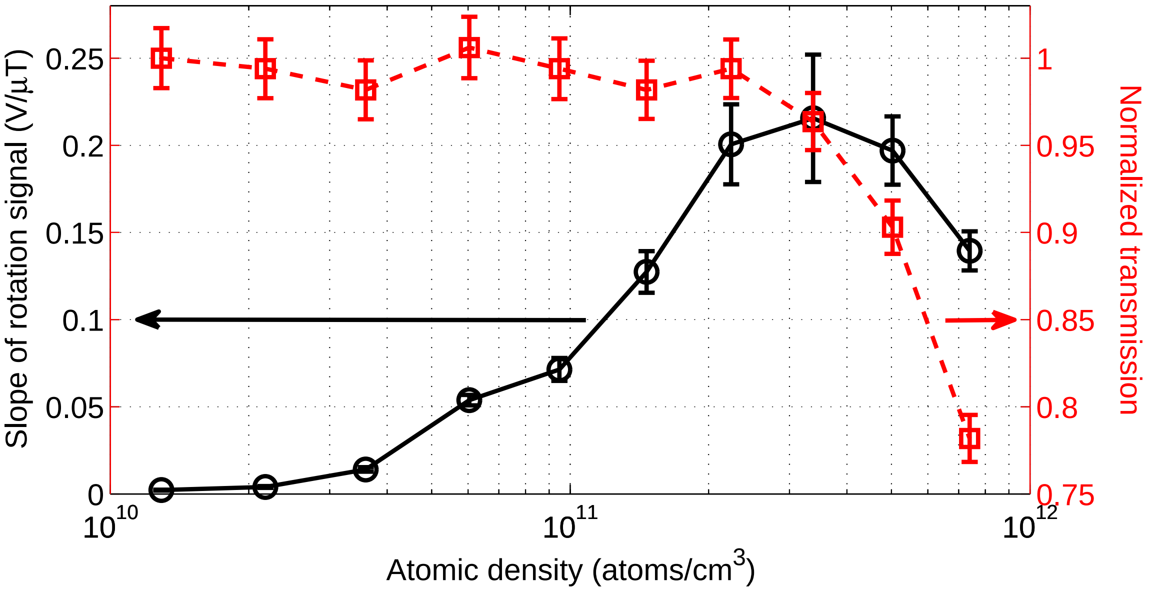

FIG. 8.3: Magnetometer response (solid) and probe transmission (dashed) vs atomic density. Density uncertainties due to temperature fluctuations correspond to the size of the markers. Laser power is 6 mW. Cell temperatures range from 25-70° C in 5 degree increments.

The ultimate sensitivity is governed by the signal-to-noise ratio according to the equation $\delta B_z = (\partial\phi/\partial B_z)^{-1}\delta\phi$, where $\partial\phi/\partial B_z$ is the slope of rotation and $\delta\phi$ is the noise level. In our experiment, we use the signal and noise of the voltage response of the oscilloscope, which is directly proportional to the angle of polarization rotation. The noise level is set by the quantum noise floor at frequencies higher than 200 kHz. We compare the noise floors of our magnetometer under two experimental conditions: first, when we probe with unsqueezed coherent light, which sets the shot noise limit, and second, when we use the polarization-squeezed light probe. Sample results are shown in Fig. 8.4. The left panel shows the noise power resulting from each probe around a 30 kHz detection frequency, where a magnetic field modulation has been added within the magnetometer cell. The noise spike resulting from the modulation is the desired signal. Note that the signal is identical for the two probes, but the noise floor is lower for the squeezed compared to the coherent probe, giving an overall improvement to the sensitivity. The right panel of Fig. 8.4 shows the full detection frequency range with a modulation now added at 220 Hz. This shows a broadband noise reduction of about 2 dB using the squeezed probe, and demonstrates the low frequency capabilities of this device, with noise reduction visible as low as 100 Hz.

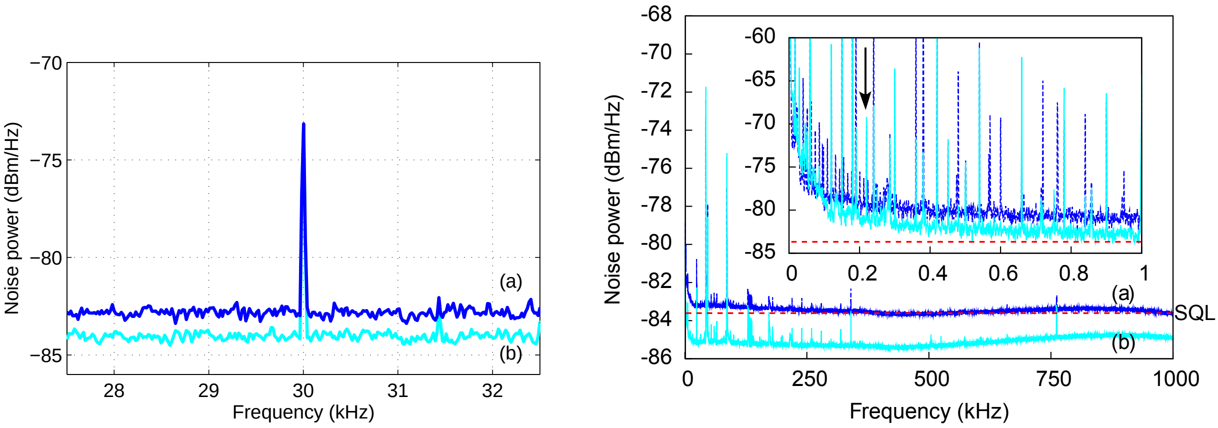

FIG. 8.4: Magnetometer quantum noise spectrum with (a) shot-noise-limited and (b) polarization-squeezed probe fields. Laser probe power is 6 mW. Left: magnetometer cell temperature of 43°C with a magnetic field modulation at 30 kHz. RBW=28.6 Hz. Right: magnetometer cell temperature of 35°C with modulation at 220 Hz. The insert shows the low frequency part of the noise spectrum (0 to 1 kHz) RBW=0.9 Hz.

We conduct this comparison at different temperatures and atomic densities. The results are depicted in Fig. 8.5. During these measurements, we modulate the internal longitudinal magnetic field at various frequencies to ensure that the noise floor of the magnetometer is unaffected by the presence of alternating magnetic field. In Fig. 8.5, the noise measurements were taken without magnetic field, but modulation can be added anywhere within the detection range, as demonstrated in Fig. 8.4.

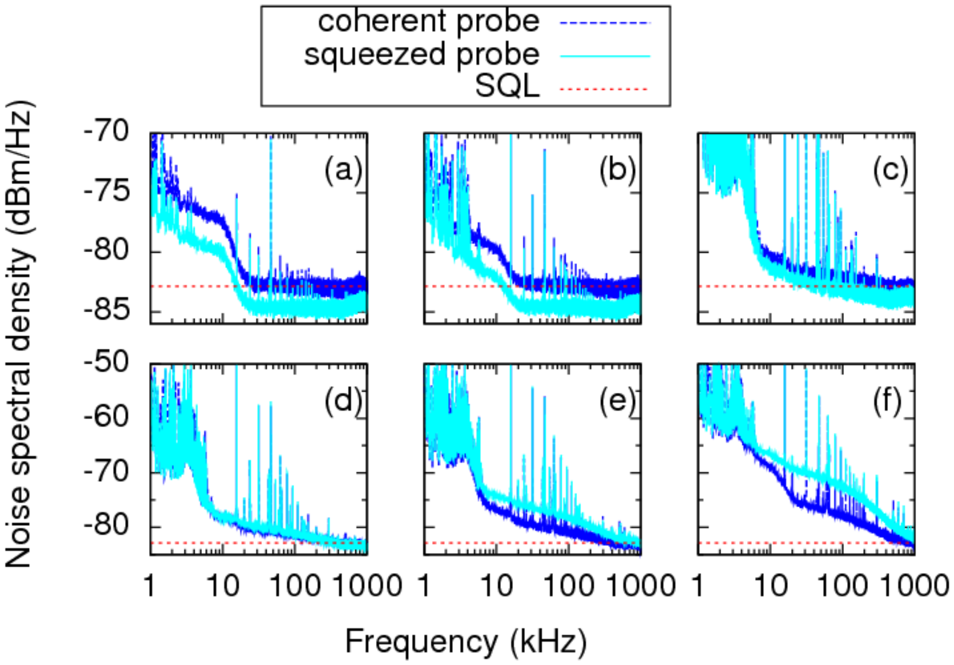

FIG. 8.5: Magnetometer quantum-noise-floor spectra with polarization-squeezed (light trace) and coherent probe (dark trace) fields taken at different temperatures/atomic densities of the magnetometer. (a) 25°C, (b) 35°C, (c) 50°C, (d) 55°C, (e) 60°C, (f) 70°C. Laser probe power is 6 mW. Spectrum analyzer resolution bandwidth is 28.6 Hz.

At lower atomic densities (cell temperatures), when classical noise does not contribute much to the overall noise budget, we see broadband noise suppression of about 2 dB from hundreds of hertz to several megahertz, which is independent of atomic density and follows the input squeezed state noise spectrum (see for example Fig. 8.4(right panel), obtained with the most careful balancing of the detector). High resonance-like peaks are due to resonant spikes in electronic dark noise of the BPD and the electronic noise of our solenoid current source. Note that in Fig. 8.5, one can see an increase of the noise above the SQL level at frequencies below 200 kHz and especially below 10−20kHz. This is due to residual intensity noise (RIN) of our laser, discussed in section 6.5, making our detection not truly shot-noise-limited at these frequencies, even with the most careful balancing of the light power at the PDs.

With increase of the atomic density in the magnetometer cell, we see that at lower frequencies noise grows significantly above the SQL level. The similarities between the RIN power spectra (Fig. 6.3) and the magnetometer spectra (Figs. 8.5(d),(e) and (f)) lead us to conclude that this contribution of the noise is from the strong x polarization of the probe. This contribution is due to the dependence of the NMOR effect on probe power, thus the RIN in the x polarization couples into the y polarization noise that our BPD detects, due to the presence of the atoms. To test this, we block the y-polarized light with a PBS after the magnetometer and compare this noise floor to that of the probe beam when it completely bypasses the atoms in the magnetometer. We find these noise levels are the same, (adjusted for optical losses in the cell), indicating that the increase in noise at high densities is due to the x-polarized noise coupling into the y-polarized field. However, we note some interesting dynamics: the squeezed probe shows a higher noise floor compared to the coherent probe, where squeezing was replaced with a normal vacuum state in the y polarization (see Figs. 8.5(d),(e) and (f)). We conjecture that this is due to the back action noise resulting from strong interactions of the light with the atoms, since we are unable to bring the noise level of the squeezed probe below the coherent probe level no matter how we adjust the squeezing angle.

We choose several noise spectral frequency components from Fig. 8.5 to better illustrate this situation in Fig. 8.6. Here, 0 dB indicates the noise level seen using the coherent probe (unsqueezed state). Note that at lower atomic densities, the squeezing clearly improves the magnetometer noise floor, and the noise spectrum is nearly independent of the detection frequency. At higher densities, squeezing is degraded due to absorption by the atoms and so we expect less noise suppression. We also see that at the highest densities, due to the back action of atoms, the total noise is amplified rather than suppressed. This effect shows that using squeezed light will only improve the magnetometer sensitivity at certain atomic densities and experimental conditions.

We calculate the magnetometer sensitivity by dividing the noise amplitude densities

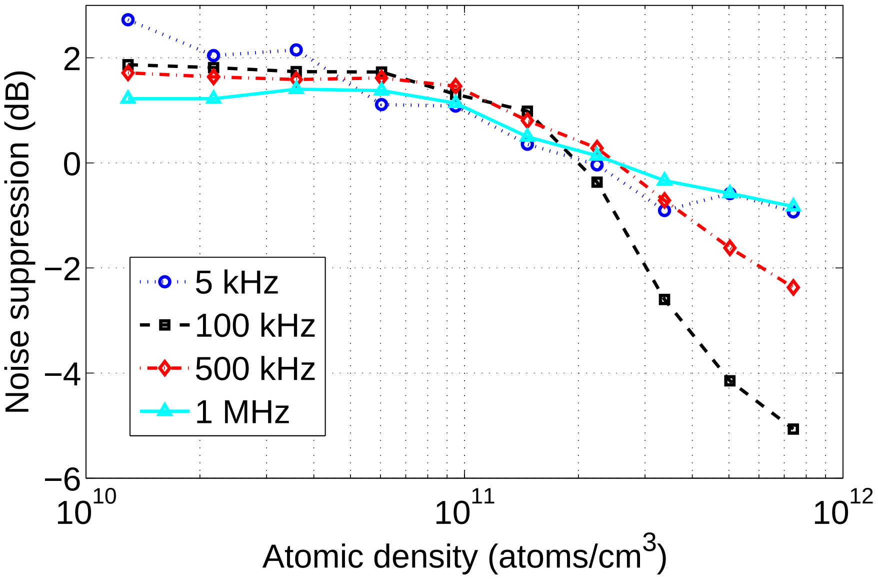

FIG. 8.6: Noise suppression level vs atomic density normalized to shot noise level for several noise frequencies. Positive values indicate noise suppression, negatives indicate noise amplification. This level is found by averaging the coherent probe noise level subtracted from the squeezed probe noise level over 100 points (2 kHz) centered around the chosen noise frequency. The average uncertainty of ±0.35 dB is not included in the plot for clarity. Laser probe power is 6 mW.

(calculated from the data presented in figure 8.5) taken at 500 kHz, by the magnetometer response shown in Fig. 8.3. Due to absorption and the increased noise described above, the NMOR magnetometer does not benefit from polarization squeezing at all atomic densities and temperatures as we show in Fig 8.7. However, benefits of the polarization-squeezed state probe are clearly visible at lower atomic densities for the chosen detection frequency. The magnetometer sensitivity can likewise be improved for any set of parameters (detection frequency, atomic density, etc.) where noise suppression below shot noise is observed.

8.3 Magnetometer summary

We demonstrated an all-atomic quantum enhanced NMOR magnetometer with sensitivities down to close to 1 pT/$\sqrt{\text{Hz}}$. This is the first demonstration of a squeezer at 795 nm capable of noise suppression below shot noise levels at low frequencies starting

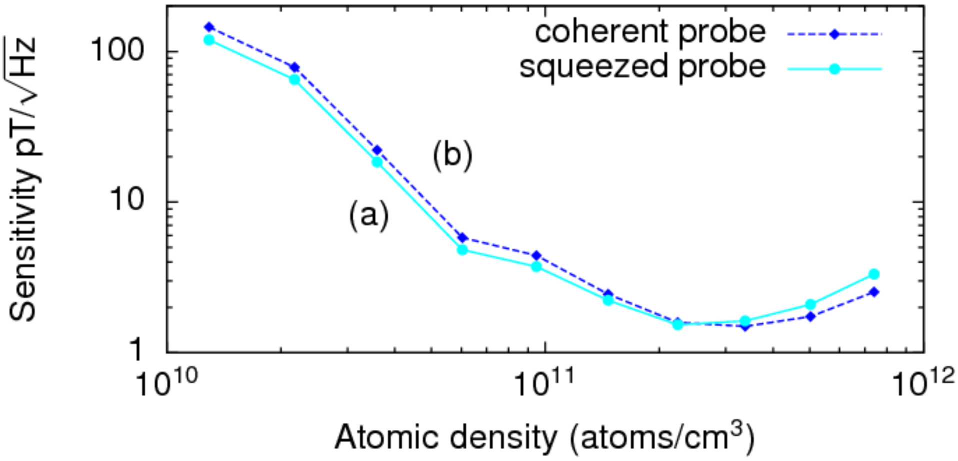

FIG. 8.7: NMOR magnetometer sensitivity as a function of the atomic density with polarization-squeezed (a) and coherent (b) (shot-noise-limited) optical probes. Errorbars are smaller than the size of the markers. Laser probe power is 6 mW. Detection frequency is 500 kHz.

from a few hundred hertz. This brings such a quantum-enhanced magnetometer into the realm of practical applications in medicine and biology where the characteristic magnetic signatures are at sub-kilohertz frequencies. This is also the first demonstration for a magnetometer which uses PSR squeezing, which offers several advantages due to the simplicity of the method. We note that the increase in noise below 200 kHz frequencies in our squeezer is not fundamental, and can be improved with the use of a laser with less intensity noise and an improved design of the BPD.

CHAPTER 9

Slow and fast squeezed light studies

9.1 Introduction

In this chapter, we study the propagation of a squeezed vacuum through an atomic vapor of ^{87}Rb atoms undergoing steep dispersion. We concentrate on the medium's ability to delay pulses of squeezed light, i.e. creating subluminal squeezed light, an important first step for EIT quantum memory. We also see evidence for superluminal, or fast light, both for coherent pulses and squeezed pulses of light. The propagation of quantum noise at group velocities faster than c is of interest for fundamental studies of quantum information transfer. Slow and fast light may find additional applications in certain measurement techniques such as interferometers and gyroscopes [133, 134]. This has prompted further studies into the propagation of squeezed light with slow and fast group velocities [135, 136, 137].

9.2 Dispersion

In section 4.6, we saw how the electric susceptibility χ of an atomic system is related to the absorption and index of refraction experienced by light in a medium. (See equation 4.78 for χ, calculated for a three-level Λ model of EIT). The real and imaginary parts of the electric susceptibility χ are related according to the Kramers-Kronig relations [82].

$$\mathrm{Re}[\chi(\nu)] = \frac{1}{\pi} P \int_{-\infty}^{\infty} \frac{\mathrm{Im}[\chi(\nu')]}{\nu' - \nu} d\nu' \tag{9.1}$$

$$\mathrm{Im}[\chi(\nu)] = -\frac{1}{\pi} P \int_{-\infty}^{\infty} \frac{\mathrm{Re}[\chi(\nu')]}{\nu' - \nu} d\nu' \tag{9.2}$$

P denotes the principal value, and the integral is taken over all frequencies. This relation indicates that the absorption and index of refraction are not independent, and so a sharp change in the absorption, which can be accomplished with a narrow EIT resonance, implies a steep dispersion $\frac{dn}{d\nu}$ of the material.

For this reason, EIT-like interactions in atomic vapors can to lead to a dramatic slowing of the group velocity of light [107]. The group velocity in a medium is related to the index of refraction and dispersion by the following.

$$v_g(\nu) = \frac{c}{n + \nu \frac{dn}{d\nu}} \tag{9.3}$$

Therefore, for normal dispersion ($dn/d\nu > 0$), the group velocity of light will be slowed in the material to speeds lower than c. This is a necessary step in EIT-based quantum memories [53]. Alternately, the dispersion can be negative (anomalous dispersion), leading to the group velocity of a wave packet being either higher than c or negative in a medium.

We investigate these effects for pulses of squeezed light, generated using the pulse shaping methods outlined in Chapter 7.

9.3 Experimental setup

We are able to investigate the changes in light pulse propagation speed using a similar experimental arrangement to that used in the magnetometer experiment, shown in Fig. 9.1. We generate a squeezed vacuum field in the first Rb vapor cell and optimize conditions for the best noise suppression. The squeezing pump laser is locked to the $F_g = 2 \rightarrow F_e =$

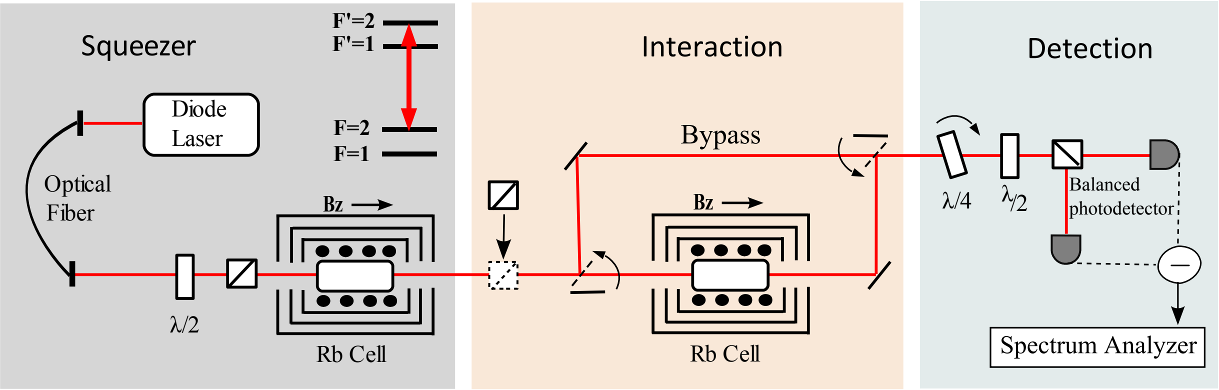
Squeezer
F'=2
F'=1
F=2
F=1
Diode Laser
Optical Fiber
λ/2
Bz
Rb Cell
Interaction
Bypass
Bz
Rb Cell
Detection
λ/4
λ/2
Balanced photodetector
Spectrum Analyzer

FIG. 9.1: Experimental setup for group velocity studies. B_z indicates the direction of applied magnetic field. $\lambda/2$ and $\lambda/4$ are half and quarter wave plates.

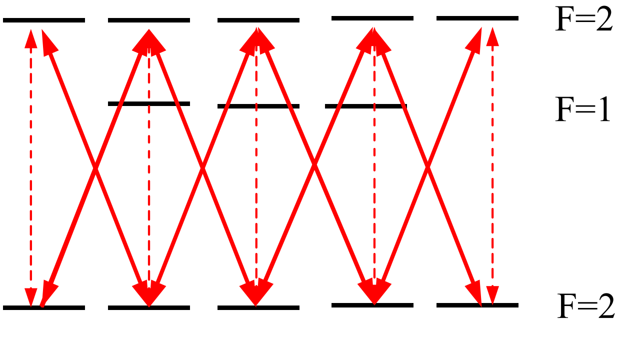

FIG. 9.2: Energy level diagram showing multiple lambda-schemes between the strong (solid) and weak (dashed) polarizations.

2 transition, and the squeezing cell temperature (T_{sq}) is held at 66°C. Here, the linearly-polarized pump field (x) copropagates with the squeezed vacuum field (y) through the second vapor cell (with 2.5 Torr of neon buffer gas), resulting in Λ-schemes consisting of the circularly-polarized components of the light interacting with the Zeeman sublevels of the ground state (see Fig. 9.2). The EIT resonance causes the medium to be dispersive, and results in an optical rotation of the probe polarization which can be detected by the balanced detection. An example of this rotation response, (which is equivalent to the dispersion lineshape of the medium), is shown in Fig. 8.2. This response gives an indication of how drastically the group velocity of light is expected to be altered. In particular, the vapor cell is shielded from external magnetic fields, and so we are concerned with the slope of the response curve at zero field.

The amount of rotation of light polarization induced by the nonlinear Faraday effect will depend upon the number of interacting atoms as well as the light intensity, as seen from equation 4.62. We therefore vary the pump/probe light intensity in this experiment to study the effects on the Faraday rotation and the group velocity in the atomic medium. The temperature of the interaction vapor cell (T_I) is held constant at 50° C. Examples of the rotation response at several laser powers are shown in Fig. 9.3. Notice the narrow feature due to repeated coherent interactions, which was present in the previous chapter, only appears at the higher laser powers where this resonance is saturated. Fig. 9.4 shows the slope of these response curves at zero magnetic field versus the pump laser power. Because the feature with positive slope is absent at low laser powers, we see that the curve in Fig. 9.4 actually crosses zero, going from negative to positives slopes with increasing power, when the extra feature appears around 4 mW. Since this response is an indication of the dispersion of the material, it follows that at this zero-crossing point, the medium switches from regular dispersion to anomalous dispersion, and we expect to see a transition from subluminal to superluminal light propagating in the vapor cell.

To gain information about light propagation speeds through the dispersive medium, the light must be in some way modulated or pulsed. To accomplish this, we rely on the

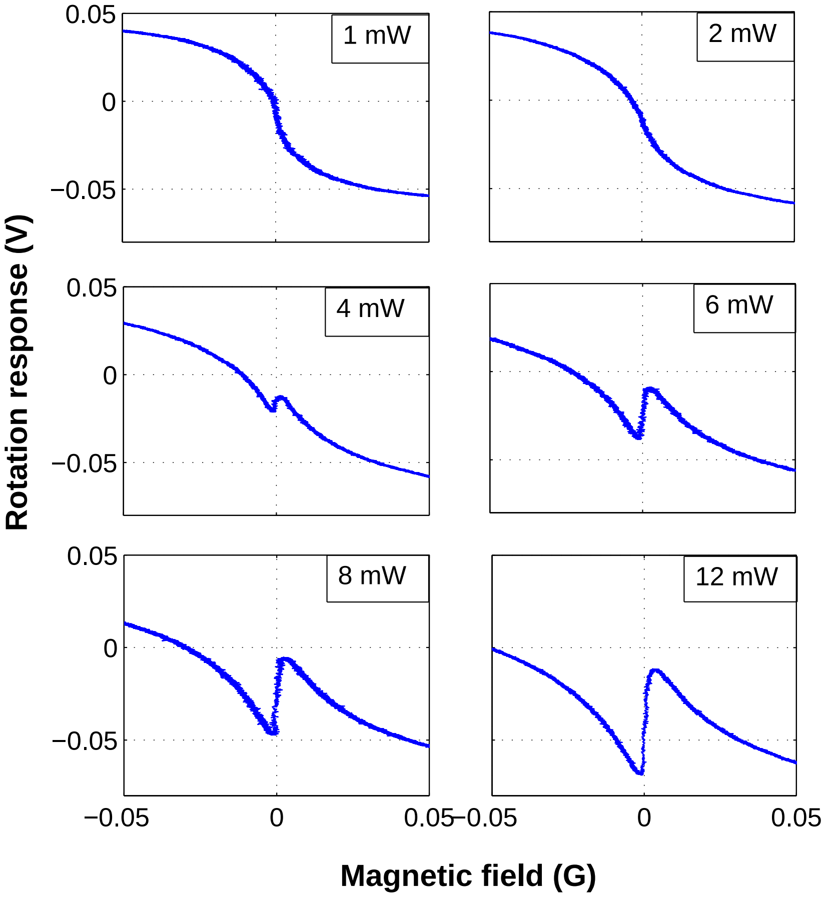

FIG. 9.3: Rotation response of the medium vs magnetic field for several laser powers. This response indicating polarization rotation is shown in arbitrary units of the voltage measured from the balanced photodiode. Overall offsets on the y-axis are meaningless. T_I=50° C.

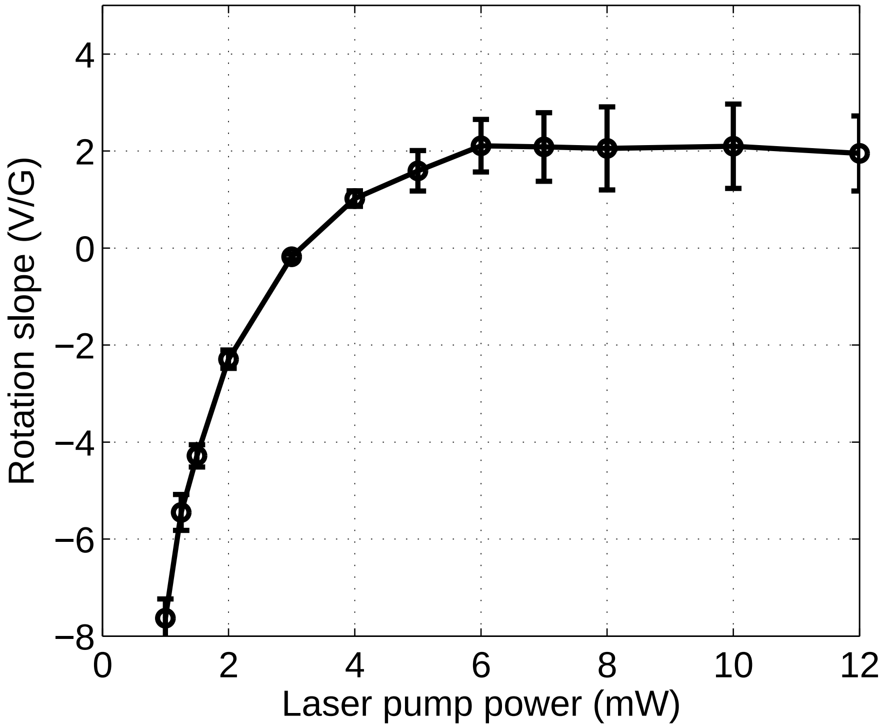

FIG. 9.4: Slope of the rotation response (in Volts per Gauss) around zero magnetic field vs the input laser power. T_I=50° C.

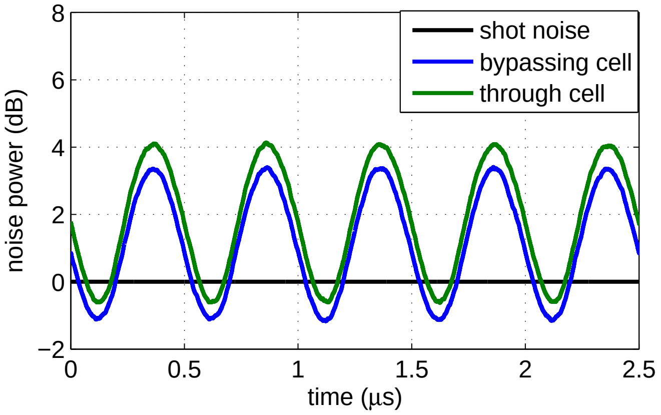

FIG. 9.5: Noise power vs time for the bypass optical path and interaction path where light passes through the second vapor cell. The noise traces can be fit to sine waves to compare the phases and determine a difference in group velocity. Differences in noise power level is attributed to absorption and atomic noise from the interaction cell. T_{Sq}=66° C, T_I=50° C.

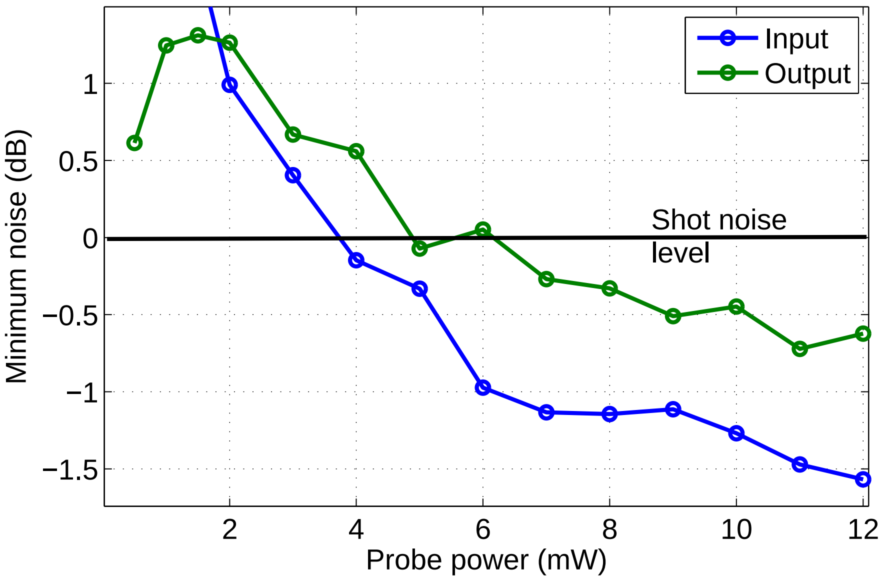

FIG. 9.6: Minimum noise level vs laser power for both the input and output signals from the interaction vapor cell. The input noise power is measured along the bypass path. The light is squeezed for noise levels under 0 dB. T_{Sq}=66° C, T_I=50° C.

pulse shaping method developed in section 7.2. By changing the magnetic field in time within the squeezing vapor cell, but holding the phase angle χ constant, the quadrature noise level of the squeezer output will change in time (see Fig. 7.1). In this way, we create a probe for the interaction vapor cell that has a near-constant intensity but a noise profile which oscillates as a sine wave with time, as shown in Fig. 9.5.

This regular noise signal, after traveling through the interaction vapor cell and reaching the detectors, can be compared with a similar signal which bypasses the cell but travels the same distance (labeled bypass). These two signals, which share a trigger, are then fit to sine functions. By comparing the small differences in the phases, we determine whether the atomic medium has caused a delay or advancement of the light pulse as compared to the arrival time of a pulse though air. Given a sine wave $\sin(\phi = 2\pi f t)$ with frequency f, the difference in phase translates to a difference of pulse arrival time by $\Delta t = \Delta\phi/(2\pi f)$. The modulation frequency used in these measurements was $f = 2$ kHz.

We also keep track of the noise level of the pulsed light compared to the shot noise level (which is unaffected by the pulsing process). Notice in Fig. 9.5, the light can only be considered squeezed when the noise power falls below the shot noise level at 0 dB. Because the pump power of the squeezing cell is being changed on subsequent measurements, and also due to some small absorption in the interaction vapor cell, the pulsed noise signals are only squeezed for a certain range of laser powers. Fig. 9.6 shows the minimum noise level detected with respect to shot noise versus the laser power at the input and output of the interaction vapor cell. The optical loss experienced in the interaction vapor, as well as possible light-atom interactions, add excess noise to the light field and degrade the squeezing levels.

9.4 Pulse delay/advancement measurements

The main results for these group velocity measurements are given in Fig. 9.7. This plot shows the arrival time of the light pulse traveling through the interaction vapor cell compared to the arrival of the same signal on the bypass path for different pump laser powers. Negative values indicate that the pulse through the atoms is delayed, meaning it arrived to the detectors later than the bypass signal. This means that the group velocity in the atoms was slower than that in air, and the light is subluminal. Positive values indicate an apparent advancement of the pulse, caused by either a negative group velocity, or a group velocity higher than c. This will indicate superluminal light. We show results both for the coherent probe (in blue) and for the squeezed vacuum noise propagating through the atomic medium (in red and pink). While the magnetic field modulation used to create noise pulses on the vacuum polarization left the intensity of the strong orthogonal polarization mostly unchanged, there was still a small rotation of the polarization of the pump beam due to the nonlinear magnetic Faraday effect in the squeezing cell. This is detected as a small voltage signal oscillating in time, which can be used directly to make comparisons of the coherent light's group velocities. This method does not rely on the noise of the signal, and is based on the strong coherent polarization (x) of the probe

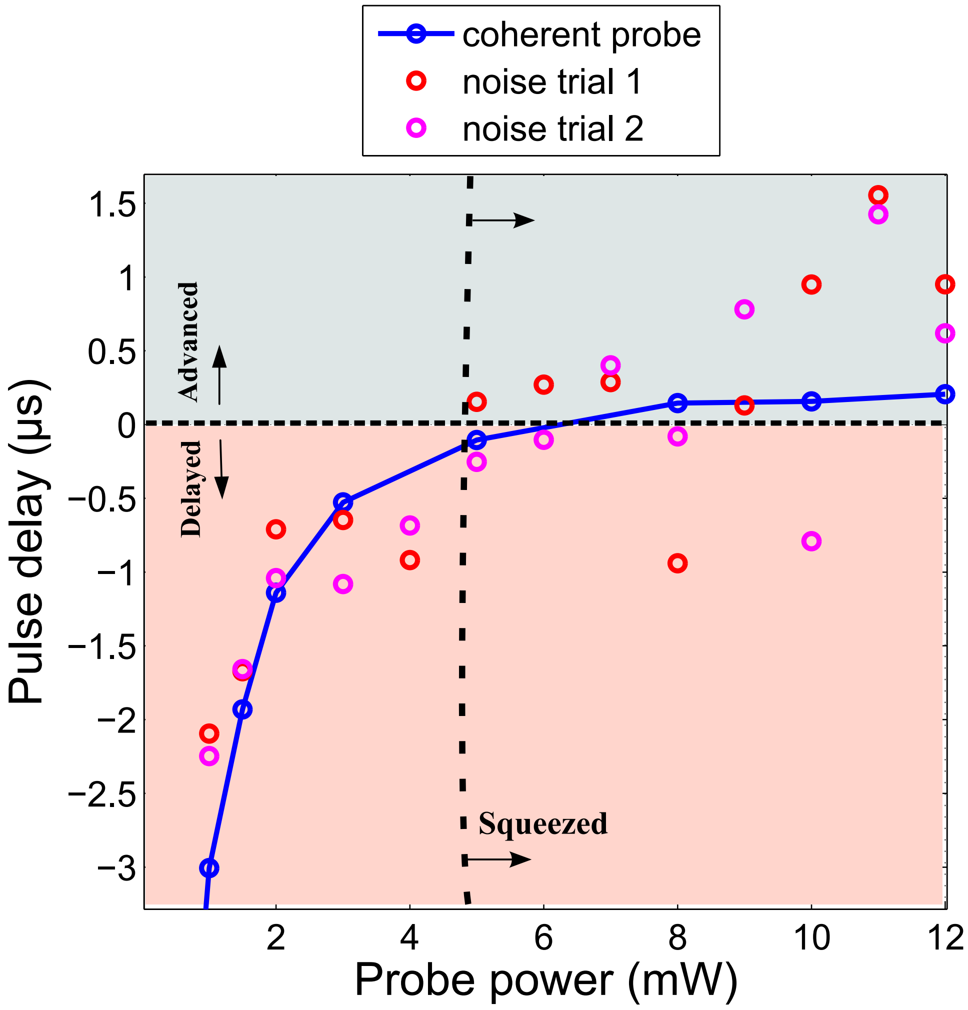

FIG. 9.7: Pulse delay versus laser power for signals traveling through the interaction vapor cell compared to those from the bypass path. Negative values indicate delays (slow light) while positive values indicate advancement (fast light). Results for the strong coherent probe (solid blue) as well as two trials for the pulses (red and pink points) are shown.

undergoing rotations, and so we label this data the *coherent probe*. Note the similarity of the delay times versus power with the coherent probe to the slope versus power from Fig. 9.4. There is a switch from slow light at low laser powers to fast light at higher powers as expected, though the exact zero crossing points are different, and we may expect to see more advancement of the light pulses at the highest powers. The discrepancy is still under investigation, but may be due to temperature, detuning, or alignment instabilities.

The remaining data points in Fig. 9.7 come from measuring the phase differences of the time-dependent sinewaves in the noise spectrum of the weak probe polarization using a spectrum analyzer. While using this balanced detection scheme and holding the phase angle between the strong and weak polarizations constant, the detection is only sensitive to the noise of the squeezed vacuum on the y polarization. The balance of the light intensity onto the photodiodes changes slightly due to the polarization rotation mentioned above, but this change is very small and does not effect the shot noise or squeezed noise levels. For the noise pulses, we see a similar trend in the pulse arrival times as for the coherent probe. The pulses are clearly slowed down in the atomic medium by as much as 2 μs compared to propagation through air for small laser pump powers. Given the length of the vapor cell used (75 mm), this indicates a group velocity through the atoms of around 40000 m/s compared to the speed of light c. As the dispersion flips from normal to anomalous, the noise pulses appear to be delayed less and show hints of advancement at the higher laser powers, indicating superluminal squeezed vacuum.

However, we can see by these two trials that the uncertainty in delay time is quite large, and advancement can not be shown definitively. While the uncertainty in measuring the phase of the signal from fitting is less than ± 0.1 μs, the data clearly can deviate by more than ± 1 μs at high pump powers. Further investigation showed that the effect of the atomic medium on the group velocity of the squeezed vacuum depended very strongly on the input polarization state. We could not purify the polarization after the squeezing cell without introducing loss to the squeezed vacuum field, and so the polarization state used as an input into the interaction cell could change over time due to fluctuations in the temperature of the squeezing vapor cell ($\pm 1°C$) and affect the results. Temperature fluctuations may result in polarization fluctuations that can lead to ellipticity and self-rotation, unwanted in this case. Therefore, a trend in the measured group velocities may be seen over a short measurement period, but under slightly different experimental conditions, the results may differ. The two trials shown in Fig. 9.7 are taken over a short time frame and under nearly identical experimental conditions. Other factors such as pulse deformation in the dense atomic medium may also have contributed to the increased uncertainty for the noise measurements.

It is important to note that while we do demonstrate a decrease of the group velocity of the noise pulses, at these low powers, the pulses are not squeezed because the pump is not strong enough to result in noise reduction below shot noise (see Fig. 9.6). To demonstrate that the light can be slowed while maintaining its noise reduction, one could use a sufficiently strong pump power to produce squeezed light, but lower the interaction probe power by attenuating the strong x polarization only, or by using a separate control beam to facilitate an EIT interaction.

9.5 Chapter summary

We have demonstrated an experimental setup which can be used to investigate the dispersive properties of an atomic vapor and the associated changes to the group velocity of squeezed vacuum states of light. By taking advantage of the influence that the magnetic field has on the noise of light during PSR squeezing generation, we show that we can effectively create pulses in the noise of squeezed vacuum to be used in applications related to quantum memory. We show the first step to such a memory protocol, the slowing of pulses of light in an atomic medium due to steep dispersion. We observe both subluminal and superluminal light measured using intensity modulation of the strong probe polarization. The measured advancement or delay depended on the laser power due to the dispersive response of the medium. While measuring the arrival of temporal pulses in the noise of the signal, we confirm the slowing of light and also see indications of fast light where the pulses are squeezed. This claim, however, is not definitive due to the large uncertainties seen when measuring the noise pulses, resulting from a strong sensitivity to the input polarization state.

This setup could be improved by having better control over the states of light which are input into the interaction cell. This includes improving the temperature stabilization in the squeezing cell and stabilizing the polarization of the probe. Also, by using a separate control beam in the interaction cell, an experimenter could achieve a larger range of absorption effects, and therefore have better control over the dispersion lineshape of the material. This would allow for more flexibility of the method and can be used to achieve the very low group velocities necessary for quantum memory protocols. As it stands, this experimental setup using pulsed PSR squeezed vacuum generation appears to be well suited for such studies where the goal is to store and recall a quantum state of light.

CHAPTER 10

EIT noise filtering experiments

10.1 Introduction

We saw in the previous chapters that squeezed light can have multiple uses ranging from optical measurement to quantum information. However, without tools to effectively manipulate the noise properties of squeezed states, their applications are somewhat limited. In the following section, we focus on another aspect of the interaction of squeezed vacuum and electromagnetically-induced transparency, in which we can use EIT as a frequency-dependent filter to manipulate the noise properties of the squeezed states.

This type of filtering of the squeezing amplitude has been demonstrated by several groups [55, 56, 57, 109, 110, 111, 112] using nonlinear crystal squeezers in application to atomic quantum memories. However, manipulation of the squeezing amplitude and squeezing angle can be important in and of itself in precision measurements as well. In particular, enhancing the sensitivity of large interferometers (such as LIGO) with squeezed light, requires large degrees of squeezing as well as frequency-dependent squeezing angles, to combat the shot noise at high detection frequencies and radiation pressure at low frequencies [138]. Such a manipulation of squeezing is possible with an optical cavity [139], but it requires a narrow cavity linewidth below 1 kHz, set by LIGO's internal cavities.

Such a high finesse cavity would be large and bulky (on the order of 10 meters or larger) even with ultra-high reflecting mirrors.

It was suggested by Mikhailov *et al.* [140] that narrow optical transmission resonances arising from coherent interaction with atoms (EIT resonances) could be used to create frequency-dependent filters for the quadrature noise amplitude and angle in squeezed light states to be used in gravitational wave detection. The previous examples demonstrating EIT filtering have been able to show the amplitude filtering effect of squeezed vacuum, but the frequency-dependent squeezing angle manipulation has not yet been demonstrated. Also, these demonstrations have relied on squeezing generation using frequency doubling nonlinear crystals for optical parametric oscillators (OPOs). While this method has been shown to generate high noise reductions, the squeezing has not been shown to extend down to the lower wavelengths required for EIT experiments due to increased losses in the nonlinear crystals. As a result, groups using nonlinear crystal based squeezers for EIT experiments, with Rb atoms at 795 nm, typically use around -3 dB noise suppressed squeezed states [56, 109, 110, 111, 112]. Crystal squeezing also suffers from a high experimental complexity and high laser power requirements.

Here, we demonstrate the EIT noise amplitude filtering and possible frequency-dependent squeezing angle manipulation in an experimental setup using only atomic vapors, for both squeezing generation and manipulation. We use our atomic PSR squeezer to generate squeezed vacuum that will then be filtered in an EIT medium. This is studied in two different configurations of EIT, first where the Λ-scheme uses two ground state Zeeman sublevels, and second, using two ground state hyperfine sublevels. These two cases of EIT are compared because different EIT characteristics can be attained for different configurations; for example different configurations may have different parameters such as peak transmission and lineshape symmetry. The desired properties of the EIT interaction used in an experiment will depend on the applications. Advantages and experimental complexities for these two cases of EIT filtering will be discussed.

The generated noise suppression of upwards of -2 dB at low sideband frequencies (20 kHz - 2 MHz) [37], as well as the simple all-atomic experimental design, using low laser powers and neither nonlinear crystals nor optical cavities, make our setup promising for this filtering application. We also study sources of excess noise which can couple into the system. Understanding the interaction of squeezed vacuum with EIT-like media is important not only in filtering, but also for vapor quantum memory protocols and other experiments using quantum states of light.

10.2 Theory

Using Caves and Shumaker's two-photon formalism [7], we start with the following expressions for amplitude ($\hat{\mathbf{X1}}$) and phase ($\hat{\mathbf{X2}}$) quadrature operators (equations 2.62, 2.63),

$$\begin{aligned} \hat{\mathbf{X1}} &= \frac{\hat{\mathbf{a}}(\omega_0+\Omega)+\hat{\mathbf{a}}^\dagger(\omega_0-\Omega)}{2} && (10.1) \\ \hat{\mathbf{X2}} &= \frac{\hat{\mathbf{a}}(\omega_0+\Omega)-\hat{\mathbf{a}}^\dagger(\omega_0-\Omega)}{2i}, && (10.2) \end{aligned}$$

in terms of the sideband frequency Ω with respect to the light carrier frequency ω_0. The quantum noise power of the corresponding quadrature is equal to the variance of the quadrature, $V1 = V2 = 1/4$ for coherent states. In this experiment, we initially measure noise powers of about -2 dB for the minimum (squeezed) quadrature and 8 dB for the maximum (antisqueezed) noise quadrature (see for example figure 10.3).

When a quantum light state interacts with a medium which has the complex field transmission coefficient

$$\mathcal{T}(\omega_0 \pm \Omega) = T_\pm e^{i\Theta_\pm}, \tag{10.3}$$

due to the changes to light transmission and phase, the noise levels are altered according to the following equation derived in Ref. [140].

$$\begin{pmatrix} V1_{out} \\ V2_{out} \end{pmatrix} = \begin{pmatrix} A_+^2 & A_-^2 \\ A_-^2 & A_+^2 \end{pmatrix} \begin{pmatrix} V1_{in} \\ V2_{in} \end{pmatrix} + \begin{pmatrix} 1-(A_+^2+A_-^2) \\ 1-(A_+^2+A_-^2) \end{pmatrix} \tag{10.4}$$

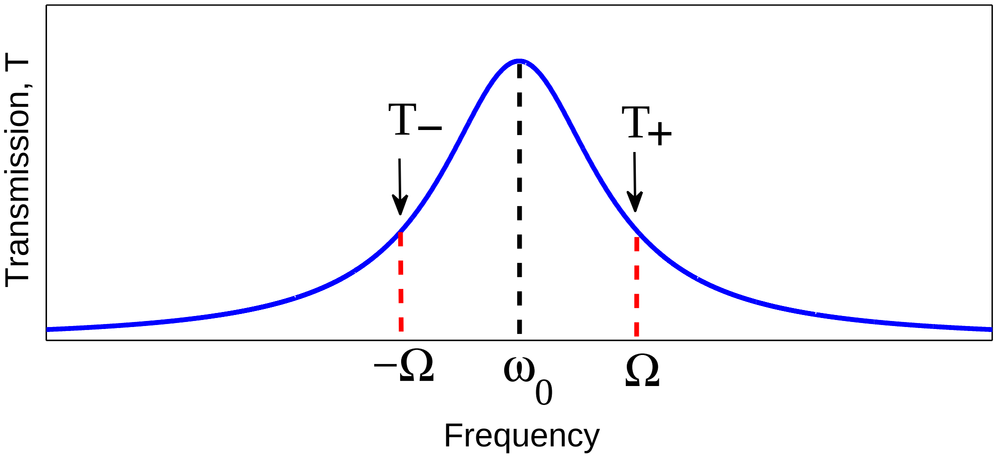

FIG. 10.1: Illustration of a Lorentzian transmission profile. ω_0 is the carrier frequency. $T_\pm$ are the transmissions at the sideband frequencies $\Omega_\pm$.

Here, $A_\pm \equiv \frac{1}{2}(T_+ \pm T_-)$. The terms $T_\pm$ are the transmissions at the positive and negative sideband frequencies, $\pm\Omega$ with respect to the carrier ω_0, as illustrated for a symmetric Lorentzian in Fig. 10.1.

We use a beamsplitter model to approximate the EIT medium as a passive attenuator of the light intensities. The first term of the above equation corresponds to attenuation/absorption of the propagating field. The second takes into account the natural vacuum state, which couples in and replaces the absorbed input field due to the loss. In the experiment, noise values are measured with respect to the shot noise, and so the normalization to the vacuum noise ($V = 1/4$) is already taken care of and does not appear in the above equation.

Due to accumulated phase shifts of the positive and negative sidebands, the squeezed state might also experience a rotation of the squeezing angle by

$$\phi = \frac{1}{2}(\Theta_+ + \Theta_-). \tag{10.5}$$

For a symmetric resonance lineshape with respect to ω_0, the Kramers-Kronig relationships dictate that $\Theta_+ = -\Theta_-$, thus ϕ is zero and no rotation occurs.

Given the input noise for the squeezed and antisqueezed quadratures of a signal, and knowing the light transmission lineshape through EIT, we can use these equations to predict the output quadrature noise levels. The treatment is identical for both the Zeeman and hyperfine EIT configurations where we are only concerned with changes to the noise brought about due to the transmission shape of the medium. In the following examples, the EIT medium can act as a low-pass filter for the quantum noise of the squeezed probe. When the EIT transmission window is centered on the carrier frequency ω_0, the highest transmission will occur for sideband frequencies ($\pm\Omega$) close to the carrier. Therefore, correlated pairs of photons at these low sideband frequencies will not be absorbed, while at higher sideband frequencies, where the atomic medium is less transmissive, the correlated pairs will be absorbed, and the squeezed noise will be replaced by shot noise. This should result in high levels of squeezed and antisqueezed quadrature noise at low detection frequencies which is filtered out at higher frequencies depending on the EIT linewidth. Also, if the transparency window is asymmetric, the unequal absorption of photon pairs can lead to a phase shift between them, and a rotation of the squeezing angle.

10.3 Zeeman EIT

As described in section 4.6, a transparency window can be created for a probe field in an atomic vapor, when a control light field of the appropriate frequency is provided, forming a Λ-scheme. First, we show the filtering results when the Λ-scheme uses two Zeeman sublevels of the $F_g = 2$ groundstate. The choice of the energy level configuration will depend on the exact application and desired transmission properties or filter shape. Zeeman EIT is easily achieved because the control field is tuned very close to the probe frequency ($\delta <$ MHz), and can originate from the squeezing pump light modulated by acousto-optical modulators (AOMs).

10.3.1 Zeeman experimental setup

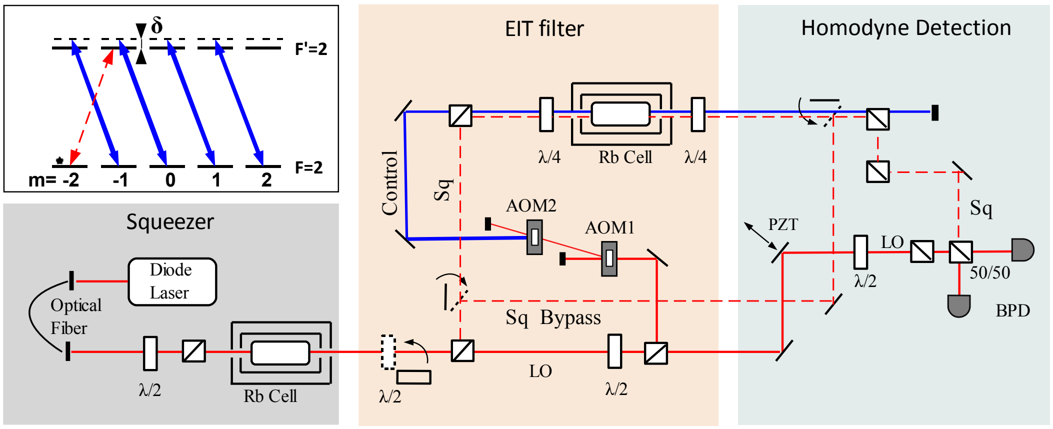

FIG. 10.2: Experimental setup: $\lambda/2$- half-wave plate, $\lambda/4$- quarter-wave plate, Sq- Squeezed vacuum, LO- Local oscillator, AOM- Acousto-optical modulator, BPD- Balanced photodetector. The insert shows relevant ^{87}Rb sublevels and optical fields. The weak probe field is depicted with dashed lines, the control with solid. δ is the two-photon detuning.

The arrangement of our experiment using Zeeman EIT is shown in Figure 10.2. Its three main components are the squeezer, where squeezed vacuum is generated, the EIT cell, where filtering occurs, and the balanced homodyne detector, which boosts the optical quantum noise above the electronic dark noise, allowing it to be measured. The squeezer used for these studies is unchanged from that described in section 6.1, and we make use of detection scheme #1, where the squeezed vacuum is separated from the LO prior to detection. The squeezing cell again contains pure isotopically-enriched ^{87}Rb vapor while the EIT cell contains an additional 2.5 T neon buffer gas just as in the previous two studies.

For this study, we lock the pump laser to the $F_g = 2 \rightarrow F_e = 2$ transition of ^{87}Rb to generate squeezed vacuum at this frequency. For the best squeezing conditions, we choose an atomic density of around $2.9 \times 10^{11}\ \frac{\text{atoms}}{\text{cm}^3}$ (corresponding to the cell temperature of 58°C) and input laser powers ranging from 10-20 mW. We measure noise suppressions of up to 2 dB for the squeezed quadrature, as well as several dB of antisqueezing. We separate this squeezed vacuum field from the orthogonal strong pump laser field with a PBS after the squeezer. The squeezed vacuum field can be directed straight into the detection optics bypassing the EIT filter cell (Sq Bypass) to check the prepared squeezed noise levels, or it can be directed through the EIT vapor cell (Sq) and then to detection.

In each measurement, we can compare the original squeezing levels with those modified by the EIT filter by sending the squeezed vacuum around the EIT cell instead of through it using flipper mirrors in the beam path. We can also compare the measured noise levels to the shot noise by completely blocking the squeezed vacuum state, thereby replacing it with normal vacuum which combines with the LO.

To facilitate EIT, we split the power of the strong laser field from the output of the squeezer and use part of it as the EIT control field, which overlaps and propagates almost colinearly with the squeezed vacuum through the EIT vapor cell. The quarter-wave plates on either side of the EIT cell are used to convert the polarizations of the squeezed and control light fields to circular orthogonal polarizations while traveling through the EIT cell, and then back to linear after the cell. We then separate the squeezed beam from the control with two polarizing beam splitters (PBS) to improve polarization separation, and send it to the homodyne detector. To further reduce the EIT control field influence, we introduced a slight angular misalignment between the beams so most of the control field misses our photodiodes and thus does not introduce large background light levels. Since the circularly-polarized control field is very strong, it optically pumps most of the atoms into the F=2, m_F=-2 ground sublevel, and effectively creates a single Λ configuration with the squeezed field and Zeeman sublevels of Rb (see insert in Fig. 10.2).

To characterize an EIT resonance, we send a weak coherent probe field (instead of a squeezed field) into the EIT cell by introducing a half-wave plate after the squeezer. Since the EIT signal depends on the two-photon detuning, we sweep this detuning. This is accomplished by two different, but essentially equivalent methods. In first case, we change the detuning of the control field with two acousto-optical modulators (AOMs), taking the negative and positive first order beams, shifted by -80 MHz and $80 + \delta$ MHz respectively. The resulting control field is detuned from the probe by δ, and we have full control over the two-photon detuning. We find that due to the AC-Stark shift induced by the control field, the EIT resonance is centered around 900 kHz two-photon detuning and we were not able to fully filter the control field out, resulting in a large beatnote resonance between the LO and the control field on our noise spectrum. We removed points around this resonance from our noise spectra (see Fig. 10.3(b)). For subsequent measurements, we used a second method of sweeping the EIT resonance. With the AOMs, we detuned the control field by 5 MHz and additionally introduced a magnetic field in the direction of light propagation in the EIT cell to compensate for this detuning shift. A calibrated sweep of this magnetic field corresponds to a change of the two-photon detuning. With this method, the LO-control field beatnote was placed outside of our detection band which improves the measured noise spectra by removing the large resonant peak (see spectra in Figs. 10.4(b) and 10.5(b)).

During the noise EIT filter measurements, we fixed the two-photon detuning δ on top of the EIT resonance, and the overall shape of the transmission resonance versus two-photon detuning is shown with respect to this fixed detuning (see Figs. 10.3(a), 10.4(a), and 10.5(a)). In this case, positive and negative frequency transmissions reflect the absolute value of $\mathcal{T}(\pm\Omega)$ in equation 10.3; i.e. we directly measure $T_\pm$. We fit the transmission measurements to the following empirical function suggested in Ref [141].

$$T_\pm = A\frac{\Gamma^2}{\Gamma^2 + (\delta_0 \pm \Omega)^2} + B\frac{\Gamma(\delta_0 \pm \Omega)}{\Gamma^2 + (\delta_0 \pm \Omega)^2} + C \tag{10.6}$$

Here, the first and second terms are the symmetric and anti-symmetric Lorentzian and the last constant term represents residual absorption of the light due to incoherent processes; Γ is the effective half-width half-maximum of the resonance; δ_0 is the shift of the EIT resonance with respect to the squeezed vacuum field (essentially zero, as we keep the two-photon detuning on top of the EIT resonance); A, B, and C are the fitting parameters. Once we have the numerical expression for $T_\pm$, we input these transmission coefficients into equation 10.4 to predict the output noise level. We did not measure the sideband phase lag $\Theta_\pm$ in our experiments, and so neglected the squeezing angle rotation in our calculations.

10.3.2 Filtering observations

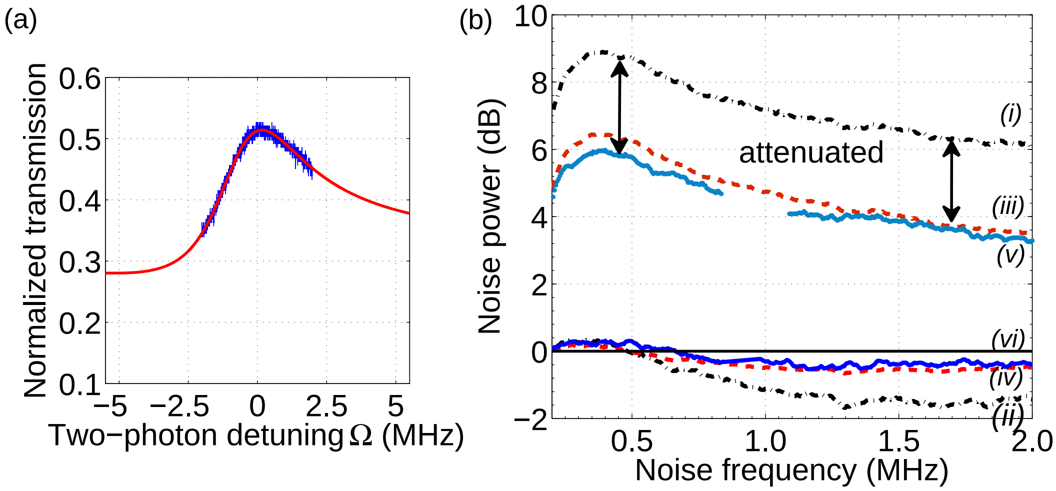

FIG. 10.3: (a) EIT lineshape: Solid line shows fit. Peak transmission= 52%, FWHM= 4 MHz, control power= 4.2 mW, EIT cell temperature T_{EIT}= 46° C. (b) Quadratures noise power spectra. (i) input max. noise, (ii) input min. noise, (iii) expected max. noise, (iv) expected min. noise, (v) measured max. noise, (vi) measured min. noise. Squeezer pump power= 21.6 mW, squeezing cell temperature T_{sq}= 59° C. We removed data points in the output noise between 0.8 and 1.1 MHz due to a large spike caused by the beatnote between the local oscillator and the control field which was detuned by 900 kHz and leaked into the detection.

The influence of the atomic medium on the squeezed vacuum state can be observed by comparing the input minimum and maximum noise levels to the levels measured after interaction. By attenuating the control field and thus decreasing the power broadening of the EIT resonance, or by slightly changing the control field alignment, we can narrow the EIT linewidth and change the transmission window used in the experiment. As an example of squeeze amplitude attenuation, we show two noise spectra and their associated EIT transmission curves in Figs. 10.3 and 10.4. In Fig. 10.3(b), we start off with a squeezed vacuum showing up to -1.5 dB noise suppression and nearly 9 dB of excess, antisqueezed noise. Any frequency dependence of the input noise levels, we attribute to laser noise which was not completely subtracted by the balanced photodiodes (see discussion in section 6.5). This prevents us from detecting the best squeezing at the lowest noise frequencies.

For the first measurement, we make the transmission curve rather broad, with full-width half-maximum (FWHM) of the resonance greater than 4 MHz (see Fig. 10.3(a)), and with a fairly small contrast between the peak transmission of 52% and the background transmission of 28%. As a result, in Fig. 10.3(b), the output noise levels are uniformly attenuated due to the light absorption, but there is no visible frequency-dependent filtering of the noise, since in the detection bandwidth of 2 MHz, transmission for all sidebands is almost the same. We also calculate the expected filtered noise spectra based on equation 10.4 and transmission coefficients ($T_\pm$) extracted from the fit of the EIT transmission data (Fig. 10.3(a)). We see a very good match between the theoretical prediction and the experimental data. The output noise follows along the same shape as the input noise close to the predicted noise levels, without changes in its frequency-dependence. We removed data points in the output noise between 0.8 and 1.1 MHz due to a large spike caused by the beatnote between the local oscillator and the control field, which was detuned by 900 kHz and leaked into the detection.

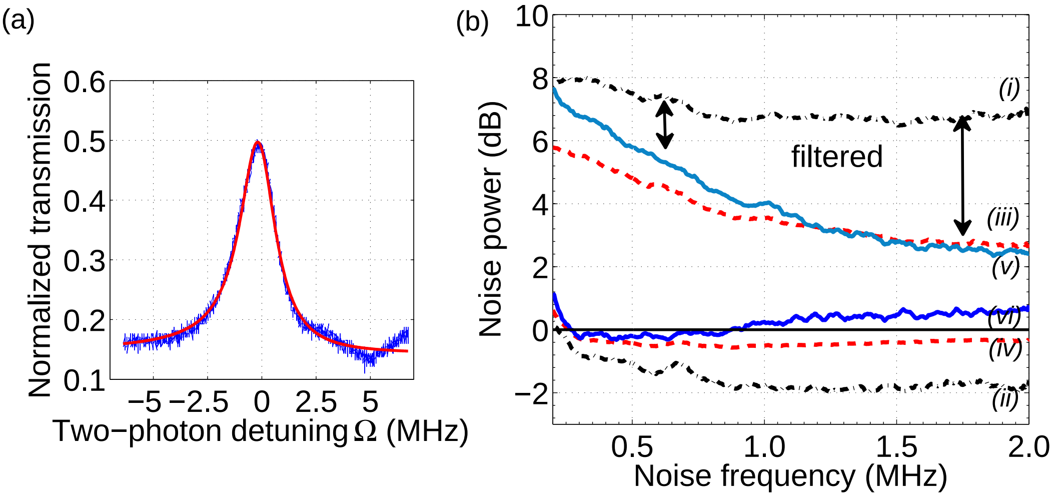

FIG. 10.4: (a) EIT lineshape: Solid line shows fit. Peak transmission= 50%, FWHM= 2 MHz, control power= 3.8 mW, EIT cell temperature T_{EIT}= 50° C. (b) Quadratures noise power spectra. (i) input max. noise, (ii) input min. noise, (iii) expected max. noise, (iv) expected min. noise, (v) measured max. noise, (vi) measured min. noise. Squeezer pump power=13 mW, squeezing cell temperature T_{sq}= 57° C.

Note the difference in Fig. 10.4. Here, as shown in Fig. 10.4(a), we narrow the EIT transmission window to about 2 MHz FWHM and increase the contrast between maximum and background transmission. Now, with similar input squeezed (-2 dB) and antisqueezed (8 dB) noise levels, the output noise shows marked frequency dependence. At lower frequencies where transmission is at a maximum, the output noise levels are closer to the inputs, but at higher frequencies, we see more and more attenuation due to the light absorption at the wings of the EIT resonance. This data set shows the simple use of the EIT window as a low-pass filter. The effects of the filter are most easily observed in the antisqueezed noise quadrature due to the high amplitude, starting with 8 dB of excess noise. The squeezed quadrature also appears to follow the shape of the filter, but due to extra noise raising the noise floor, this minimum level rises above shot noise rather than settling closer to it.

We attribute this extra noise to the several potential sources. First, our numerical prediction model assumes that there is no squeezing angle rotation influencing the noise in Figs. 10.3 and 10.4. This is clearly an oversimplification, because a small visible asymmetry of the EIT resonance in Fig. 10.4 dictates, according to the Kramers-Kronig relations, that some frequency-dependent rotation should be present, which may show up as a deviation from the predicted noise levels. A second possibility is the simplicity of our model, which treats the EIT resonance as a passive absorptive filter and disregards the back action of light noise onto the atoms as well as the atomic noise contribution. This simple approach may be successful up to a point, but could lead to deviations from experiment when excess noise contributions become sizable. We note that in this experiment, the noise level resulting from blocking the squeezed probe before the EIT cell was identical to that seen when the probe was blocked after the atoms and just before detection (shot noise). This leads us to believe the atomic noise contribution is small in this case, and that most of the excess noise must then be due to back action of the light noise. Lastly, as mentioned, any laser noise which is imperfectly balanced by the homodyne detector can raise the noise floor and add apparent frequency dependence.

Fig. 10.5 depicts a very interesting effect which appears to be frequency-dependent squeeze angle rotation. Here, because of the asymmetry of the EIT lineshape, there is a resulting phase shift between the left and right noise sidebands leading to a rotation of the squeezing angle, which now changes with frequency. We see that the LO phase chosen for the best noise suppression at one noise frequency, is not the phase giving the

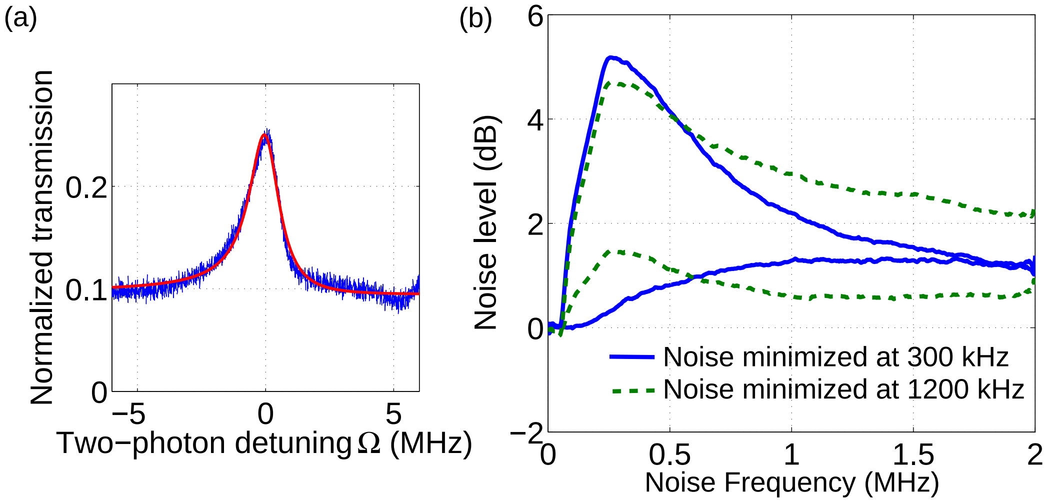

FIG. 10.5: (a) EIT lineshape: Solid line shows fit. Peak transmission= 25%, FWHM= 1.4 MHz, control power= 2.3 mW, EIT cell temperature T_{EIT}= 50° C. (b) Quadratures noise power spectra: with noise power minimization at 300 kHz (solid-blue line) and at 1.2 MHz (dashed-green line). Squeezer pump power=15 mW, squeezing cell temperature T_{sq}= 57° C.

minimum noise level at all frequencies. This indicates that the squeezing angle has actually become frequency-dependent: as it rotates with frequency, it requires different phases for different noise frequencies in order to measure the maximum squeezing. Note that the noise spectrum resulting from choosing the proper phase at a lower frequency (300 kHz), looks very different from the result when the minimum noise is found by choosing the phase angle at a higher noise frequency (1200 kHz).

To the best of our knowledge, this is first reported measurement of the squeezing angle rotation done with atoms which was previously theoretically predicted in Ref. [140]. Until now the only successfully reported way to rotate the squeezing angle was with cavities [139]. Unfortunately, our data has a lot of excess noise and sub-shot-noise reduction did not survive after the passage through EIT.

We note that for experimental conditions corresponding to Figs. 10.3 and 10.4, we did not observe such rotation. Here the squeezing angle seems to show good frequency independence. The difference in Fig. 10.5 is unclear, as the EIT asymmetry does not look drastically different. It is possible that sources of excess noise that are not well-understood, in some way contribute to this apparent squeezing angle rotation.

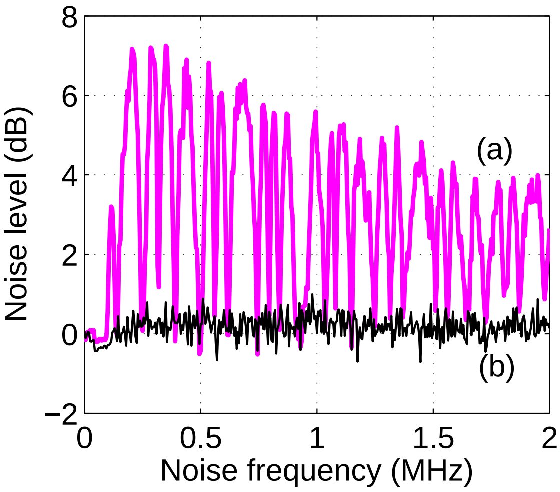

FIG. 10.6: Noise power spectrum with control field set to 6.9 mW (a) and blocked (b). LO phase angle is continuously scanned.

We also demonstrate the capability to completely replace the squeezed state with unsqueezed ordinary coherent vacuum state by changing the EIT media to a strong absorber by switching off the control field. Fig. 10.6, shows the output noise levels of the quantum state after the EIT filtering cell, first (a), while the control field is on and we sweep the local oscillator phase while recording the noise spectrum, and second (b), in the same situation but with the control beam completely blocked. Note that while the control beam is on, we see high phase-dependent noise levels and the squeezed vacuum is transmitted through the atoms. However, with the control off, we do not have EIT conditions and our vacuum state is absorbed by the atoms. Thus, the output noise level corresponds to shot noise, identical to the noise spectrum generated by blocking the squeezed path just before the BPD. As expected, the quantum noise is not transmitted through the atomic medium, so the noise level returns to shot noise and does not depend on the LO phase. Such a switchable filter can be of interest for quantum repeaters and quantum memory protocols.

While these experiments using Zeeman EIT have demonstrated filtering capabilities of the Rb atoms, we are limited by peak transmissions of only 50% and extra noise which enters the system due to unknown processes within the EIT cell. This makes it difficult to preserve a measurable amount of quadrature noise reduction at the ouput of the second vapor cell.

10.4 Hyperfine EIT

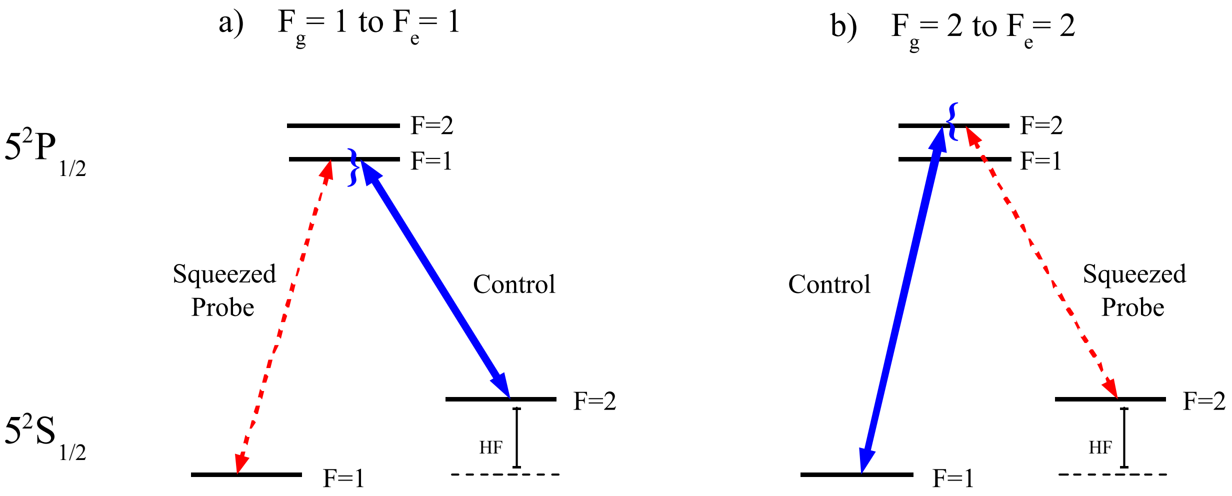

FIG. 10.7: Energy level diagrams for hyperfine EIT. (a) Probe laser on $F_g = 1 \rightarrow F_e = 1$. (b) Probe laser on $F_g = 2 \rightarrow F_e = 2$.

Next, we demonstrate results using an alternate energy level configuration in which EIT is observed with the use of two hyperfine ground states of ^{87}Rb. We investigate tuning the squeezed probe light in resonance with either the $F_g = 1 \rightarrow F_e = 1$ or $F_g = 2 \rightarrow F_e = 2$ transitions as shown in Fig. 10.7. These transitions can be accessed by detuning the control field farther from the carrier frequency of the squeezed vacuum so that the frequency difference matches the hyperfine splitting (6.834 GHz). This allows us to probe a slightly different interaction from the previous experiment, and gives us more flexibility in the possible EIT windows, at the cost of increased complexity of the experiment. EIT can be realized either with the probe and control beam both linearly polarized and perpendicular to each other ($lin \perp lin$), or using two opposite circular polarizations. While both configurations were studied, the results of this section were obtained using $lin \perp lin$ fields where the peak transmission of the atoms was higher.

10.4.1 Hyperfine experimental setup

The initial experimental setup used for EIT filtering was nearly identical to the Zeeman EIT filtering setup shown in Fig. 10.2. The main difference is the origin of the control laser field, which must now be detuned from the squeezing frequency by 6.834 GHz, the ground state hyperfine splitting of ^{87}Rb. The available AOMs are insufficient for this purpose, and so instead, we make use of an electro-optic modulator (EOM) that can modulate at the required frequency. To maintain phase coherence, we passed a portion of the original pump laser through the EOM to create sidebands at modulation frequencies of ± 6.754 GHz, after which the beam passed through an etalon to transmit only one of the sidebands while reflecting the other sideband and carrier. The etalon temperature could be tuned to transmit either the red-shifted or blue-shifted sideband, depending on the transition being probed. To generate the required control power, this field was injection-locked into a slave laser (JDSU SDL-5431-G1 laser diode) which could output tens of milliwatts of power. The output of the slave was then shifted by an additional 80 MHz using an AOM giving the desired detuning of 6.834 GHz, and the beam was cleaned with a single-mode fiber and directed through the EIT cell, overlapping the probe. The EIT transmission of the medium can then be measured by sweeping the EOM modulation around the hyperfine splitting, and the control power can be changed to affect the linewidth and transmission of the transparency window.

The noise levels of the squeezed light probe after traveling through the EIT medium are again compared to those recorded when the beam bypasses the Rb cell. However, in this configuration, we could not obtain meaningful EIT filtering results because of an interesting extra interaction of the light beams with the atoms, which brings a large amount of excess noise into the system.

10.4.2 Undesirable excess phase-dependent noise

We initially sought filtering results from the hyperfine interaction similar to Fig. 10.4, and measured noise power noise spectra on the $F_g = 1 \rightarrow F_e = 1$ transition with high peak transmission. However, for a given EIT transmission, where most phase-dependent noise should be absorbed and filtered above 250 kHz, we instead observed large broadband phase-dependent noise (Fig. 10.8(c,d)). This occurred when the EIT window was centered at 0 Hz detection frequency, and showed no frequency dependence in the noise transmission as is expected from the atomic filter. The natural question arose if this noise was influenced by the excess quadrature noise produced in the squeezing cell, and modified by the atoms in the EIT cell, or was due to an independent mechanism. To investigate the source of this noise, we inserted a PBS after the squeezing vapor cell in the probe beam path, so that the squeezed vacuum polarization was rejected and replaced with coherent vacuum. In this case, where we expected only shot noise with no phase-dependence, we again observed the extra phase-dependent noise at the output of the EIT cell. This confirmed that the origin of the extra noise was independent of the quantum state of the input field, but while present, this noise source will obscure any quantum noise measurements. Examples of this effect for both coherent and squeezed probes are shown in Fig. 10.8. We can gain many insights into the source of this extra noise from this figure. We show the noise measurements for both a coherent vacuum probe (a, b), with the PBS inserted after the squeezing cell, and for a squeezed vacuum probe (c, d) without the PBS. These measurements were taken at different EIT cell temperatures to change the atomic density of Rb. While using the coherent probe, the atomic medium should be probed with normal vacuum, and we expect to detect only shot noise. While the detected noise is close to shot noise at low atomic densities (Fig. 10.8(a)), a phase-dependence can still be seen, and this noise is greatly amplified at high atomic densities (Fig. 10.8(b)). The density dependence of this noise is shown in more detail in Fig. 10.9.

This led us to discover that the probe beam being sent into the EIT cell was not

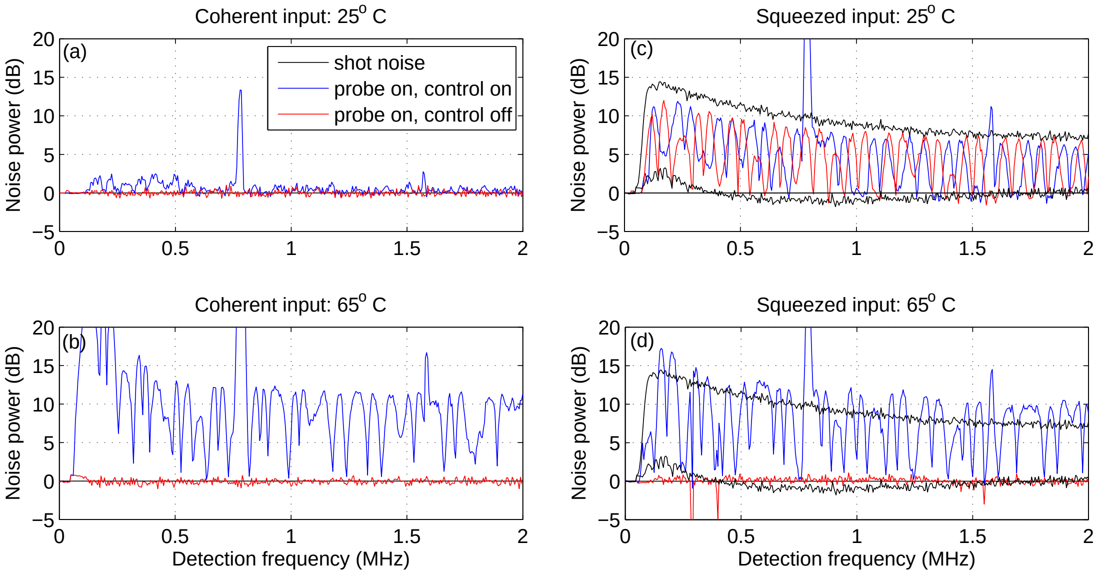

FIG. 10.8: Noise power vs detection frequency after interaction with the EIT vapor cell. (a) Coherent probe at 25°. (b) Coherent probe at 65°. (c) Squeezed probe at 25°. (d) Squeezed probe at 65°. Input minimum and maximum noise levels shown in black (c, d). The coherent probe uses a PBS to block the squeezed vacuum polarization. RBW=10 kHz, VBW=30 Hz. Local oscillator phase is scanning. Probe on $F_g = 1 \rightarrow F_e = 1$.

truly a vacuum or squeezed vacuum. When the vacuum probe is separated from the strong squeezing pump polarization (LO), due to a limited extinction ratio of the PBS, coherent photons of the pump field in the orthogonal polarization leak into the probe field. It is evident that this leaked field, though small ($\sim$4.5 μW), contributes to the phase-dependent noise seen, because when the probe is blocked entirely with an opaque object, shot noise is again measured. The amplitude of this noise is also found to depend on the amount of leakage light which is present in the probe field as seen in Fig. 10.10, further verifying that the leaked light contributes to the phase-dependent noise. These results were found by using a weak coherent probe, and changing its power using neutral density filters. This leakage polarization, however, is not easy to remove completely from the probe field without degrading the squeezed vacuum state. Also, the influence of these coherent photons is interesting, because coherent photons alone should not display phase-dependent noise, and the double modulation (EOM and AOM) of the control field prohibits

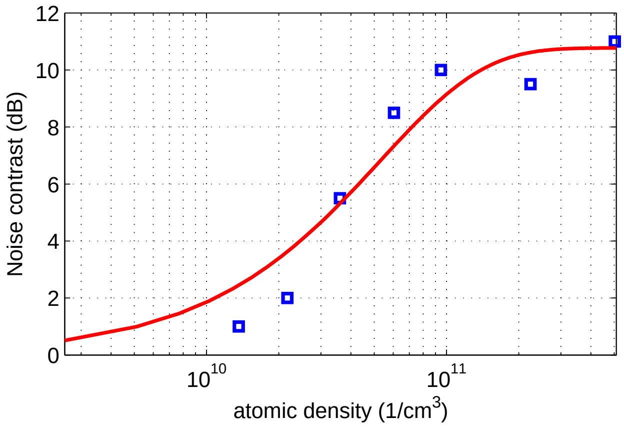

FIG. 10.9: Average excess noise contrast (max - min) vs atomic density. $F_g = 1 \rightarrow F_e = 1$ transition. The exponential fit is to guide the eye.

any overlap in control and probe frequencies which could lead to beatnotes in the noise spectrum. As seen in Fig. 10.8, this noise is only detected when both the probe field and the control field are present, and with the control off, the noise recorded is at the level of shot noise. (The only exception is in (c), where due to the low atomic density, the squeezed probe is not absorbed by the atoms, and so phase-dependent noise from the quantum state is seen. In the case of the squeezed probe, the noise levels observed with the control beam off were consistent with the resonant Rb absorption.) Also, because the amount of noise at the output of the EIT cell is shown to be dependent on atomic density, its source must come from an interaction of the control field, probe leakage, and the atoms.

These observations lead us to speculate that a four-wave mixing process in the Rb EIT cell may be responsible for the observed phase-dependent noise. This is consistent with the fact that the amplitude of noise clearly depends on the atomic density of Rb. The leakage photons in the probe field may be seeding a 4WM process when combined with the control field in the atomic medium. We saw other signs of 4WM, such as transmission gains and antisymmetric lineshapes, while measuring the vapor transmission in some arrangements of this experiment at high atomic densities.

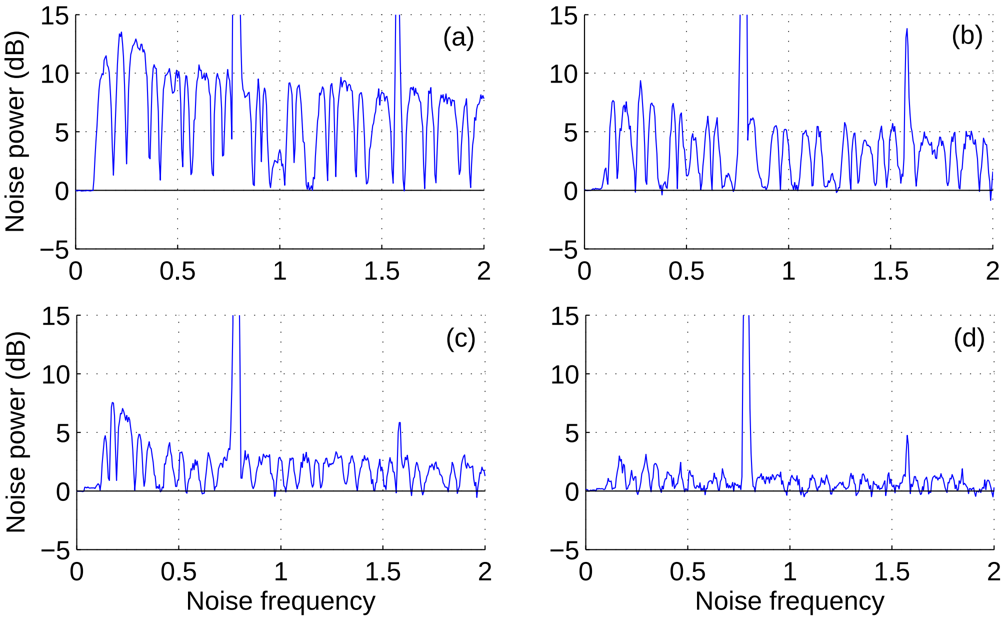

FIG. 10.10: Noise power vs detection frequency at several probe leakage powers. Leakage probe power is approximately (a) 4.3 μW, (b) 1.6 μW, (c) 0.6 μW,(d) 0.2 μW. $F_g = 1 \rightarrow F_e = 1$. T_{EIT}=55° C.

10.4.3 Hyperfine filtering observations

This source of noise, whether it is caused by 4WM or a different process, can cause significant problems in squeezing experiments and quantum noise measurements and warrants further study. It would appear that when this noise is present, it will combine with the phase-dependent noise of the quantum squeezed state and obscure any meaningful results. Care should be taken to achieve the best possible polarization separation so that coherent photons do not leak into the squeezed vacuum field.

Due to the exact mechanism behind it, the excess phase-dependent noise did not seem to be a problem for the case of Zeeman EIT reported previously. For hyperfine EIT filtering, we opted to avoid this noise source by altering the experimental setup. The arrangement used to obtain the results below is shown in Fig. 10.11. Because the necessary polarization purity was not achieved using the reflected port of a PBS, we chose to switch the polarizations of the pump and vacuum to instead transmit the squeezed vacuum field through a high quality Glan polarizer (GP). The 95% transmission of the polarizer slightly degrades the squeezing levels, but keeps leakage of the wrong polarization to a minimum ($\sim$0.2 μW). This means we also have to split the LO from the original laser field before the squeezing cell, but care is taken to ensure good mode-matching of the beams at detection (97-98% visibility). In addition, we switched our studies to the $F_g = 2 \rightarrow F_e = 2$ transition, because the laser detuning resulting in high EIT peak transmissions near the $F_g = 1 \rightarrow F_e = 1$ transition, unfortunately did not coincide with detunigs favorable for high levels of noise reduction. Using this new arrangement, we are able to eliminate most of the excess phase-dependent noise and observe EIT filtering. An example is shown in Fig. 10.12. Notice that the antisqueezed noise appears to be filtered, and roughly matches the EIT transmission window of 240 kHz (FWHM). The filtering was also observed to change according to the EIT width when we altered the control laser power. However, the noise reduction of the minimum noise quadrature did not survive at the output of the EIT Rb cell. This is likely due to atomic interactions and back action noise in the vapor cell, with possible contributions from the extra noise source described above, resulting from the (now less prevalent) leaked photons from the strong light polarization. By purposely misaligning the GP to add extra light power to the probe beam, we again see a large amount of extra noise coupling into the system and far exceeding the input quadrature noise levels (Fig. 10.12 top curve). Also, the peak

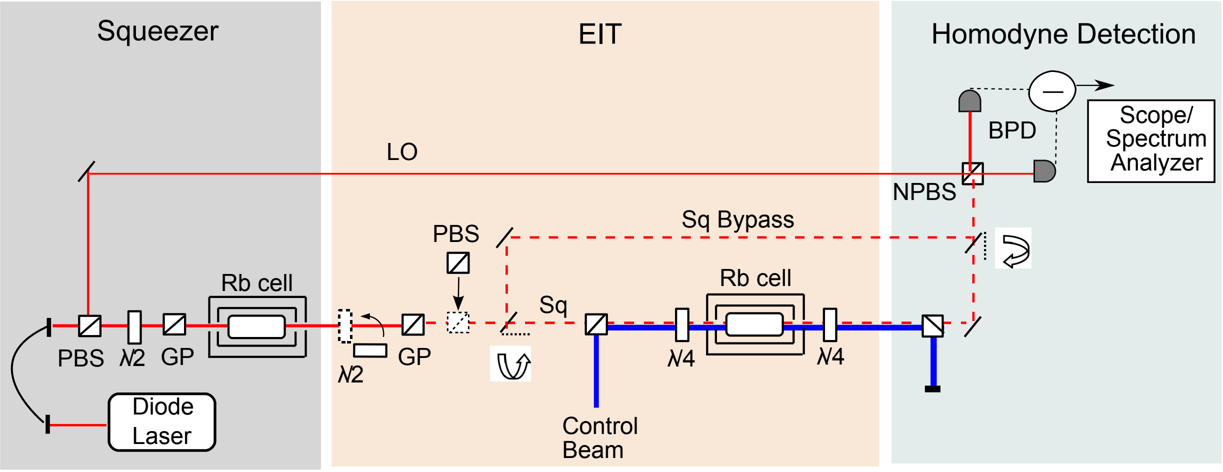

FIG. 10.11: Modified EIT filtering experimental setup.

transmission in this EIT configuration was comparably low ($< 35\%$). Unfortunately, for laser detunings displaying the highest EIT transmissions, such as red-detuned from the $F_g = 1 \rightarrow F_e = 1$ resonance, squeezed light below shot noise levels was not generated (see Fig. 6.4), and the medium was more susceptible to nonlinear processes at high optical depths. Further experiments may be needed to locate a parameter space where EIT transmission and quantum noise reduction are simultaneously optimized.

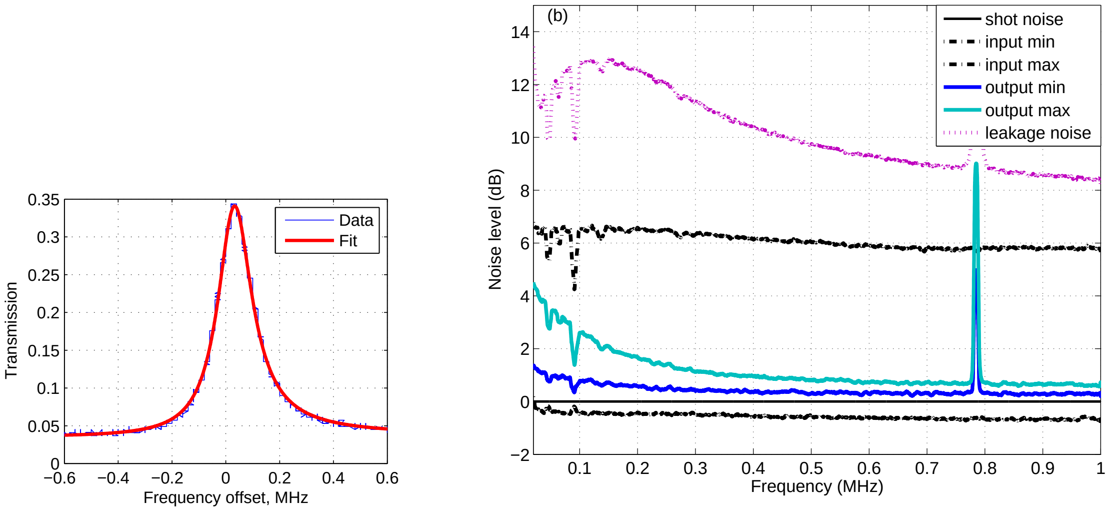

FIG. 10.12: (a) EIT transmission: Peak=34%, FWHM=155 kHz. (b) Noise power vs detection frequency after EIT interaction. Shot noise is 0 dB. Shown are the input min. and max. noise (black dotted), the output min. and max. noise (solid blue), and the output max. noise when about 2 μW of the wrong polarization is added to the probe beam (dotted pink). $F_g = 2 \rightarrow F_e = 2$ transition.

10.4.4 Noninvasive EIT probe

Finally, we introduce a slightly different type of filter where the EIT transparency window is detuned from the squeezed probe carrier frequency ω_0. This shows how this experimental setup can also be used in the area of noninvasive measurements. It was demonstrated in Ref. [58] that squeezed vacuum could be used to measure the cavity parameters of an optical cavity, while using states with very few photons. Here, we demonstrate a similar procedure to measure the transmission of an EIT medium by looking at changes in the noise of a squeezed vacuum state injected into the atomic vapor.

This interaction of squeezed light with atomic vapor is an extension of the EIT filtering and squeezing angle rotation described in the previous sections. When the EIT window is centered on the carrier frequency (ω_0), the positive and negative correlated sidebands of the squeezed light ($\omega_0 \pm \Omega$) are attenuated by equal amounts (for a symmetric lineshape) due to the EIT absorption, leading to the atomic medium acting as a low-pass filter. Now, if we offset the EIT window away from ω_0, those photons falling within the transparency window will be transmitted, while their correlated partner photons will be outside the window and completely absorbed. This will destroy the correlations between the photons, and lead to excess quantum noise only within the transparency window, and shot noise outside of it. The noise in this case shows no phase-dependence, which arises from interference of the local oscillator with positive and negative noise sidebands. The resulting excess noise can be understood by considering equation 10.4 and setting T_- to zero. In this case, A_- is no longer zero (as in the case of symmetric transmission), and additional noise results in $V1_{out}$ and $V2_{out}$.

In Fig. 10.13, we set up an asymmetric EIT resonance, with the probe tuned to the $F_g = 1 \rightarrow F_e = 1$ transition, and detune the control frequency away from the two-photon resonance with ω_0 by ±1.3 MHz. Upon probing the medium with our squeezed vacuum beam, we measure the noise spectra seen in Fig. 10.13(b) and (c). Note that the transmission shape of the EIT window is reproduced in the noise spectrum of the quantum probe. For the negative two-photon detuning, the observed shape is reversed because now the negative noise sideband is transmitted.

Another example is shown in Fig. 10.14. Here, the probe is tuned to the $F_g = 2 \rightarrow F_e = 2$ transition and the control field is detuned from the two-photon resonance by 500 kHz. Noise spectra of the output vacuum states are shown for the case of three control powers, and thus three EIT widths. The noise traces clearly change in response to a narrowing EIT window. By fitting the peaks to a Lorentzian shape (Eq. 10.6), we find that the EIT widths measured in the noise spectra agree with those recorded using the intensity of a coherent weak probe to within 5%.

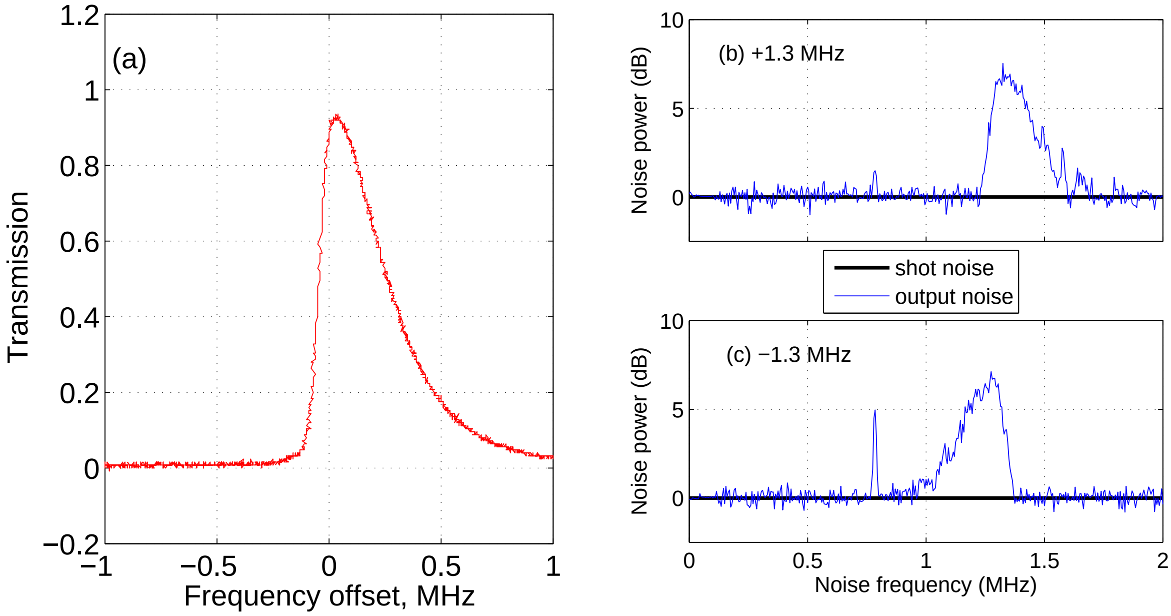

FIG. 10.13: (a) EIT transparency window. Lineshape recorded using 10 μW coherent probe and measuring light intensity. (b, c) Noise spectrum from squeezed vacuum probe, EIT detuned (b) +1.3 MHz and (c) −1.3 MHz. Squeezed vacuum is produced at ω_0 which is in resonance with the $F_g = 1 \rightarrow F_e = 1$ transition.

It is important to note that in these measurements, we are making use only of noise above the shot noise level, resulting from the loss of sideband correlations. This application, then, is not technically quantum-limited, and it could in principle be carried out with classically noisy light. However, squeezed light allows for higher signal contrasts and less photons in the noninvasive measurement. A similar technique is used by Lett *et al.* in Ref. [142] to extract spatial information from an object using the correlations in squeezed twin beams.

10.5 EIT noise filtering summary

We have shown an experimental demonstration of EIT frequency-dependent squeeze amplitude attenuation of a quantum squeezed vacuum field using only atomic vapors. In our experiments, the atoms act as a low-pass filter for squeezed and antisqueezed noise. By detuning this EIT window away from the carrier frequency, we can also reconstruct

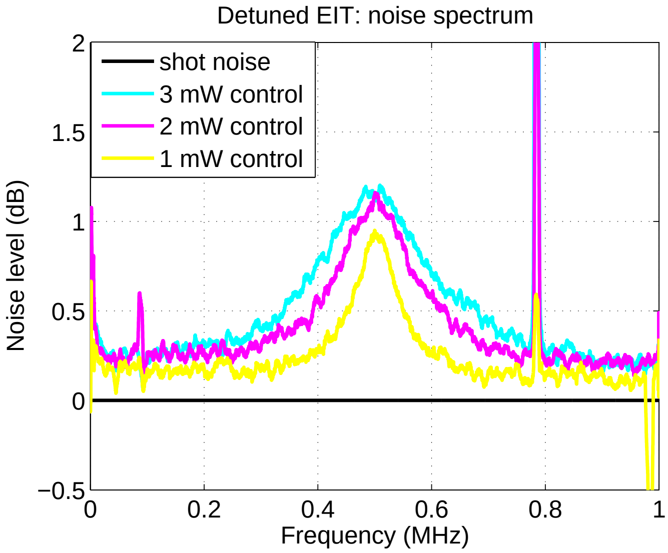

FIG. 10.14: Noise spectrum for detuned EIT with three control powers: 3, 2, and 1 mW. EIT widths (FWHM) are 240, 150, and 90 kHz respectively.

the transmission lineshape of the medium in the excess noise of the light. The relative ease of controlling the transmission window in vapor cell experiments makes this method promising for creating several different types of noise filters for squeezed vacuum. This controllable squeezed vacuum source may be easily incorporated into precision measurement experiments due to its simple, all-atomic design, and low loss.

We also observe an apparent frequency-dependent rotation of the squeezing angle as the vacuum propagates through EIT. This effect is likely due to the asymmetry of the transmission window and could also be used to create more complicated quantum-noise shapers. This type of interaction is desirable for applications like LIGO, to rotate the squeezing angle with frequency for noise reduction at all detection frequencies [140], though the color of light used in gravitational wave interferometry is different.

We note the less well-understood excess noise sources which couple into this experiment and degrade the noise suppression. Spontaneous emission and back action are likely sources of excess noise which make it difficult to preserve sub-shot-noise characteristics of the light after interaction with the vapor. We also analyze a complex source of excess phase-dependent noise, present for the case of a hyperfine EIT interaction. This noise is found to originate from an unknown atomic interaction involving the control beam and the leakage photons in the probe channel within the Rb vapor. This process is likely a four-wave mixing effect seeded by the leakage of coherent light into the probe beam, and can be suppressed by reducing this leakage. The contribution of these noise sources cannot be explained by simple treatment of the EIT resonance as a media with complex transmission coefficients. A full quantum mechanical treatment of the light-atom interaction would be needed to fully describe the situation. These dynamics of quantum noise propagation, along with any excess noise sources, will be important to any precision optical measurement or quantum memory experiment that uses the interaction of quantum states of light with resonant atomic media.

CHAPTER 11

PSR and quadrature noise studies in cold atomic vapor

It is predicted that high levels of PSR squeezing can be obtained using cold Rb atoms, in a Doppler-free region where sharp peaks in the noise spectrum can be exploited [72]. Polarization-squeezed light has previously been generated by Josse *et al.* via the Kerr effect in cold cesium atoms in a cavity [85]. Here we highlight our studies [143, 144] of the PSR effect and the quadrature noise of laser light traveling through a cold sample of ^{87}Rb held in a magneto-optical trap (MOT). Several experimental challenges arise when working with cold atoms, such as a non-zero magnetic field. We present clear evidence for PSR as well as phase-dependent quantum noise which results from the light's interaction with the cold atomic medium. These results are compared with theoretical predictions and with similar effects seen in hot atomic vapor cells.

11.1 Polarization rotation in cold ^{87}Rb atoms

We first study the polarization rotation due to the Rb atoms. The highest rotation may lead to the highest potential for noise suppression. As can be seen from equation

3.2 for the self-rotation angle, the amount of rotation will depend on three main factors: (1) the rotation will increase with increasing laser intensity, (2) the amount and direction of rotation will depend on the initial ellipticity ϵ, and (3) the strength and direction of rotation will both depend on the laser detuning from the atomic resonances.

11.1.1 Experimental setup

To measure the angle of rotation, a simple balanced detection scheme is used to observe the changes in polarization of the light with respect to a fixed axis. A schematic diagram of the experimental arrangement is shown in Fig. 11.1. The rubidium atom trap is set up in a standard six beam magneto optical trapping configuration. This trap, and associated diagnostics, has been described in detail in Ref. [145]. In the arrangement, light from an external cavity diode laser delivers a total power of $\approx$ 20 mW to the atomic sample. This trapping laser is spectrally detuned 18 MHz below the $F_g = 2 \rightarrow F_e = 3$ ^{87}Rb D$_2$ hyperfine transition. A weaker repumper laser having a power of $\approx$ 3 mW is tuned to resonance with the $F_g = 1 \rightarrow F_e = 2$ D$_2$ transition, thus maintaining most of the atomic population in the $5^2S_{1/2}$, $F = 2$ ground state. A level scheme with the different laser frequencies used is shown in Fig. 11.2. Absorption imaging of the sample shows that it contains about 7×10^7 ^{87}Rb atoms. Ballistic expansion measurements give a typical temperature of 300 μK for the atom sample. The sample is well-described as a sphere with a spatially Gaussian atom distribution having a Gaussian radius of about 500 μm. The sample has a peak density of about 7×10^9 atoms/cm^3 and an optical density on the order of 2 for the transitions of this study. The trap magnetic field gradient is variable, with a typical value of 5 G/cm. Application of the MOT and repumper lasers to the sample is manipulated by computer switched acousto-optical modulators (AOMs). In most measurements, the trapping beams were turned off while the probe was on. The repumping laser and the trap magnetic field were left on continuously. Turning the trapping beams off during the measurement results in the expansion of the atomic cloud, with its radius growing at an approximate ballistic

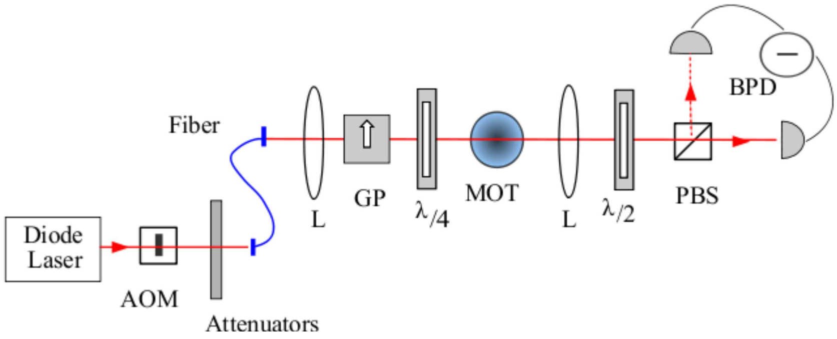

FIG. 11.1: Schematic diagram of the experimental arrangement.

rate of 200 $\frac{\mu m}{ms}$. An external cavity diode laser tuned to the ^{87}Rb D_1 line ($\lambda \sim 795$ nm) serves as the probe beam. The probe frequency is scanned across the $F_g = 2 \rightarrow F_e = 1$ and $F_g = 2 \rightarrow F_e = 2$ hyperfine transitions and monitored with a wavemeter. An AOM is used for fast switching of the probe beam, while neutral density filters are used for power attenuation. The light beam is launched into a single-mode optical fiber to achieve a high quality and nearly Gaussian output beam intensity distribution. The fiber output passes through a high quality Glan polarizer (GP) to ensure linear polarization and a quarter-wave plate to control the ellipticity. We use a pair of lenses (L) to focus the driving laser in the interaction region to a beam diameter of around 250 μm ($1/e$ intensity level). The Rb cloud is larger than the beam diameter and serves as a reservoir of cold atoms during the experiment. Maximum available probe beam power is ≈ 10 mW.

Once the probe laser exits the MOT chamber, a half-wave plate sets the probe beam light polarization angle to 45° with respect to a polarizing beam splitter (PBS) which then separates two orthogonal components. These two beams are then directed to a custom built balanced photodetector (BPD) where the signals from the two polarization components are subtracted. Rotating the quarter-wave plate before the MOT to control the ellipticity also changes the angle of the major polarization axis of the beam; the half-wave plate is adjusted to bring this angle back to 45° by zeroing the balanced signal in the absence of the atomic sample. As a consequence of this, any imbalance of the orthogonal polarization components is due to rotation of the polarization ellipse caused by the atoms. The rotation

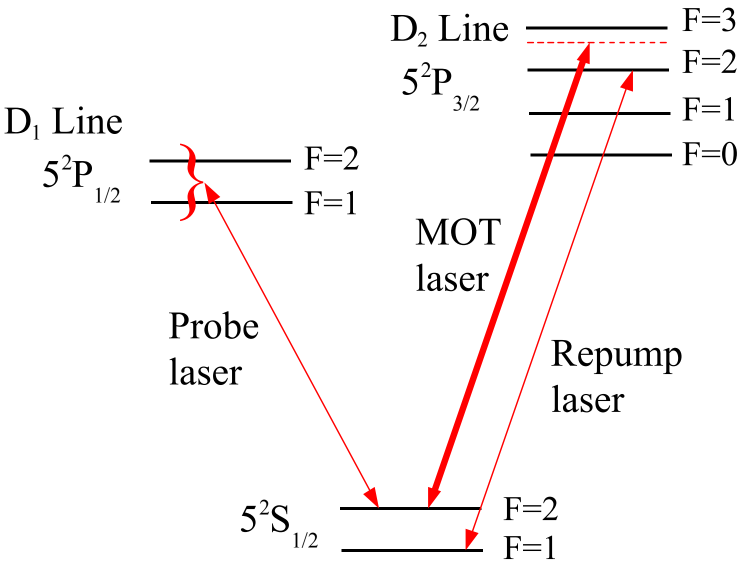

FIG. 11.2: Partial diagram of the ^{87}Rb levels scheme indicating the trapping and probe transitions.

angle is proportional to the subtracted signal according the expression:

$$\frac{I_1-I_2}{I_1+I_2} = \sin^2(\frac{\pi}{4}+\varphi) - \cos^2(\frac{\pi}{4}+\varphi) = \sin(2\varphi) \simeq 2\varphi \qquad (11.1)$$

where I_1 and I_2 are the intensities incident upon the two photodetectors and φ is the rotation angle in radians.

11.1.2 Experimental results

In the experiments, we investigated the angle of rotation due to PSR under a variety of different conditions to explore a large zone of experimental parameter space. We first sought the best conditions of the MOT for the largest obtainable self-rotation. This included the presence or absence of the trapping laser beam, the repumping beam, and the MOT gradient magnetic field. We then varied the initial ellipticity of the probe laser to confirm the presence of polarization self-rotation. Following this, the laser power was varied while holding the initial ellipticity and laser detuning fixed. To investigate the effect of laser detuning, we measured the rotation at a number of probe frequencies ranging over two GHz and compared these results with theoretical predictions. These measurements were all taken as a function of time. This permitted us to observe the effects on rotation of the MOT expansion and light-induced atomic motion.

Sample Preparation and Initial Conditions

To prevent the influence of the trapping beams on the dynamics, we turned off the MOT trapping beams while the probe beam was on. In each 40 ms experimental cycle, the trapping beams were turned off (at $t = 0$) for 5 ms, after which the atom cloud recovers during the remaining 35 ms. The probe beam was turned on from $t = 1$ to $t = 5$ ms. During this 4 ms measurement interval, the atomic cloud expanded due to its thermal motion. The interaction of the atoms with the probe beam resulted in optical pumping into the $F_g = 1$ ground level. We experimentally observed that, as a result of this effect, if the repumping laser was turned off, a substantially smaller rotation signal resulted. This effect is illustrated in Fig. 11.3 comparing the obtained signals with the repumping laser on and off during the measurement interval. In this record, taken at large detuning, leaving the repumping laser on increased the observed rotation by roughly a factor of three and changed the time evolution of the signal. At smaller detunings, the probe beam has a much greater effect on the atoms. In the absence of the repumper laser, there is almost no rotation. This observation promoted us to leave the repumper on continuously in all other measurements.

We would like to note, that although the repumper beams are mostly circularly-polarized, they propagate in 6 different orthogonal directions through the cold atom sample. Further, the sample is optically thin at the repumper transition, so the light intensity is uniform over the sample volume. For this reason, the optical pumping due to the repumper generates unpolarized fluorescence, and thus does not create significant polarization in the ground states of interest. As a result, the repumper does not directly contribute to the polarization rotation effect, except that it enlarges its strength (as demonstrated in Fig. 11.3) because there are more atoms in the $F_g = 2$ level. In the numerical simulations, the presence of the repumper is treated as a constant repumping/decay rate to sublevels of the

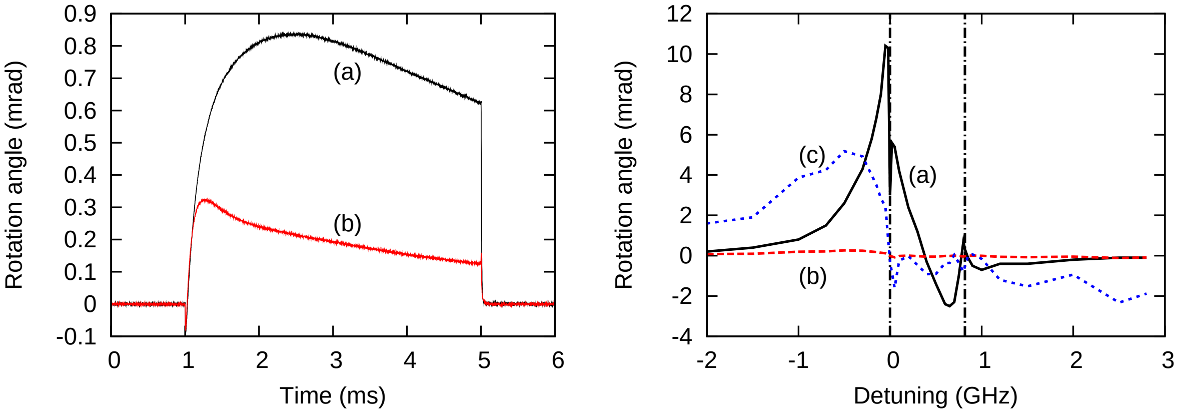

FIG. 11.3: (Left) The probe field self-rotation angle as a function of time, with t = 0 referring to the MOT laser switch off time. We compare the case of the repumper laser on (a) and off (b). Probe laser power = 600 μW, detuning = -1 GHz . (Right) Rotation angle vs. detuning with repumper laser on (a) and off (b). (c) is the result in (b) but 20 times magnified. Measurement taken at 3 ms. Vertical dash-dot lines mark locations of the $F_g = 2 \rightarrow F_e = 1$ and $F_g = 2 \rightarrow F_e = 2$ D$_1$ line transitions corresponding to 0 GHz and 0.82 GHz detunings.

$5^2S_{1/2}$ $F_g = 2$ state which is absorbed into the γ parameter (see Fig. 11.4 and discussion).

The atomic dynamics were also substantially affected by the fact that the atoms are pushed by the radiative force exerted by the probe beam. The corresponding average acceleration is: $a = p\hbar k\Gamma/m$ where k is the light wavenumber, m the atomic mass, Γ the excited state radiative decay rate and p the probability for the atom being in the excited state. p depends on the probe intensity and detuning as well as on the repumping rate ($p \leq 1/2$). If p approaches 1/2 (a worst case scenario), the acceleration is of the order 10^5 m/s^2 for ^{87}Rb. In the 4 ms interaction time such acceleration would cause a 0.6 GHz Doppler shift and a 0.8 m displacement. Although in the experiment the actual value of p is typically much smaller than 1/2 (especially at large detuning) this estimate gives an indication of how disruptive for the MOT the light pushing effect could be at small detunings and large probe intensities. We attribute spectrally narrow sharp changes in rotation spectra to the light pushing effect occurring near the resonance detunings (note them in Fig. 11.3 at 0 and 0.82 GHz).

The magnetic field gradient necessary for the operation of the MOT is present in the interaction region. Attempts to turn off the electric current in the coils generating the MOT magnetic field resulted in magnetic transients lasting longer than 10 ms due to eddy currents in the largely metallic MOT chamber. Thus, in spite of the anticipated deleterious effect to the purity of the PSR effect, the MOT magnetic field gradient was left on continuously during the experiment. Although the nature of the MOT guarantees a zero magnetic field at the center of the atom cloud through which the probe beam is aligned to pass, the substantial field gradient means that the atoms, experiencing a nearly zero average B field, are nonetheless subject to a spatially inhomogeneous field over the sample volume. In addition to this, the radiative forces exerted by the probe light on the atoms push the atomic cloud away from the zero of the magnetic field. Since leaving the field gradient on continuously was necessary to avoid magnetic transients, PSR was studied in a region where the atoms experience a nonzero magnetic field.

11.1.3 Self-rotation and Faraday rotation

For an isolated atomic transition, if the ellipticity ϵ and the length of interaction L are held constant, the self-rotation angle presents an antisymmetric dispersive shape as a function of the spectral detuning with respect to the unperturbed atomic transition. In multilevel systems, off resonance transitions associated with the presence of nearby states may distort the symmetry of the PSR response around a given transition [83].

However, this assumes that there is no external magnetic field influencing the atoms. In this experiment, the magnetic confinement field could not be switched off reliably, and so the atoms experience a small magnetic field. It is well known that the presence of an applied magnetic field will also cause circular birefringence leading to polarization rotation due to the Faraday effect as discussed in section 4.4. The Zeeman shifts caused by the magnetic field will change the resonant frequencies for σ^+ and σ^-, again leading to a phase shift between the components and rotation of the polarization. Therefore, in an atomic sample where a small external magnetic field is present, the observed rotation will depend on both PSR and Faraday rotation.

The influence of the two mechanisms is illustrated in Fig. 11.4 showing a numerical simulation of the PSR effect for the $F_g = 2 \rightarrow F_e = 1$ and $F_g = 2 \rightarrow F_e = 2$ hyperfine transitions of the D$_1$ line of ^{87}Rb. This simulation was carried out by A. Lezama, and more details can be found in App. B. We note that in Fig. 11.4, the spectral location of the $F_g = 2 \rightarrow F_e = 1$ transition corresponds to zero detuning, and so the $F_g = 2 \rightarrow F_e = 2$ resonance then corresponds to a positive 815 MHz detuning. Fig. 11.4(a) shows the rotation due to the Faraday effect alone, which is due to the presence of an applied magnetic field. The angle of rotation has a fixed sign determined by the orientation of the magnetic field. Notice the difference in magnitude of the Faraday effect for the two hyperfine transitions. Fig. 11.4(b) shows the PSR effect alone (no magnetic field) for two opposite incident field ellipticities ($\pm 25°$). As expected, the resonances have dispersion-like shapes with small asymmetries due to the neighboring transition. The decrease of the rotation angle with increasing detuning from resonance is considerably slower than for the Faraday effect. Interestingly enough, the magnitude of the PSR effect is quite similar for the two hyperfine transitions although with opposite signs. Fig. 11.4(c) shows the combined effect of the two mechanisms. The Faraday effect is responsible for the lack of symmetry for opposite ellipticities and for the imbalance between the two transitions. In all cases, the PSR effect is dominant for larger detunings. To study PSR and compare the experimental reality to these predictions, we measure the rotation angle in the atoms as a function of initial light ellipticity, probe laser power, and probe laser detuning

Rotation vs Initial Ellipticity

In order to examine the dependence of the polarization rotation on the probe ellipticity, the incident light ellipticity was varied by rotating a quarter-wave plate placed in the probe beam immediately before it entered the MOT chamber. The ellipticity ϵ is given by the angle of rotation of the quarter-wave plate from a reference point corresponding to zero ellipticity. The measured ellipticity dependence for the probe laser tuned to -80 MHz and $+80$ MHz relative to the $F_g = 2 \rightarrow F_e = 1$ D$_1$ transition is shown in Fig. 11.5. As expected, the rotation angle reverses sign around the zero of ellipticity, and rotation increases

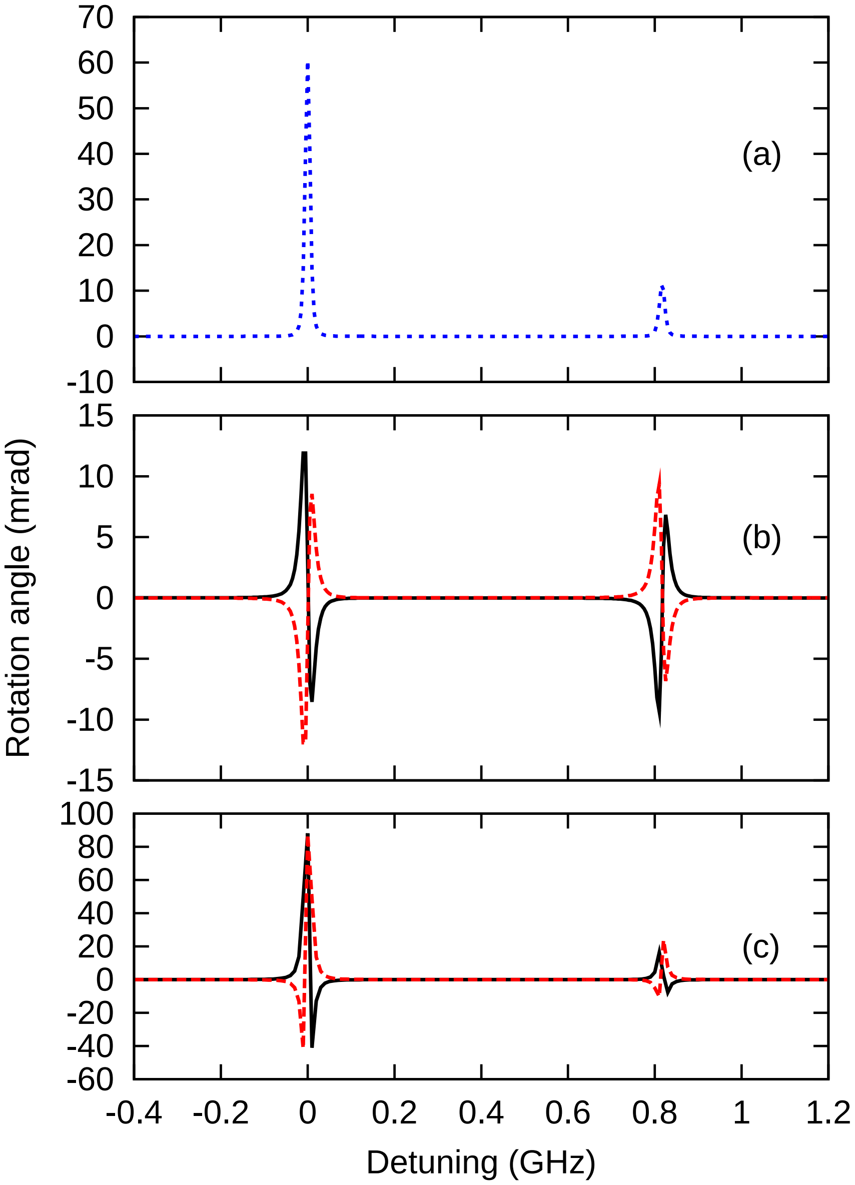

FIG. 11.4: Calculated polarization rotation around the $F_g = 2 \rightarrow F_e = 1$ (corresponds to zero detuning) and $F_g = 2 \rightarrow F_e = 2$ hyperfine transitions as a function of detuning. (a) Pure Faraday rotation ($B = 0.01\Gamma, \epsilon = 0$). (b) Pure PSR rotation ($B = 0, \epsilon = \pm 25^\circ$), black solid (red dashed) lines correspond to positive (negative) ellipticity. (c) Combined Faraday and PSR effects ($B = 0.01\Gamma, \epsilon = \pm 25^\circ$). Parameters: $C = 3$, $I = 2$ mW/cm^2, $\gamma = 0.001\Gamma$.

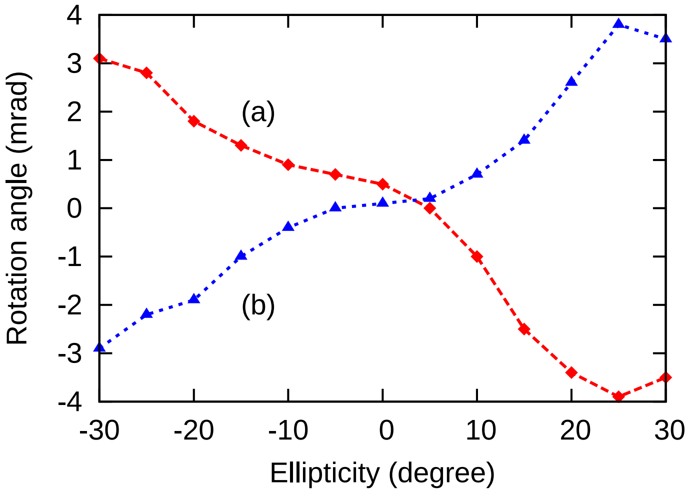

FIG. 11.5: Probe rotation angle vs. initial ellipticity at 3 ms measured at 80 MHz (a) and at -80 MHz (b) detunings relative to the $F_g = 2 \rightarrow F_e = 1$ transition. Probe laser power = 1.8 μW.

with larger initial ellipticities. The small shift of the point of zero rotation with respect to zero ellipticity is indicative of the presence of a small magnetic field in the measurement region. For the two detunings shown, the rotation has opposite signs, as expected from the nearly dispersive shape of the PSR resonances. These results confirm the occurrence of polarization self-rotation.

The color map presented in Fig. 11.6 shows the time evolution of the polarization rotation for different incident ellipticities at a probe power of 1.8 μW. A dependence on ellipticity similar to that shown in Fig. 11.5 (at 3 ms) is observed for the entire 4 ms measurement period. A decrease of the rotation is observed for long times; this effect we attribute to MOT expansion. Given these results, in subsequent measurements of PSR, the probe beam was always given a large initial ellipticity of $\pm 25°$. This ensures that PSR is the dominant process rotating the polarization ellipse of light and selects the largest rotation.

Rotation vs Probe Power

To investigate the effect of light intensity on self-rotation, we measure the rotation angle at various probe powers ranging from 0.3 μW to 2.0 mW. The full results are shown

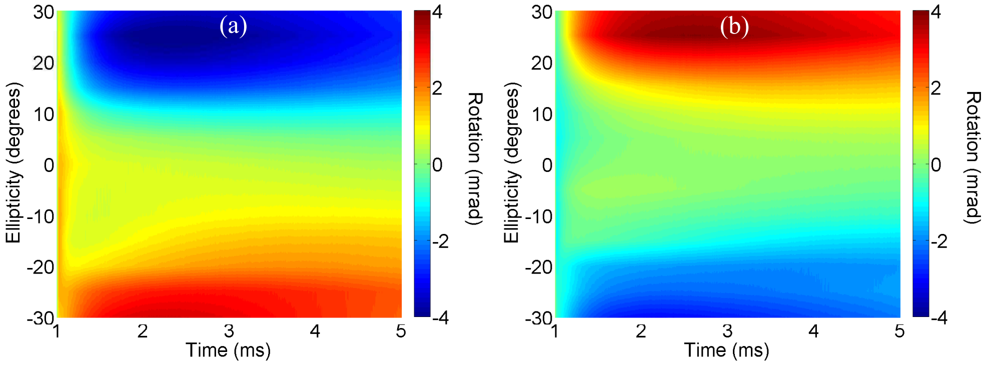

FIG. 11.6: Probe laser rotation angle vs. initial ellipticity and time measured at two detunings. Probe laser power = 11.4 μW, detunings are +80 MHz (a) and -80 MHz (b).

in Fig. 11.7 with the probe laser locked at -80 MHz from the unperturbed $F_g = 2 \rightarrow F_e = 1$ transition with both positive and negative incident ellipticity. A time slice taken at 3 ms expansion time is shown in Fig. 11.8 (left). Although we expected the self-rotation to increase with laser power, the full dynamics of the observed effect is more complicated. For low laser powers, the self-rotation effect does appear to steadily increase with power. However, upon reaching a certain power of the order of 100 μW, different behavior is observed depending on the sign of the incident ellipticity. For a positive initial ellipticity, the rotation generally continues to increase with increasing power, but the increase slows and begins to level off. For the opposite ellipticity, the self-rotation stops increasing and diminishes before increasing again at higher powers.

We interpret the different behavior for the two opposite ellipticities as the consequence of the existence of an average nonzero magnetic field in the interaction region. Such a field is present because the probe light pushes the atoms away from the region of zero magnetic field. As a result of the MOT symmetry and the initial probe alignment, the mean magnetic field is oriented along the light propagation axis. In the presence of a magnetic field, the light polarization experiences a Faraday rotation which has a nonlinear dependence on light intensity. The Faraday effect becomes significant as the resonant Rabi frequency of the light becomes comparable to the detuning. Since the sign of the polarization rotation due to the Faraday effect is independent of the light ellipticity, its effect enhances the

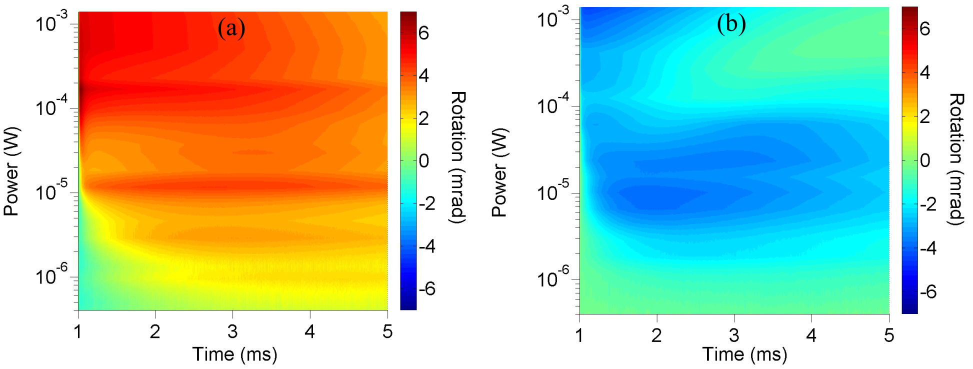

FIG. 11.7: Rotation angle vs probe laser power and time at opposite initial ellipticities. Probe laser detuning is −80 MHz, probe ellipticities are +30° (a) and −30° (b).

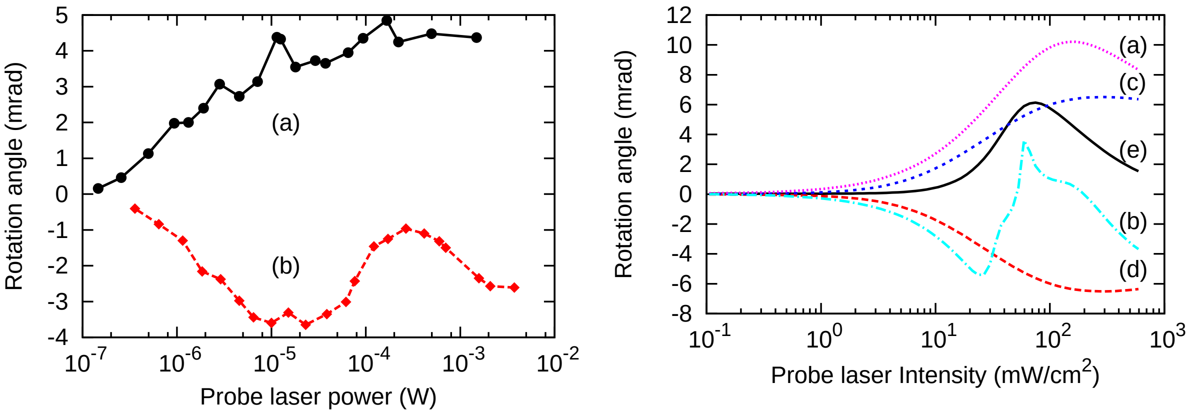

FIG. 11.8: (Left) Rotation angle vs probe laser power for different probe ellipticities. Probe detuning is −80 MHz, ellipticity +30° (a) and −30° (b). (Right) Simulated rotation angle vs. probe laser power for different ellipticities and magnetic fields. Probe laser detuning is −80 MHz, ellipticities are +30° (a,c), −30° (b,d), and 0° (e). Magnetic fields are B= 0.01Γ (a,b,e) and B= 0Γ (c,d).

rotation for one ellipticity and reduces the rotation for the opposite one. A numerical simulation of the combined PSR and Faraday effects, performed by our collaborator A. Lezama, is presented in Fig. 11.8 (right). The calculation was carried out for a constant magnetic field $B = 0.01\Gamma$, a figure that corresponds to the estimated field 1 mm away from the MOT center. In the experiment however, as a consequence of the cold atom cloud expansion and the atom acceleration by the probe field, the magnetic environment is variable in time resulting in additional complexity. However, when a small constant magnetic field is included in the simulation, the rotation displays similar behavior as seen in the experiment.

Rotation vs. Probe Detuning

The laser frequency was varied around the $F_g = 2 \rightarrow F_e = 1$ and $F_g = 2 \rightarrow F_e = 2$ hyperfine transitions during the measurement of the rotation angle in order to obtain the polarization self-rotation spectrum. The closer the laser frequency is to the transition frequency (small detunings), the stronger the light-atom interaction will be and therefore a larger self-rotation would be expected. However, in this cold atom system, a smaller detuning also means a stronger mechanical effect of the probe laser accelerating the atoms and disturbing the MOT. It is clear then that laser detuning and laser power together will determine the self-rotation effects seen in the atomic sample. Fig. 11.9(a, b, c, and d) shows the measured rotation angle versus laser detuning at four different powers and two opposite incident ellipticities. Fig. 11.9(a',b',c', and d') shows the calculated rotations for similar light intensities assuming the presence of a constant magnetic field along the probe beam propagation direction. The general trend of the experimental observation is well reproduced by the simulations. As the intensity increases, the resonances become power broadened while the peak rotation diminishes. At the highest power the broadening is such that the two hyperfine transitions overlap. For small detunings very close to the resonance ($<$ 100 MHz), the self-rotation angle is higher at small powers than for greater laser powers. This is due to the fact that at higher probe powers and small detunings, the MOT is strongly disturbed due to light pressure and rotation is diminished. At lower laser powers, the laser frequency can be closer to the resonance while not disturbing the atomic cloud, leading to a relatively higher rotation. However, at larger detunings, there is almost no rotation in the lower laser power beams, but we do still see some rotation for the higher laser powers. It appears as though the detuning spectrum for rotation spreads out as the laser power is increased, leading to smaller rotations close to resonance but larger ones at high detunings. Both transitions must be taken into account, as we can see that the rotation effects from the transitions overlap at high laser powers.

This general complex interdependence of the self-rotation angle on laser detuning and different powers is qualitatively plausible. However, beyond that, we see that the experimental data matches the calculations fairly well in shape and in size of the self-rotation angle. The main difference between the experimental plots and the simulations is that in the experiment, the rotation is always nearly zero at zero detuning, but not in the simulations. This is due to the strong perturbation of the atom cloud caused, near resonance, by the radiative force produced by the probe beam (compare Fig. 11.9(c,d) and Fig. 11.9(c', d') at near resonance detunings). Such a mechanical effect is not accounted for in the simulations. The overall agreement between the simulation and the observed spectra strongly supports the assumption of an average nonzero magnetic field throughout the sample. Because the Faraday rotation is highest at zero detuning, we see high rotation here in the simulations, especially at higher powers when the Faraday effect dominates over PSR. The similarity between the experimental data and the calculated data is fairly good at larger detunings where the MOT is not disturbed. We also note the asymmetry between positive and negative rotations and the difference between the strengths of the first and second transitions. The experimental data shown in Fig. 11.9(a, b, c, and d) was taken at 3 ms cloud expansion. The complete time evolution is shown in Fig. 11.10. The time dependence is understandably stronger for smaller detunings where the light has a stronger mechanical effect, pushing the atoms and disturbing the MOT.

The confirmation of self-rotation in the cold atomic medium leads us to next search for phase-dependent noise and squeezing in cold Rb. Whether squeezing is present will depend on whether the rotation is large enough, governed by the above dynamics of the MOT sample and the interplay of laser power, detuning, light pressure, and magnetic field.

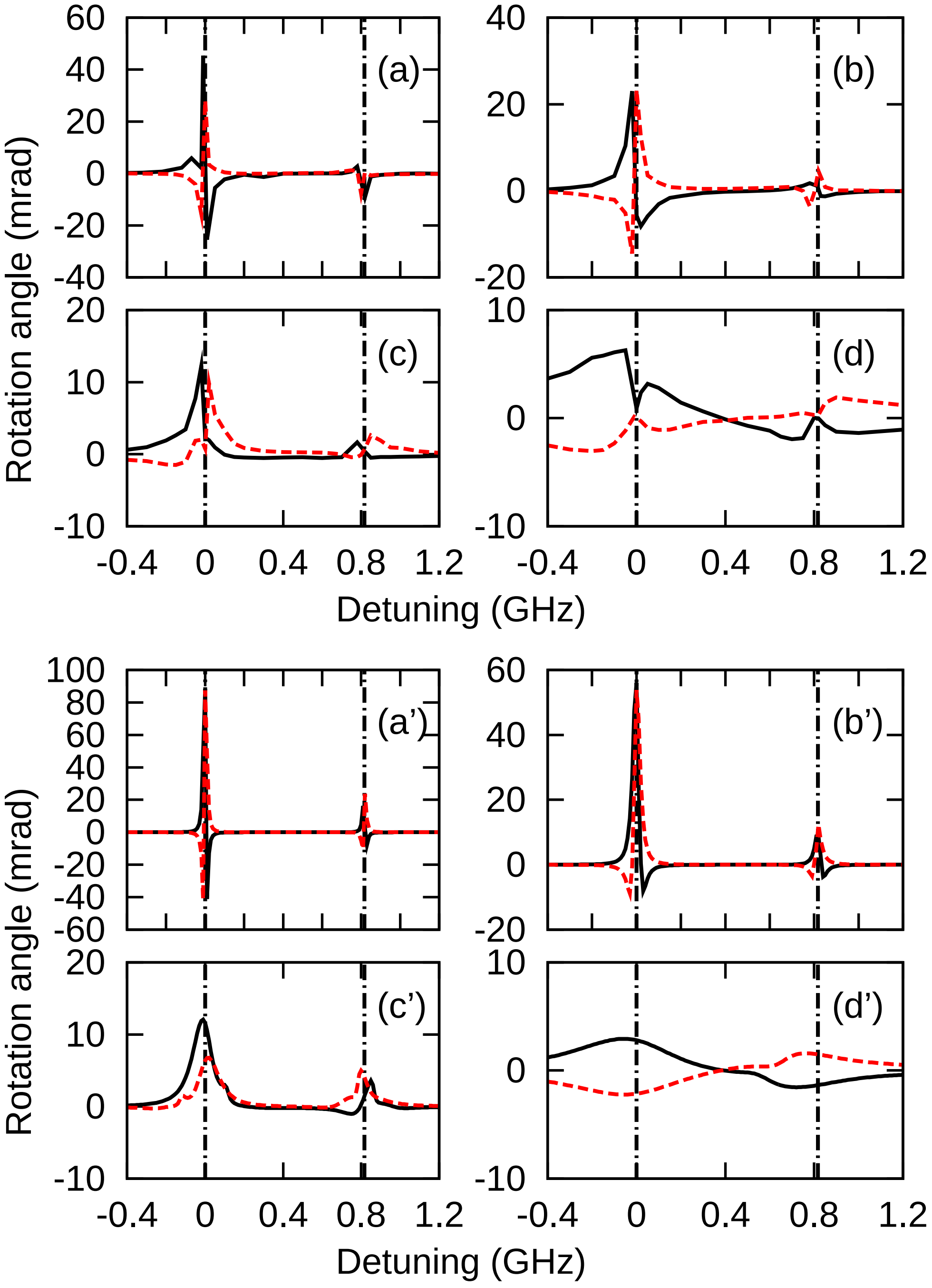

FIG. 11.9: Comparison of the experimental data (top 4 plots) and calculated (bottom 4 plots) rotation angle dependence on probe laser detuning at opposite initial ellipticities +25° (solid lines) and $-25°$ (dashed lines) for different probe laser powers: 2 μW (a and a'), 10 μW (b and b'), 100 μW (c and c'), and 2000 μW (d and d'). Experimental data is taken at 3 ms. Results of calculations are for beam cross-section $= 10^{-3}$ cm^2, B$= 0.01\Gamma$, $\gamma = 0.001\Gamma$, and C$= 3$. Vertical dash-dot lines mark locations of the $F_g = 2 \rightarrow F_e = 1$ and $F_g = 2 \rightarrow F_e = 2$ D$_1$ line transitions corresponding to 0 GHz and 0.82 GHz detunings.

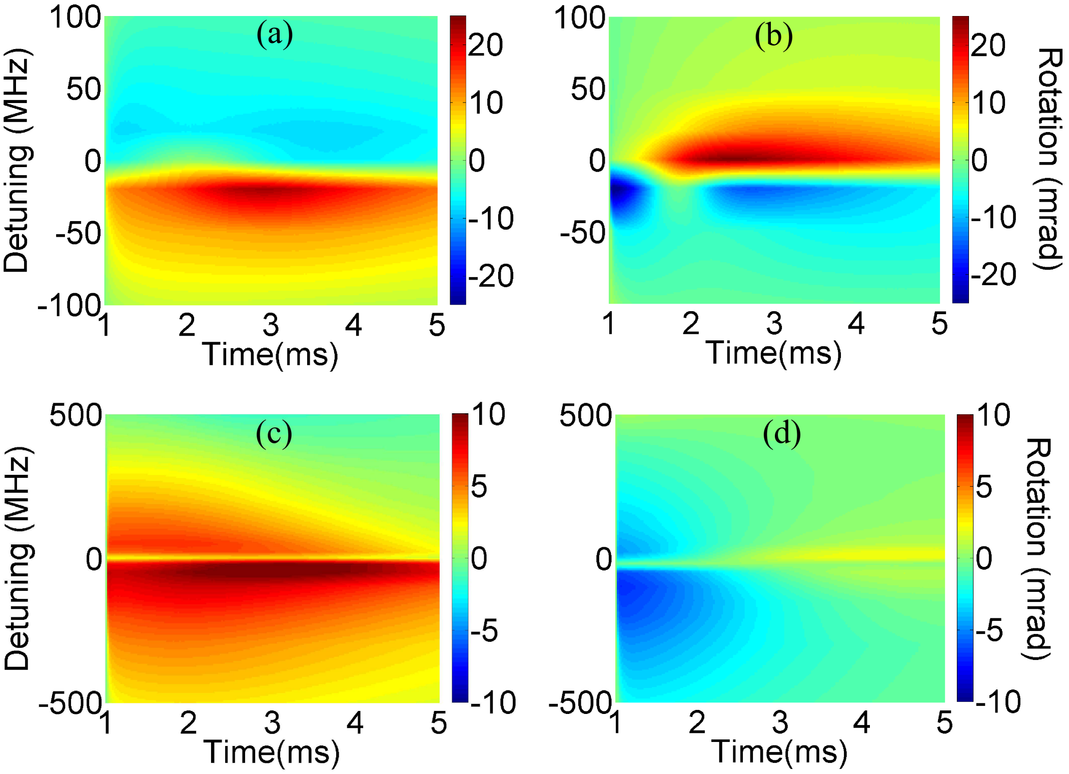

FIG. 11.10: Dependence of rotation angle on probe laser detuning and measurement time for different probe laser powers and ellipticities: power 10 μW, $\epsilon = +25°$ (a); power 10 μW, $\epsilon = -25°$ (b); power 600 μW, $\epsilon = +25°$ (c); power 600 μW, $\epsilon = -25°$ (d).

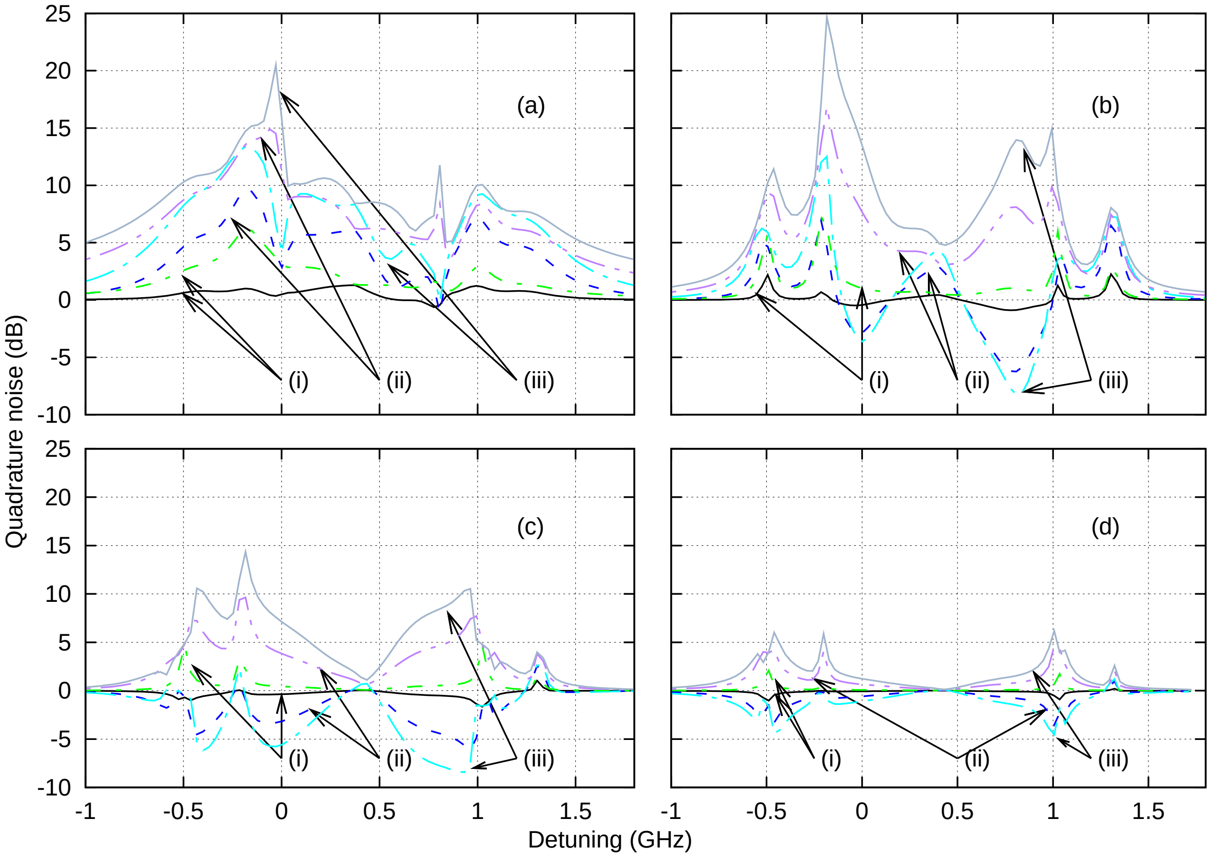

FIG. 11.11: Phase-dependent noise vs detuning for different cooperativity parameters and decay rates. Parameters are $\gamma = 10^{-1}\Gamma$ (a), $\gamma = 10^{-2}\Gamma$ (b), $\gamma = 10^{-3}\Gamma$ (c), and $\gamma = 10^{-4}\Gamma$ (d); (i) C=100, (ii) C= 900, (iii) C= 1700; $\Omega = 30\Gamma$, $B = 0$ in all cases.

11.2 Quadrature noise of light interacting with a cold atomic gas

Our studies in cold ^{87}Rb atoms verified the presence of the PSR effect, though in a regime where this effect combines with Faraday rotation due to the non-zero magnetic field. This indicates that there may be a set of conditions in the cold atoms where the self-rotation can lead to squeezed vacuum generation as it has in warm vapor cells. We now use a similar experimental setup to measure the quadrature noise of the probe light after it propagates through the cold cloud of atoms. Monitoring the phase-dependent noise allows us to search for conditions favorable to PSR squeezing in cold Rb.

We start by showing numerical simulations carried out by our collaborator A. Lezama in Fig. 11.11, to find the expected noise levels under various conditions. The maximum and minimum quadrature noise levels of the output vacuum field are shown as a function of the driving laser detuning from the $F_g = 2 \rightarrow F_e = 1$ transition. Results are presented for different values of the decay rate γ and the cooperativity parameter C, which is proportional to the optical density. Further details of the calculations can be found in App. B and in Ref. [87]. It can be seen that the level of squeezing as well as the contrast (difference between maximum and minimum quadrature noise) grows with increased C (optical density). The contrast diminishes as the laser detuning increases. As expected, the noise approaches the SQL noise level for both quadratures for a very far detuned laser, since in this case the light does not interact with the atoms.

11.2.1 Experimental setup

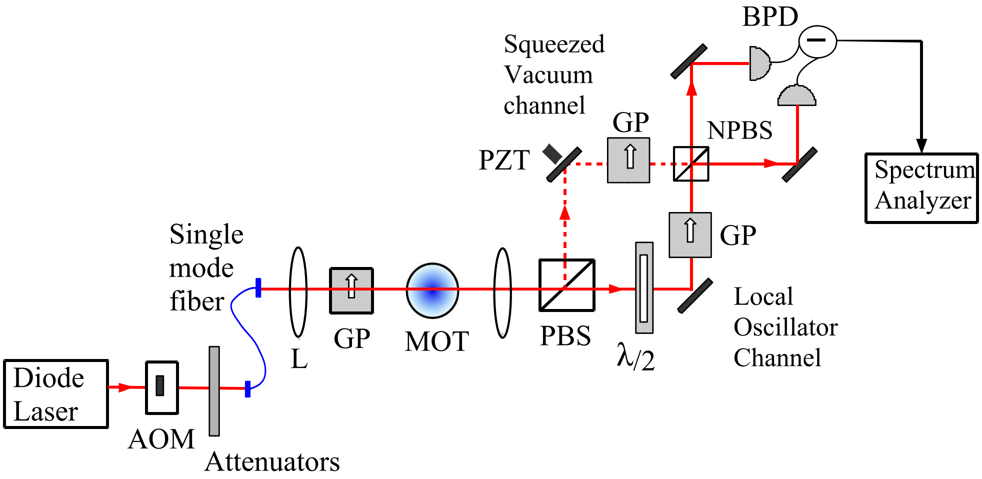

FIG. 11.12: Schematic diagram of the experimental setup used for noise measurements.

A schematic diagram of the experimental apparatus is shown in Fig. 11.12. The MOT and probe laser are the same as described in the previous section with a few key differences. The studies on PSR showed that if the MOT lasers are off, the typical lifetime of an atom in the beam is less then a ms (especially near resonance) due to light pressure exerted by the driving beam. Since we want to perform continuous squeezing experiments, we keep the MOT lasers on to continuously repopulate the cloud with Rb atoms. The presence of the MOT trapping beam helps to maintain the atomic cloud centered around the zero of the magnetic field.

The probe beam after the Glan polarizer now has a linear polarization upon entering the atoms, with no quarter waveplate to add ellipticity. This strong beam (up to 10 mW) will act as a pump for the squeezing process and we will measure the fluctuations on the orthogonal vacuum field to search for phase-dependent noise.

To monitor the noise quadratures of the vacuum field, we make use of the balanced homodyne detection method (detection scheme #1) described in section 5.3.2. After propagation through the atoms, we separate the linearly polarized driving field from the orthogonal vacuum with a polarizing beamsplitter (PBS). The strong port is attenuated to 100 μW and serves as a local oscillator (LO) in the homodyne scheme. The LO field is rotated by an extra 90° with a half-wave plate in order to match the polarization of the vacuum channel. The vacuum channel and LO fields pass through Glan polarizers in order to improve the extinction ratio of the PBS, and are finally mixed on a non-polarizing beam splitter (NPBS). The beamsplitter outputs are then directed to the two matched photodiodes where the two photo currents are electronically subtracted. This makes up the balanced photodetector (BPD). We analyze the remaining noise with a spectrum analyzer at a 1.4 MHz detection frequency. The vacuum channel and the LO maintain good mode-matching and the phase angle between them is swept to measure the noise in the different quadrature projections.

11.2.2 Experimental results

Fig. 11.13 shows an example of the observed phase-dependent noise. The 0 dB noise level corresponds to the shot noise, which we determine by introducing a solid block into the vacuum channel. Noise below 0 dB indicates squeezing. We note that the overall stability of the shot noise level is about ±0.2 dB, which is governed by the fluctuations of the LO power and stability of the spectrum analyzer.

Due to the relatively small number of atoms ($\approx 10^5$) interacting with the PSR driving

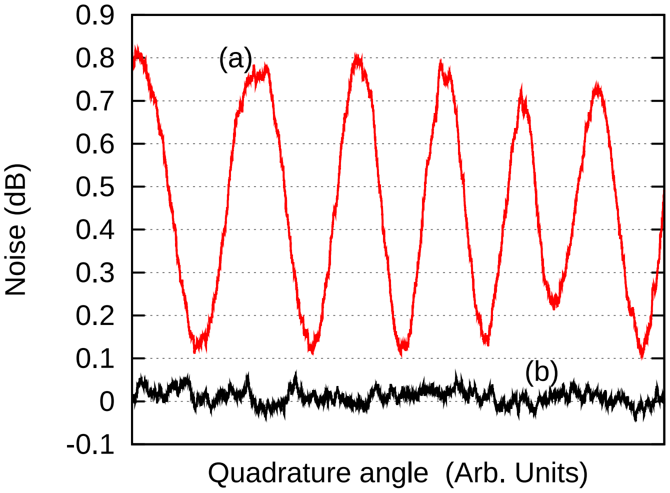

FIG. 11.13: Noise power in the squeezed channel vs the quadrature angle. Phase-dependent excess noise: Laser power = 1.3 mW, Detuning = -200 MHz (a) modified quantum noise in the vacuum channel, (b) shot-noise level. The noise trace is measured at 1.4 MHz central frequency of the SA, RBW= 100 kHz, and is averaged over 512 traces.

beam, the overall noise contrast is below 0.8 dB, which is significantly smaller in comparison to noise contrasts typically observed in hot Rb cells where squeezing is seen. It is important to note in this comparison that the number of interacting atoms in the hot cell is approximately one thousand times higher. The experimentally observed optical density is only around 2, which is far from the high cooperativity parameters required to achieve the significant noise contrast presented in Fig. 11.11. The phase-dependent noise however is clearly visible, and noise versus detuning measurements are taken to compare with theoretical predictions.

In order to record the minimum and maximum noise level dependence on the pump laser detuning, we set our laser to a given detuning (controlled with a commercial wave meter with 10 MHz accuracy), and record noise versus quadrature angle similar to that shown in Fig. 11.13. On such a trace, we note the maximum and minimum noise levels, which provide two data points for each detuning shown in Fig. 11.14(a,b, and c). Note that at detunings exactly matching the atomic transitions (0 and 815 MHz), we have zero noise contrast and the overall noise level drops to shot noise. We attribute this to the strong light pressure of the driving beam on the atoms at frequencies very close to the transitions, which blows away the atomic cloud. We take such contrast measurements versus detuning spectra at several driving laser powers and see that contrast initially grows with power, but then the contrast decreases due to a stronger effect of light pushing the atoms away from the interaction region. We also note that the highest contrast position moves away from the transition frequencies with increasing power (more negative for $F_g = 2 \rightarrow F_e = 1$ transition, and positive for $F_g = 2 \rightarrow F_e = 2$) due to power broadening of the transition resonance. This effect is often seen in the PSR squeezing with hot Rb [73]. The theoretical predictions of the noise spectra match the shapes of the experimental traces quite well, as shown in Fig. 11.14(d). In this simulation, we have taken $\gamma = 0.1\Gamma$ and $B = 0$. The relatively large value of γ was chosen to account for the fact that the atomic ground state coherence is strongly perturbed by the MOT trapping and repumping beams. Our previous studies indicate that the ambient magnetic field in the MOT region is on the order of $B = 0.01\Gamma$ (in units of the corresponding Zeeman frequency shift). Since $B \ll \gamma$, the magnetic field influence is negligible and the zero magnetic field approximation may be justified.

11.3 Summary and future improvements

PSR in cold atomic vapor

We have studied several aspects of polarization self-rotation in cold rubidium atoms. We have focused our study on the $F_g = 2 \rightarrow F_e = 1$ and $F_g = 2 \rightarrow F_e = 2$ D_1 hyperfine transitions of ^{87}Rb. We find that with this experimental setup, PSR is readily observable. As expected, the rotation depends on the incident ellipticity of the light. The rotation also depends on the probe power, growing with increased power at large detunings. However, at higher laser power, the probe beam begins to disturb the MOT, pushing atoms away from the trapping zone and to a region where the magnetic field is no longer zero, on average. The rotation at these higher powers does not appear to continue increasing with power, but

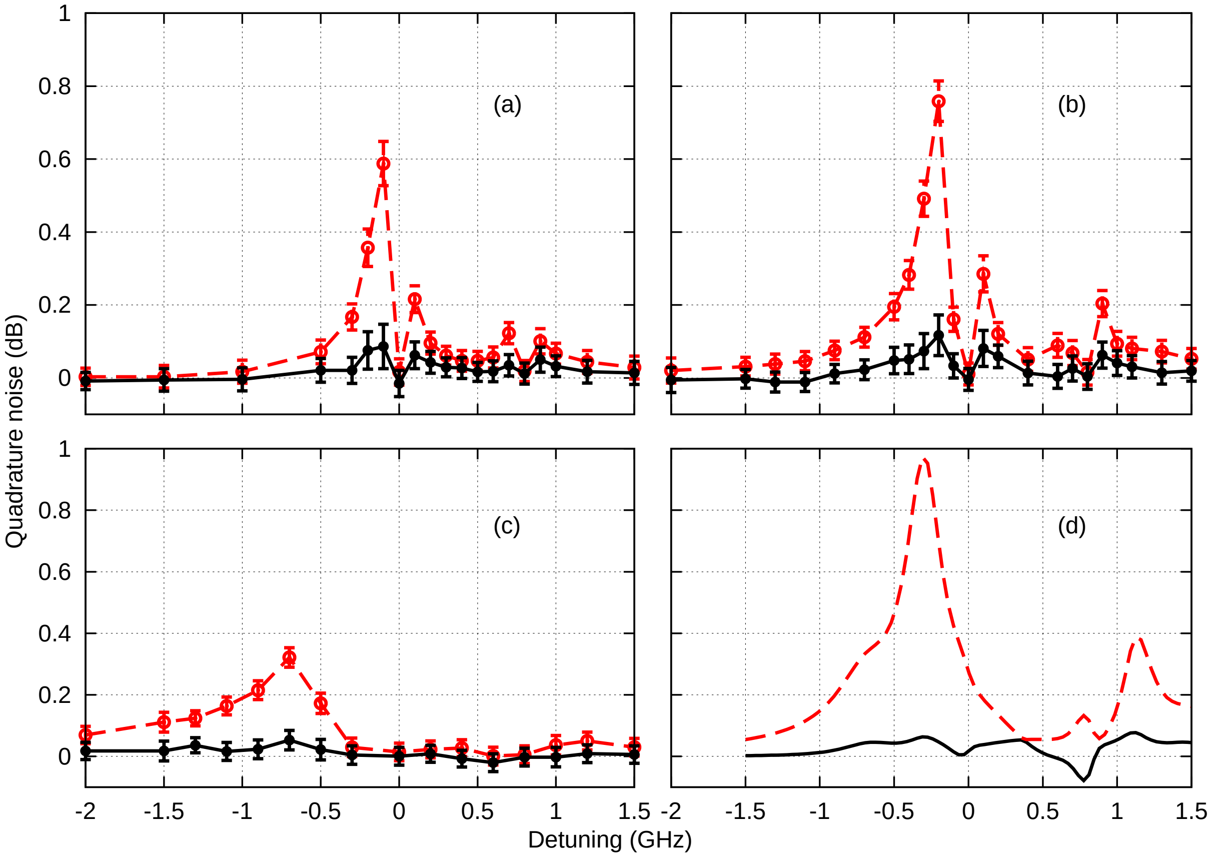

FIG. 11.14: Results of the experiment (a, b, and c) and numerical simulations (d) for minimum (solid line) and maximum (dashed line) noise levels dependence on the PSR driving laser detuning for different PSR driving laser powers. (a) laser power 0.47 mW, (b) 1.3 mW, (c) 7.5 mW. Parameters for numerical simulation (d) power = 10 mW, beam cross- 10^{-3} cm^2, $\gamma = 0.1\Gamma$, C= 10, $B = 0$.

becomes less quantitatively predictable due to the motion of the atoms and the non-zero magnetic field. We see from the rotation measurements at different detunings that the effect we observe is not symmetric around the transition, confirming the fact that many of the atoms contributing to self-rotation are experiencing some small magnetic field. If a longitudinal static magnetic field is included in the self-rotation numerical simulations, the measured behavior is quite similar to the calculations which include the effect of Faraday rotation. We also point out that, with increasing laser power, the rotation spectrum in frequency space appears to spread and the rotation decreases due to the increased light pressure the probe has on the atoms as well as a greater magnetic field effect. We can observe self-rotation at very large detunings upwards of 500 MHz at higher laser powers approaching milliwatt levels.

PSR squeezing prospects in cold atoms

We have also observed overall quantum noise modification via the PSR effect in a cold ^{87}Rb atomic medium, which is in good agreement with the numerical simulations.

We do not have compelling results showing squeezing below the SQL. We do however see clear phase-dependent excess noise and, depending on conditions, several points where the minimum noise level is very near shot noise. The degree of polarization self-rotation may not be large enough to observe measurable squeezing under these conditions. In fact, the predicted squeezing is on the order of a tenth of a dB for conditions similar to this experiment (see 11.14(d)), which is at the limit of our current resolution.

We attribute the lack of obvious squeezing to a low number of atoms interacting with the PSR driving beam in our current cold atom arrangement. We believe that an instrument with a higher optical density will result in stronger squeezing with noise below the SQL, as predicted by the numerical simulations. Such cold atom traps are well within the experimental reach of the current state of technology; for instance, it is possible to have a large magneto-optical trap with up to 10^{10} atoms [146], or to create an asymmetric cigar-shaped MOT so that the longer dimension can be aligned with the PSR driving beam [147, 148] thus achieving a quite substantial optical density and a considerably higher number of interacting atoms.

Other improvements to the experiment should also increase the chances for observing PSR squeezing in cold atoms. We confirmed the presence of a nonzero magnetic field experienced by some of the atoms, which is known to increase the excess noise and degrade squeezing during the PSR process in hot atoms (see section 6.10). To avoid this field, a glass vacuum chamber could be used for the MOT to allow for fast turn-off of the confinement magnetic fields without eddy currents. One of the main difficulties in this experiment was the light pressure at small laser detunings, which disturbed the atomic cloud. It is possible that this could be solved with a counter-propagating beam used to balance the motion of the atoms. Even with these difficulties, the presence of phase-dependent noise modulation indicates that squeezed vacuum generation via the PSR effect should be possible in a cold atomic medium given the right experimental conditions.

CHAPTER 12

Conclusions and outlook

In this dissertation, we have carried out a series of experiments studying quantum squeezed vacuum states generated in ^{87}Rb vapor via the polarization self-rotation effect. Quantum states of light have proven to be an interesting area of study, and may be very important in quantum information applications as well as optical measurements. PSR in atomic vapors has provided a robust squeezing source which is incredibly simple and low-cost to operate.

Once optimized in hot vapors, this single pass vapor configuration gives about -2 dB of noise suppression compared to the level of shot noise near three atomic resonances on the D$_1$ line of ^{87}Rb , $F_g = 1 \rightarrow F_e = 1$, $F_g = 2 \rightarrow F_e = 1$, and $F_g = 2 \rightarrow F_e = 2$. Our best recorded squeezing was on the $F_g = 2 \rightarrow F_e = 2$ transition and showed a maximum of -2.6±0.3 dB reduction, comparable to the highest squeezing levels found to date using this method [74]. We also found that the noise reduction is seen at detection frequencies as low as 100 Hz, though the result is obscured by classical laser noise present in the experiment. We have found that these noise reduction levels can be achieved in simple heated Rb vapor cells using modest laser powers ($<$ 10 mW).

By using a source of squeezed vacuum at 795 nm, we can further test and manipulate the quantum states by probing a second atomic medium of ^{87}Rb . To prove the utility of squeezed vacuum in precision measurements, we built a prototype optical magnetometer based on nonlinear Faraday rotation in a hot Rb vapor, with a sensitivity on the order of 1 pT/$\sqrt{Hz}$. We probed it with a squeezed light state to show that the reduced noise quadratures will allow for quantum enhancement to the sensitivity of the device for a particular range of atomic densities. At higher densities, we note the interesting dynamics of the interaction of the light and atoms which adds excess noise to the measurement.

We also probed an atomic medium under conditions of EIT to learn more about the interactions of quantum light with resonant media. By modulating the magnetic field during squeezing generation, we were able to produce pulses of squeezed vacuum, and we used the dispersive properties of the medium to change the group velocity of the light. While this study is ongoing, we do see signs of both slow light and fast light for the pulses of quantum noise.

While using continuous squeezed vacuum, we again probe an EIT medium and observe filtering of the quantum noise due to the frequency dependence of the absorption. While we can observe filtering effects on the excess phase-dependent noise, the input squeezing levels are often not high enough to survive the interaction with the EIT medium, due to extra sources of noise that couple into the system. Other methods for squeezing generation with higher noise reduction levels, such as nonlinear crystals, are still better suited for filtering and atomic memory applications. However, PSR experiments prove to be much simpler, and the high antisqueezing noise levels can also be used in some experiments. This squeezed vacuum source also remains a good candidate for noninvasive measurements and provides a simple source of excess phase-dependent noise.

We also investigated the PSR effect in cold ^{87}Rb vapor to search for higher levels of squeezed vacuum generation. While interesting observations of self-rotation in the presence of a small magnetic field were made, the atomic density in our MOT was not high enough for squeezed vacuum production. Cold atoms do look promising for squeezing however, as phase-dependent noise was detected at the output of the cold rotation medium.

The squeezing levels achieved via PSR are currently about 2-3 dB below shot noise, but these suppression levels have been steadily increasing and a broader search of the parameter space may yet find further improvements for this squeezing source. Also, even at these levels, the noise reduction is easily detectable, and the squeezed states are produced at frequencies convenient for atomic physics studies. The simplicity of PSR squeezing makes it useful in many proof-of-principle experiments and studies in atomic physics. The squeezing measurements in these experiments can also be improved by identifying and eliminating more of the excess noise sources which can limit the noise suppression. This includes using a laser with less amplitude noise at low frequencies, and providing more stability of the polarization, phase, and alignment of the light beams. Also, using higher quality optics with less loss and a better extinction ratio of polarizations could be beneficial.

Finally, more theoretical work is required to fully characterize the quantum noise of these states as well as their interaction with atoms, and to identify the materials and conditions to give the maximum possible squeezing levels while avoiding undesirable excess noise sources.

APPENDIX A

Cavity vs free-space modes

After quantization of the electromagnetic field, we have an operator for the electric field as a sum of cavity modes. However, we wish to work with light fields in free space. We can make the transition as follows.

We write down the field, including the time-dependence explicitly [82].

$$\hat{\mathbf{E}}(z,t) = \sum_j \frac{E_0}{\sqrt{2}} \left[\hat{\mathbf{a}}_j \, e^{i(k_j z - \omega_j t)} \right] \tag{A.1}$$

$E_0 = \sqrt{\hbar\omega_j/\epsilon_0 V}$ is a real positive amplitude associated with the electric field per photon. We now imagine moving the cavity mirrors very far apart. As the mirrors move apart, the spacing between cavity modes shrinks and, for a nearly monochromatic field, we can view our frequency modes in terms of average values plus small deviations.

$$k_j = \overline{k} + \Delta k_j, \qquad \omega_j = \overline{\omega} + \Delta\omega \tag{A.2}$$

With these substitutions, our operator now takes the form

$$\hat{\mathbf{E}}(z,t) = \frac{E_0}{\sqrt{2}} \hat{\mathbf{A}}(z,t) e^{i(\overline{k}z - \overline{\omega}t)}, \tag{A.3}$$

where we have defined a new operator $\hat{\mathbf{A}} = \sum_j \hat{\mathbf{a}}_j \, e^{i\Delta k_j(z-ct)}$. Note that equation A.3 for the free-space field has the same form as equation A.1 for the cavity modes but with the slightly different annihilation operator. We find that this new operator has slightly different commutation relations.

$$\left[\hat{\mathbf{A}}_k, \hat{\mathbf{A}}_{k'}^\dagger\right] = \sum_{k,k'} \left[\hat{\mathbf{a}}_k, \hat{\mathbf{a}}_{k'}^\dagger\right] e^{i\Delta k(z-ct)} e^{-i\Delta k'(z'-ct')} \tag{A.4}$$

$$= \sum_k e^{i\Delta k[z-z'-c(t-t')]} \tag{A.5}$$

In the continuum limit, the summation is replaced by an integral over $dk = d\Delta k$ and we arrive at

$$\left[\hat{\mathbf{A}}_k, \hat{\mathbf{A}}_{k'}^\dagger\right] = \frac{L}{c}\delta(t-t'). \tag{A.6}$$

We get a delta function (now Dirac delta for a continuous function) with an extra factor of length over the speed of light. For practical purposes, this factor can be absorbed into the amplitude E_0 and the distinction between the free-space and cavity modes will not be important in most cases.

APPENDIX B

Description of numerical simulations

The numerical simulations to model the combined effect of PSR and Faraday rotation in a cold atomic ^{87}Rb sample, as well as to predict the effects on the noise levels, were carried out by Dr. Arturo Lezama. Full descriptions of similar methods can be found in Refs. [87, 149]. Here we provide a brief summary.

PSR and Faraday effect modeling

To compare the experimental results with theoretical predictions in section 11.1, a numerical calculation of the PSR angle for parameters approaching the experimental conditions is performed. The calculation is carried out for a homogeneous atomic sample of motionless atoms, and factors such as the inhomogeneous magnetic field and the motion of the atoms were not taken into account. The PSR angle was numerically calculated by solving the optical Bloch equations for the atomic system in the presence of an elliptically-polarized monochromatic classical light field with ellipticity ϵ.

Taking into account the level structure of the D_1 transition of the ^{87}Rb atom, a single ground state hyperfine level with total angular momentum $F_g = 2$ and two excited hyperfine levels with angular momenta $F_e = 1$ and $F_e = 2$ are included. All Zeeman substates are taken into account for these three levels. The decay of the excited states is due to spontaneous emission at a rate Γ. In addition, the transit time decay is accounted for by an overall decay rate parameter γ ($\gamma \ll \Gamma$). The constant magnetic field strength B is measured in units of the corresponding Zeeman frequency shift. The incident field with electric field amplitude E has a Rabi frequency $\Omega = \mu E/\hbar$ where μ is the *reduced* dipole moment matrix element for the $5S_{1/2} \rightarrow 5P_{1/2}$ D_1 transition. In the modeling, the atomic medium has an optical depth $4C$ where $C \equiv \frac{\eta L \nu \mu^2}{2\epsilon_0 \Gamma c \hbar}$ is the cooperativity parameter (η is the atomic density, L the medium length, and ν the light frequency).

The Bloch equations are numerically solved for the steady state normalized density matrix ρ. The polarization ellipse rotation angle φ is given by the accumulated phase difference between the two circular components of the light.

Noise modeling

To properly describe the light fluctuations after interaction with the atomic sample, as shown in Fig. 11.11, the quantum fluctuations of the atomic operators need to be incorporated into the treatment. This can be achieved via the Heisenberg-Langevin Equations that incorporate the atomic fluctuations through the use of stochastic forces. To model the experimental situation from section 11.2, the numerical treatment used in [72] is applied to an ensemble of cold atoms. As in the previous model, both relevant upper hyperfine states of ^{87}Rb ($F_e = 1, 2$) and one ground state ($F_g = 2$) are taken into account with the complete Zeeman structure of all three levels. The decay rate of the upper states is Γ ($\Gamma = 2\pi \times 6$MHz) and the overall phenomenological decay rate for atomic coherences and populations is γ ($\gamma \ll \Gamma$). The parameters B, Ω, μ, and C are defined in the same way as in the PSR simulation.

The Heisenberg-Langevin Equations for atoms and fields are numerically solved in steady state. For this, the loss of atoms at a rate γ is compensated by source terms representing the arrival of fresh atoms isotropically distributed in the ground state Zeeman sublevels. As a consequence, the parameter γ governs, at the same time, the decay of coherence (in the absence of light) and the arrival of fresh atoms into the system.

APPENDIX C

List of electronics used

- **Laser 1:** DL100 Toptica external cavity diode laser and controller. Linewidth ∼1MHz. Low noise above 20kHz. Used for all hot atom experiments.
- **Laser 2:** ECDL-7960R diode laser. Linewidth ∼1MHz. Used as probe in cold atom studies.
- **Slave laser:** JDSU SDL-5431-G1 diode in Thorlabs temperature stabilized mount. Used to generate control beam in filtering experiments.
- **Balanced photodetector:** Matched Hamamatsu S5106 photodiodes and subtracting circuit using low-noise high-bandwidth TI OPA37U operational amplifier. Quantum efficiency ∼95%. Used for all noise measurements.
- **Spectrum analyzer 1:** HP 8596E. 9kHz-12.8GHz. Used for the majority of noise measurements.
- **Spectrum analyzer 2:** HP 8568B. 100Hz-1.5GHz. Used for cold atom noise measurements.
- **Oscilloscope and Fourier analyzer:** Lecroy Waverunner 640Zi. 4GHz, 40GS/s. Used to record time-dependent noise traces (Squeezing pulses, slow and fast light).

Spectrum analyzer mode used for low frequency noise detection and magnetometer study.

- **PZT controller:** Thorlabs 3-axis Piezo controller MDT693A. Swept PZT current to scan phase of LO.
- **Phase-locking circuit:** Home-made PI circuit. Locked PZT to coherent oscillating signal to hold phase-dep. noise constant.
- **Voltage Preamplifier:** Low noise SRS SR560. Used to amplify signal in magnetometry experiment and in low frequency noise detection in combination with Lecroy scope.
- **Temperature controllers:** Newport i-Series, Model 1853. Controlled heaters on vapor cells.
- **Current source:** Home-made current source. Controlled modulation of B-field in cells.
- **AOMs:** IntraAction AOM-80 MHz. Controlled with IntraAction ME Signal Generator. Used for laser power attenuation and control field modulation.
- **EOM:** IntraAction 6.835 GHz. Controlled with Agilent E8257D PSG Analog Signal Generator. 250Hz-20GHz. Used for control field modulation in hyperfine EIT setup.
- **Function Generators:** SRS DS345 Synthesized Function Generator. Various uses.

APPENDIX D

Permissions

Some of the content of this dissertation was reproduced or adapted from the following articles with permission from the publishers:

- Travis Horrom, Gleb Romanov, Irina Novikova, and Eugeniy E. Mikhailov. All-atomic generation and noise-quadrature filtering of squeezed vacuum in hot Rb vapor. *Journal of Modern Optics*, Taylor and Francis 2012.

- Travis Horrom, Irina Novikova, and Eugeniy E Mikhailov. All-atomic source of squeezed vacuum with full pulse-shape control. *Journal of Physics B: Atomic, Molecular and Optical Physics*, 45(12):124015, Institute of Physics 2012.

- Travis Horrom, Robinjeet Singh, Jonathan P. Dowling, and Eugeniy E. Mikhailov. Quantum-enhanced magnetometer with low-frequency squeezing. *Phys. Rev. A*, 86:023803, American Physical Society 2012.

- Travis Horrom, Arturo Lezama, Salim Balik, Mark D. Havey, and Eugeniy E. Mikhailov. Quadrature noise in light propagating through a cold ^{87}Rb atomic gas. *Journal of Modern Optics*, 58(21):1936, Taylor and Francis 2011.

- Travis Horrom, Salim Balik, Arturo Lezama, Mark D. Havey, and Eugeniy E. Mikhailov. Polarization self-rotation in ultracold atomic ^{87}Rb. *Phys. Rev. A*, 83(5):053850, American Physical Society 2011.

BIBLIOGRAPHY

[1] E. Merzbacher. *Quantum Mechanics*. John Wiley & Sons, Inc, 3 edition, 1998.

[2] H.A. Bachor and T.C. Ralph. *A Guide to Experiments in Quantum Optics*. Physics Textbook. Wiley, 2 edition, 2004.

[3] D. F. Walls. Squeezed states of light. *Nature*, 306:141–146, Nov 1983.

[4] H. Yuen and J. Shapiro. Optical communication with two-photon coherent states–part i: Quantum-state propagation and quantum-noise. *Information Theory, IEEE Transactions on*, 24(6):657 – 668, Nov 1978.

[5] Horace P. Yuen and Jeffrey H. Shapiro. Generation and detection of two-photon coherent states in degenerate four-wave mixing. *Opt. Lett.*, 4(10):334–336, Oct 1979.

[6] C. M. Caves. Quantum-mechanical noise in an interferometer. *Phys. Rev. D*, 23(8):1693, Apr 1981.

[7] Carlton M. Caves and Bonny L. Schumaker. New formalism for two-photon quantum optics. i. quadrature phases and squeezed states. *Phys. Rev. A*, 31:3068–3092, May 1985.

[8] Bonny L. Schumaker and Carlton M. Caves. New formalism for two-photon quantum optics. ii. mathematical foundation and compact notation. *Phys. Rev. A*, 31:3093–3111, May 1985.

[9] R. E. Slusher, L. W. Hollberg, B. Yurke, J. C. Mertz, and J. F. Valley. Observation of squeezed states generated by four-wave mixing in an optical cavity. *Phys. Rev. Lett.*, 55(22):2409–2412, Nov 1985.

[10] R. M. Shelby, M. D. Levenson, S. H. Perlmutter, R. G. DeVoe, and D. F. Walls. Broad-band parametric deamplification of quantum noise in an optical fiber. *Phys. Rev. Lett.*, 57:691–694, Aug 1986.

[11] Ling-An Wu, Min Xiao, and H. J. Kimble. Squeezed states of light from an optical parametric oscillator. *J. Opt. Soc. Am. B*, 4(10):1465–1475, Oct 1987.

[12] Min Xiao, Ling-An Wu, and H. J. Kimble. Precision measurement beyond the shot-noise limit. *Phys. Rev. Lett.*, 59:278–281, Jul 1987.

[13] B. Yurke, P. Grangier, R. E. Slusher, and M. J. Potasek. Generating and detecting short-duration pulses of squeezed light. *Phys. Rev. A*, 35:3586–3589, Apr 1987.

[14] R. E. Slusher, B. Yurke, P. Grangier, A. LaPorta, D. F. Walls, and M. Reid. Squeezed-light generation by four-wave mixing near an atomic resonance. *J. Opt. Soc. Am. B*, 4(10):1453–1464, Oct 1987.

[15] D.F. Walls eds. H.J. Kimble. Special issues on squeezed states of light. *J. Opt. Soc. Am. B*, 4:1450–1741, 1987.

[16] S. F. Pereira, Min Xiao, H. J. Kimble, and J. L. Hall. Generation of squeezed light by intracavity frequency doubling. *Phys. Rev. A*, 38:4931–4934, Nov 1988.

[17] A. Sizmann, R.J. Horowicz, G. Wagner, and G. Leuchs. Observation of amplitude squeezing of the up-converted mode in second harmonic generation. *Optics Communications*, 80(2):138 – 142, 1990.

[18] P. Krz, R. Paschotta, K. Fiedler, and J. Mlynek. Bright squeezed light by second-harmonic generation in a monolithic resonator. *EPL (Europhysics Letters)*, 24(6):449, 1993.

[19] R. Paschotta, M. Collett, P. Kürz, K. Fiedler, H. A. Bachor, and J. Mlynek. Bright squeezed light from a singly resonant frequency doubler. *Phys. Rev. Lett.*, 72:3807–3810, Jun 1994.

[20] Shuichiro Inoue, Hitoshi Ohzu, Susumu Machida, and Yoshihisa Yamamoto. Quantum correlation between longitudinal-mode intensities in a multimode squeezed semiconductor laser. *Phys. Rev. A*, 46:2757–2765, Sep 1992.

[21] Yong-Qing Li and Min Xiao. Generation and applications of amplitude-squeezed states of light from semiconductor diode lasers. *Opt. Express*, 2(3):110–117, Feb 1998.

[22] C. F. McCormick, V. Boyer, E. Arimondo, and P. D. Lett. Strong relative intensity squeezing by four-wave mixing in rubidium vapor. *Opt. Lett.*, 32(2):178–180, Jan 2007.

[23] A. Sinatra, J. F. Roch, K. Vigneron, Ph. Grelu, J.-Ph. Poizat, Kaige Wang, and P. Grangier. Quantum-nondemolition measurements using cold trapped atoms: Comparison between theory and experiment. *Phys. Rev. A*, 57:2980–2995, Apr 1998.

[24] Andreas Sizmann and Gerd Leuchs. The optical kerr effect and quantum optics in fibers. *Prog. Opt.*, 39:373–469, 1999.

[25] Ruifang Dong, Joel Heersink, Joel F. Corney, Peter D. Drummond, Ulrik L. Andersen, and Gerd Leuchs. Experimental evidence for raman-induced limits to efficient squeezing in optical fibers. *Opt. Lett.*, 33(2):116–118, Jan 2008.

[26] Jiangrui Gao, Fuyun Cui, Chenyang Xue, Changde Xie, and Peng Kunchi. Generation and application of twin beams from an optical parametric oscillator including an α-cut ktp crystal. *Opt. Lett.*, 23(11):870–872, Jun 1998.

[27] J. Laurat, T. Coudreau, N. Treps, A. Maitre, and C. Fabre. Conditional preparation of a quantum state in the continuous variable regime: Generation of a sub-poissonian state from twin beams. *Phys. Rev. Lett.*, 91:213601, Nov 2003.

[28] V. Boyer, A. M. Marino, and P. D. Lett. Generation of spatially broadband twin beams for quantum imaging. *Phys. Rev. Lett.*, 100:143601, Apr 2008.

[29] Moritz Mehmet, Stefan Ast, Tobias Eberle, Sebastian Steinlechner, Henning Vahlbruch, and Roman Schnabel. Squeezed light at 1550 nm with a quantum noise reduction of 12.3 db. *Opt. Express*, 19(25):25763–25772, Dec 2011.

[30] Tobias Eberle, Sebastian Steinlechner, Jöran Bauchrowitz, Vitus Händchen, Henning Vahlbruch, Moritz Mehmet, Helge Müller-Ebhardt, and Roman Schnabel. Quantum enhancement of the zero-area sagnac interferometer topology for gravitational wave detection. *Phys. Rev. Lett.*, 104:251102, Jun 2010.

[31] Gregory M Harry and the LIGO Scientific Collaboration. Advanced ligo: the next generation of gravitational wave detectors. *Classical and Quantum Gravity*, 27(8):084006, 2010.

[32] P. Grangier, R. E. Slusher, B. Yurke, and A. LaPorta. Squeezed-light enhanced polarization interferometer. *Phys. Rev. Lett.*, 59:2153–2156, Nov 1987.

[33] Min Xiao, Ling-An Wu, and H. J. Kimble. Detection of amplitude modulation with squeezed light for sensitivity beyond the shot-noise limit. *Opt. Lett.*, 13(6):476–478, Jun 1988.

[34] C. D. Nabors and R. M. Shelby. Two-color squeezing and sub-shot-noise signal recovery in doubly resonant optical parametric oscillators. *Phys. Rev. A*, 42:556–559, Jul 1990.

[35] E. S. Polzik, J. Carri, and H. J. Kimble. Spectroscopy with squeezed light. *Phys. Rev. Lett.*, 68(20):3020–3023, May 1992.

[36] Florian Wolfgramm, Alessandro Cerè, Federica A. Beduini, Ana Predojević, Marco Koschorreck, and Morgan W. Mitchell. Squeezed-light optical magnetometry. *Phys. Rev. Lett.*, 105:053601, Jul 2010.

[37] Travis Horrom, Robinjeet Singh, Jonathan P. Dowling, and Eugeniy E. Mikhailov.

Quantum-enhanced magnetometer with low-frequency squeezing. *Phys. Rev. A*, 86:023803, Aug 2012.

[38] Vittorio Giovannetti, Seth Lloyd, and Lorenzo Maccone. Quantum-enhanced measurements: Beating the standard quantum limit. *Science*, 306(5700):1330–1336, 2004.

[39] M. A. Taylor, J. Janousek, V. Daria, J. Knittel, B. Hage, H.-A. Bachor, and W. P. Bowen. Biological measurement beyond the quantum limit. *Nature Photonics*, 7:229–233, March 2013.

[40] R.E. Slusher and B. Yurke. Squeezed light for coherent communications. *Lightwave Technology, Journal of*, 8(3):466 –477, Mar 1990.

[41] N. Gisin and R. Thew. Quantum communication. *Nature Photonics*, 1:165 –171, Mar 2007.

[42] H.K. Lo, T. Spiller, and S. Popescu. *Introduction to Quantum Computation and Information*. World Scientific, 1998.

[43] Z.Y. Ou, S.F. Pereira, and H.J. Kimble. Realization of the einstein-podolsky-rosen paradox for continuous variables in nondegenerate parametric amplification. *Applied Physics B*, 55:265–278, 1992.

[44] A. Furusawa, J. L. Srensen, S. L. Braunstein, C. A. Fuchs, H. J. Kimble, and E. S. Polzik. Unconditional quantum teleportation. *Science*, 282(5389):706–709, 1998.

[45] T. C. Ralph and P. K. Lam. Teleportation with bright squeezed light. *Phys. Rev. Lett.*, 81:5668–5671, Dec 1998.

[46] T. C. Ralph. Continuous variable quantum cryptography. *Phys. Rev. A*, 61:010303, Dec 1999.

[47] S. F. Pereira, Z. Y. Ou, and H. J. Kimble. Quantum communication with correlated nonclassical states. *Phys. Rev. A*, 62:042311, Sep 2000.

[48] B. Kraus and J. I. Cirac. Discrete entanglement distribution with squeezed light. *Phys. Rev. Lett.*, 92:013602, Jan 2004.

[49] J. S. Neergaard-Nielsen, B. Melholt Nielsen, C. Hettich, K. Mølmer, and E. S. Polzik. Generation of a superposition of odd photon number states for quantum information networks. *Phys. Rev. Lett.*, 97:083604, Aug 2006.

[50] Alexei Ourjoumtsev, Rosa Tualle-Brouri, Julien Laurat, and Philippe Grangier. Generating optical schrodinger kittens for quantum information processing. *Science*, 312(5770):83–86, 2006.

[51] Nobuyuki Takei, Takao Aoki, Satoshi Koike, Ken-ichiro Yoshino, Kentaro Wakui, Hidehiro Yonezawa, Takuji Hiraoka, Jun Mizuno, Masahiro Takeoka, Masashi Ban, and Akira Furusawa. Experimental demonstration of quantum teleportation of a squeezed state. *Phys. Rev. A*, 72:042304, Oct 2005.

[52] JL. Le Gout and S. eds. Moiseev. Special issue on quantum memory. *J. Phys. B: At. Mol. Opt. Phys.*, 45:124001–124021, 2012.

[53] A.I. Lvovsky, B.C. Sanders, and W. Tittel. Optical quantum memory. *Nature Photonics*, 3:706–714, 2009.

[54] Jürgen Appel, Eden Figueroa, Dmitry Korystov, M. Lobino, and A. I. Lvovsky. Quantum memory for squeezed light. *Phys. Rev. Lett.*, 100(9):093602, Mar 2008.

[55] Kazuhito Honda, Daisuke Akamatsu, Manabu Arikawa, Yoshihiko Yokoi, Keiichirou Akiba, Satoshi Nagatsuka, Takahito Tanimura, Akira Furusawa, and Mikio Kozuma. Storage and retrieval of a squeezed vacuum. *Physical Review Letters*, 100(9):093601, 2008.

[56] Eden Figueroa, Mirko Lobino, Dmitry Korystov, Jurgen Appel, and A. I. Lvovsky. Propagation of squeezed vacuum under electromagnetically induced transparency. *New Journal of Physics*, 11(1):013044, 2009.

[57] Manabu Arikawa, Kazuhito Honda, Daisuke Akamatsu, Satoshi Nagatsuka, Keiichirou Akiba, Akira Furusawa, and Mikio Kozuma. Quantum memory of a squeezed vacuum for arbitrary frequency sidebands. *Phys. Rev. A*, 81:021605, Feb 2010.

[58] Eugeniy E. Mikhailov, Keisuke Goda, and Nergis Mavalvala. Noninvasive measurements of cavity parameters by use of squeezed vacuum. *Physical Review A (Atomic, Molecular, and Optical Physics)*, 74(3):033817, 2006.

[59] Vincent Boyer, Alberto M. Marino, Raphael C. Pooser, and Paul D. Lett. Entangled images from four-wave mixing. *Science*, 321(5888):544–547, 2008.

[60] Jeremy B. Clark, Zhifan Zhou, Quentin Glorieux, Alberto M. Marino, and Paul D. Lett. Imaging using quantum noise properties of light. *Opt. Express*, 20(15):17050–17058, Jul 2012.

[61] Mari W. Maeda, Prem Kumar, and Jeffrey H. Shapiro. Observation of squeezed noise produced by forward four-wave mixing in sodium vapor. *Opt. Lett.*, 12(3):161–163, Mar 1987.

[62] A. Lambrecht, J.M. Courty, S. Reynaud, and E. Giacobino. Cold atoms: A new medium for quantum optics. *Applied Physics B*, 60:129–134, 1995.

[63] Seng-Tiong Ho, Xiaolong Zhang, and Maria K. Udo. Single-beam squeezed-state generation in semiconductor waveguides with x(3) nonlinearity at below half-band gap. *J. Opt. Soc. Am. B*, 12(9):1537–1549, Sep 1995.

[64] A. M. Fox, M. Dabbicco, G. von Plessen, and J. F. Ryan. Quadrature squeezed light generation by cross-phase modulation in semiconductors. *Opt. Lett.*, 20(24):2523–2525, Dec 1995.

[65] L. Boivin and H. A. Haus. $\chi(3)$ squeezed vacuum generation without a sagnac interferometer. *Opt. Lett.*, 21(2):146–148, Jan 1996.

[66] Moti Margalit, Charles Yu, Erich Ippen, and Hermann Haus. Cross phase modulation squeezing in optical fibers. *Opt. Express*, 2(3):72–76, Feb 1998.

[67] A. B. Matsko, I. Novikova, G. R. Welch, D. Budker, D. F. Kimball, and S. M. Rochester. Vacuum squeezing in atomic media via self-rotation. *Physical Review A*, 66:043815, Oct 2002.

[68] I. Novikova, A. B. Matsko, and G. R. Welch. Large polarization self-rotation in rubidium vapor: application for squeezing of electromagnetic vacuum. *Appl. Phys. Lett.*, 81:193 –+, 2002.

[69] J. Ries, B. Brezger, and A. I. Lvovsky. Experimental vacuum squeezing in rubidium vapor via self-rotation. *Physical Review A*, 68:025801, 2003.

[70] M. T. L. Hsu, G. Hetet, A. Peng, C. C. Harb, H.-A. Bachor, M. T. Johnsson, J. J. Hope, P. K. Lam, A. Dantan, J. Cviklinski, A. Bramati, and M. Pinard. Effect of atomic noise on optical squeezing via polarization self-rotation in a thermal vapor cell. *Physical Review A (Atomic, Molecular, and Optical Physics)*, 73:023806–9, Feb 2006.

[71] Eugeniy E. Mikhailov and Irina Novikova. Low-frequency vacuum squeezing via polarization self-rotation in rb vapor. *Opt. Lett.*, 33(11):1213–1215, 2008.

[72] Eugeniy E. Mikhailov, Arturo Lezama, Thomas W. Noel, and Irina Novikova. Vacuum squeezing via polarization self-rotation and excess noise in hot rb vapors. *Journal of Modern Optics*, 56(18&19):1985–1992, 2009.

[73] Imad H. Agha, Gaétan Messin, and Philippe Grangier. Generation of pulsed and continuous-wave squeezed light with 87rb vapor. *Opt. Express*, 18(5):4198–4205, 2010.

[74] S. Barreiro, P. Valente, H. Failache, and A. Lezama. Polarization squeezing of light by single passage through an atomic vapor. *Phys. Rev. A*, 84:033851, Sep 2011.

[75] N.J. Cerf, G. Leuchs, and E.S. Polzik. *Quantum Information With Continuous Variables of Atoms and Light.* Imperial College Press, 2007.

[76] M. M. Kash, V. A. Sautenkov, A. S. Zibrov, L. Hollberg, G. R. Welch, M. D. Lukin, Y. Rostovtsev, E. S. Fry, and M. O. Scully. Ultraslow group velocity and enhanced nonlinear optical effects in a coherently driven hot atomic gas. *Phys. Rev. Lett.*, 82(26):5229–5232, JUN 28 1999.

[77] Chien Liu, Zachary Dutton, Cyrus H. Behroozi, and Lene Vestergaard Hau. Observation of coherent optical information storage in an atomic medium using halted light pulses. *Nature*, 409:490–493, Jan 25 2001.

[78] D. F. Phillips, A. Fleischhauer, A. Mair, R. L. Walsworth, and M. D. Lukin. Storage of light in atomic vapor. *Phys. Rev. Lett.*, 86(5):783–786, Jan 2001.

[79] Nathaniel B. Phillips, Alexey V. Gorshkov, and Irina Novikova. Optimal light storage in atomic vapor. *Phys. Rev. A*, 78:023801, Aug 2008.

[80] G. Hétet, O. Glöckl, K. A. Pilypas, C. C. Harb, B. C. Buchler, H.-A. Bachor, and P. K. Lam. Squeezed light for bandwidth-limited atom optics experiments at the rubidium d1 line. *Journal of Physics B*, 40:221–226, 2007.

[81] Travis Horrom, Irina Novikova, and Eugeniy E Mikhailov. All-atomic source of squeezed vacuum with full pulse-shape control. *Journal of Physics B: Atomic, Molecular and Optical Physics*, 45(12):124015, 2012.

[82] P. Meystre and M. Sargent III. *Elements of Quantum Optics.* Springer, 4 edition, 2007.

[83] S. M. Rochester, D. S. Hsiung, D. Budker, R. Y. Chiao, D. F. Kimball, and V. V. Yashchuk. Self-rotation of resonant elliptically polarized light in collision-free rubidium vapor. *Phys. Rev. A*, 63(4):043814, Mar 2001.

[84] Anatolii S Chirkin, A A Orlov, and D Yu Parashchuk. Quantum theory of two-mode interactions in optically anisotropic media with cubic nonlinearities: Generation of quadrature- and polarization-squeezed light. *Quantum Electronics*, 23(10):870, 1993.

[85] V. Josse, A. Dantan, L. Vernac, A. Bramati, M. Pinard, and E. Giacobino. Polarization squeezing with cold atoms. *Phys. Rev. Lett.*, 91(10):103601, Sep 2003.

[86] I. Novikova, A. B. Matsko, and G. R. Welch. Large polarization self-rotation in rubidium vapour: application for squeezing of electromagnetic vacuum. *Journal of Modern Optics*, 49(14):2565–2581, 2002.

[87] A. Lezama, P. Valente, H. Failache, M. Martinelli, and P. Nussenzveig. Numerical investigation of the quantum fluctuations of optical fields transmitted through an atomic medium. *Physical Review A*, 77:013806–11, 2008.

[88] W. Wasilewski, K. Jensen, H. Krauter, J. J. Renema, M. V. Balabas, and E. S. Polzik. Quantum noise limited and entanglement-assisted magnetometry. *Phys. Rev. Lett.*, 104:133601, Mar 2010.

[89] P. L. Kelley. Self-focusing of optical beams. *Phys. Rev. Lett.*, 15:1005–1008, Dec 1965.

[90] S. T. Ho, N. C. Wong, and J. H. Shapiro. Single-beam squeezed-state generation in sodium vapor and its self-focusing limitations. *Opt. Lett.*, 16(11):840–842, 1991.

[91] D. Budker, D. F. Kimball, S. M. Rochester, and V. V. Yashchuk. Nonlinear magneto-optical rotation via alignment-to-orientation conversion. *Phys. Rev. Lett.*, 85:2088–2091, Sep 2000.

[92] D. Budker, W. Gawlik, D.F. Kimball, S.M. Rochester, V.V. Yashchuk, and A. Weis. Resonant nonlinear magneto-optical effects in atoms. *Rev. Mod. Phys.*, 74(4):1153–1201, Oct 2002.

[93] A. B. Matsko, I. Novikova, M. S. Zubairy, and G. R. Welch. Nonlinear magneto-optical rotation of elliptically polarized light. *Phys. Rev. A*, 67:043805, Apr 2003.

[94] Irina Novikova, Andrey B. Matsko, and George R. Welch. Influence of a buffer gas on nonlinear magneto-optical polarization rotation. *J. Opt. Soc. Am. B*, 22(1):44–56, Jan 2005.

[95] I. Novikova, A. B. Matsko, and G. R. Welch. Large polarization rotation via atomic coherence. *Opt. Lett.*, 26:1016–1018, Jul 2001.

[96] A. Wojciechowski, E. Corsini, J. Zachorowski, and W. Gawlik. Nonlinear Faraday rotation and detection of superposition states in cold atoms. *Phys Rev A*, 81(5):053420, May 2010.

[97] Daniel A. Steck. Rubidium 87 d line data. Dec 2010.

[98] Dmitry Budker and Michael Romalis. Optical magnetometry. *Nat Phys*, 3:227–234, Apr 2007.

[99] I. Novikova, A. B. Matsko, V. A. Sautenkov, V. L. Velichansky, G. R. Welch, and M. O. Scully. Ac-stark shifts in the nonlinear faraday effect. *Opt. Lett.*, 25:1651–1653, 2000.

[100] E. Arimondo. Coherent population trapping in laser spectroscopy. *Progress in Optics*, XXXV:259–354, 1996.

[101] S. E. Harris. Electromagnetically induced transparency. *Physics Today*, 50(7):36, Jul 1997.

[102] J. P. Marangos. Topical review electromagnetically induced transparency. *J. Mod. Opt.*, 45:471 –+, 1998.

[103] Pavel Kolchin. Electromagnetically-induced-transparency-based paired photon generation. *Phys. Rev. A*, 75:033814, Mar 2007.

[104] M. O. Scully and M. S. Zubairy. *Quantum Optics*. Cambridge University Press, Cambridge, UK, 1997.

[105] Kirk McKenzie, Eugeniy E. Mikhailov, Keisuke Goda, Ping Koy Lam, Nicolai Grosse, Malcolm B. Gray, Nergis Mavalvala, and David E. McClelland. Quantum noise locking. *Journal of Optics B*, 7:S421–S428, 2005.

[106] A. Ratnapala, C. J. Vale, A. G. White, M. D. Harvey, N. R. Heckenberg, and H. Rubinsztein-Dunlop. Laser frequency locking by direct measurement of detuning. *Opt. Lett.*, 29(23):2704–2706, Dec 2004.

[107] S. E. Harris, J. E. Field, and A. Kasapi. Dispersive properties of electromagnetically induced transparency. *Phys. Rev. A*, 46(1):R29 – R32, Jul 1992.

[108] O. Schmidt, R. Wynands, Z. Hussein, and D. Meschede. Steep dispersion and group velocity below c/3000 in coherent population trapping. *Phys. Rev. A*, 53(1):R27 – R30, Jan 1996.

[109] Jürgen Appel, Eden Figueroa, Dmitry Korystov, M. Lobino, and A. I. Lvovsky. Quantum memory for squeezed light. *Physical Review Letters*, 100(9):093602, 2008.

[110] D. Akamatsu, K. Akiba, and M. Kozuma. Electromagnetically induced transparency with squeezed vacuum. *Phys. Rev. Lett.*, 92(20):203602, May 2004.

[111] Daisuke Akamatsu, Yoshihiko Yokoi, Manabu Arikawa, Satoshi Nagatsuka, Takahito Tanimura, Akira Furusawa, and Mikio Kozuma. Ultraslow propagation of squeezed

vacuum pulses with electromagnetically induced transparency. *Physical Review Letters*, 99:153602–4, Oct 2007.

[112] M. Arikawa, K. Honda, D. Akamatsu, Y. Yokoil, K. Akiba, S. Nagatsuka, A. Furusawa, and M. Kozuma. Observation of electromagnetically induced transparency for a squeezed vacuum with the time domain method. *Opt. Express*, 15(19):11849–11854, Sep 2007.

[113] Klemens Hammerer, Anders S. Sørensen, and Eugene S. Polzik. Quantum interface between light and atomic ensembles. *Rev. Mod. Phys.*, 82:1041–1093, Apr 2010.

[114] M. V. Gurudev Dutt, L. Childress, L. Jiang, E. Togan, J. Maze, F. Jelezko, A. S. Zibrov, P. R. Hemmer, and M. D. Lukin. Quantum register based on individual electronic and nuclear spin qubits in diamond. *Science*, 316(5829):1312–1316, 2007.

[115] S. Cortez, O. Krebs, S. Laurent, M. Senes, X. Marie, P. Voisin, R. Ferreira, G. Bastard, J-M. Gérard, and T. Amand. Optically driven spin memory in n-doped inasgaas quantum dots. *Phys. Rev. Lett.*, 89:207401, Oct 2002.

[116] A. I. Lvovsky and M. G. Raymer. Continuous-variable optical quantum-state tomography. *Rev. Mod. Phys.*, 81:299–332, Mar 2009.

[117] Alexander I. Lvovsky, Barry C. Sanders, and Wolfgang Tittel. Optical quantum memory. *Nat Photon*, 3:706–714, Dec 2009.

[118] I. Novikova, R.L. Walsworth, and Y. Xiao. Electromagnetically induced transparency-based slow and stored light in warm atoms. *Laser and Photonics Reviews*, 6(3):333–353, 2012.

[119] Alexey V. Gorshkov, Axel André, Michael Fleischhauer, Anders S. Sørensen, and Mikhail D. Lukin. Universal approach to optimal photon storage in atomic media. *Phys. Rev. Lett.*, 98:123601, Mar 2007.

[120] Alexey V. Gorshkov, Axel André, Mikhail D. Lukin, and Anders S. Sørensen. Photon storage in λ-type optically dense atomic media. i. cavity model. *Phys. Rev. A*, 76:033804, Sep 2007.

[121] Alexey V. Gorshkov, Axel André, Mikhail D. Lukin, and Anders S. Sørensen. Photon storage in λ-type optically dense atomic media. ii. free-space model. *Phys. Rev. A*, 76:033805, Sep 2007.

[122] Alexey V. Gorshkov, Axel André, Mikhail D. Lukin, and Anders S. Sørensen. Photon storage in λ-type optically dense atomic media. iii. effects of inhomogeneous broadening. *Phys. Rev. A*, 76:033806, Sep 2007.

[123] Alexey V. Gorshkov, Tommaso Calarco, Mikhail D. Lukin, and Anders S. Sørensen. Photon storage in λ-type optically dense atomic media. iv. optimal control using gradient ascent. *Phys. Rev. A*, 77:043806, Apr 2008.

[124] Irina Novikova, Alexey V. Gorshkov, David F. Phillips, Anders S. Sørensen, Mikhail D. Lukin, and Ronald L. Walsworth. Optimal control of light pulse storage and retrieval. *Phys. Rev. Lett.*, 98:243602, Jun 2007.

[125] Irina Novikova, Nathaniel B. Phillips, and Alexey V. Gorshkov. Optimal light storage with full pulse-shape control. *Phys. Rev. A*, 78:021802, Aug 2008.

[126] Shanchao Zhang, Shuyu Zhou, M. M. T. Loy, G. K. L. Wong, and Shengwang Du. Optical storage with electromagnetically induced transparency in a dense cold atomic ensemble. *Opt. Lett.*, 36(23):4530–4532, Dec 2011.

[127] I. Novikova and G. R. Welch. Magnetometry in dense coherent media. *J. Mod. Opt.*, 49:349–358, 2002.

[128] D. Budker, D. F. Kimball, S. M. Rochester, V. V. Yashchuk, and M. Zolotorev. Sensitive magnetometry based on nonlinear magneto-optical rotation. *Phys. Rev. A*, 62(4):043403, 2000.

[129] H.C. Seton, J.M.S. Hutchison, and D.M. Bussell. Liquid helium cryostat for squid-based mri receivers. *Cryogenics*, 45(5):348 – 355, 2005.

[130] M. Fleischhauer, A. B. Matsko, and M. O. Scully. Quantum limit of optical magnetometry in the presence of ac stark shifts. *Phys. Rev. A*, 62:013808, Jun 2000.

[131] J. Hald, J. L. Sorensen, C. Schori, and E. S. Polzik. Entanglement transfer from light to atoms. *Journal of Modern Optics*, 47(14-15):2599–2614, 2000.

[132] A. S. Zibrov, I. Novikova, and A. B. Matsko. Observation of ramsey fringes in an atomic cell with buffer gas. *Opt. Lett.*, 26:1311, 2001.

[133] U. Leonhardt and P. Piwnicki. Ultrahigh sensitivity of slow-light gyroscope. *Phys. Rev. A*, 62:055801, Oct 2000.

[134] M. S. Shahriar, G. S. Pati, R. Tripathi, V. Gopal, M. Messall, and K. Salit. Ultrahigh enhancement in absolute and relative rotation sensing using fast and slow light. *Phys. Rev. A*, 75:053807, May 2007.

[135] Yakir Aharonov, Benni Reznik, and Ady Stern. Quantum limitations on superluminal propagation. *Phys. Rev. Lett.*, 81:2190–2193, Sep 1998.

[136] A. Kuzmich, A. Dogariu, L. J. Wang, P. W. Milonni, and R. Y. Chiao. Signal velocity, causality, and quantum noise in superluminal light pulse propagation. *Phys. Rev. Lett.*, 86(18):3925–3929, Apr 2001.

[137] F. Carreño, Oscar G. Calderón, M. A. Antón, and Isabel Gonzalo. Superluminal and slow light in λ-type three-level atoms via squeezed vacuum and spontaneously generated coherence. *Phys. Rev. A*, 71:063805, Jun 2005.

[138] H. J. Kimble, Yuri Levin, Andrey B. Matsko, Kip S. Thorne, and Sergey P. Vyatchanin. Conversion of conventional gravitational-wave interferometers into quantum nondemolition interferometers by modifying their input and/or output optics. *Phys. Rev. D*, 65:022002, 2002.

[139] Simon Chelkowski, Henning Vahlbruch, Boris Hage, Alexander Franzen, Nico Lastzka, Karsten Danzmann, and Roman Schnabel. Experimental characterization of frequency-dependent squeezed light. *Phys. Rev. A*, 71:013806, Jan 2005.

[140] Eugeniy E. Mikhailov, Keisuke Goda, Thomas Corbitt, and Nergis Mavalvala. Frequency-dependent squeeze amplitude attenuation and squeeze angle rotation by electromagnetically induced transparency for gravitational wave interferometers. *LANL e-Print archive*, 2005.

[141] S. Knappe, M. Stahler, C. Affolderbach, A. Taichenachev, V. Yudin, and R. Wynands. Simple parametrization of dark-resonance line shape. *Appl. Phys. B*, 76:57–63, 2003.

[142] A.M. Marino, J.B. Clark, Q. Glorieux, and P.D. Lett. Extracting spatial information from noise measurements of multi-spatial-mode quantum states. *The European Physical Journal D*, 66:1–9, 2012.

[143] Travis Horrom, Salim Balik, Arturo Lezama, Mark D. Havey, and Eugeniy E. Mikhailov. Polarization self-rotation in ultracold atomic ^{87}rb. *Phys. Rev. A*, 83(5):053850, May 2011.

[144] Travis Horrom, Arturo Lezama, Salim Balik, Mark D. Havey, and Eugeniy E. Mikhailov. Quadrature noise in light propagating through a cold ^{87}rb atomic gas. *Journal of Modern Optics*, 58(21):1936–1941, 2011.

[145] S. Balik, M. D. Havey, I. M. Sokolov, and D. V. Kupriyanov. Optical pumping dynamics and near-resonance light scattering in an ultracold sample of ^{87}rb atoms. *Phys. Rev. A*, 79(3):033418, Mar 2009.

[146] G L Gattobigio, T Pohl, G Labeyrie, and R Kaiser. Scaling laws for large magneto-optical traps. *Physica Scripta*, 81(2):025301, 2010.

[147] Joel A. Greenberg, Marcos Oria, Andrew M. C. Dawes, and Daniel J. Gauthier. Absorption-induced trapping in an anisotropic magneto-optical trap. *Opt. Express*, 15(26):17699–17708, Dec 2007.

[148] Yen-Wei Lin, Hung-Chih Chou, Prashant P. Dwivedi, Ying-Cheng Chen, and Ite A. Yu. Using a pair of rectangular coils in the mot for the production of cold atom clouds with large optical density. *Opt. Express*, 16(6):3753–3761, Mar 2008.

[149] P. Valente, H. Failache, and A. Lezama. Comparative study of the transient evolution of hanle electromagnetically induced transparency and absorption resonances. *Phys. Rev. A*, 65(2):023814, Jan 2002.

VITA

Travis Horrom

Name: Travis Scott Horrom

Date and Place of Birth: May 8, 1986, Baltimore, MD, USA

Address: Department of Physics, College of William and Mary,
P.O. Box 8795. Williamsburg, VA 23185-8795

E-mails: tshorrom@email.wm.edu, tshorrom@gmail.com

Education

- Ph.D. Physics, College of William and Mary, 2013.
- M.S. Physics, College of William and Mary, 2010.
- B.A. Physics, St. Mary's College of Maryland, 2008.

Research Experience

- Experimental Quantum Optics Group. College of William and Mary.

  -"Quantum Squeezed Light Studies." William and Mary. Fall 2009-Spring 2013.

  -"Noise/PSR in Cold Atoms." Collaboration (WM, ODU, IFFC). Old Dominion University. Summer 2010.

  -"Atomic Clock Experiment." William and Mary. Summer 2009.
- Senior Research Project. St. Mary's College of MD. - "Study of an Ultrafast Mode-Locked Laser System." Patuxent Naval Air Station. Fall 2007-Spring 2008.

- Summer Undergraduate Research Fellowship. National Institute of Standards and Technology. -“Errors in FTIR Spectrophotometers.” NIST Optical Technology Division. Summer 2007.

Teaching Experience

- Teaching Assistant. Experimental Modern Physics, Spring Semester 2010, 2011.
- Teaching Assistant. General Physics Laboratory, Fall Semester 2009.
- Teaching Assistant. Astronomy Laboratory, Fall Semester 2008, Spring Semester 2009.

Honors and Awards

- NASA Virginia Space Grant Consortium Graduate Research Fellowship, 2012-2013.
- Arts & Science OGSR/Graduate Student Association Conference Funds, College of William and Mary, 2012, 2011.
- Excellence in Natural & Computational Sciences honorable mention. Graduate Research Symposium, Williamsburg, VA, 2011.
- William and Mary A&S Graduate Student Research Grant, 2010.
- Physics Department Award. St. Mary’s College of MD, 2008.
- NIST Summer Undergraduate Research Fellowship, Summer 2007.

Publications

- Travis Horrom, Gleb Romanov, Irina Novikova, and Eugeniy E. Mikhailov. All-atomic generation and noise-quadrature filtering of squeezed vacuum in hot Rb vapor. *Journal of Modern Optics*, 2012.

- Travis Horrom, Irina Novikova, and Eugeniy E Mikhailov. All-atomic source of squeezed vacuum with full pulse-shape control. *Journal of Physics B: Atomic, Molecular and Optical Physics*, 45(12):124015, 2012.

- Travis Horrom, Robinjeet Singh, Jonathan P. Dowling, and Eugeniy E. Mikhailov. Quantum-enhanced magnetometer with low-frequency squeezing. *Phys. Rev. A*, 86:023803, 2012.

- Travis Horrom, Arturo Lezama, Salim Balik, Mark D. Havey, and Eugeniy E. Mikhailov. Quadrature noise in light propagating through a cold ^{87}Rb atomic gas. *Journal of Modern Optics*, 58(21):1936, 2011.

- Travis Horrom, Salim Balik, Arturo Lezama, Mark D. Havey, and Eugeniy E. Mikhailov. Polarization self-rotation in ultracold atomic ^{87}Rb. *Phys. Rev. A*, 83(5):053850, 2011.

- Eugeniy E. Mikhialov, Travis Horrom, Nathan Belcher, and Irina Novikova. Performance of a prototype atomic clock based on lin||lin coherent population trapping resonances in Rb atomic vapor. *J. Opt. Soc. Am. B*, 27(3), 2010